Continuous Hydrothermal Synthesis of Nanomaterials for Rechargeable Battery Applications

Ian David Johnson

A thesis submitted to

University College London

in partial fulfilment of the requirements for the degree of

Doctor in Engineering

Supervisor: Professor Jawwad Darr

Department of Chemistry,
University College London,
20 Gordon Street,
London, WC1H OAJ

2017

Declaration

I, Ian David Johnson, confirm that the work presented in this thesis is my own. Where information has been derived from other sources, I confirm that this has been indicated in the thesis.

Ian D. Johnson

Abstract

This thesis investigates Continuous Hydrothermal Flow Synthesis (CHFS) as a method to produce materials for rechargeable batteries. The key advantages of this technology are the scalability (up to 2 kg h^{-1} production rate), rapidity (synthesis time on order of seconds) and low reaction temperature (≤ 400 °C) of this method, which is capable of producing materials in the nanoscale. Nanoparticles (< 100 nm diameter) are of high interest for rechargeable battery applications, due to their high surface area and enhanced charge/discharge kinetics.

Various materials (and their doped analogues) for Li-ion and Mg-ion batteries were made, including the olivine family of materials ($LiFePO_4$ and $LiMnPO_4$), layered oxides ($LiCoO_2$ and $LiNi_xMn_yCo_zO_2$) and spinels ($MgCr_2O_4$). Many of these phases have never been synthesised previously *via* CHFS, and display enhanced performance compared to other literature reports.

The effects of dopants on the crystallography and electrochemical performance of these compounds were examined using a variety of techniques, including EXAFS, muon spectroscopy and Rietveld refinement. This allowed the discovery of novel composition-structure-property relationships, and the optimisation of arrays of materials across a phase diagram.

In summary, CHFS has been employed to generate novel battery materials at semi-industrial scale, which were evaluated for electrochemical performance.

Acknowledgements

Firstly, I would like to thank my supervisor, Professor Jawwad Darr, for all his help and support throughout this PhD. He has been so encouraging of my ideas, and always had time for me. Most importantly, he has always been extremely generous with food and drink at group social events. We were always going to get on.

I should also acknowledge the input of former group members who helped to train me on the CHFS reactors – Dr. Neel Makwana and Dr. Clement Denis deserve special praise. I would also like to thank all members of the CMTG during my time there, for making the group what it is, and being such a friendly bunch – Liam, Tom, Chris, Carlos, Marco, Kalyani, Meggi, Dustin, Charlotte, Paul and Alistair. I would like to specially mention the support of Dr. Pete Marchand and Dr. Dougal Howard, who provided excellent advice, and are very good friends. On that note, I should also acknowledge Ben Williamson – broagh!

For technical assistance with UCL equipment, I would like to acknowledge Mr. Martin Vickers, Dr. Jeremy Cockcroft, Prof. John McArthur and Dr. Steven Firth among others.

I would like to thank the EPSRC for partially funding my PhD, without which it would not have been possible!

Additionally, Professor Jordi Cabana at the University of Illinois at Chicago was instrumental in kick-starting my multivalent-ion battery research. I am extremely grateful to him for the opportunity to go to UIC, which I count as the highlight of my PhD.

Finally, I would like to thank my friends and family for their love and support. Special thanks go to Mum and Dad, who “helped me get to where I am today”. Also, to my dear wife Gaby, thank you so much.

This thesis is dedicated to my grandparents, Peter and Shiela Galvin, who were both extremely supportive of me throughout my university years, and sadly passed away during the course of this thesis.

Publications

Publications relating to the work presented in this thesis:

1. Johnson, I. D., Loveridge, M., Bhagat, R. & Darr, J. A. Mapping Structure-Composition-Property Relationships in V and Fe Doped $LiMnPO_4$ Cathodes for Lithium-Ion Batteries. *ACS Comb. Sci.* **18,** 665−672 (2016).

2. Loveridge, M. J. *et al.* Towards High Capacity Li-ion Batteries Based on Silicon-Graphene Composite Anodes and Sub-micron V-doped $LiFePO_4$ Cathodes. *Sci. Rep.* **6,** 37787 (2016).

3. Johnson, I. D. *et al.* High power Nb-doped $LiFePO_4$ Li-ion battery cathodes; pilot-scale synthesis and electrochemical properties. *J. Power Sources* **326,** 476–481 (2016).

4. Johnson, I. D. *et al.* Pilot-scale continuous synthesis of a vanadium-doped $LiFePO_4$/C nanocomposite high-rate cathodes for lithium-ion batteries. *J. Power Sources* **302,** 410–418 (2016).

Other publications:

1. Evans, G. P. *et al.* Room temperature vanadium dioxide–carbon nanotube gas sensors made via continuous hydrothermal flow synthesis. *Sensors Actuators B Chem.* (2017). doi:10.1016/j.snb.2017.07.152

2. Howard, D. P. *et al*. Conducting Al and Ga-doped zinc oxides; rapid optimisation and scale-up. *J. Mater. Chem. A* **4**, 12774 (2016).

3. Lübke, M. *et al*. High power nano-Nb_2O_5 negative electrodes for lithium-ion batteries. *Electrochim. Acta* **192**, 363–369 (2016).

4. Lübke, M. *et al*. High power TiO_2 and high capacity Sn-doped TiO_2 nanomaterial anodes for lithium-ion batteries. *J. Power Sources* **294**, 94–102 (2015).

Table of Contents

List of Figures

List of Tables

List of Equations

List of Symbols

Nucleation and Growth Theory

°C	Degrees Centigrade
C	Concentration
μ	Chemical Potential
G	Gibbs Free Energy
T	Temperature
S	Degree of Supersaturation
γ	Interfacial Energy
r	Nuclei Radius
v	Molecular Volume
J	Nucleation Rate
k	Rate Constant
D	Diffusion Coefficient
s	Solubility
C_p	Specific Heat Capacity
ε	Dielectric Constant
K_w	Ionic Product

Properties of Supercritical Water

R_e	Reynolds Number
ρ	Density
d	Inner pipe diameter
v	Fluid Velocity
μ	Fluid Viscosity
Q	Flow Rate

Electrochemistry

V	Voltage
Λ	Capacity
I	Current
D_{Li}	Lithium Diffusion Coefficient
v	Scan Rate

Rietveld Refinement

y	Intensity

Particle Size Characterisation

S	Specific Surface Area
D_S	Average Particle Diameter

Muon Spectroscopy

μ	Muon
v	Neutrino
Δ	Local Field Distribution
v_{Li}	Li^+ hopping rate

List of Abbreviations

Abbreviation	Meaning
1D	One-dimensional
2D	Two-dimensional
3D	Three-dimensional
BET	Brunauer–Emmett–Teller
BPR	Back-Pressure Regulator
CCCV	Constant-Current Constant-Voltage
CCM	Central Collision Mixer
CHFS	Continuous Hydrothermal Flow Synthesis
CHN	Carbon Hydrogen Nitrogen
CJM	Confined Jet Mixer
CTAB	hexadecyltrimethylammonium bromide
CV	Cyclic Voltammetry
D.I.	Deionised
DEC	Diethyl Carbonate
DFT	Density Functional Theory
DMC	Dimethyl Carbonate
DSC	Differential Scanning Calorimetry
EC	Ethylene Carbonate
EDS	Energy-Dispersive X-Ray Spectroscopy
EV	Electric Vehicle
EXAFS	Extended X-Ray Absorption Spectroscopy
FEC	Fluorethylene Carbonate
FE-SEM	Field-Emission Scanning Electron Microscope
FLG	Few-Layer Graphene
GUI	Graphical User Interface
HPLC	High-Performance Liquid Chromatography
HPRV	High Pressure Relief Valve
ICP-AES	Inductively-Coupled Plasma Atomic Emission Spectroscopy
IR	Infrared
LF	Longitudinal Field
LSW	Lifshitz-Slyozov-Wagner
MAUD	Material Analysis Using Diffraction
NMP	N-Methyl Pyrrolidinone
NMR	Nuclear Magnetic Resonance
PAA	Polyacrylic Acid
PDF	Powder Diffraction File
PEEK	Polyether ether ketone
PFA	Perfluoroalkoxy
PHEV	Plug-in Hybrid Electric Vehicle

Abbreviation	Meaning
ppm	parts per million
PVDF	Polyvinylidine Fluoride
rpm	rotations per minute
SEI	Solid-Electrolyte Interphase
TEM	Transmission Electron Microscopy
TGA	Thermogravimetric Analysis
UCL	University College London
USABC	United States Advanced Battery Consortium
VC	Vinylidine Carbonate
VESTA	Visualisation for Electronic and Structural Analysis
WMG	Warwick Manufacturing Group
XPS	X-Ray Photoelectron Spectroscopy
XRD	X-Ray Diffraction
ZF	Zero Applied Field
μSR	Muon Spectroscopy

1. Literature review

1.1. Nanoparticles

Nanoparticles are defined as materials with at least one dimension in the range 1 – 100 nm.[1] They are termed "nanoparticles" independent of morphology, and include 3D structures (e.g. spheres and cuboids),[2,3] 2D structures (e.g. sheets and ribbons),[4] and 1D structures (e.g. rods and tubes),[5] and can be composed of organic,[6] inorganic,[7] and metallic matter.[8] Recently, there has been increasing academic and industrial interest in the synthesis and production of nanoparticles for a variety of applications,[9] such as healthcare,[8] catalysis,[10] and energy storage among others.[11]

As particles become smaller than 100 nm, their surface area per unit mass increases considerably (Figure 1.1). Therefore, if the desirable property of a material is determined by its particle surface, nanosizing the material should make it more effective. In addition, many materials of industrial interest are composed of expensive and/or rare metals, and therefore increasing material activity by nanosizing can reduce the amount required, lowering the cost of the end application or device.[12]

Moreover, the fundamental properties of a material can change as it is nanosized, such as its chemical reactivity and its magnetic, electronic, optical and mechanical properties. For example, Cu nanoparticles have been shown to fracture under applied strain *via* a different mechanism compared to bulk Cu, and exhibit remarkably different mechanical properties as a result.[13] Gold is largely inert to chemical reaction in the bulk phase, but is an effective CO oxidation catalyst in nanoparticle form.[10] NiO is another interesting case, where it becomes magnetic below a particle size of ~50 nm.[11,14] In summary, nanoparticles are of high academic interest, and also present exciting opportunities for application in a variety of industries.

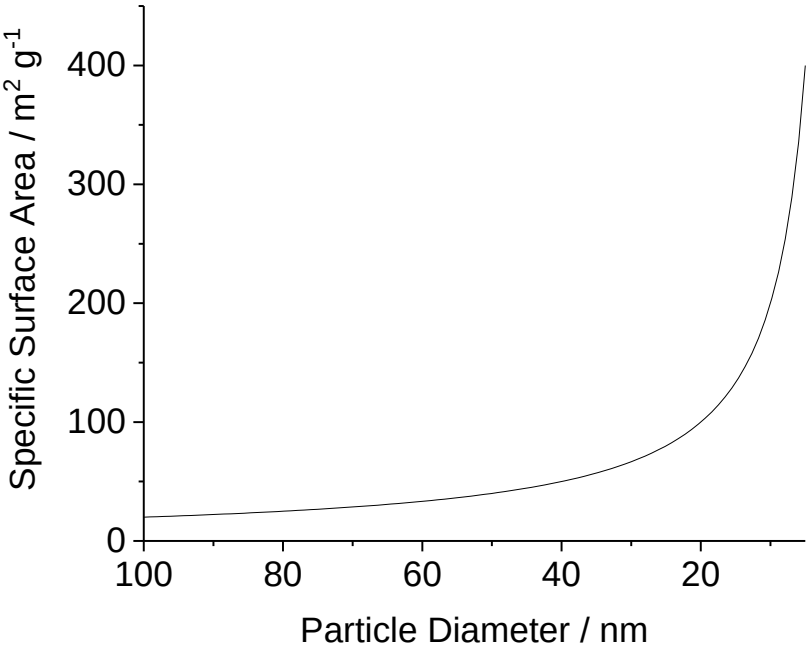

Figure 1.1 – The effect of reducing particle diameter (from 100 nm to 5 nm) on specific surface area, assuming spherical particle morphology and an arbitrary density of 3 g cm^{-3}.

1.1.1. Synthesis Methods

Ideally, nanoparticle synthesis methods should: be rapid, have low reaction temperature, use simple apparatus, be high-yield and produce high-performance particles. The synthesis of nanoparticles can be divided into two broad groups – known as "Top-Down" and "Bottom-Up" synthesis. "Top-Down" methods involve taking bulk particles (of one or multiple phases) and breaking them down into nanoparticles. In contrast, "Bottom-Up" methods build nanoparticles from smaller constituents (ions and atoms). A schematic of the two methods is provided in Figure 1.2.

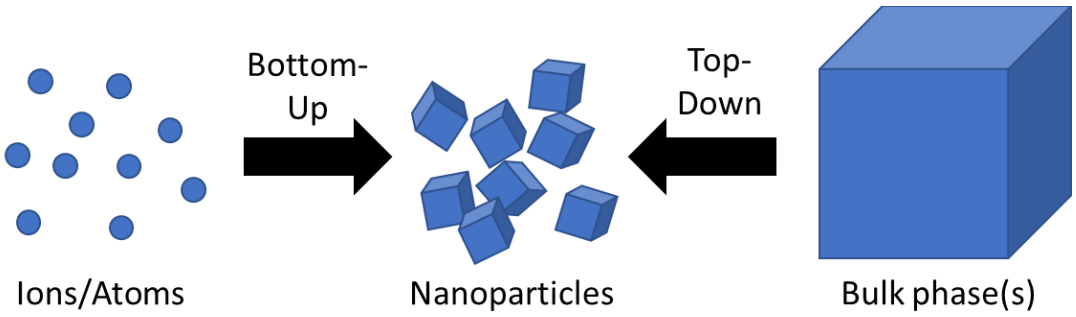

Figure 1.2 – A schematic of Top-Down and Bottom-Up synthesis methods.

1.1.1.1. Top-Down Synthesis Methods

Top-Down synthesis methods are comprised of mechanical attrition (ball-milling), lithography and etching techniques. Lithography and etching involve nanoscale pattern formation (or pattern transfer) onto a bulk substrate, and while they are interesting academically, they are not suitable for industrial-scale synthesis.[15,16] The most common industrial top-down method is ball-milling, where bulk precursor(s) are broken down by grinding action. If there are multiple precursors, these will typically require additional heating and grinding steps to form the new, nano-structured phase *via* a solid-state reaction.[17] Ball-milling combined with solid-state synthesis has been very successful for producing nanoparticles at the industrial scale due to the comparatively simple synthesis apparatus and ability to use solid feedstocks (negating the use of expensive solvents). However, there are significant drawbacks to this method; the heating and grinding steps are typically time-intensive (hour or day timescales) and energy-intensive (reaction temperatures > 1000 °C). Moreover, due to the relative difficulty in mixing solids, the combined precursors will often contain regions rich (and poor) in either precursor (Figure 1.3). Therefore, the reaction to form the new phase only occurs at the boundary of the two precursors, and often the inhomogeneity present in the mixture is transferred to the products, manifesting as inhomogeneous distributions of elements.

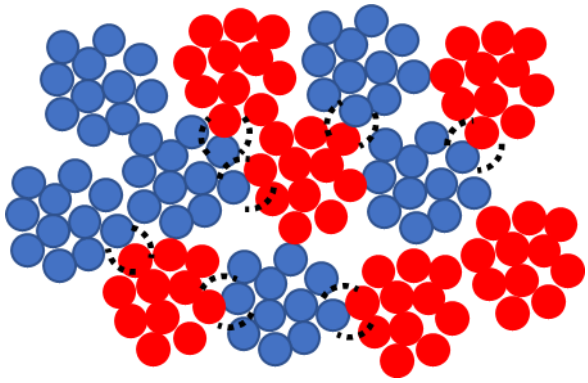

Figure 1.3 – A schematic of the solid-state reaction between two precursors (red and blue). The reaction primarily occurs at the interface between agglomerates of the two phases, as indicated by the dotted lines.

It is clear, therefore, that developing lower temperature and more rapid synthetic techniques that produce more homogeneous products is of great importance to industry, and for these reasons bottom-up approaches are being investigated to replace traditional top-down techniques.

1.1.1.2. Bottom-Up Synthesis Methods

There is a very wide array of bottom-up methods that have been explored in recent years; these include hydrothermal,[7] solvothermal,[18] emulsion-drying,[19,20] spray pyrolysis,[21,22] sol-gel,[23,24] and precipitation.[25,26] The potential precursors of these reactions are typically much more varied than solid-state synthesis; the waste products (e.g. counter-ions) must only be soluble in the reaction solvent, whereas solid-state by-products are usually gaseous to avoid impurity phases. Furthermore, the reaction solvent itself can be modified. Therefore, there is intrinsically greater optimisation achievable in bottom-up compared to top-down methods due to the higher number of reaction variables.

Sol-gel methods involve combining precursors in solution, which undergoes partial reaction to form a stable suspension of particles in solvent (the sol). This sol slowly evolves towards the gel system by forming enmeshed 3D networks of solvent and particles. The gel is then aged, where the networks of particles convert to a solid mass and expel solvent. Finally, the remaining aged gel is dried and heated to remove any remaining solvent, and convert surface hydroxide species to oxide.[23,24] If the solvent decomposes to form carbon, this technique can successfully make enmeshed networks of carbon and final product phase.[27–30]

Emulsion-drying is very similar to the sol-gel method; aqueous precursors are dispersed in an oil phase, forming a colloidal intermediate, which sediments from the oil phase. This sediment is dried and calcined to form the product. This technique successfully reduces agglomeration of the intermediate particles, reducing primary particle size of the product.[19,20]

The precipitation method is akin to conventional solid-state synthesis in many respects, except one of the reacting phases is liquid as opposed to solid. Therefore, solid precursor is combined with an liquid precursor (either aqueous or dissolved in solvent) to form a slurry, dried and heat-treated to produce the product phase.[25,26]

Spray pyrolysis requires atomised precursors (using peristalsis or ultrasound) dispersed in a carrier gas. The dispersion is flowed into a heated reactor section, where

solvent evaporates from the droplets of precursor and forms the product phase. This can successfully produce nanosized particles, although often with low crystallinity, and can require calcining to form the desired product.[21,22]

While these methods possess their own distinct advantages, the batch hydrothermal method can be regarded as the most industrially relevant, due to the low cost and environmental compatibility of the water solvent.[7,31] Before discussing the hydrothermal method in detail, it is first important to explore the nucleation and growth dynamics of nanoparticles from liquid and gas phases, which is the subject of the next section.

1.1.2. Nanoparticle Formation Dynamics

Nanoparticles form from both liquid and gas media in five discrete steps: i) precursor formation, ii) nucleation, iii) growth, iv) ageing/coarsening and v) termination.[31–33] Precursor formation is the initial reaction of the solvated precursors to form a zero-charge complex, where the example in the aqueous case is given in Equation 1.1.

$$M^{z+}(H_2O)_n \rightleftharpoons [M(OH)_z(H_2O)_{n-z}]^0 + zH^+$$

Equation 1.1 – The formation of the zero-charge precursor from hydrated metal cations, where *z* is the formal charge of the metal ion, and *n* is the degree of hydration of the aqueous metal precursor.

The zero-charge complex effectively "polymerises" *via* condensation of the zero-charge precursor to form an initial solid phase (nucleation), which reacts further with aqueous precursors (growth) to grow larger until the precursors are exhausted. Beyond this point, larger particles form from interactions between the solid particles produced from the growth phase (ageing/coarsening). Termination occurs when the particles stop growing.

These processes can be visualised by examining the concentration of zero-charge complex as a function of reaction (Figure 1.4), as described by the LaMer model,[33] and the number/size of particles generated (Figure 1.5) as a function time. The first process (i) is the rapid formation of the zero-charge complex precursor at the beginning of the reaction; no particles are formed until the concentration of the precursor reaches C_{min}, the critical concentration required for nucleation. Beyond this concentration, nucleation rate increases abruptly and nuclei are formed extremely rapidly (Figure

1.5). If the nucleation rate is faster than the precursor generation rate (as it often is), the precursor concentration decreases sharply after the onset of nucleation, giving a concentration maximum within the nucleation step, C_{max}. As the concentration decreases to C_{min}, the nucleation rate is severely reduced, and precursor preferentially reacts with existing nuclei. The growth process is a first or second order kinetic process, and is therefore faster than nucleation at concentrations close to C_{min} (which is typically a much higher order kinetic process as discussed in Section 1.1.2.1). However, if the concentration > C_{min} for a significant period of time, both nucleation and growth can occur simultaneously, and leads to large particle size distributions as the primary nuclei grow larger than the later nuclei. It is therefore important to separate the nucleation and growth steps in synthesis to ensure controlled growth to give more uniform particle sizes. Growth continues until the precursor concentration is reduced to C_s, the solubility limit of the solid phase. At this point, ageing of the particles in suspension *via* processes such as Ostwald ripening (discussed in Section 1.1.2.3) and aggregation generate larger particles at the expense of smaller ones, decreasing particle number and increasing particle size. When the reaction is terminated, all of the above processes stop, and the particle sizes and number remain constant.

It is important to differentiate termination of crystallite size growth and particle size growth. In practise, it is relatively facile to terminate the former by reducing the temperature, or removing the products from the reaction mixture, preventing further chemical reactions at the surfaces of particles. However, particle size growth will inevitably continue as crystallites aggregate in suspension unless they are stabilised, which can be achieved using steric or electrostatic stabilisation.[23] All samples produced in this thesis were dried after synthesis to give aggregates of nanoparticles, so for this thesis "termination" is defined as the end of crystallite growth.

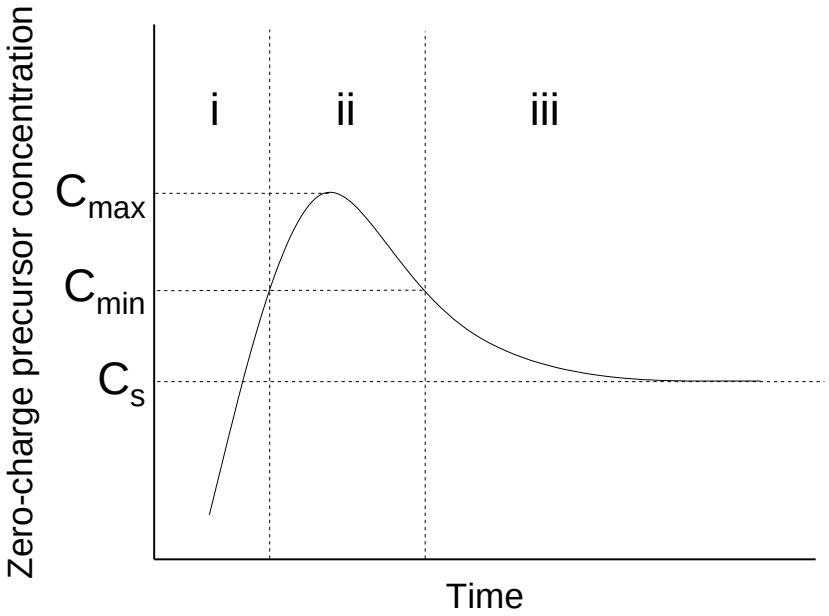

Figure 1.4 – The zero-charge precursor concentration as a function of time during precipitation of the solid phase, with the various steps of formation indicated by the vertical dashed lines. The solubility of the solid phase (C_s), the critical concentration of nucleation (C_{min}) and maximum concentration (C_{max}) are indicated by horizontal dashed lines. Adapted with permission from "LaMer, V. K. & Dinegar, R. H. Theory, Production and Mechanism of Formation of Monodispersed Hydrosols. *J. Am. Chem. Soc.* **72**, 4847–4854 (1950)". Copyright 1950 American Chemical Society. [33]

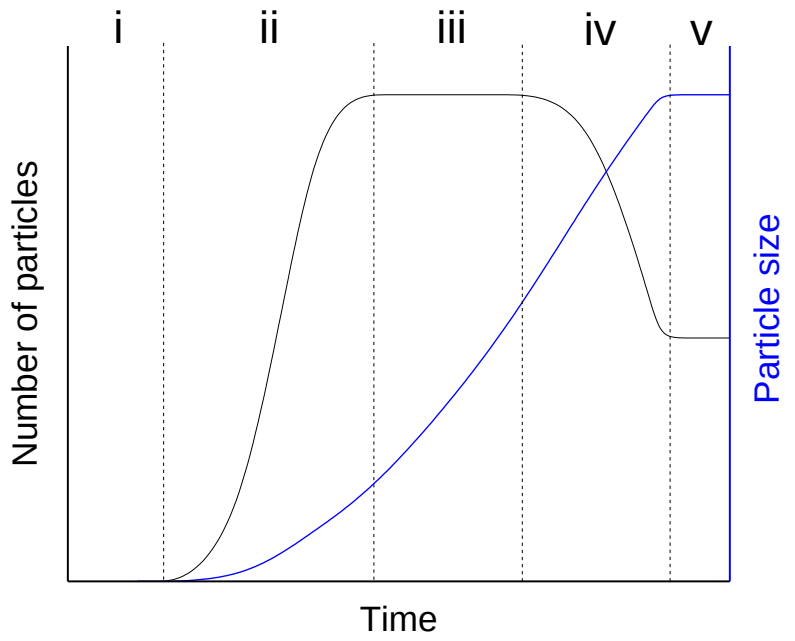

Figure 1.5 – The change in particle number and size during the various stages of particle formation, assuming the nucleation and growth steps are reasonably separated.[32]

1.1.2.1. Nucleation Dynamics

This section discusses the parameters affecting the size and rate of formation of nuclei. The free enthalpy change of nuclei P_n (generated from *n* molecules of precursor P) depends upon the difference in chemical potential ($\mu_s - \mu_L$) between the solid (μ_s) and solution (μ_L), and includes a contribution from the surface energy of the nucleus ($A\gamma$), where *A* is the surface area of the solid, and γ is the interfacial energy (Equation 1.2).[34]

$$\Delta G = n(\mu_s - \mu_L) + A\gamma$$

Equation 1.2 – The free enthalpy change of nuclei forming from solvated precursors.

Making the approximation that chemical activity is equal to concentration, the difference in chemical potential can be expressed according to Equation 1.3, where C_S is the solubility of the solid phase, C_L is the precursor concentration in solution, and *S* is the supersaturation ratio, C_S/C_L.

$$(\mu_s - \mu_L) = kTln(C_s/C_L) = -kTlnS$$

Equation 1.3 – The chemical potential difference expressed in terms of supersaturation ratio, *S*.

Assuming spherical nuclei, the free energy of nucleation can be expressed according to Equation 1.4, where *r* is the nuclei radius, *v* is the molecular volume of the precursors, and *n* is the number of molecules of precursor.

$$\Delta G = -nkTlnS + n^{2/3}(36\pi v^2)^{1/3}\gamma$$

Equation 1.4 – The free enthalpy of nucleation expressed in terms of supersaturation ratio *S*, nuclei volume *v* and precursor molecules *n*.

Under supersaturated conditions ($S > 1$), and assuming a positive interfacial energy, the first term in the free energy equation is negative, and the second is positive. Plotting ΔG as a function of precursor molecules *n* yields the function plotted in Figure 1.6. The formation of small nuclei ($n < Q$) is energetically unfavourable, whereas larger nuclei ($n > Q$) are favourable. There is a free energy maximum, ΔG^*, which is an effective transition state and activation energy barrier which potential nuclei must pass through in order to nucleate.

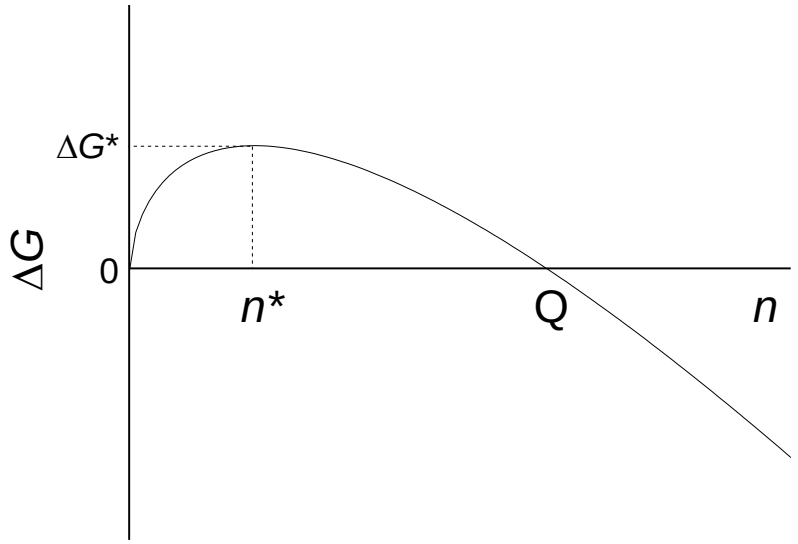

Figure 1.6 – Variation in free energy (ΔG) as a function of precursor molecules n. The number of precursor molecules in a critical nucleus, n^*, the activation energy for nucleation, ΔG^*, and the point where $\Delta G = 0$, Q, are indicated.[32]

The number of precursor molecules contained within this transition state is defined by the point where the first derivative $\delta(\Delta G)/\delta n = 0$. This gives the number of precursor molecules in a critical nucleus, n^*, as described in Equation 1.5, and the activation energy, ΔG^*, as described in Equation 1.6.

$$n^* = \frac{32\pi\gamma^3 v^2}{3(kTlnS)^3}$$

Equation 1.5 – The size of the critical nucleus, n^*, expressed in terms of surface energy γ, molecular volume v, temperature T and supersaturation ratio S.

$$\Delta G^* = \frac{16\pi\gamma^3 v^2}{3(kTlnS)^2}$$

Equation 1.6 – The size of the activation energy barrier, ΔG^*, expressed in terms of surface energy γ, molecular volume v, temperature T and supersaturation ratio S.

n^* can be converted to a critical radius, r^* as given by Equation 1.7. Higher surface energies increase r^*, whereas higher temperatures or greater degrees of supersaturation decrease r^*. The rate at which critical nuclei form, J, depends on the nucleation activation energy, ΔG_N, which contains the activation energy term previously derived (ΔG^*), but also includes the activation energy for the condensation reaction necessary to grow the nuclei (olation and/or oxolation), ΔG^R, and is typically 35 kJ mol^{-1}, although acid or base catalysis can reduce this by an order of magnitude.[35] The J_0 term is the collision frequency between precursor molecules (Equation 1.8).

$$r^* = \frac{2\gamma v}{kTlnS}$$

Equation 1.7 – The size of the critical nucleus radius, r^*, expressed in terms of surface energy γ, molecular volume v, temperature T and supersaturation ratio S.

$$J = J_0 \exp - \left[\frac{\Delta G^* + \Delta G^R}{kT}\right] = J_0' \exp\left[\frac{-16\pi\gamma^3 v^2}{3(kT)^3(lnS)^2}\right]$$

Equation 1.8 – The nucleation rate J, where $J_0' = J_0\exp(-\Delta G^R/kT)$.

Within a narrow concentration range, it is possible to express J more simply as $J = k_n C^n$, where $n \sim n^*$.[34] Therefore, as n^* is usually greater than 2, the kinetics of nucleation are of higher order than growth kinetics, as stated earlier.

1.1.2.2. Growth Dynamics

Once nuclei have formed, they grow from solution by two distinct mechanisms: diffusion-limited growth and growth limited by surface reaction, where the rate-limiting step is diffusion of the precursor to the particle surface, or surface reaction prior to growth, respectively.

Diffusion-limited growth can be expressed according to Equation 1.9, where $\delta r/\delta t$ is the rate of radius (r) growth as a function of time (t), C_s is the solubility of the solid and D is the diffusion coefficient of the solute with concentration C and molar volume v.[32,34]

$$\frac{\delta r}{\delta t} = \frac{D(C - C_S)v}{r}$$

Equation 1.9 – The rate of particle growth under the diffusion-limited growth regime.

In contrast, surface reaction-limited growth is determined by Equation 1.10, where k_m is a rate constant, and C_m is the approximate number of surface precursor molecules on the nuclei.

$$\frac{\delta r}{\delta t} = k_m r^2 C_m$$

Equation 1.10 – The rate of particle growth under the surface reaction-limited growth regime.

The key difference between these mechanisms is the effect of particle size upon the rate of growth; larger particles grow more slowly with diffusion-limited growth, whereas they grow faster under surface-reaction limited growth. The parameters which

can affect both nucleation and growth from the expressions derived in this section are temperature, reaction time, and precursor concentration (specifically the supersaturation ratio). It is vitally important that both growth and nucleation are controlled to target particles of a desired composition, size and particle-size distributions.

1.1.2.3. Ageing/Coarsening Dynamics

At the end of the growth stage, particle-particle interactions grow in dominance as particle growth mechanisms. These consist of coalescence, oriented attachment, Ostwald ripening, and agglomeration.

Agglomeration is driven by the interfacial energy of the particle surface, which is especially high for nanoparticles. Nanoparticles will agglomerate in suspension unless they are stabilised by steric surface agents, or by changing their surface charge to create sufficient repulsion between them.[23] However, to produce dry nanoparticulate powders (which was necessary throughout this thesis), agglomeration is almost unavoidable.

Oriented attachment and coalescence are very similar ageing mechanisms; both describe when two particles chemically fuse together to form a larger particle. Oriented attachment describes two particles joined on a particular crystallographic plane,[36] whereas coalescence describes particles fused together with no preferred attachment plane. Such fused particles can be single crystals or polycrystalline depending on the ageing time of the specific reaction.

Ostwald ripening is the process where larger particles grow whilst consuming smaller particles. This is due to the increased solubility of smaller particles as described by the Gibbs-Kelvin equation (Equation 1.11), where s_r is the solubility of a particle of radius r and s_∞ is the solubility of a particle of infinite radius (flat surface). Therefore, smaller particles will preferentially dissolve during ageing and grow on larger particles.

$$s_r = s_\infty \exp\left(\frac{2\gamma v}{kTr}\right)$$

Equation 1.11 – The solubility of a particle of radius *r*.

The mathematical description of Ostwald ripening is described by Lifshitz-Slyozov-Wagner (LSW) theory.[37,38] The derivation of LSW theory is complex, but the main effect of Ostwald ripening on particle size is shown in Equation 1.12, where $\langle r \rangle$ is the average particle radius, $\langle r_0 \rangle$ is the average initial particle radius and *D* is the diffusion coefficient of the constituent particle material. The growth of particle radius is therefore proportional to the cube root of time, and therefore reducing reaction time is the simplest way to minimise Ostwald ripening.

$$\langle r \rangle^3 - \langle r_0 \rangle^3 = \frac{8\gamma S_\infty v^2 D}{9kT} t$$

Equation 1.12 – The effect of Ostwald ripening on particle size as a function of time.

1.1.3. Effect of Reaction Media on Nanoparticle Synthesis

1.1.3.1. Hydrothermal and Solvothermal Synthesis (Batch)

Common methods for solid state synthesis are hydrothermal and solvothermal syntheses, where hydrothermal synthesis is a subset of solvothermal synthesis, employing water solvent specifically.[7,23,39,40] In both methods, the solvents and precursors are placed inside sealed vessels (such as an autoclave), where the solid phase nucleates upon heating for a set reaction time. The autogenous pressure generated when solvents are heated in a sealed vessel keeps them in a predominantly liquid state, meaning they can be heated to temperatures well above their atmospheric pressure boiling points. While some syntheses use high enough temperatures to change the phase of solvent to a supercritical fluid (discussed in Section 1.1.3.2),[40] the majority exploit the enhanced reactivity of metal salts at elevated temperatures in liquid solvent (typically 100 – 250 °C).

The main advantage of hydrothermal/solvothermal syntheses in comparison to sol-gel or co-precipitation techniques is that they often make crystalline particles immediately, and do not require a calcination step. However, their reaction times are still relatively long (timescales on the order of hours), and solvothermal processes are often uneconomic due to the expensive and environmentally unfriendly solvent.

Hydrothermal processes are inevitably cheaper due to the water solvent, but often produce large particles.[41] The particle size can be reduced by employing surfactants, such as polyethylene glycol,[42,43] hexadecyltrimethylammonium bromide (CTAB),[44] and ascorbic acid,[45,46] which bind to the growing particle surface, although these also incur a cost. Moreover, these synthetic techniques are batch processes, which can suffer from batch-to-batch variation and are comparatively difficult to scale-up to industrial production. For these reasons, Continuous Hydrothermal Flow Synthesis (CHFS) has been pursued as a possible alternative, utilising the benefits of cheap water solvent, but additionally exploiting the properties of supercritical water to produce nanoparticles without surfactant in a continuous manner.[47] Therefore, the next section explores the special properties of supercritical water and the reasons for its use in CHFS.

1.1.3.2. Supercritical Water

A supercritical fluid is a state of matter which is observed when a liquid is heated and pressurised above its critical point.[48] This state has interesting properties, sharing characteristics with both liquids (e.g. can dissolve solids) and gasses (e.g. can be compressed). Aside from water solvent, CO_2 and alcohols have been explored in their supercritical state for a variety of applications. The critical point of water is at 374 °C and 22.1 MPa (Figure 1.7).[49] As the temperature of water increases above the supercritical temperature, T_c, the physical and chemical properties of water change drastically, as indicated by Figure 1.8. For example, the heat capacity C_p increases to a maximum at the supercritical point, which is characteristic of a phase transition.

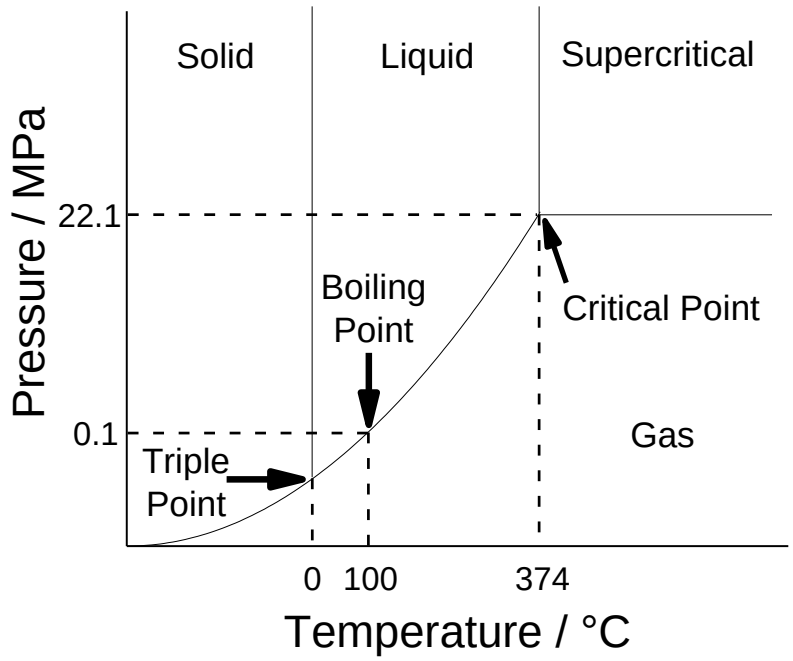

Figure 1.7 – The phase diagram of water, indicating the critical point and triple point of water. The boiling point of water under atmospheric conditions is also included as a reference. Phase boundaries are indicated by solid lines, and key pressures/temperatures indicated with dashed lines.

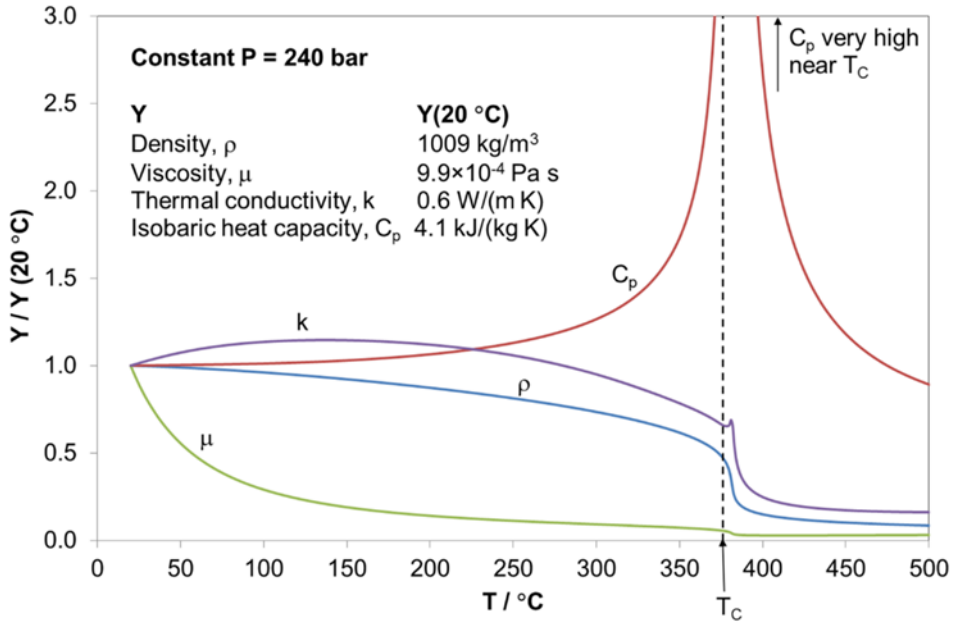

Figure 1.8 – The effect of temperature on the density, viscosity, thermal conductivity and heat capacity of water at a constant pressure of 240 bar. Reprinted with permission from "Darr, J. A., Zhang, J., Makwana, N. M. & Weng, X. Continuous Hydrothermal Synthesis of Inorganic Nanoparticles; Applications and Future Directions. *Chem. Rev*. **in press**, 1–141 (2017)". Copyright 2017 American Chemical Society.[47]

Furthermore, the dielectric constant (ε) decreases rapidly from the value observed for room-temperature water (80) to the supercritical point (ε ~5), and decreases further

beyond this point ($\varepsilon < 2$ at 400 °C).[50] These ε values are approximately equal to those of ethyl acetate ($\varepsilon = 6.02$) and hexane ($\varepsilon = 1.88$),[51] respectively, and indicate hydrogen bonds between water molecules are being broken through the phase transition. Indeed, a combination of IR, Raman, ^{1}H NMR spectroscopy and neutron scattering confirm the breakdown of the large hydrogen-bonded network present in liquid water, with only small, locally-bonded clusters remaining in supercritical water.[52–56] Therefore, the supersaturation concentration of inorganic metal salts is much lower in supercritical water compared to room temperature water, as they are solvated far less effectively. For example, $NiBr_2$ dissolved in ambient conditions has a first solvation shell of six water molecules surrounding Ni^{2+}. However, in supercritical water, the first solvation shell is distorted tetrahedral and much more anionic, with structural formulas $Ni^{2+}Br^-_x(H_2O)_{4-x}$ observed, where x = 1, 2 or 3.[57] Furthermore, the metal-oxygen coordination bond of hydrated cations has been shown to contract with increasing temperature,[58] suggesting the formation of formal metal-oxygen bonds (as present in solid oxides) is more facile in supercritical water solvent.

Moreover, the hydrolysis of water-coordinated cations to form the zero-charge complex discussed in Section 1.1.2.1 is more rapid in supercritical water. This is due to the change in the ionic product (K_w, Equation 1.13a) as a function of increasing temperature. Both $[H^+]$ and $[OH^-]$ are approximately 1×10^{-7} mol dm^{-3} in room temperature, ambient pressure water, giving a K_w value of 1×10^{-14} mol^2 dm^{-6}. It is useful at this point to define pK_w in Equation 1.13b, where the pK_w of water at room temperature is *ca*. 14.

$$\text{a) } K_w = [H^+][OH^-]$$
$$\text{b) } pK_w = -log_{10}(K_w)$$

Equation 1.13 – a) The ionic product of water, K_w, in terms of proton and hydroxide concentration, $[H^+]$ and $[OH^-]$, respectively. b) The relationship between pK_w and K_w.

Figure 1.9 displays the variation of pK_w with temperature, and it can be seen that the pK_w values are significantly lower than 14 around the supercritical point at pressures greater than 34.5 MPa. This corresponds to an increased concentration of both $[H^+]$ and $[OH^-]$ by about an order of magnitude. Given acid or base can catalyse the oxolation reaction, reducing the activation energy barrier of nucleation as described in

Section 1.1.2.1, the increased ionic character of supercritical water will result in more rapid nanoparticle nucleation.

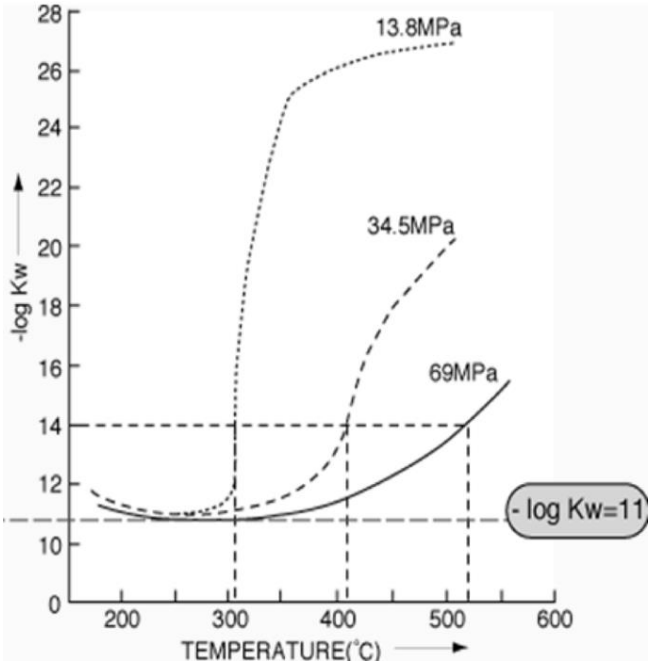

Figure 1.9 – The effect of temperature and pressure on the ionic constant of water. Reprinted with permission from "Darr, J. A., Zhang, J., Makwana, N. M. & Weng, X. Continuous Hydrothermal Synthesis of Inorganic Nanoparticles; Applications and Future Directions. *Chem. Rev*. **in press**, 1–141 (2017)". Copyright 2017 American Chemical Society.[47]

If ambient metal salt precursors are combined with supercritical water, the degree of supersaturation will be extremely high, leading to rapid nucleation of small particles. This idea has encouraged many researchers to apply such a synthesis method to produce a wide array of nanoparticles, as detailed in the next section.

1.1.4. Continuous Hydrothermal Synthesis

1.1.4.1. Introduction to Continuous Hydrothermal Synthesis

When ambient, aqueous precursors are combined with supercritical water, the zero-charge precursor discussed in Section 1.1.2.1 forms rapidly under the hydrolysing conditions. An example of formation from a typical metal nitrate precursor is given in Equation 1.14a. This is considered to partially dehydrate to form a hydroxide intermediate (Equation 1.14b).[59] This precursor then dehydrates further *via* a series of condensation reactions to form the metal oxide, as shown in Equation 1.14c. This is a simplification, as in many cases other chemical species (such as oxidants) are involved in the reaction, and the coordination shell surrounding the metal ion often changes at

higher temperatures as previously discussed.[60] In addition, some metal salts decompose *via* hydroxides and oxyhydroxides in slow steps, i.e. the initial production of the reaction may not be the fully dehydrated oxide. It is important to note the nitrate ion forms nitric acid as a by-product in this example, so hydrothermal reactions often include base not only to catalyse oxide formation, but to ensure a neutral or basic pH to prevent dissolution of the metal oxide product.

$$\text{a) } \mathrm{M^{z+}(NO_3)_z \rightarrow M^{z+}(H_2O)_n + zNO_3^- \rightleftharpoons [M(OH)_z(H_2O)_{n-z}]^0 + zHNO_3}$$

$$\text{b) } \mathrm{[M(OH)_z(H_2O)_{n-z}]^0 \rightrightarrows M(OH)_z + (n-z)H_2O}$$

$$\text{c) } \mathrm{M(OH)_z \rightrightarrows MO_{z/2} + (z/2)H_2O}$$

Equation 1.14 – a) The hydrolysis of a metal nitrate precursor to form the zero-charge precursor. b) partial dehydration of the zero-charge precursor to form a metal hydroxide intermediate. c) The dehydration of the zero-charge precursor to form a metal oxide.

1.1.4.2. Reactor Designs

Two early approaches to CHFS reactor design were developed separately by Pacific Northwest Laboratories and the Arai group in Japan. The former employed a relatively simple process relying on only one pump, which continuously pumped dissolved metal salts into a heated pipe section in a furnace.[61,62] Nanoparticles rapidly nucleated in flow, and the product slurry was cooled by rapid expansion of the suspension at the end of the process, and the resulting vapour was condensed and collected (Figure 1.10). This apparatus could successfully produce particles of Fe_2O_3, CuO, NiO and ZrO_2 among others.[61,62] While the simplicity of the apparatus prevented the need to consider mixing dynamics between supercritical and ambient feeds, it was too inflexible for wide application. Moreover, although narrow pipe diameters were used in the furnace section, enabling rapid heat transfer, inevitably the precursors will have reacted to form particles at temperatures significantly below the target furnace temperature, i.e. the synthesis temperature was not well defined.

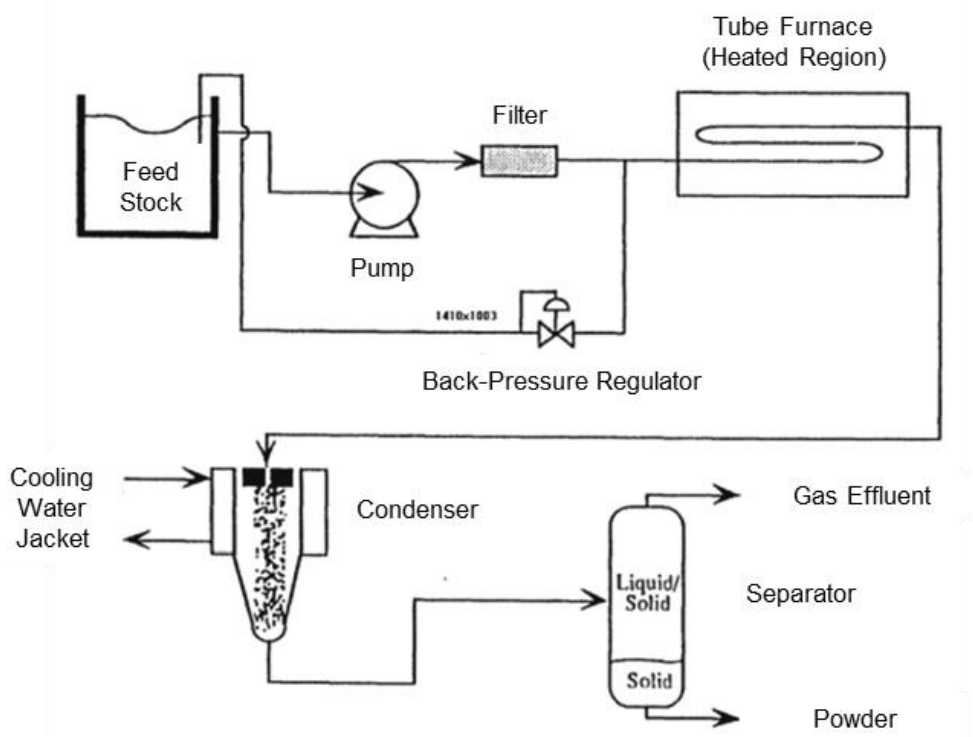

Figure 1.10 – A schematic of the CHFS process developed by Pacific Northwest Laboratories, U.S. Adapted from reference 62.

A more versatile and widely-adopted approach was pioneered in the 1990s. The key innovation was the continuous combination of preheated supercritical water and ambient precursors at a mixing point (Figure 1.11) to produce a high-temperature combined stream, from which nanoparticles were produced. This mixing point arrangement is discussed in detail in Section 1.1.4.3.

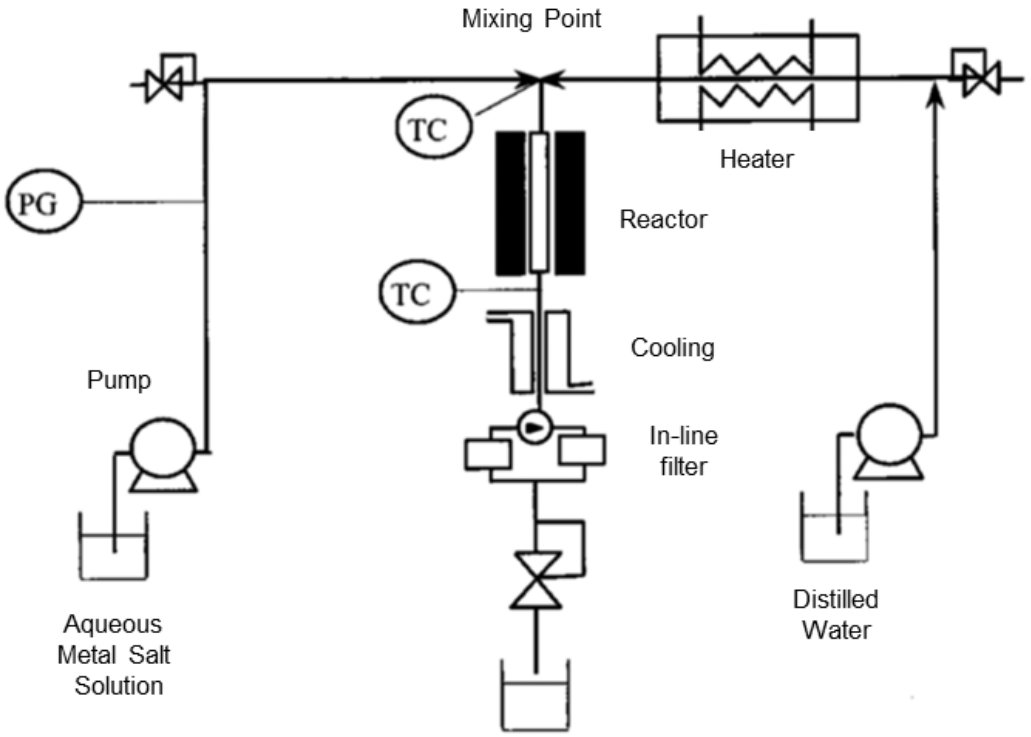

Figure 1.11 – A schematic of the CHFS process developed by the Arai group, where "PG" and "TC" are pressure-gauges and thermocouples, respectively. Reprinted from "Adschiri, T., Hakuta, Y. & Arai, K. Hydrothermal Synthesis of Metal Oxide Fine Particles at Supercritical Conditions. *Ind. Eng. Chem. Res.* **39**, 4901–4907 (2000)", Copyright 2000, with permission from Elsevier.[63]

This design offered numerous advantages in comparison to the single pump apparatus. Firstly, the temperature was well defined at the mixing point, assuming rapid mixing and minimal heat transfer between ambient and supercritical feeds prior to mixing. Secondly, the pH of the reaction could be controlled. Typically, the HPLC pumps used in these processes cannot pump suspensions of any kind, i.e. they are limited to solutions. As metal salts and bases often combine to form an initial precipitate (often the metal hydroxide), defined mixing points allow metal salts and bases to be combined in process, i.e. precipitates only form downstream of the pumps. This allowed researchers to overcome early problems with CHFS processes, which often produced low yields or impure products due to the lack of pH control.[64] Finally, more complex reaction chemistry could be explored due to the inherent flexibility of the reactor design. For example, multiple mixing points have been utilised to synthesise nanoparticles at high temperature, and then coat the particles with surfactants at a second, lower temperature mixing point.[65] Therefore, it is this reactor design which has been most commonly used throughout literature reports, and has been primarily

adopted by the CMTG at UCL. The CMTG reactor apparatus is discussed in Section 2.1.

1.1.4.3. Mixer design and geometry

There are three criteria which successful mixers should satisfy: the supercritical water and precursor feeds should mix rapidly to ensure homogenous reaction temperature and concentration, circumvent premature heating of the metal salts, and avoid blockages. A very wide array of configurations and geometries have been attempted, most notably by Lester *et al.*, and this section aims to give a brief overview of key developments in mixer design and geometry towards these aims.[66]

It is useful at this point to define the Reynolds number, R_e, which is calculated using Equation 1.15, where d is the internal pipe diameter, and v, ρ, and μ are the velocity, density and viscosity of the fluid, respectively. R_e is a dimensionless quantity which describes the flow of fluid within a pipe. At R_e values < 2000, laminar flow is observed, and if R_e > 4000 the mixing is turbulent. At intermediate values (2000 < R_e < 4000), the mixing is "transitional" and has mixed laminar/turbulent behaviour. Equation 1.15 reveals the experimental parameters which affect R_e; increasing the pump flow rates increases v, and using narrower pipes increases v (for a fixed flow rate) and decreases d. Increasing the mixing point temperature also increases R_e due to the dominant effect of reducing the reaction mixture viscosity.

$$R_e = \frac{\rho d v}{\mu}$$

Equation 1.15 – The expression for Reynolds number, R_e, in terms of fluid density ρ, inner pipe diameter d, fluid velocity v, and fluid density μ.

The first reported mixer to be employed by Adschiri *et al*. in their seminal publication in 1992 was a tee-piece mixer.[59] Tee-piece mixers can operate in a wide variety of temperatures, pressures, flow-rates and orientations, and can be assembled from commercially available components, and hence this mixer continues to be commonly used by many researchers.[67–69] Investigation of the effect of reaction variables on nanoparticle size was performed recently by Aoki *et al.*,[68] who found increased mixing (i.e. greater R_e) and higher temperatures favoured the formation of smaller CeO_2 particles. However, marginal benefit was observed when R_e was increased above 10000 (Figure 1.12).

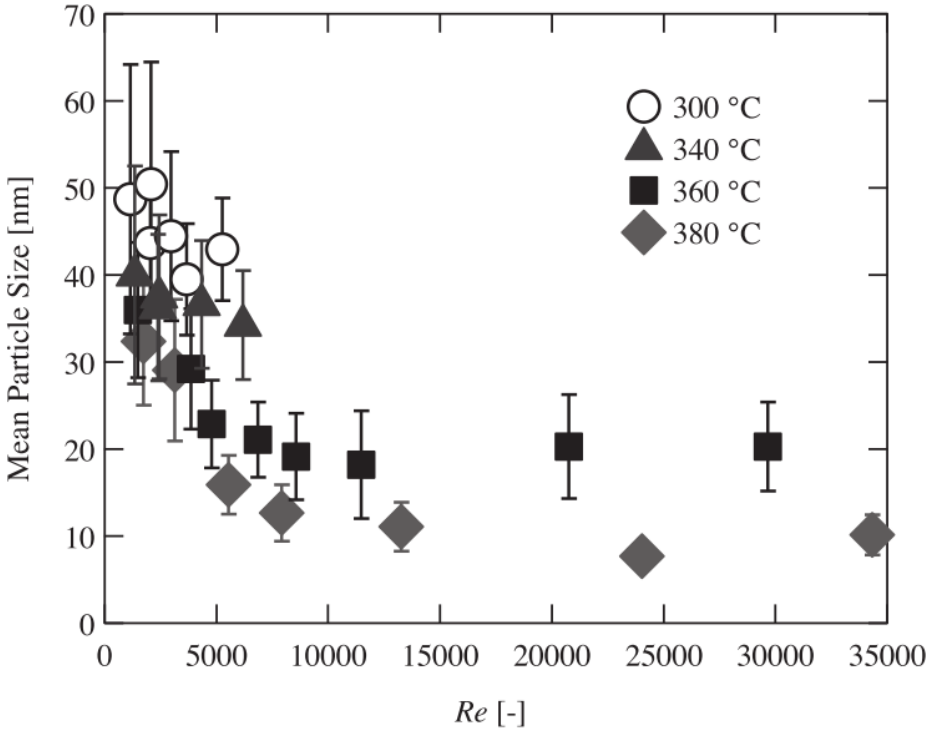

Figure 1.12 – The effect of temperature and Reynolds number on CeO_2 particle size synthesised *via* CHFS. Reprinted from "Aoki, N. *et al*. Kinetics study to identify reaction-controlled conditions for supercritical hydrothermal nanoparticle synthesis with flow-type reactors. *J. Supercrit. Fluids* **110**, 161–166 (2016)", Copyright 2016, with permission from Elsevier.[68]

It is clear from the work of Aoki *et al*. that the mixing dynamics have a huge impact on the size of particles produced.[68] Therefore, more advanced mixer designs such as swirling micro mixers and central collision mixers (CCM) have been pioneered by various groups, and are illustrated in Figure 1.13. In the former case, Kawasaki *et al*. employed dual supercritical water feeds, which were fed into the mixer at an angle of 60° to the precursor feed (Figure 1.13a).[70] This produced a swirling flow of the combined feeds, and reduced the particle size and particle size distribution of NiO compared to the tee-piece mixer. This was despite the greater Reynolds number value in the tee-piece mixer (96000 vs 58000), which implied the mixing geometry also contributed to the nucleation dynamics of nanoparticles. Sue *et al*. pioneered the CCM, which employed a six-branch mixer (Figure 1.13b).[71] Supercritical water entered *via* the four equatorial branches, and the precursor and product entered and exited axially. The main benefit of this design was the reduction in heterogeneous nucleation of product on the pipe walls, as opposed to homogenous nucleation in flow. This was evidenced by smaller particles and narrower particle-size distributions produced by the CCM.

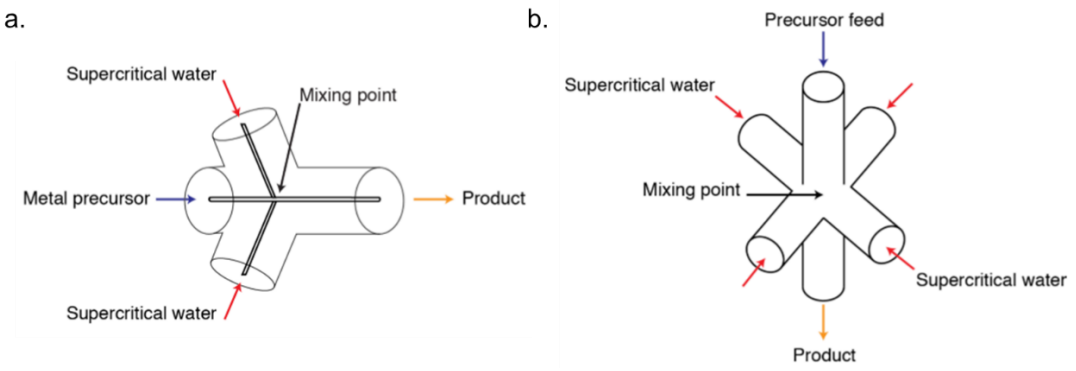

Figure 1.13 – Schematics of a) the swirling mixer and b) the central collision mixer. Adapted with permission from "Kawasaki, S., Sue, K., Ookawara, R., Wakashima, Y. & Suzuki, A. Development of Novel Micro Swirl Mixer for Producing Fine Metal Oxide Nanoparticles by Continuous Supercritical Hydrothermal Method. *J. Oleo Sci.* **59**, 557–562 (2010)" Copyright 2010 Japan Oil Chemist's Society. Adapted with permission from "Sue, K. et al. Continuous Hydrothermal Synthesis of Fe_2O_3 Nanoparticles Using a Central Collision-Type Micromixer for Rapid and Homogeneous Nucleation at 673 K and 30 MPa. *Ind. Eng. Chem. Res*. **49**, 8841–8846 (2010)". Copyright 2010 American Chemical Society. Adapted with permission from C. J. U. Denis' Thesis.[70–72]

Lester *et al*. used computer simulations to investigate the mixing dynamics in tee-piece mixers. They found the different densities of supercritical water and ambient water feeds (371 *vs*. 998 kg m^{-3}) resulted in buoyancy forces dominating the mixing interaction, and in such a regime the tee-piece mixer was ineffective.[73] As a result, they designed counter-current mixers (Figure 1.14) which exploited the difference in densities to aid, rather than hinder, mixing.[74] In this design, the precursor and supercritical feeds were arranged coaxially; precursors were pumped vertically to meet a downward flow of supercritical water, and the products exited vertically.

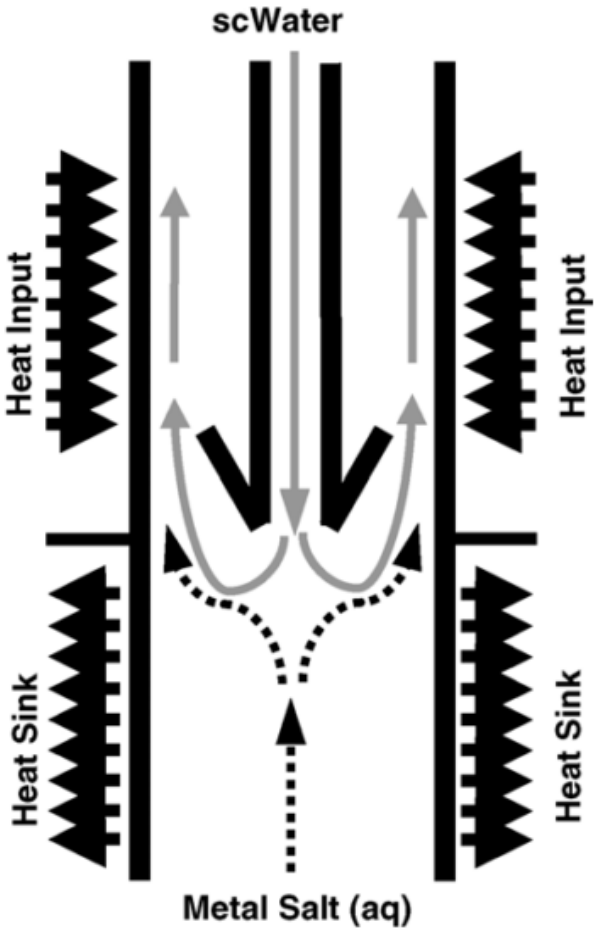

Figure 1.14 – A schematic of the counter-current mixer. Reprinted from "Lester, E. *et al*. Reaction engineering: The supercritical water hydrothermal synthesis of nano-particles. *J. Supercrit. Fluids* **37**, 209–214 (2006)", Copyright 2006, with permission from Elsevier.[74]

More recently, the CMTG at UCL investigated the counter-current mixer under a range of different reaction conditions.[75] While the mixer design prevented blockages, with unbalanced feeds (i.e. greater supercritical water flow rate) the mixer displayed unstable mixing dynamics, with intermittent jetting of the supercritical feed deep into the precursor feed. This provided an uncertain mixing point of poorly-defined temperature, and is therefore unsuitable for controlled nanoparticle synthesis. Moreover, heat exchange between the supercritical water and precursor stream was observed, reducing the observed mixing point temperature; in fact, the desired reaction temperature was only achieved significantly beyond the mixing point.

In light of these problems, UCL authors pioneered the Confined Jet Mixer (CJM).[76] This relies upon a co-current mixing regime, where aqueous precursors are fed in through two equatorial feeds to meet an axial hot water feed (Figure 1.15) and the

products leave the mixer vertically. This is achieved using a "pipe-in-pipe" configuration, where supercritical water enters the mixer *via* an inner pipe within a cross-piece. In-situ temperature measurements confirmed complete mixing of the two feeds within ~40 ms of the mixing points, and the momentum of the supercritical jet was found sufficient to carry the nanoparticulate slurry away from the mixer. Moreover, higher supercritical water flow-rates could be used to achieve higher mixing-point temperatures, and a scale-up study on ZnO showed the mass yield of the reaction could be increased by a factor of 40 without significant change in particle size.[76] Therefore, the CJM was used throughout this thesis, and the specific CJM arrangements are discussed in Section 2.1.2.

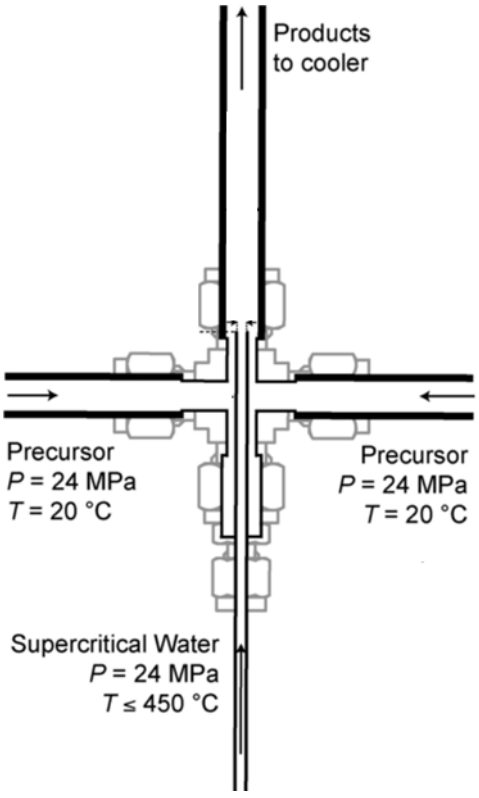

Figure 1.15 – A schematic of the Confined Jet Mixer. Reprinted with permission from "Gruar, R., Tighe, C. & Darr, J. Scaling-up a confined jet reactor for the continuous hydrothermal manufacture of nanomaterials. *Ind. Eng. Chem. Res.* **52**, 5270–5281 (2013)". Copyright 2013 American Chemical Society.[76]

1.2. Rechargeable Batteries

With global population predicted to exceed 10 billion within 50 years, global energy consumption is correspondingly likely to increase.[77] The majority of worldwide energy production stems from fossil fuels, which are a finite resource and have negative

environmental consequences when used (such as global warming). As a result, renewable energy sources such as wind and solar power are currently in development to replace them. However, these power sources are often erratic or intermittent in nature and do not provide constant, reliable power. Wind power, for example, depends on the strength and direction of wind, and is therefore reliant on the weather. Energy storage provides a potential solution to this problem; if energy can be stored at times of peak generation, and used at times of low generation, this could enable much wider uptake of renewable energy generation worldwide.

One potential candidate for such energy storage devices is rechargeable batteries. These convert electrical energy to chemical energy, thereby storing it, and have mostly been utilised in small portable devices, such as mobile phones. However, they have recently been considered for transport applications, such as the electric vehicle (EV) and plug-in hybrid electric vehicle (PHEV). If these vehicles can attain mass-market penetration, this would go some way towards decarbonising transport. Furthermore, large-scale stationary rechargeable batteries have been built recently for load-levelling applications at the grid level, and offer promise for larger-scale grid storage.[78] However, rechargeable batteries fall short of petroleum fuel in one key aspect; their energy densities are much lower. This results in a much shortened driving range of EVs (typical range 100 – 200 miles) compared to petrol cars (over 500).[79] Consequently, there is great need to improve energy storage devices to enable EVs.

1.2.1. Battery Fundamentals

Batteries consist of multiple electrochemical cells stacked in series, which contain three main components; anode, cathode and electrolyte. To provide electrical power, cells convert chemical energy into electrical energy. This is achieved by pairing two "half-reactions" at the anode and cathode, and it is the potential difference (as defined by the standard electrochemical series) between the anodic and cathodic reaction which determines the voltage provided by the battery. For example, in a $LiFePO_4$/Li cell, the Fe^{2+}/Fe^{3+} couple is paired with the Li/Li^+ couple to provide a cell voltage of ~3.4 V (this differs from the theoretical values from Table 1.1 as these are calculated using gaseous or aqueous metals). The energy density of a cell can be calculated according to Equation 1.16, where Equation 1.16a gives the gravimetric energy

density, and Equation 1.16b gives the volumetric energy density, which are measures of the energy stored per unit mass or unit volume, respectively.

Table 1.1 – The standard electrochemical series, including key electrochemical half-reactions.[80–83]

Half-reaction			E_0 / V
$Li^+ + e^-$	⇌	Li(s)	−3.04
$Cs^+ + e^-$	⇌	Cs(s)	−3.03
$Li^+ + C_6(s) + e^-$	⇌	$LiC_6(s)$	−2.84
$Na^+ + e^-$	⇌	Na(s)	−2.71
$2H^+ + 2e^-$	⇌	$H_2(g)$	0
$Fe^{3+} + e^-$	⇌	Fe^{2+}	0.77
$CoO_2(s) + 4H^+ + e^-$	⇌	$Co^{3+} + 2H_2O$	1.42

$$a)\ E_{\text{grav}} = \frac{\bar{V}\Lambda}{mass} \qquad b)\ E_{\text{vol}} = \frac{\bar{V}\Lambda}{volume} \qquad c)\ \bar{V} = \frac{\int_0^{\Lambda} V d\Lambda}{\Lambda}$$

Equation 1.16 – a) the gravimetric energy density E_{grav} and b) volumetric energy density E_{vol} of a cell in terms of the average voltage (defined in c) and cell capacity, Λ.

There are two broad categories of battery technology – primary and secondary.[84] Primary batteries provide only a single discharge before they require disposal or recycling, whereas secondary batteries rely on reversible chemistry and can be recharged multiple times to provide multiple discharges. While primary batteries remain an active area of research, they are beyond the scope of this thesis, and are not discussed further.

The first commercial secondary batteries were the lead-acid and Ni-Cd batteries, which relied on aqueous electrolytes.[85] In a battery, the anode provides electrons upon discharge, and the cathode receives them, i.e. they act as reductant and oxidant, respectively. The open circuit voltage, V_{oc}, depends upon the electrode potentials of anode and cathode, μ_A and μ_C, according to Equation 1.17a. However, this voltage must reside within the voltage window of the electrolyte (E_g), defined by the electrolyte HOMO and LUMO according to Equation 1.17b.[85] Specifically, if the LUMO of the electrolyte is lower than μ_A, the electrolyte will be reduced. Likewise,

if the electrolyte HOMO is greater than μ_C, it will be oxidised. In the case of aqueous electrolytes, these reactions are essentially the hydrogen and oxygen evolution reaction, respectively. This limits the maximum voltage of an aqueous cell to 1.3 V, and therefore non-aqueous electrolytes were advanced to enable wider cell potential windows to be used, and led to the discovery of the rechargeable Li-ion battery. A schematic of an aqueous battery in terms of relative electron energies is given in Figure 1.16.

$$a)\ V_{\mathrm{OC}} = \frac{\mu_{\mathrm{A}} - \mu_{\mathrm{C}}}{e} \qquad b)\ E_{\mathrm{g}} = E_{\mathrm{LUMO}} - E_{\mathrm{HOMO}}$$

Equation 1.17 – a) The open circuit voltage, V_{OC} of an electrochemical cell, where e is the magnitude of the electron charge. b) The voltage stability window of an electrolyte, E_g, in terms of the energy of its LUMO (E_{LUMO}) and HOMO (E_{HOMO}).

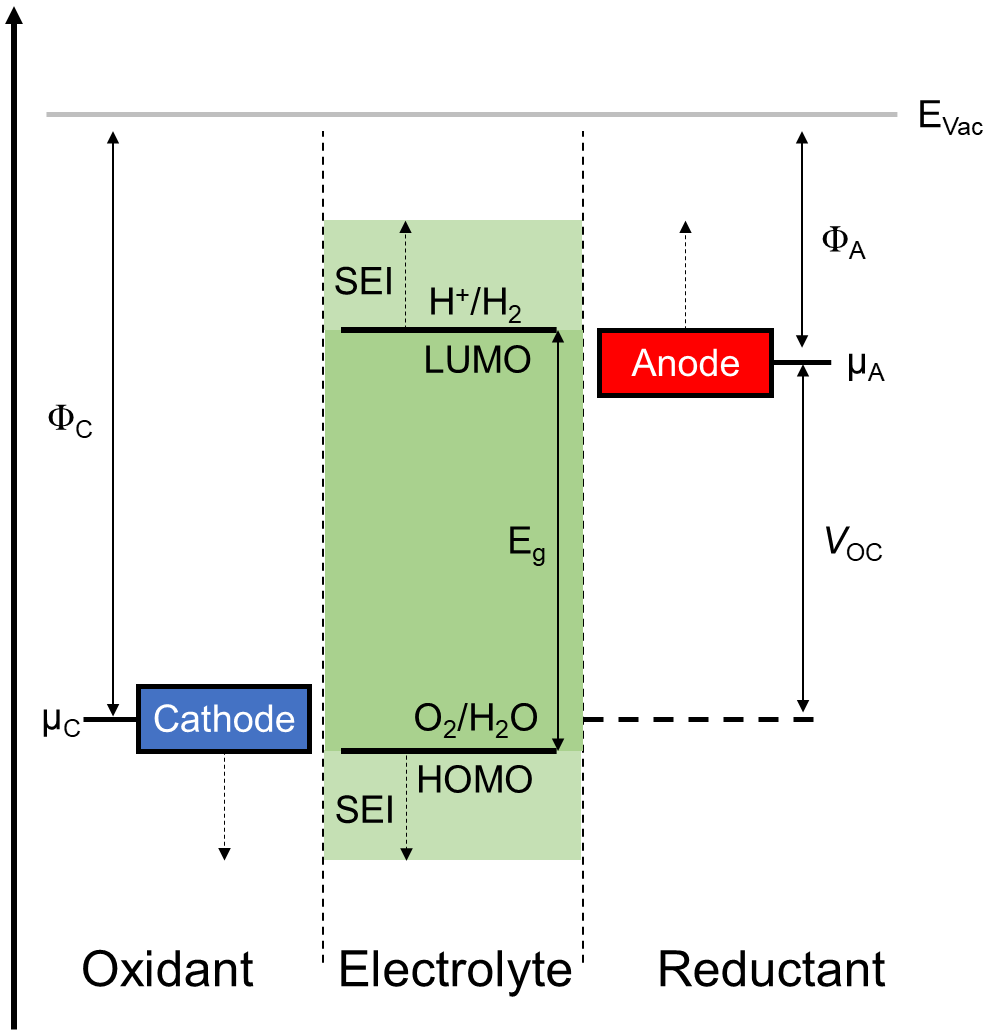

Figure 1.16 – An open-circuit energy diagram of an aqueous cell. E_{Vac} is the energy of the vacuum, E_g is the voltage window of the electrolyte, and Φ_A and Φ_C are the work functions of anode and cathode respectively. If the anodic or cathodic potentials are beyond the voltage window, electrolyte decomposition will occur unless a stabilising Solid Electrolyte Interface (SEI) layer forms. Adapted with permission from "Goodenough, J. B. & Kim, Y. Challenges for Rechargeable Li Batteries. *Chem. Mater*. **22**, 587–603 (2010)". Copyright 2010 American Chemical Society.[85]

1.2.2. Li-ion batteries

Li-ion batteries were identified as the natural candidate for high energy-density rechargeable batteries for numerous reasons. Firstly, certain lithium salts are soluble in non-aqueous solvents, extending E_g to approximately 3.3 V (from 1.3 V for aqueous cells). In addition, the Li/Li^+ couple is situated at very negative potentials (Table 1.1), giving a large cell voltage when partnered with a transition metal redox couple. Furthermore, Li is the third-lightest element, reducing the relative mass of Li-ion cells and increasing their gravimetric capacity, and has a relatively small ionic radius (0.76

Å for six-coordinate Li^+),[86] allowing it to intercalate readily into host structures (discussed further later in this section).

It should be noted that the μ_A of the Li anode lies beneath the LUMO of the known non-aqueous organic electrolytes, so use of Li metal anodes (or electrodes such as graphite at similar potentials) is only possible due to the formation of a passivation layer, known as the Solid Electrolyte Interphase (SEI).[87,88] The electrolyte is reduced to form SEI, which is an electron-insulating, Li-conducting layer, and therefore prevents further reaction of the electrolyte with the anode and extends the operating voltage of the cell to > 4.0 V. This is discussed further in Section 1.2.2.2.

A schematic of a commercial graphite/$LiCoO_2$ cell is given in Figure 1.17. The cell is assembled in the discharged state (i.e. $LiCoO_2$ is fully lithiated, and graphite is fully delithiated). Upon charge, Li is removed from the $LiCoO_2$ cathode into the electrolyte, and at the anode, Li subsequently intercalates into the graphite structure, with electrons flowing around the external circuit to balance charge. Upon discharge, the reverse process occurs: Li is removed from graphite and inserted into $Li_{1-x}CoO_2$, and electrons flow around the external circuit to power a device (Figure 1.17).[89] This can be expressed in the anodic, cathodic and overall cell reactions in Equation 1.18. It should be noted that the terms “anode” and “cathode” in secondary batteries are only technically correct upon discharge, as when the cell is charged the terminology should swap. However, as the first cells were primary cells (where they were only used for discharge), convention fixes the position of anode and cathode, despite this being incorrect during charging.

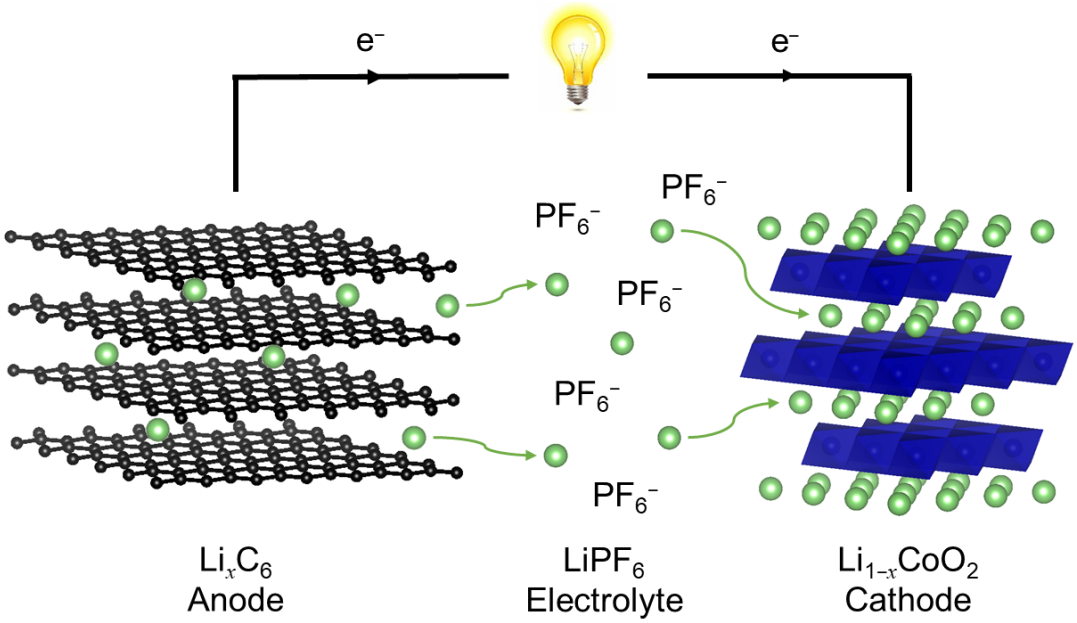

Figure 1.17 – A schematic of a commercial graphite/$LiCoO_2$ cell during discharge, with $LiPF_6$-based electrolyte. Upon discharge, Li^+ is removed from graphite into the electrolyte at the anode. At the cathode, Li^+ moves from the electrolyte and intercalates within the $Li_{1-x}CoO_2$ structure. Electrons flow around an external circuit to balance charge, powering a device. The structures of graphite and $LiCoO_2$ were drawn using VESTA software from PDF Card Nos. 01-089-7219 and 01-070-2685 respectively.[90]

$$a)\ Li_xC \rightarrow C + xLi^+ + xe^-$$
$$b)\ xLi^+ + xe^- + Li_{1-x}CoO_2 \rightarrow LiCoO_2$$
$$c)\ Li_xC + Li_{1-x}CoO_2 \rightarrow C + LiCoO_2$$

Equation 1.18 – a) The anodic half-reaction, b) the cathodic half-reaction, and c) the overall graphite/$LiCoO_2$ cell reaction upon discharge.

1.2.2.1. Electrode Materials

Commercial Li-ion battery materials have been dominated by intercalation or insertion-type electrodes. In this class of battery materials, Li^+ is incorporated into a host structure, which possesses 1D Li^+ tunnels (e.g. $LiFePO_4$),[91] 2D Li^+ layers (e.g. $LiCoO_2$),[89] or 3D Li^+ networks (e.g. $LiMn_2O_4$ spinel),[92] and upon charge and discharge Li is reversibly incorporated into or removed from these host structures (Figure 1.17). The main attraction of insertion/intercalation materials is their high capacity retention with cycling, which is a result of the stable host structure ensuring high reaction reversibility, and minimal volume changes of the electrode between charged and discharged states. However, the host structure is effectively "dead weight" in the cell and reduces its energy density. Examples of insertion anodes include graphite,[6]

$Li_4Ti_5O_{12}$ and TiO_2,[93–95] and insertion cathodes include $LiFePO_4$, $LiCoO_2$, $LiMn_2O_4$ and various vanadium oxides.[96,97]

By contrast, conversion and alloying anode and cathode materials offer much higher capacities compared to intercalation electrodes. This is because they do not rely on a host structure, and instead rely on chemical conversion of a metal salt (Equation 1.19a),[98,99] or alloying of Li into another metal (Equation 1.19b).[100] These classes of electrodes suffer from irreversibility issues and problems due to volume expansion. For example, in the case of conversion materials, often formation of Li_2O is partially irreversible, i.e. capacity is lost as a function of cycling due to formation of Li_2O "dead zones".[101] Furthermore, the volume expansion leads to irreversible capacity loss due to fracturing of the electrode material which can cause disconnected regions in the electrode.[102] The repeated expansion/contraction also results in continual SEI formation with cycling as a result of the new electrode surface area formed, which will reduce capacity in a full cell with limited lithium content.[103] Conversion anodes are numerous, and include Fe_2O_3,[104] Fe_3O_4,[105] and Mn_3O_4,[106] and alloying anodes include Sn and Si metal.[107,108] Conversion cathodes are comparatively few, and consist of FeF_3,[109] S and O.[110,111]

$$a)\ 2xLi^+ + 2xe^- + MO_x \rightleftharpoons xLi_2O + M$$
$$b)\ xLi^+ + xe^- + M \rightleftharpoons Li_xM$$

Equation 1.19 – a) The conversion reaction of a metal oxide and b) the alloying reaction in Li-ion battery electrodes, where "M" is a metal ion (Si is deemed a metal in these cases).

Ideally, Li metal would be employed as an anode in commercial devices, with a high specific capacity of 3680 mA h g^{-1}. However, Li metal does not plate or strip uniformly from the anode upon charge/discharge, leading to the formation of dendrites on the anode surface.[112] Over time, these dendrites grow across the cell, through the separator until they come into electrical contact with the cathode. This causes a dangerous short circuit which can result in fire and/or explosion. Therefore, Li metal is not currently used as a commercial anode, and safer (lower energy density) graphite is favoured instead.

More detailed introductions on the specific electrode materials investigated within this thesis are included as individual introductions at the beginning of each chapter.

1.2.2.2. Electrolytes and Solid-Electrolyte Interphase

Typical electrolytes for Li-ion batteries are comprised of a lithium salt (most commonly $LiPF_6$) in a mixture of organic carbonates. These carbonates are usually ethylene carbonate (EC) combined with diethyl carbonate (DEC) or dimethyl carbonate (DMC).[113] They possess an ideal combination of low viscosity, low electronic conductivity, high ionic conductivity and relatively high chemical stability.[87] EC is nearly always included as electrolyte solvent as it decomposes to form a stable SEI on the anode on the first charge cycle.[114] However, this usually produces gaseous by-products which must be removed after the first charge in commercial pouch cells. Typically, additives such as vinylidene carbonate (VC) or Li_2CO_3 can be included to partially prevent this; VC polymerises without forming gaseous products before EC decomposition occurs, thereby reducing gas evolution.[115,116] Furthermore, a Li_2CO_3 additive can generate a more compact SEI which is more stable to repeated cycling.[117]

The SEI layer has been extremely difficult to analyse experimentally for many reasons. Firstly, it is an extremely thin layer (typically < 10 nm) which limits the usefulness of certain characterisation methods such as X-Ray Diffraction.[118] Furthermore, components of the SEI are partially soluble in the electrolyte and reduce the degree to which these two components can be distinguished. Finally, a battery is a sealed system, with many of the components of the SEI potentially air- or moisture-sensitive. It is therefore difficult to determine whether the phases observed in a disassembled cell are true SEI components, or degradation products of these components post-disassembly. However, common consensus has been reached by various researchers using FTIR and XPS techniques, who have found the anodic SEI is composed of a mixture of inorganic components and polymeric/organic components.[119–123] The inorganic components (e.g. LiF, LiOH, Li_2CO_3) form a dense layer close to the electrode surface, and the polymeric/organic components (e.g. $(CH_2OCO_2Li)_2$, ROLi, $ROCO_2Li$) form a layer close to the electrolyte.

Cathodic SEI layers have also been investigated, although to a far lesser extent. Analysis of SEI layers on oxide cathodes suggested that cathodic SEI layers are not stable, and do not protect the electrolyte from further decomposition with additional

cycles.[123,124] This continued reaction increases the thickness of the cathode SEI layer, reducing the reversible capacity observed in a half cell due to reduced Li^+ diffusion kinetics. Furthermore, the consumption of electrolyte reduces the active Li^+ in a full cell, and will result in reduced full cell capacity. Different cathodic SEI chemistries were observed for different cathodes; for metal oxides, LiF and Li_2CO_3 impurities were detected, whereas salt-based products (LiF, $LiPF_6$, Li_xF_y and $Li_xPO_yF_z$) were observed for carbon-coated $LiFePO_4$ SEI films.

1.2.2.3. The Development of Nanometric Electrode Materials for High-Power Applications

An area of high academic and industrial interest is the development of electrode materials which are capable of delivering high storage capability at high charge and discharge rates. Typically, as the current load increases on a cell, the observed voltage and capacity decreases due to limiting kinetics within an electrode, resulting in reduced energy density. The rate-limiting step commonly observed is the solid-state diffusion of Li^+ within the electrode material, as Li must diffuse from the centre to the surface of an active material particle. The mean diffusion time of Li^+, t_{mean}, is related to the mean diffusion length (L) and the diffusion coefficient of the material (D_{Li}) according to Equation 1.20.[126] As an example, the mean diffusion time decreases from 10 s to 1 ms moving from 1 µm to 10 nm particles (assuming an arbitrary diffusion coefficient $D_{Li} = 10^{-9}$ cm^2 s^{-1}). Therefore, the high-power performance of an electrode material is often significantly increased with nanosizing.

$$t_{mean} = \frac{L^2}{D_{\mathrm{Li}}}$$

Equation 1.20 – The mean diffusion time, t_{mean}, as function of mean diffusion length (L) and diffusion coefficient (D_{Li}).

However, there are drawbacks to the use of nanometric electrode materials. Their higher specific surface area results in greater SEI formation on the first charge.[125] Furthermore, some nanosized electrode materials form unstable SEI (even in the case of insertion/intercalation electrodes), causing continuous electrolyte decomposition with cycling, which would significantly impair cycling performance in a full cell with limited electrolyte and Li content.[125] This is because some nanomaterials can catalyse SEI and/or electrolyte degradation, effectively narrowing the electrochemical window

of stability of the electrolyte.[126] Clearly, this degradation needs to be minimised (or eliminated) before such high-power, nanometric materials can be used in commercial full cells. Additionally, the packing densities of nanomaterials are much reduced compared to micron-sized materials, leading to lower volumetric energy density of the electrode. Therefore, reducing particle size necessitates a trade-off between power capability and energy density.

1.3. Research Questions and Hypotheses

This chapter has established the development of CHFS processes as nanoparticle synthesis methods, and the fundamentals of battery operation. The research questions and hypotheses are these:

- Can battery materials be synthesised *via* CHFS at semi-industrial scale (e.g. kg per day) which show comparable or improved electrochemical performance in Li-ion batteries compared to other synthesis methods?

It is hypothesised that the reduced particle sizes achievable with CHFS technology will directly increase high-power performance. Furthermore, it is suggested that CHFS can achieve metastable dopant concentrations within target phases (such as $LiFePO_4$ and $LiMnPO_4$), and this will allow access to compositions with unprecedented performance due to the altered structural or electronic properties.

- Can an optimal CHFS-made $LiFePO_4$ material be produced at the kg scale, incorporated into a full Li-ion cell, and made into a Li-ion pouch-cell?

Typically, cutting-edge research electrode materials do not retain increased performance relative to industrial, micron-sized materials when scaled up to pouch cells (components of electric vehicle batteries). It is hypothesised that the scalability of the CHFS method can produce high-performance $LiFePO_4$ which can be scaled-up to be components of pouch cells, whilst still outperforming industrial materials.

- Can muon spectroscopy be used to differentiate Li^+ diffusion dynamics between doped $LiFePO_4$ and pure $LiFePO_4$?

The electrochemical performance of $LiFePO_4$ has been enhanced with dopants such as V and Nb, although the mechanism of improvement is still unclear. The Li^+ diffusion mechanism (requiring phase boundary motion) in $LiFePO_4$ prevents this from being measured electrochemically. It is hypothesised that muon spectroscopy can unambiguously differentiate Li^+ diffusion behaviour within doped and pure $LiFePO_4$ as it is an *in-situ* technique which does not involve delithiation dynamics.

- Can Li-ion cathode material $LiMnPO_4$ be improved by co-doping two different metals into the structure?

The high energy-density cathode material $LiMnPO_4$ is still not a commercial cathode material as it is extremely kinetically limited. Both Fe^{2+} and V^{3+} dopants have been found to improve performance, and it is hypothesised that the two dopants improve $LiMnPO_4$ in different (yet complimentary) ways, and that co-doped samples will display enhanced performance compared to $LiMnPO_4$ doped with just Fe or V.

- Can the cathode material $LiCoO_2$ be made *via* CHFS in a more economic manner than is currently reported in the literature? Can this be achieved by substituting Li-containing precursors with cheaper K-containing precursors, or by lowering the reaction temperature? Additionally, can doped phases of $LiCoO_2$, specifically $LiNi_xMn_yCo_zO_2$, be generated by substituting Co with these metals whilst retaining the layered $LiCoO_2$ structure?

$LiCoO_2$ has already been synthesised using CHFS, but typically requires extremely high excesses of LiOH (20 × excess in some cases) to generate pure-phase $LiCoO_2$. It is hypothesised that LiOH can be replaced with cheaper KOH to give an overall base excess, whilst minimising Li waste. Furthermore, it is hypothesised that the typical reaction temperature (400 °C) can be lowered to increase the mass yield of the CHFS reaction. Finally, the doped $LiCoO_2$ compounds ($LiNi_xMn_yCo_zO_2$) show significant energy density improvement compared to the pure phase, but have not yet been synthesised *via* CHFS. It is postulated that these phases can be achieved *via* CHFS by substituting Co with Ni and Mn precursors.

- Can nanosized $MgCr_2O_4$ be used as an Mg-ion cathode material?

$MgCr_2O_4$ has been identified as a potential Mg-ion cathode material, although these materials typically show little or no performance because of large kinetic barriers. It is postulated that if $MgCr_2O_4$ can be made in the nanoscale, hopefully < 10 nm, a greater proportion of the constituent Mg will be found at or near the particle surface, and should enable Mg-ion activity to be observed.

In summary, this thesis will explore known cathode materials for Li-ion batteries, trying to improve upon the typical performance observed in literature. Furthermore, these syntheses will be conducted at pilot-scale as much as possible (kg per day) to prove the industrial relevance of the materials. Finally, there are efforts to synthesise hard-to-achieve phases never previously made *via* CHFS, some of which will hopefully be investigated for the emerging field of Mg-ion batteries.

2. Materials and Methods

This chapter describes the experimental methods and techniques used throughout this thesis. The CHFS reactors employed to fabricate the nanomaterials are described, including the details of the various mixing conditions employed, and the design of the CJM. There are also details of the necessary post-synthesis processing of the nanomaterials, followed by physical and electrochemical characterisation methods. This chapter contains general information regarding these topics, and specific methodologies are given for the relevant syntheses in each chapter.

2.1. Continuous Hydrothermal Synthesis

Within the Clean Materials Technology Group, the original CHFS reactors were designed and built by Dr. P. Boldrin and Prof. J. Darr at Queen Mary University of London. These prototypes typically produced overall flow rates (of product slurry) of 40 mL min^{-1}.[127,128] In the past decade, larger-scale versions were developed by Dr. C. Tighe and Dr. R. Gruar at University College London as described in Dr Gruar's thesis.[129] These are typically capable of 160 mL min^{-1} and 800 mL min^{-1} overall flow rate for the Lab-Scale and Pilot-Scale reactor, respectively. This section fully describes the construction of the apparatus, including specific mixing arrangements.

2.1.1. Reactor apparatus

2.1.1.1. Pilot-Scale reactor

A schematic of the Pilot-Scale reactor apparatus is displayed in Figure 2.1. All components used (described in full below) were commercially available to enable facile maintenance and repair.

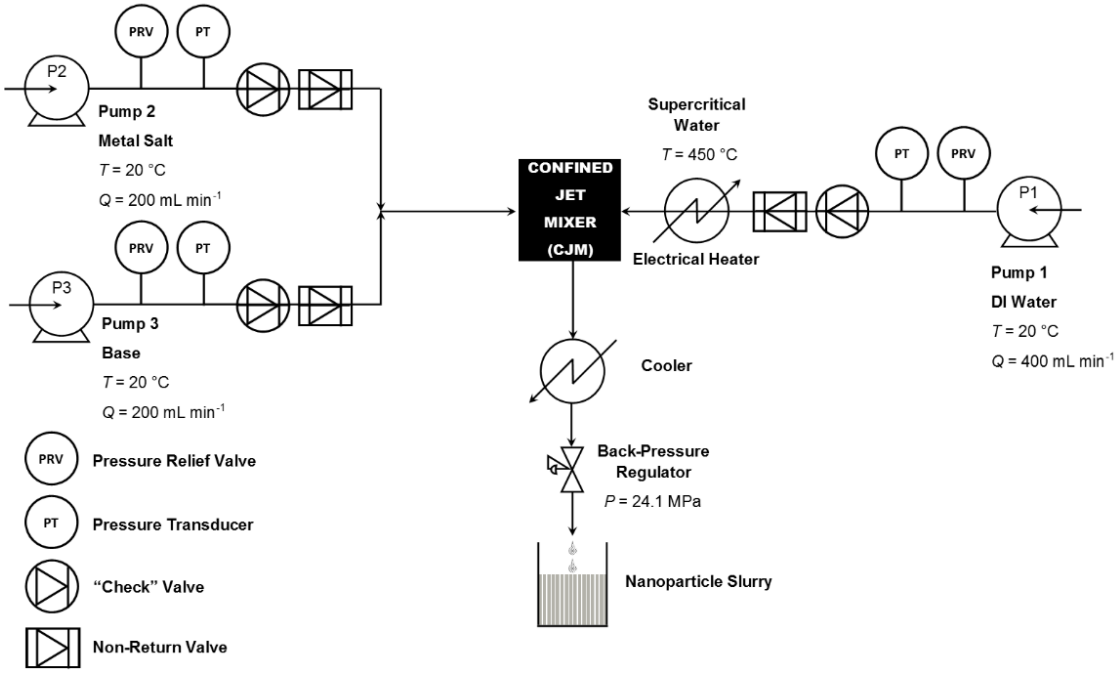

Figure 2.1 – A general schematic for the Pilot-Scale Reactor including all major components.

Three pumps (Primeroyal K, Milton Roy Europe, Sunderland, UK) provided three separate feeds of either D.I. water or aqueous metal precursors. The pump inlets were connected *via* three-way valves to D.I. storage tanks (100 L capacity) or conical precursor containers (1.5 L capacity) using Swagelok 316L ½" stainless steel piping (Swagelok, Kings Langley, U.K.). These valves enabled the rapid switching between the D.I. water feed and the precursors. The outputs of the pumps were connected to pulsation dampeners (Pipehugger HP, Liquid Dynamics, Wichita, Kansas, U.S.) precharged to a pressure of 200 bar (N_2 gas) which ensured consistent output flow. The output from the pulsation dampeners (¼" stainless steel piping) was first connected to a pressure transducer, which allowed the observation of individual pump output pressures. A pressure-relief valve (HPRV, Parker, Warwick, U.K.) set to 276 bar was connected downstream of the pressure transducers, a necessary safety feature which prevented overpressure in the case of pipe blockage. The final components between the pump and the mixing point (CJM, Figure 2.1) were two valves; a Lift Check Valve (50 Series, Swagelok) and a non-return valve (CH Series, Swagelok) in series, which prevented back-flow in the instance of pump failure.

The hot water feed for the process was provided by P1, which pumped D.I. water at 400 mL min^{-1} through four custom-made heaters built by Watlow, U.K. These heaters were fabricated from a tight coil of 6 meters of ½" Inconel seamless tubing, encased

in bronze with four 1.5 kW heating rods (Firerod™, Watlow, Nottingham, U.K.) cast in the centre of the coil. Each heater provided 6 kW of heating capacity, giving a total heating capacity of 24 kW, and heated the water to 450 °C. These heaters were connected in parallel using ¼" stainless steel piping, and a thermocouple was placed downstream of the recombination point to monitor the output temperature. There were additional thermocouples placed within each heater to monitor the individual heater temperatures.

Pumps P2 and P3 provided the precursors for the experiments, where P2 typically provided aqueous metal salts and P3 provided aqueous base. The flows of P2 and P3 combined in a Swagelok ⅜" tee-piece, where the combined flow was subsequently bifurcated by a second ⅜" tee-piece before flowing into the Pilot-Scale Confined Jet Mixer (described further in Section 2.1.2.1). Within this mixer, the hot water feed from P1 combined with the mixed precursor flows from P2 and P3. The output from this mixer flowed through a 0.9 m section of ¾" pipe, giving a residence time of *ca*. 6.5 s before reducing to ¼" pipe and flowing through a pipe-in-pipe counter-current heat exchanger. This reduced the temperature of the output slurry to below 60 °C. Finally, the slurry exited the apparatus *via* a back-pressure regulator (Swagelok KHB series) and was collected in a plastic container open to the atmosphere.

The Pilot-Scale reactor was monitored and controlled by a LabView GUI developed by Dr C. Tighe. The flow rates of all pumps and the heater output were calibrated and controlled through this interface.

2.1.1.2. Low-Temperature Lab-Scale reactor

The lab-scale reactor for low-temperature synthesis (mixing temperature typically in the range 335 – 375 ºC) was constructed as shown in Figure 2.2, with different mixing configurations possible in the relevant locations indicated by components A and B. The construction was identical for all components aside for these mixing points for low-temperature reactions.

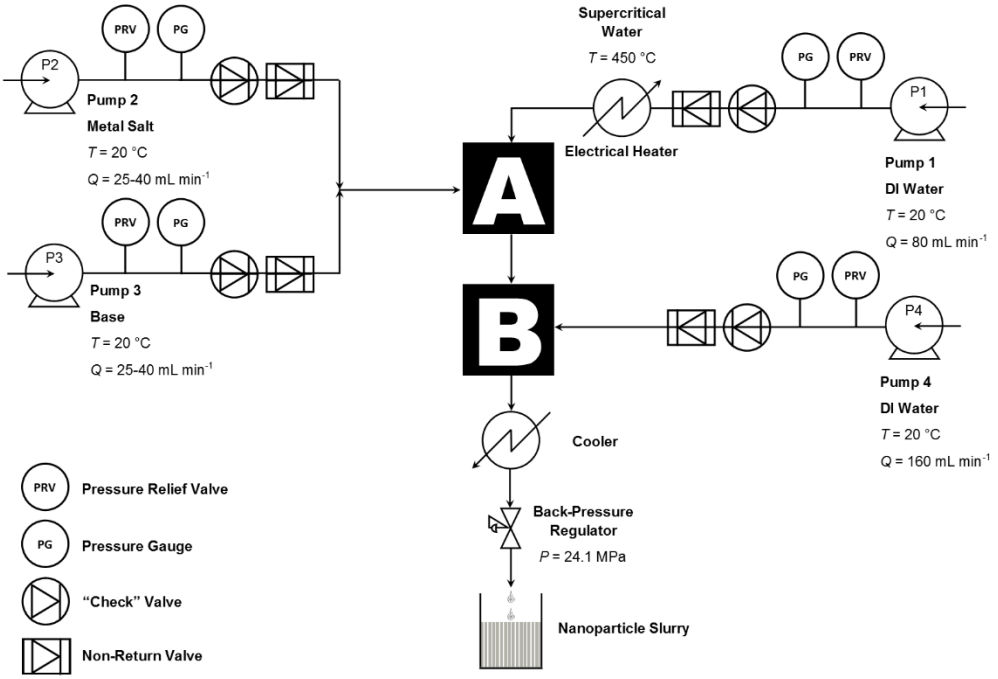

Figure 2.2 – A general schematic for the Low-Temperature Lab-Scale reactor including all major components, with different mixing configurations possible in locations A and B.

The reactor was constructed from off-the-shelf components (Swagelok 316L stainless steel fittings and tubing), allowing for facile customisation and maintenance of the process. Four pumps (Primeroyal K, Milton Roy Europe, Sunderland, UK) each provided a flow of either D.I. water (P1 and P4, Figure 2.2) or aqueous precursors (P2 and P3). The flow rates were controlled by actuators on the pumps which were calibrated using LabView software (LabView, National Instruments, Berkshire, U.K.). The pumps were connected to conical storage vessels for precursors (1 L capacity with an inlet made from ¼" piping and fittings) and a large D.I. water reservoir (100 L capacity with an inlet made from ½" piping and fittings) which were both connected to the pump *via* a 3-way ball valve (40GGG Series, Swagelok). This allowed the feed to be changed rapidly between these two sources during operation of the process. The outputs of the pumps were connected to pressure gauges (EN 837-1, WIKA Instruments Ltd., Redhill, U.K.), pressure relief valves (HPRV, Parker Hannefin Ltd., Warwick, U.K.) set to a relief pressure of 276 bar, a check valve and a non-return valve in series, identical to those described in Section 2.1.1.1. The relief valves prevented dangerous pressure build-up in the reactor due to blockages which can occur during synthesis, and the non-return valves prevented back-flow into the pump from the reactor. Pump P1 fed D.I. water (occasionally containing H_2O_2 in some experiments to generate an oxidising environment) through two custom-made heaters with a

combined power output of 7 kW. The design of the heaters is fully described in Dr N. Makwana's thesis.[130] The heaters were programmed using a Eurotherm controller (Eurotherm, Worthing, U.K.) set to achieve a temperature of 450 ºC with a ramp rate of 10 ºC min^{-1}. The aqueous precursors (typically a metal salt and a base at room temperature) were pumped by pumps P2 and P3 into the process, which premixed in a ¼" Swagelok tee-piece before flowing into the mixing arrangement market with component A. Within the main confined jet mixing arrangement (described in Section 2.1.2.1) the mixed feeds from P2 and P3 combined with the hot water stream from P1. The products from this CJM mixing point either flowed directly through a 1 m section of ⅜" pipe into a pipe-in-pipe counter-current cooling section (meaning pump P4 was not used), or into component B. Component B could incorporate a second CJM mixer to combine the products of the first mixer with the P4 output before the cooling section; the second CJM mixer was not employed within this thesis. However, section B could include 6 m of heated ¼" pipe section in an oven (Elite Thermal Systems Ltd., Market Harborough, U.K.) to extend the residence time, and was employed in certain experiments as indicated in the relevant chapters. The cooling section reduced the product temperature to below 60 ºC before it passed through a back-pressure regulator (BPR), which maintained a pressure of 240 bar on the system. Two BPR technologies were employed in this thesis on the Lab-Scale: a Tescom BPR (model 26-1762-24-194, Emerson Process Management Regulator Technologies, Inc., South Lanarkshire, UK) and an Equilibar BPR (model EB1HP2 HF, 316 stainless steel with a 1 mm thick PEEK diaphragm, Equilibar, Fletcher, North Carolina, U.S.). The nanoparticle slurry was collected in a plastic container open to the atmosphere after exiting the BPR.

2.1.1.3. High-Temperature Lab-Scale reactor

In order to achieve a mixing point temperature of > 375 ºC, a significant modification of the lab-scale reactor was necessary. Due to the comparatively large heat capacity of water at ~370 ºC and 240 bar (Figure 1.8), a high degree of imbalance between the hot water feed and the precursor feeds is necessary. In practice, this typically resulted in 80 mL min^{-1} of 450 ºC D.I. water and 10 mL min^{-1} combined precursor feeds to give a theoretical mixing point temperature of 402 ºC.[131] The Milton Roy Primeroyal K pumps described in the previous section were not suitable for such low flow rates, as the internal non-return valves within the pumps only function correctly at > 25 mL

min^{-1} (Figure 2.3). Therefore, the precursors were provided by two Gilson-type pumps (Gilson 305, Figure 2.3, pumps G1 and G2) operating at flow rates between 5 – 7.5 mL min^{-1} each. Pump G1 provided an aqueous metal salt precursor, whereas pump G2 provided aqueous base. The outputs of pumps G1 and G2 flowed through 1/8" pipe connected to pressure gauges, pressure relief valves and non-return valves in series as described in the previous section. The outputs of the Gilson pumps combined in a 1/8" tee-piece, which subsequently flowed into a 4-way switch valve. This switch valve was also connected to pump P4 (described in the previous section), an exhaust pipe with a Tescom BPR and the mixing point in the reactor. The 4-way valve (7921F4Y, LAA UK Ltd., Middlesex, U.K.) enabled the Gilson pumps to be pressurised and depressurised in isolation from the reactor, i.e. pump P4 and the Gilson pumps could be interchanged by the valve. This was a practical consideration, allowing any maintenance of the Gilson pump flows during synthesis, as the operational use of them was less robust than the Milton Roy pumps.

During synthesis, the combined output of G1 and G2 flowed into the mixing point and combined with the hot water feed from P1. The output slurry flowed through section C, which was either a 1.4 m section of ¼" pipe, or a 6 m section of ¼" pipe contained in an oven. After section C, the output flowed through the same cooler and BPR segment as described in Section 2.1.1.2.

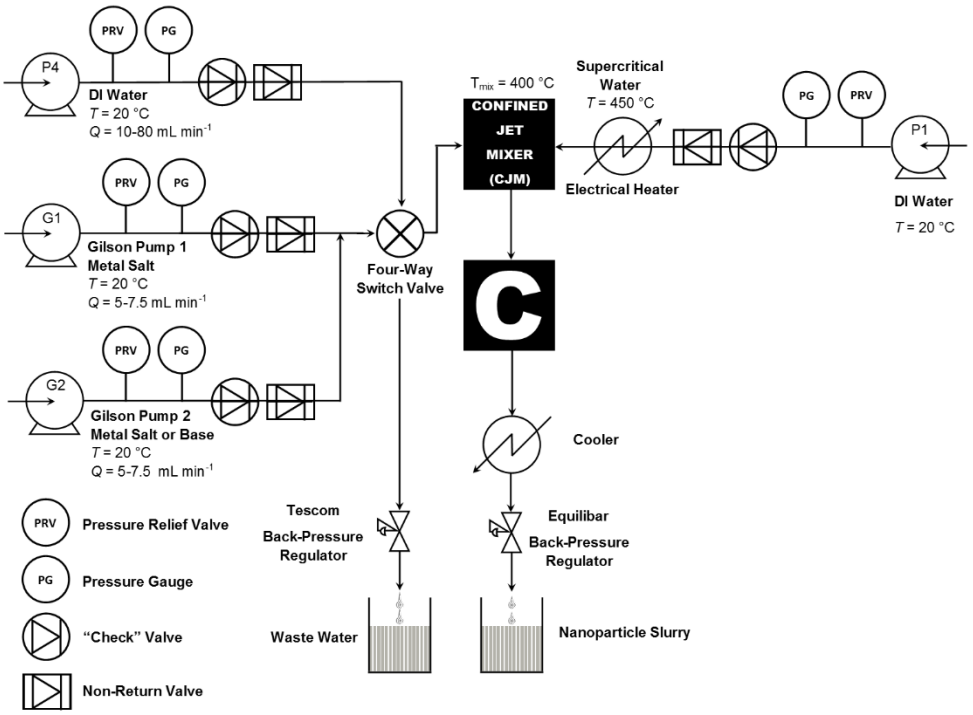

Figure 2.3 – A schematic of the High-Temperature Lab-Scale process, including all major components.

2.1.2. Confined Jet Mixer Details

The geometry of mixing has a significant effect on the dynamics of hot water and precursor combination as described in the Chapter 1. The CJM was employed on the Lab-Scale and Pilot-Scale process within this study, and was designed and built by Prof. J. Darr, Dr C. Tighe and Dr R. Gruar.[76] The hot water and precursor feeds were combined in a co-axial geometry (Figure 2.4), and the mixed product flowed upwards. Rapid mixing could be achieved in this configuration, with a uniform product feed achieved in the order of milliseconds.[76] The hot water piping (Y) was fitted into the cross union (X) *via* a bored-through fitting (Z), where the output of Y generally resided within the combined output pipe (Q). The mixed precursor feeds from P2 and P3 were fed into the mixer symmetrically through the inlets indicated in Figure 2.4. The schematic of the CJM is virtually identical between the variants employed in this thesis, but possessed different piping and fitting sizes.

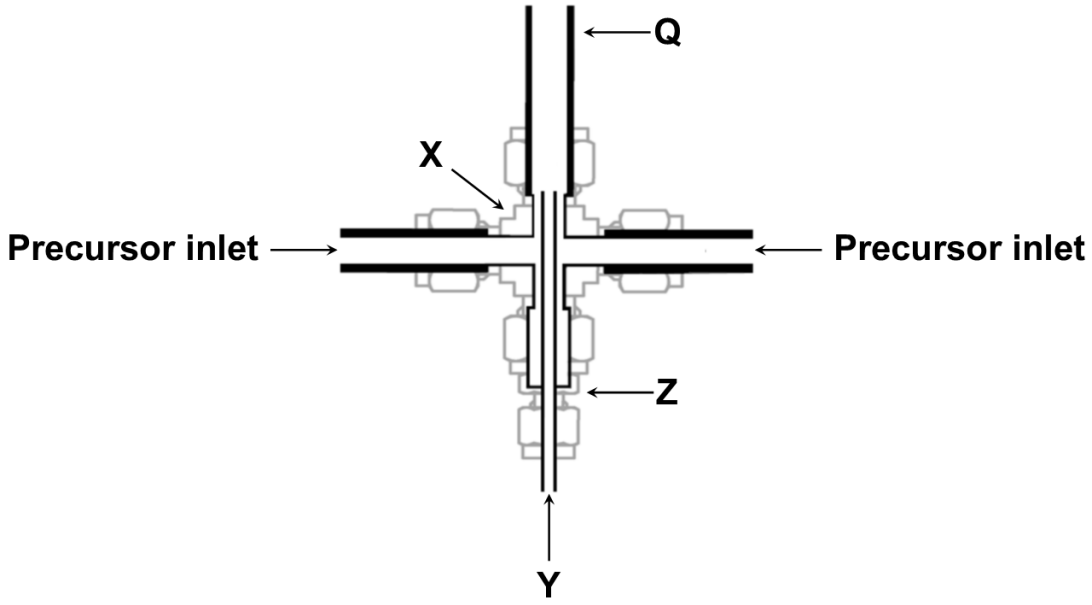

Figure 2.4 – A general schematic of the Confined Jet Mixer, constructed from a cross union (X), hot water piping (Y), bored-through fitting (Z), output pipe (Q) and precursor inlets.

2.1.2.1. Single Confined Jet Mixer Configuration

The Single CJM configuration was used exclusively within this thesis. A general schematic of the mixer is shown in (Figure 2.4), where the key innovation is the pipe-in-pipe geometry employed. The hot water feed (with flow rate Q_{SW}) is emitted within a cross mixer X from the internal pipe Y as a jet, where rapid mixing between the jet and room-temperature, aqueous precursors (flow rate Q_P) occurs beyond the hot water outlet. The Reynolds numbers and mixing temperatures of the output slurry were calculated using the properties of pure water as described by the model of Wagner and Pruβ.[131] Three sizes of mixer were employed, and are described in Table 2.1. For certain experiments, a longer residence time was achieved by incorporating a heated pipe section in an oven beyond the mixing point, and these extended residence times are displayed in Table 2.1.

Table 2.1 – The sizes of the cross mixers (X) and hot water piping (Y) used in different mixers for the different reactor scales. The flow rates of the supercritical water feed (Q_{SW}) and combined precursor feeds (Q_P) and the resulting mixing temperature (T_{mix}), Reynolds number (R_e) and residence time (t) are also indicated, with the lengthened residence time with the oven addition displayed in the final column.

Reactor	X / inches	Y / inches	Q_{sw} / mL min^{-1}	Q_P / mL min^{-1}	T_{mix} / °C	R_e	t / s	With oven / s
Pilot-scale	3/4	1/4	400	400	335	15978	6.5	-
Low-Temperature Lab-Scale	3/8	3/16	80	80	335	6939	7.2	-
				50	378	7977	6.5	15
High-Temperature Lab-Scale	1/4	1/8	80	10	402	14076	1.0	-
				15	391	14345	1.1	5

2.1.3. Materials Synthesis

This section describes the general procedures of nanoparticle synthesis and post-synthesis processing to produce dry, clean powders. Specific details of these methods are described in the relevant chapters where appropriate.

2.1.3.1. Sample production procedure

The key advantage of CHFS as a synthesis technique is the ability to produce multiple compounds rapidly; typically, > 66 samples per day are achievable at < 1 g per sample. Alternatively, 20 samples at > 1 g per sample can also be made within a day. This is made possible by the three-way switch valves mentioned in Section 2.1.1, where the precursor pumps can quickly switch between D.I. water and aqueous precursors. When an experiment was performed, the precursor pumps were switched from D.I. water to aqueous precursors. After a short time delay (typically three minutes), nanoparticulate slurry became visible from the output of the BPR. As there will be diffusion between the D.I. water and the precursor solution in the pipes (Figure 2.5), the first two minutes of product were discarded due to the lower than desired precursor concentration when the interdiffusion zone flowed into the CJM.

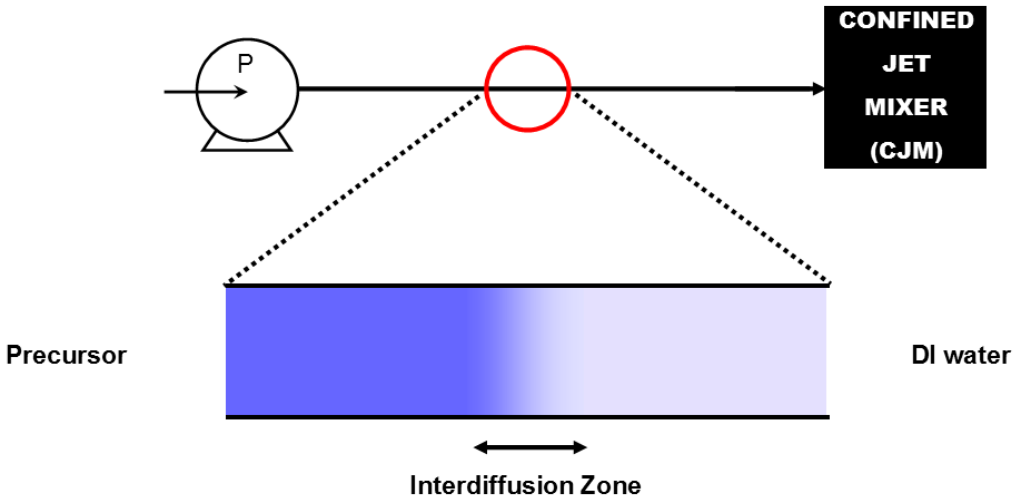

Figure 2.5 – A schematic illustrating the interdiffusion zone observed between precursors and D.I. water within the feed pipe flowing from the precursor pump P into the Confined Jet Mixer.

After these two minutes, the product slurry was collected beyond this point in a plastic beaker. At the end of the reaction, the precursors pumps were switched back to D.I. water and slurry collected for 2 minutes after, due to the aforementioned time delay in precursor delivery from the pumps to the reactor. Any slurry produced after this point was discarded. The system was flushed continuously with D.I. water afterwards until no remaining product could be seen exiting the BPR, and at this point a fresh precursor solution could be pumped into the reactor. In this way, contamination between samples was reduced between reactions, although typically the plan of reactions was tailored to minimise the effect of contamination. For example, if an array of doped metal oxides was synthesised, the pure metal oxide was synthesised first, followed by samples with increasing dopant concentration.

2.1.3.2. Sample processing procedures

As there were always aqueous by-products (excess base and/or waste counter ions) present in the as-synthesised slurries, it was necessary to remove these by-products before further processing. Depending upon the agglomeration properties of the synthesised nanoparticles, different cleaning procedures were adopted. If the nanoparticles agglomerated easily, the supernatant was decanted and the concentrated paste was typically centrifuged at 4500 rpm for 5 minutes. The centrifuged sludge was repeatedly resuspended in D.I. water and centrifuged until the conductivity of the supernatant was reduced below a typical value of 100 µS m^{-1}.

However, some samples were very well dispersed and did not agglomerate easily. These samples were agglomerated by dissolving NaCl in the product slurry. The supernatant was discarded, and the concentrated slurry was typically centrifuged at 1500 rpm for 5 minutes. The resultant paste was transferred to dialysis tubing (Visking Dialysis Tubing, Medicell Membranes Ltd., London, U.K.), sealed within the tubing using cable ties, and the filled tubes suspended in a storage tank filled with stirred D.I. water to allow the aqueous ions to diffuse out of the tubes. The D.I. water in the storage tank was replaced periodically, either until its conductivity remained consistently below 10 μS m^{-1}, or the conductivity of the slurry within the tubes was reduced below 150 μS m^{-1}.

2.1.3.3. Drying methods

Two separate drying methods were adopted throughout this thesis. The majority of powders were dried using a freeze-drier; as this method does not rely on heating, agglomeration and Ostwald ripening upon drying was reduced. In this method, the cleaned nanoparticle paste was frozen and freeze-dried by slowly heating from -60 °C to 25 °C, over 24 h under a vacuum of < 13 Pa using a VirTis Genesis 35 XL (SP Scientific, New York, U.S.). Alternatively, for samples where high surface area was not crucial, the pastes were dried in a vacuum oven (Kelvitron® T, Heraeus Instruments, Neston, U.K.) set to 40 °C.

2.1.3.4. Heat-Treatments

For certain samples, post-synthesis heat-treatments were conducted either to increase the crystallinity of the product, remove crystalline defects (such as antisite defects) or to convert a carbonaceous coating to graphitic carbon. Specific details of the treatments are given in each section. Experiments to increase crystallinity were typically performed in a muffle furnace (CWF 1300, Carbolite, Hope, U.K.) in a zirconia crucible if the heating time exceeded 10 minutes. However, for certain powders a rapid anneal was desired. In these cases, the Rapid Annealing Process was used (Figure 2.6). A crucible was inserted into a section of 3/8" pipe, which resided within a larger outer pipe (1") which was securely clamped. The crucible was inserted and removed from the work tube of the tube furnace by sliding the inner pipe within the outer pipe. The outer pipe secured the inner pipe, thereby ensuring the crucible

remained inside the work tube without the inner pipe coming into direct contact with the work tube.

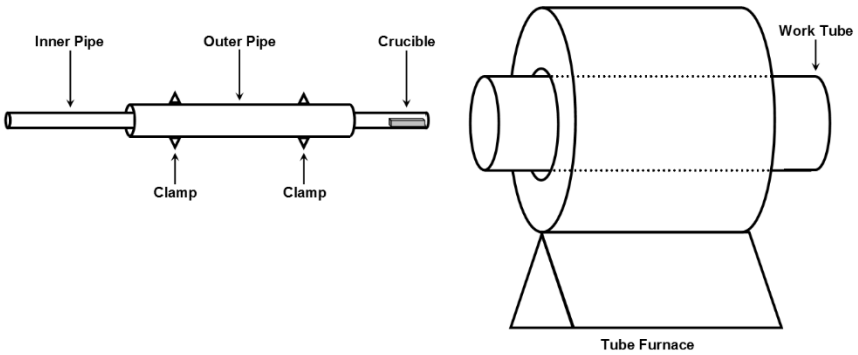

Figure 2.6 – A schematic of the Rapid Annealing Process.

In the case of generating graphitic coatings, the samples were heated in zirconia crucibles within a zirconia work tube with gas-tight end caps with a constant flow of inert gas (Ar).

2.1.4. Material Characterisation Techniques

This section details the analytical techniques used to characterise the powders made *via* CHFS. Specific details of the analysis methods are given in the relevant chapters.

2.1.4.1. X-Ray diffraction and Rietveld refinement

A variety of XRD apparatus and configurations were used throughout this thesis, and are included in detail below in order of increasing data quality:

a. A Bruker D4 Endeavour diffractometer in Bragg-Brentano flat-plate reflection geometry using Cu-Kα radiation (λ = 1.54 Å) in the 2θ range 5 to 60° with a step size of 0.05° in 2θ and a count time of 2 or 4 s. The sample was rotated in the beam with a post-sample graphite monochromator selecting both Cu-$K\alpha_1$ and Cu-$K\alpha_2$, and 0.5° divergent and receiving slits.
b. A Stoe StadiP diffractometer in transmission mode (coupled θ-2θ geometry), using Mo-Kα radiation, with the sample sandwiched between two plastic foil disks held together with a thin layer of silicon grease. Patterns were typically collected between 2 – 40° 2θ, with a step size of 0.5° 2θ and a collection time of 3 - 20 s per step.

c. A Stoe StadiP diffractometer in transmission mode (Debye-Scherrer geometry) using Mo-Kα radiation, with the sample contained within a 0.3 mm borosilicate glass capillary. Patterns were typically collected between 2 - 60° 2θ, with a step size of 0.5° 2θ and a collection time of 80 - 100 s per step. Multiple patterns (typically 3 or 4) were collected in this manner and summed to produce the final pattern. In this way, if the sample went out of alignment or degraded in the beam, a difference would be observable in the repeated diffraction patterns.

For configurations **b** and **c**, a pre-sample Ge (111) monochromator selected the Mo-$K\alpha_1$ radiation only (λ = 0.709 Å) and included a 0.5 mm collimator restricted to 3 mm height. The sample was rotated in the beam, and the diffraction intensity recorded using a Dectris Mython 1k silicon strip detector covering 18° 2θ.

Configurations **a** and **b** were most commonly used for phase purity assessment and basic Rietveld refinement, whereas configuration **c** was required to obtain high-quality XRD data for more sophisticated Rietveld analysis. Specific details of the collections are included in the relevant chapters.

2.1.4.2. Rietveld refinement

Rietveld refinement is the process by which a well-defined existing crystalline structure, including unit cell parameters and atomic positions, are used as a basis to calculate these parameters from an experimental XRD pattern. This is achieved by varying numerous parameters, including: scale factor, background contributions, particle size and strain contributions, unit cell parameters and atomic positions. These values are systematically varied by Rietveld software to minimise the difference between the structural model and the observed XRD pattern, using the least-squares refinement method (Equation 2.1).

$$M = \sum_i w_i (y_i^{obs} - \frac{1}{c} y_i^{calc})^2$$

Equation 2.1 – The sum of squares equation used to refine XRD patterns, where *M* is the sum of squares, w_i is a weighting parameter which incorporates the standard uncertainty of data collection, y_i^{obs} is the experimentally measured diffraction intensity, y_i^{calc} is the calculated diffraction intensity generated by the refinement software and the reference crystal structure, and *c* is a scale parameter.

This refinement is repeated numerous times (typically tens or hundreds of cycles) until convergence is achieved, i.e. *M* does not decrease significantly with further refinements. Once convergence is reached, goodness-of-fit parameters R_{wp} and χ^2 are assessed to determine the numerical quality of the fit. R_{wp} is simply the square root of the sum of squares *M*, scaled by the weighted intensity (Equation 2.2a). R_{exp} is a measure of the lowest expected R_{wp} value (given the degree of standard uncertainty as defined by w_i, Equation 2.2b), with the number of data points *N*. χ^2 is the ratio of R_{wp} and R_{exp} (Equation 2.2c).

$$a)\ R_{wp} = \sqrt{\frac{\sum_i w_i (y_i^{obs} - \frac{1}{c} y_i^{calc})^2}{\sum_i w_i (y_i^{obs})^2}}$$

$$b)\ R_{exp} = \sqrt{\frac{N}{\sum_i w_i (y_i^{obs})^2}}$$

$$c)\ \chi^2 = \frac{R_{wp}}{R_{exp}}$$

Equation 2.2 – a) the R_{wp} factor, b) the R_{exp} factor, and c) the χ^2 factor employed within Rietveld refinement, where w_i is a weighting parameter which incorporates the standard uncertainty of data collection, y_i^{obs} is the experimentally measured diffraction intensity, y_i^{calc} is the calculated diffraction intensity generated by the refinement software and the reference crystal structure, and *c* is a scale parameter.

Therefore, R_{wp} is considered an absolute value of the quality of the fit, and χ^2 is the relative quality of the fit considering the quality of the experimental XRD pattern. Typically, "good values" of R_{wp} are < 5%, and χ^2 should reside between 1 – 1.5. However, this should be treated with some caution, as these fitting parameters can be made lower by increasing the variables in the fit (as many of the variables are co-dependent, this can reduce the usefulness of the extracted data). Furthermore, it should be stressed that the fit should always be assessed visually to determine its quality. Within this thesis, all refinements are included for visual inspection in Chapter 11 - Appendix I.

Rietveld refinement was carried out using MAUD (Material Analysis Using Diffraction) software,[132] using high-quality references from the ICSD (Inorganic Crystal Structure Database) to fit the diffraction patterns. It should be noted that the

borosilicate glass capillary contributed a broad diffraction peak centred on 10° 2θ, which was accounted for by including an amorphous silica phase in the fit. Additionally, diffraction data from a LaB_6 standard was collected to extract instrumental peak broadening parameters (asymmetric, Caligoti, and Gaussian broadenings, specifically) and to check for instrument misalignment (Figure 11.1, Chapter 11 - Appendix I).

The XRD patterns were generally fitted according to the following protocol (Figure 2.7), where additional terms within the refinement were varied according to the order shown. It should be noted that the quality of the data set (determined by the data collection methods as described in Section 2.1.4.1) determined how many parameters were refined, i.e. higher quality data could be refined with more terms.

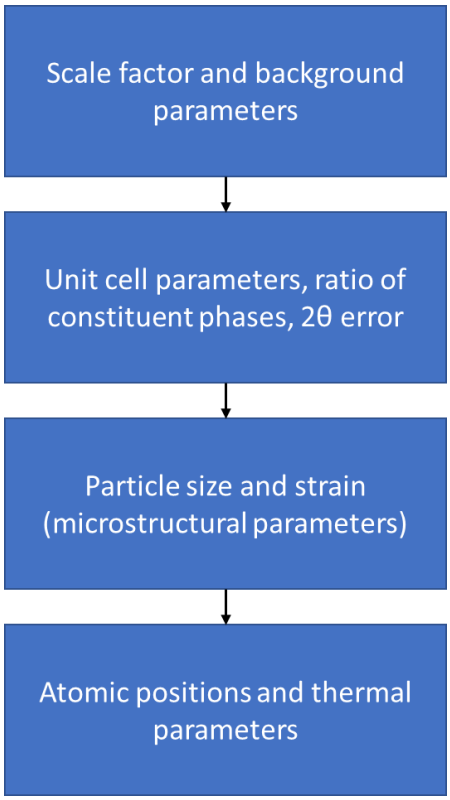

Figure 2.7 – The general protocol for performing Rietveld refinement, describing the order in which variables were included and refined. Therefore, the additional refinement terms were refined alongside previous terms in this flowchart.

2.1.4.3. Transmission Electron Microscopy

Transmission Electron Microscopy (TEM) images of nanoparticles were collected using a 200 keV JEOL JEM-2100 fitted with an Oxford Instruments X-MaxN 80-T

Silicon Drift Detector (SDD, GATAN). Samples were prepared for imaging by ultrasonically dispersing them in methanol and pipetting a drop of the resulting suspension onto carbon-coated Cu or Au grids (Agar Scientific, UK). The solvent was evaporated, leaving a deposition of particles on the wafer, and the grid was inserted into the TEM microscope for analysis.

2.1.4.4. Field Emission Scanning Electron Microscopy

Field emission scanning electron microscopy (FE-SEM) images of nanoparticles were obtained with a JEOL JSM-6700F microscope. Samples were prepared for imaging by ultrasonically dispersing them in methanol and pipetting a drop of the resulting suspension onto Si wafer (<100> orientation, Si-Mat Silicon Materials, Kaufering, Germany). The solvent was evaporated, leaving a deposition of particles on the wafer, which was inserted into the FE-SEM microscope for analysis.

2.1.4.5. Raman Spectroscopy

Raman spectra were collected on a Raman microscope system (Renishaw inVia^{TM}) with a laser excitation wavelength of 514.5 nm. Scans were conducted over the range 200 – 2000 cm^{-1} in Chapters 3 and 6, and the range 200 – 4000 cm^{-1} in Chapter 8, where each individual scan was taken over 30 s, and the summation of 4 individual scans produced the final spectrum (2 minutes collection time). The laser was set to 10% of full power for samples in Chapters 3 and 6, and set to 100% power in Chapter 8.

2.1.4.6. CHN Analysis

A scientific CHN-analyser determined the carbon, hydrogen and nitrogen composition of selected samples. Samples were combusted, and the gaseous products were passed through a reduction furnace. The final gasses (CO_2, H_2O, N_2) were analysed to obtain the concentration of each element. All tests were conducted by the Analytical Services department of the UCL Department of Chemistry.

2.1.4.7. Brunauer–Emmett–Teller analysis

Samples were prepared for Brunauer–Emmett–Teller (BET) analysis by weighing approximately 50 mg of sample into a small section of Al foil, which was also weighed. This foil was wrapped into a tight cylinder, and inserted into a glass tube,

and heated to 150 °C under flowing N_2 gas overnight to dry. The surface area of the sample was measured using a Micromeritics TriStar II *PLUS* (assuming a mass of 50 mg). After analysis, the mass of the sample and foil was reweighed, where any mass loss was assumed to be evaporated water. Therefore, the true sample mass (m, mg) could be calculated by subtracting the mass of the evaporated water from the sample mass before drying. Therefore, the sample specific surface area (S_{BET}, $m^2\ g^{-1}$) was calculated by multiplying the output value from the equipment (S_{OUT}) by the ratio indicated by Equation 2.3.

$$S_{BET} = S_{OUT} \times \frac{50}{m}$$

Equation 2.3 – The ratio used to calculate S_{BET} from S_{OUT} and m.

The average particle size could be estimated from S_{BET} using the equivalent sphere approximation (Equation 2.4), where D_S is the average particle diameter, and ρ is the material density (either assumed to be the bulk material density or calculated from crystallographic data). This approximation was occasionally applied to non-spherical particles, and is presented in these cases only as an interpretable number extracted from the surface area.

$$D_S = \frac{6000}{S_{BET}\rho}$$

Equation 2.4 – The equivalent sphere approximation, where S_{BET} is the specific surface area found from BET analysis, and ρ is the density of the material.

2.1.4.8. X-ray Photoelectron Spectroscopy

X-ray Photoelectron Spectroscopy (XPS) was performed using a Thermo Scientific K-alpha photoelectron spectrometer using monochromatic Al-Kα radiation. Survey scans were collected in the binding energy range 0 – 1100 eV at a pass energy of 200 eV. For the main peaks, higher resolution scans were recorded with pass energies of 50 eV. Peak positions were calibrated using the adventitious carbon 1s peak at 284.7 eV using CasaXPS™ software.

2.1.4.9. Inductively-Coupled Plasma Atomic Emission Spectroscopy

Inductively-Coupled Plasma Atomic Emission Spectroscopy (ICP-AES) was collected using a Varian 720 ICP-AES to determine ratios of elements within a sample. Typically, this was achieved by dissolving the sample in acid (such as 69% HNO_3, Analytical Grade, VWR Chemicals, Pennsylvania, U.S.A.) and diluting the resulting solution in dilute acid (typically 1% HNO_3) until the dissolved ions reached the desired concentration (typically 20 ppm). Standard solutions of ions were prepared in the following manner:

Precursor salts of the desired ions were dissolved in 1% HNO_3 to achieve a concentrated precursor stock of known concentration (e.g. 2000 ppm Fe). This was then pipetted using a micropipettor and diluted further with 1% HNO_3 to achieve standard solutions across a range of concentrations (e.g. 10, 20 and 30 ppm). A blank standard solution (i.e. just 1% HNO_3) was also included, which allowed an intensity-concentration calibration line to be calculated. Therefore, the measured intensity of an ion within a sample solution could be converted into a concentration in ppm. By simultaneously collecting data on multiple ions at once, the molar ion ratios of samples could be calculated.

2.1.4.10. Thermogravimetric Analysis – Differential Scanning Calorimetry

Simultaneous differential scanning calorimetry (DSC) and thermogravimetric analysis (TGA) was carried out using a Netzsch STA 1500 using a heating rate of 5 ºC min^{-1} from 25 to 1000 °C in air. Samples were analysed within an alumina crucible and under a constant flow of air. A background scan was conducted with an empty crucible in the same temperature range and heating rate to subtract from the raw data, which eliminated buoyancy effects.

2.1.5. Electrochemical Analysis

Throughout this thesis, the nanoparticles fabricated *via* CHFS were assessed using electrochemical methods to determine their suitability as Li-ion electrode materials. Details of the assembly and testing are described in this section.

2.1.5.1. Electrode Preparation (Li-ion)

All of the Li-ion electrode materials in this thesis were processed into thin electrodes spread on Al foil (cathode materials) or Cu foil (anode materials). This was achieved by preparing an electrode ink, which consisted of a mixture of the active material, conductive carbon and polymer binder in an N-methyl-2-pyrrolidone (NMP, > 99.5%, Sigma-Aldrich, St. Louis, USA) solvent. This mixture was fixed to a specific ratio (typically 80:10:10 active material:conductive carbon:polymer binder).

Typically, the polymer binder, polyvinylidine fluoride (PVDF, PI-KEM) was dissolved in NMP to make a 10 wt% PVDF solution. 1.000 ± 0.005 g of this solution was combined with 0.8000 ± 0.0005 g active material and 0.1000 ± 0.0005 g conductive carbon (carbon black, Super P^{TM}, Alfa Aesar, U.K.) to make a thick paste. This paste was diluted with more NMP until the correct consistency was achieved, i.e. a drop of slurry would slowly fall off the end of a spatula. The amount of NMP used varied, with low surface area materials requiring 2 ml total NMP content (solid content 33%) and high surface area materials requiring 4 ml total NMP (solid content 20%). This slurry was homogenised using a ball-mill (Pulverisette 7, FRITSCH, Brackley, U.K.) for 30 – 60 minutes to produce a smooth ink.

The ink was spread onto Al or Cu foil (PI-KEM, Staffordshire, U.K.) using a doctor blade (EQ-SE-KTQ-100, PI-KEM), which could be set to a specific blade gap. Blade gaps between 100 - 250 µm were used to achieve the desired electrode thickness. The doctor blade was slowly pushed across the foil with a drop of the ink in front of the blade, which produced a uniform, flat layer of the ink on the foil. Finally, the solvent was removed with heat (using an oven or hot-plate) to produce the dried electrode sheet. A demonstrational film performed by the author of slurry making and electrode fabrication are available at reference [133].

2.1.5.2. Coin cell fabrication (Li-ion)

The Li-ion coin cells were either assembled in an Ar-filled glove box (O_2 and H_2O < 10 ppm) or a dry room (dew point < −40°C) to prevent side reactions of Li metal and the electrolytes with water. A schematic of the coin cell components is displayed in Figure 2.8. Circular discs of the electrode sheets (15 mm or 16 mm diameter) were

placed within the cathode case of a 2032-type coin cell (PI-KEM, Staffordshire, U.K.). A 20 mm diameter separator disc (Whatman or Celgard) was layered on top of the electrode, and electrolyte was added dropwise until the separator was saturated. This was followed by the anode (a 15 mm diameter Li metal disc, PI-KEM), a 15 mm stainless steel disc (0.5 mm thickness, PI-KEM) and a wave spring (PI-KEM). The wave spring and steel disc ensured the components of the cell were under compression and were in good physical contact. Finally, an anode case and gasket ring (PI-KEM) were placed on top of the cell, and sealed using a crimper set to a pressure of 0.8 tons (MSK-160D, PI-KEM). A schematic of the assembly is shown below (Figure 2.8), and a demonstrational video of coin cell assembly performed by the author is available at reference [134].

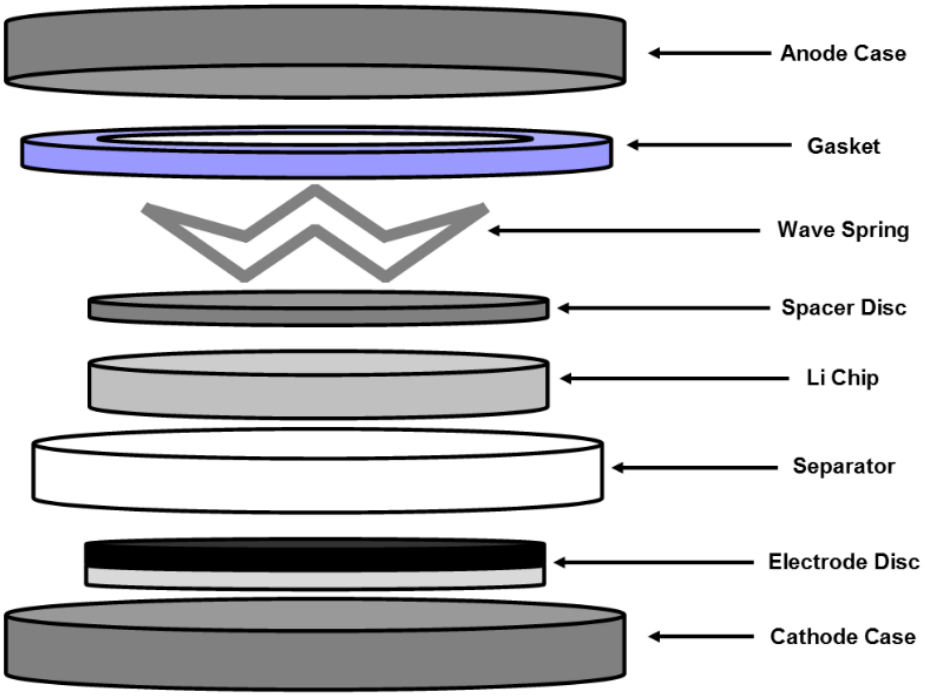

Figure 2.8 – A schematic of a Li-ion coin cell including all components, where the Spacer Disc, Wave Spring, Anode Case and Cathode Case were all fabricated from stainless steel, and the Gasket was polypropylene. The Separator was either Whatman or Celgard.

2.1.5.3. Potentiostatic analysis

Potentiostatic analysis was employed throughout this thesis in the form of cyclic voltammetry (CV). The potential of the cell vs. Li/Li^+ is increased or decreased linearly as a function of time between two limits (Figure 2.9a), and the current measured and plotted against potential (Figure 2.9b). For a reversible redox process, there is a

positive and negative current peak centred on the equilibrium potential. Therefore, this technique reveals the potentials where an electrode is active (Faradaic reactions).

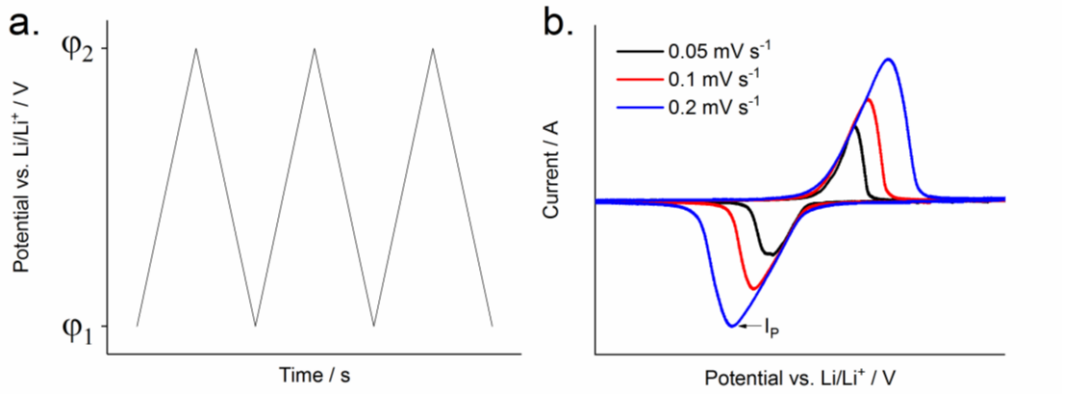

Figure 2.9 – a. A plot showing the standard testing regime of a potentiostatic test. The potential *vs.* Li/Li^+ is varied linearly between two potential values (φ_1 and φ_2) as a function of time. b. A typical CV plot with the trace from multiple scan rates, indicating a Faradiac reaction, with the peak discharge current I_P indicated for the 0.2 mV s^{-1} scan rate.

The Randles-Sevcik equation was used to estimate a Li^+ diffusion coefficient within the sample crystal structure from the peak discharge currents (I_p) observed during cyclic voltammetry tests at different scan rates (v, Equation 2.5). For a diffusion-limited process, a plot of I_P vs $v^{0.5}$ yields a straight line, where the lithium diffusion coefficient (D_{Li}) can be extracted from the gradient.[135] The diffusion coefficients obtained are also dependent upon the mass loading and electrode architecture, so are used only for comparison between similar electrodes (which were prepared identically).

$$I_P = (2.69 \times 10^5) C.A.D_{Li}^{\frac{1}{2}} n^{\frac{3}{2}} v^{\frac{1}{2}}$$

Equation 2.5 – The Randles-Sevcik equation, where I_p is the peak current (in Amperes), C is the initial concentration of Li^+ in the sample (calculated from crystallography data, mol cm^{-3}), A is the electrode area (cm^2), D_{Li} is the diffusion coefficient (cm^2 s^{-1}), n is the number of electrons involved in the redox pair, and v is the potential scan rate (V s^{-1}).[135]

2.1.5.4. Galvanostatic analysis

Two methods of galvanostatic analysis were conducted within this thesis. The first of these, constant-current tests, involved applying specific currents (current which is weighted to the active mass of the electrode) to charge and discharge the cell. A charge current was applied until the cell reached an upper potential limit, at which point a discharge current was applied until a lower potential limit was achieved (Figure 2.10a).

The voltage and capacity are recorded during testing (Figure 2.10b). Repeated charge/discharge was performed at different applied currents, and the capacities and voltage recorded. This reveals how well the electrode retains capacity with increasing current load.

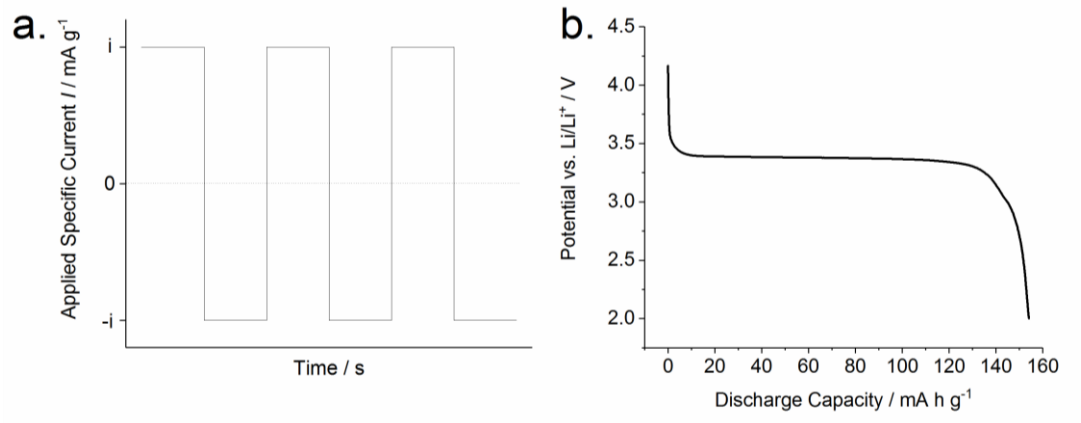

Figure 2.10 – A plot showing the standard testing regime of a constant current test. The current is varied between two values (i and −i), and switching occurs when specific potential limits are reached (in this specific case, the limits are 4.3 and 2 V).

The other galvanostatic methods employed were constant-current constant-voltage (CCCV) tests. This is also contained constant-current steps. However, when the upper voltage limit is reached, the voltage is held until the measured current drops below a certain value (typically 3% of the charge rate in this thesis). This test was employed for materials which were very kinetically limited, and required the voltage hold to achieve significant charge capacity.

It is important to discuss the unit "C-rate" which describes specific current throughout this thesis. A charge/discharge current of 1C is the current required to charge/discharge the electrode under test (assuming 100% theoretical capacity) in 1 hour. Therefore, a C-rate of C/2 and 2C will charge or discharge the electrode in 2 and 0.5 hours, respectively. The current required for a C-rate test is described by Equation 2.6, where Λ and m are the specific capacity and mass of the active material in the electrode, respectively:

$$I(mA) = Crate(h^{-1}) \times \Lambda(mA\ h\ g^{-1}) \times \mathrm{m}(g)$$

Equation 2.6 – The current required for a C-rate test, in terms of desired C-rate, theoretical capacity (Λ) and mass of active material (m).

C-rate tests are the most common method for comparing the relative performance of electrodes; because the current is mass-weighted, minor deviations in electrode masses have a negligible impact on observed performance.

3. Investigation of $LiFePO_4$ and Doped Variants as Li-ion Battery Cathode Materials

3.1. Aims

This chapter concerns the continuous hydrothermal synthesis of the $LiFePO_4$ cathode material, including an investigation into the effects of V and Nb dopants. A variety of precursor concentrations were employed to attempt to synthesise different stoichiometries of dopants within $LiFePO_4$. In addition, carbon coatings were generated by including a carbonaceous precursor.

3.2. Background

3.2.1. Discovery of $LiFePO_4$ as a cathode material

$LiFePO_4$ was initially developed by Padhi *et al*. in the late 1990s as the culmination of an investigation of Fe-based Li-ion cathodes.[91] The compound $LiFeO_2$ was the first potential candidate, and operated on the Fe^{4+}/Fe^{3+} redox couple. However, Li did not deintercalate from the structure within the stable electrolyte window described in Section 1.2.2.2. Subsequently, compounds based on the Fe^{3+}/Fe^{2+} redox couple were attempted, although they often had lower operating voltages *vs*. Li, which reduced their energy density and therefore their viability as a cathode. Incorporation of the PO_4^{3-} polyanion increased the potential of the Fe^{3+}/Fe^{2+} couple to 3.45 V vs. Li/Li^+. This was due to polarisation of the O^{2-} anions by the S or P atoms, which reduced the Fe-O orbital interactions and raised the Fe valance orbital energy. This higher voltage ensured $LiFePO_4$ had a reasonable energy density compared to other cathode materials. Furthermore, $LiFePO_4$ has excellent cycle stability, high tolerance of abusive operating conditions and is non-toxic, meaning it is the cathode material of choice for applications where cost and stability are most important.

3.2.2. Structure

$LiFePO_4$ possesses the olivine structure (*Pnma* space group, orthorhombic symmetry) where the Li and Fe atoms occupy octahedral sites and the P atoms occupy tetrahedral sites within a distorted hexagonal close-packed oxyanion array (Figure 3.1).[91] The LiO_6 octahedra (blue) form edge-sharing chains parallel to the *b*-axis, where each FeO_6

octahedron (orange) is joined to two LiO_6 octahedra, and each PO_4 tetrahedron (green) is joined to two LiO_6 octahedra and one FeO_6 octahedron.

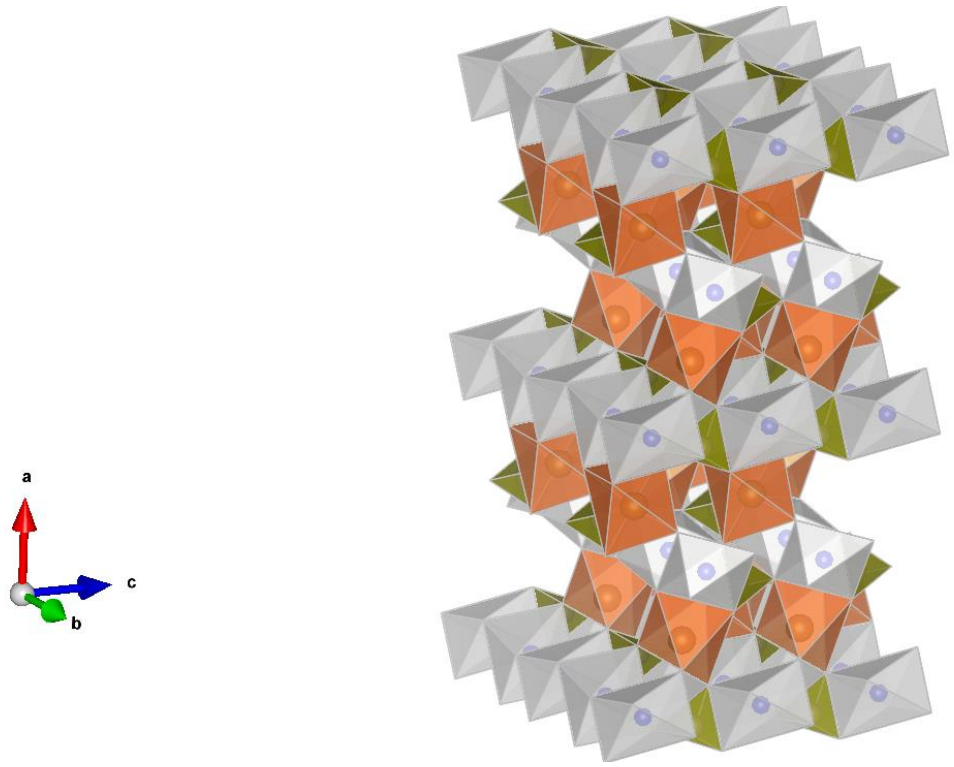

Figure 3.1 – The structure of $LiFePO_4$, indicating LiO_6 octahedra (blue), FeO_6 octahedra (orange) and PO_4 tetrahedra (green). The structure was drawn using VESTA software from PDF Card No. 01-070-6684.[90]

When the structure is delithiated, the resulting $FePO_4$ phase retains the orthorhombic symmetry of the parent $LiFePO_4$ structure, albeit with distorted lattice parameters (Table 3.1). However, the degree of distortion is minor overall (6.6% volume change), and this is reflected in the similarity in bond lengths between structures. For example, the Fe-O bond lengths only change by a maximum of 0.28 Å.[136] The relatively small volume change is partially responsible for the excellent cyclability of $LiFePO_4$ cathodes; firstly, the material is less prone to cracking during cycling (although this is still observed for large particles),[137] and secondly, the volume contraction matches the corresponding expansion of graphite anodes (which are the most common Li-ion anode), avoiding pressure changes in the cell with cycling.[138]

Table 3.1 – The lattice parameters and unit cell volume of $LiFePO_4$ and the delithiated $FePO_4$ structures.[136]

	$LiFePO_4$	$FePO_4$
a / Å	10.3290(3)	9.8142(2)
b / Å	6.0065(2)	5.7893(2)
c / Å	4.6908(2)	4.7820(2)
V / $Å^3$	291.02	271.70

The $LiFePO_4$ structure is very stable at elevated temperatures; it does not undergo significant exothermic reaction in a Li-ion cell until above 280 °C (compared to 150°C for $LiCoO_2$).[139] In addition, there are no detrimental side reactions of $LiFePO_4$ with the electrolyte below 85 °C, which is attributed to the strong P-O bonds preventing oxyanion reaction.[140]

3.2.3. Reactivity

When $LiFePO_4$ is charged in an Li-ion cell, Li^+ is removed, and the remaining structure is $FePO_4$. There are two possible mechanisms for this reaction: a two-phase (Equation 3.1a) or solid-solution mechanism (Equation 3.1b). This reaction occurs in reverse when the cell is discharged, regenerating the original $LiFePO_4$ phase.

$$\text{a) } LiFePO_4 \rightarrow xFePO_4 + (1-x)LiFePO_4 + xLi^+ + xe^-$$

$$\text{b) } LiFePO_4 \rightarrow Li_{(1-x)}FePO_4 + xLi^+ + xe^-$$

Equation 3.1 – a) the two-phase delithiation mechanism b) the solid solution delithiation mechanism of a $LiFePO_4$ cathode. The reaction happens in reverse upon discharge.

The primary explanation of the delithiation/lithiation reaction mechanism was the "core-shell" model.[91] According to this theory, when $LiFePO_4$ is charged it converts to $FePO_4$ at the surface. This forms a shell of $FePO_4$, which grows inwardly as Li is removed further, and the core $LiFePO_4$ shrinks until the cell is charged. Similarly, a shell of $LiFePO_4$ forms on the $FePO_4$ surface and grows inward upon discharge. The "mosaic" model is an extension of this theory, where the key difference is that the new phase can nucleate in locations other than the particle surface.[141] These mechanisms account well for the incomplete reaction of these phases upon charge/discharge, as the "shell" phase can inhibit conversion of the "core" phase. However, they are not compatible with the anisotropic (1D) nature of Li^+ diffusion in $LiFePO_4$, as it would

be impossible for the core species to reduce uniformly. Therefore, the "new core-shell" model was developed to take this into account, whereby Li^+ moves in and out of the particles only through *b*-axis channels (described later in this section). In this model, the core phase is always $FePO_4$, which possesses a smaller unit cell and is therefore more stable (Figure 3.2).[142] This model has been experimentally validated, although the precise geometry of the phase boundary has been found to vary between samples.[142,143]

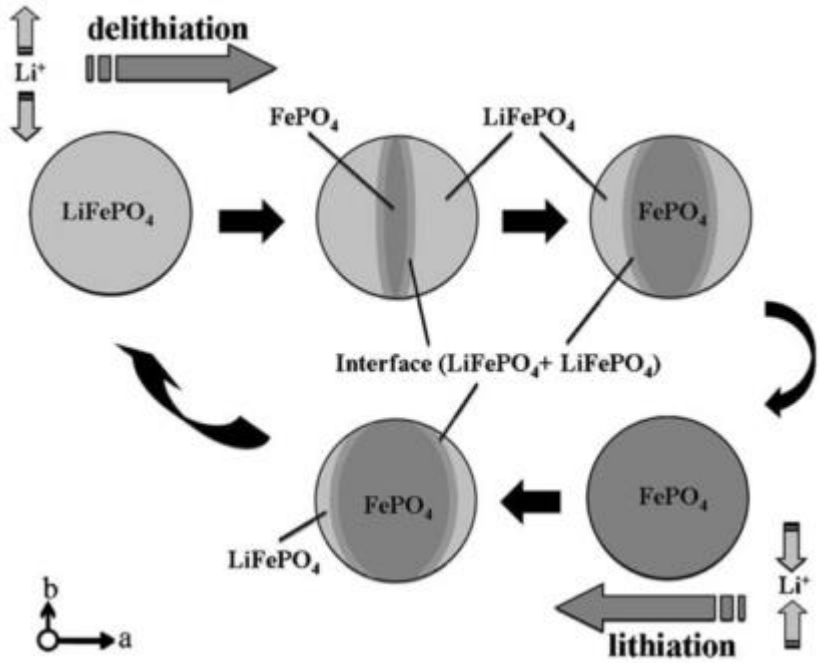

Figure 3.2 - The new core shell model[142–144], showing preferential growth of the $FePO_4$ phase as the core phase upon delithiation, with Li removed along the *b* axis. The reverse occurs upon charging, i.e. Li is inserted along the *b* axis to form a $LiFePO_4$ surface phase. Reprinted with permission from "Yuan, L.-X. *et al.* Development and challenges of $LiFePO_4$ cathode material for lithium-ion batteries. *Energy Environ. Sci.* **4,** 269–284 (2011)". Copyright 2011 Royal Society of Chemistry.[144]

A contrasting mechanism is the domino-cascade model, which assumes there is an Li concentration gradient at the interface between the $LiFePO_4$ and $FePO_4$ phases.[145] This would necessitate a large charge-carrier concentration at this interface, meaning it has a much higher ionic and electronic conductivity compared to the end-member phases. Therefore, the propagation of this boundary should be relatively rapid compared to the initial formation of a new phase within a specific particle, and individual particles will convert from one phase to another almost instantaneously. This means a partially charged $LiFePO_4$ cathode will contain distinct $LiFePO_4$ and $FePO_4$ particles, with no phase boundaries within particles observed.

A more nuanced description of the two-phase mechanism involves a specific combination of all of the mechanisms above, and is primarily supported with Raman spectroscopy data.[146,147] *In-situ* neutron powder diffraction was employed by Sharma *et al.* to investigate the charge/discharge process, and they suggested a four-step process (Equation 3.2) where steps **2a** and **2b** occur concurrently.[148] The discharge process is the reverse of Equation 3.2. $Li_{1-\beta}FePO_4$ and $Li_{\alpha}FePO_4$ are lithium-rich and lithium-poor solid-solution phases respectively, where the miscibility parameters α and β are < 0.05 for most $LiFePO_4$ samples.[149,150]

$$\underset{\text{domino-cascade}}{\overset{1}{LiFePO_4}} \rightarrow \underset{\text{solid-solution}}{\overset{2a}{Li_{1-\beta}FePO_4}} \rightarrow \underset{\text{new core-shell}}{\overset{2b}{Li_{1-\beta'}FePO_4}} \rightarrow \underset{\text{solid-solution}}{\overset{2c}{Li_{\alpha}FePO_4}} \rightarrow FePO_4$$

Equation 3.2 – A detailed description of the possible charge process, where $\beta' \geq \beta$, involving the domino-cascade, solid-solution, new core-shell and solid-solution mechanisms.

Another possible reaction mechanism is achieving solid-solution diffusion across the entire lithiation range. This has numerous advantages; the higher concentration of lithium vacancies that are present in a solid solution enable faster diffusion. In addition, the electronic conductivity can increase as a result of the coexistence of Fe^{2+} and Fe^{3+} in the same phase. Finally, the operating voltage varies as a function of Li content during discharge (rather than remaining steady at 3.45 V vs. Li/Li^+). Therefore, the voltage is a simple indicator of the remaining capacity of the battery and can assist battery state-of-health calculations.[148] The first evidence of the solid-solution mechanism was provided by Delacourt *et al.*, which was observed exclusively above 300 °C (Figure 3.3).[149,150] This mechanism can become dominant at room temperature by increasing miscibility factors α and β, which is achieved by either reducing particle size or introducing cationic disorder.[151]

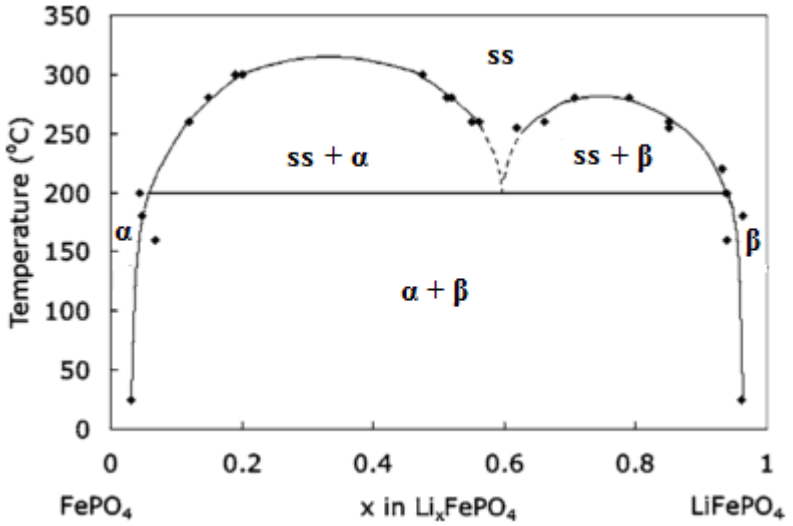

Figure 3.3 - The phase diagram of Li_xFePO_4, where α, β and ss are the lithium-poor, lithium-rich and solid-solution phases respectively. Adapted with permission from "Dodd, J. L., Yazami, R. & Fultz, B. Phase Diagram of Li_xFePO_4. *Electrochem. Solid-State Lett.* **9**, 151–155 (2006)". Copyright 2006 Electrochemical Society.[149]

In-situ XRD analysis by Liu *et al.* of the lithiation/delithiation processes has recently provided further insights into the conversion mechanism.[152] A conventional two-phase reaction mechanism is observed during slow delithiation. However, the reaction proceeds *via* a metastable solid-solution mechanism during rapid delithiation. Finally, when the current is paused during charge/discharge, the particles "relax" back into an equilibrium configuration (separate $LiFePO_4$ and $FePO_4$ particles, Figure 3.4).

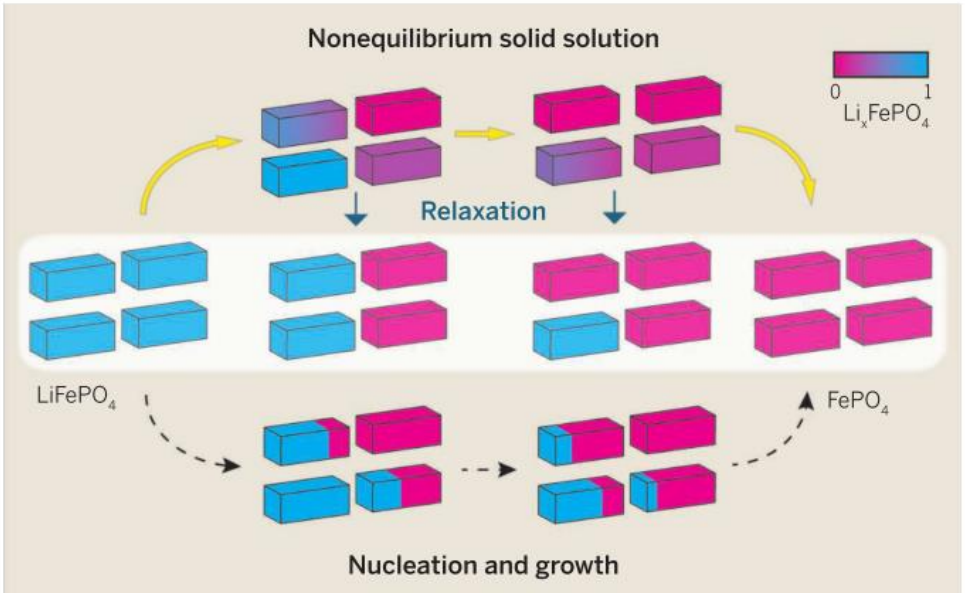

Figure 3.4 - The conversion mechanism between $LiFePO_4$ and $FePO_4$. Reprinted with permission from Liu, H. *et al*. Capturing metastable structures during high-rate cycling of $LiFePO_4$ nanoparticle electrodes. *Science* **344**, 1480–1487 (2014). Copyright 2014 The American Association for the Advancement of Science.[152]

The diffusion behaviour of Li^+ within $LiFePO_4$ has been relatively difficult to investigate as Fick's Law cannot be applied to the phase boundary. Computational methods have shed light on this process, and all suggest that Li^+ diffuses parallel to the *b*-axis in one-dimensional channels.[153–156] More recently, experimental verification of these results was provided by Nishimura *et al.*[157] The expected diffusion pathway was confirmed by anisotropic harmonic lithium vibrations from Rietveld analysis (Figure 3.5a). Maximum entropy methods were combined with neutron diffraction data for $Li_{0.6}FePO_4$ at 620 K to give Li^+ nuclear density plots. Lithium diffusion is limited to 1D channels in the [0 1 0] direction (Figure 3.5b), with virtually no diffusion between channels (Figure 3.5c) (the colour blue denotes Li^+ density).

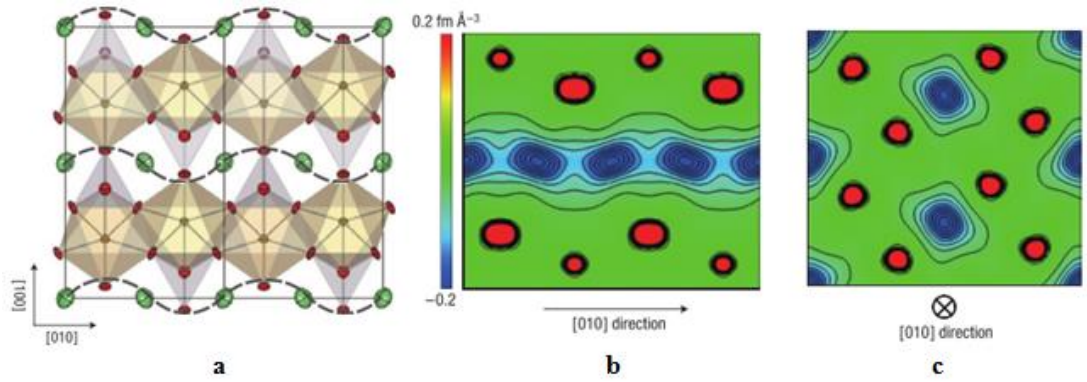

Figure 3.5. Experimental evidence for Li-ion diffusion in 1D channels along *b*-axis channels from neutron diffraction data. Adapted with permission from Nishimura, S. *et al*. Experimental visualization of lithium diffusion in Li_xFePO_4. *Nat. Mater*. **7**, 707–711 (2008). Copyright 2008 Nature Publishing Group.[157]

The one-dimensional nature of Li^+ diffusion often reduces the experimentally measured diffusion coefficient in LFP; "antisite" defects, where Fe ions occupy Li sites, can block these channels. The phase boundary motion and Li^+ diffusion coefficient are lowered as a result, and the capacity of $LiFePO_4$ is also reduced if regions of the cathode are inaccessible. Therefore, interconversion between $LiFePO_4$ and $FePO_4$ is kinetically limited. The capacity of LFP is also limited at high discharge rates by its low electronic conductivity, as simultaneous electron transfer is required with Li^+ intercalation. Hence, the low ionic and electronic conductivity of $LiFePO_4$ limits its electrochemical performance.[140,158]

3.2.4. Improving the performance of $LiFePO_4$

Given the poor electrochemical performance of bulk $LiFePO_4$, efforts have focussed on improving ionic and electronic conductivity. This has been achieved by such methods as carbon coating the $LiFePO_4$ particles, reducing the particle size, inclusion of dopants and particle morphology control.

3.2.4.1. Particle Size

Reducing $LiFePO_4$ particle size can significantly improve its achievable capacity; the average Li^+ diffusion distance is less in a smaller particle, and hence Li^+ can be more easily removed or inserted. Antisite defects, which effectively block the 1D Li^+ diffusion channels, are less likely to seal both ends of a channel in a smaller particle, resulting in higher attainable capacity. In addition, small particles are less prone to

cracking with the volume changes of phase transformation upon repeated cycling.[137] Furthermore, reducing particle size increases the solid-solution regime behaviour of $LiFePO_4$, which is more rapid than the two-phase mechanism.

However, there are negative attributes to the use of nanoparticles in electrodes. The greater surface area of nanoparticles has a threefold effect on electrochemical performance; firstly, nanoparticles are more susceptible to dissolution with cycling due to the relative instability of particle surfaces, which will increase capacity fade between cycles.[159] Secondly, the defects present at particle surfaces are highly reactive and can react with the electrolyte to form a greater amount of SEI, increasing the active Li loss on the first cycle and possibly on subsequent cycles, which will also contribute to capacity fade.[160] Finally, smaller particles generally pack less well than larger particles (with a greater proportional void volume) and therefore the electrode volumetric energy density is lowered for nanoparticles (assuming the same gravimetric energy density).

3.2.4.2. Carbon Coating

In contrast to particle size effects, the main effect of carbon coating is to improve electron transport across the particle surface. This has also been achieved by incorporating particulate metals (such as silver), however the cost of these metals prevents commercial application.[161] Carbon has a similar effect, and is relatively inexpensive. The effect of carbon coating was originally investigated by Ravet *et al*., and has been a widely researched topic since.[162] There are other beneficial effects of carbon coatings; the reducing conditions required to produce surface carbon can eliminate Fe(III) impurity phases.[163] In addition, Li^+-conductive impurity phases such as Fe_2P can be generated in these conditions, further improving performance.[164] Carbon coating can also reduce the reactivity of the particle surface, limiting dissolution and SEI formation.[165] It is important to note that carbon coating does reduce the energy density of the cathode, and therefore research has focussed on achieving efficient carbon coatings with minimum carbon content.

Optimisation of the carbon coating has been achieved by varying the continuity, the thickness and the degree of graphitisation. Wang *et al.* demonstrated the beneficial effect of a complete coating of carbon, with excellent rate performance achieved.[166]

There is also an optimal carbon coating thickness; if the coating is too thick, permeation of electrolyte to the particle surface is limited and impedes Li^+ diffusion, whereas if it is too thin electron transfer is not sufficiently enhanced.[167] Finally, the nature of the surface carbon is crucial; sp^2 carbon demonstrates better electronic and ionic conductivities compared to sp^3 carbon, and therefore increased graphitisation boosts performance.[168]

Investigating particle size and carbon coating effects has raised the question: which effect is dominant? There has been considerable difficulty separating the effects, as carbon acts as a nucleating agent and often reduces particle size. A review of nine $LiFePO_4$ samples from a range of publications suggested particle size had the greatest effect on electrochemical performance, implying phase transformation between $LiFePO_4$ and $FePO_4$ was limited by Li^+ diffusion.[169] However, a survey of a wider array of 42 publications found the reverse; below 400 nm, carbon coating the particles had the greatest impact on performance, suggesting that the transfer of electrons to and from the $LiFePO_4$ particles is the most kinetically limiting factor upon charge/discharge.[170] This conclusion, drawn from a larger sample, may better describe their relative effects.

3.2.4.3. Particle Morphology

As mentioned in Section 3.2.3, Li^+ is inserted/removed along the *b*-axis of the $LiFePO_4$ structure. Therefore, particle width across this axis affects the ease of insertion and removal of Li^+. Fortuitously, a common morphology for $LiFePO_4$ particles are platelets, with the plate normal parallel to the *b*-axis, so micron-sized particles can attain reasonable performance with this morphology.[42] Another consideration is the particle packing properties, as spherical particles pack more efficiently in the electrode structure compared to other morphologies. Therefore, spherical morphology is generally desired for nanoparticles, as nanoparticles pack less efficiently than their micron-sized counterparts.

3.2.4.4. Doping of $LiFePO_4$

There are two categories of metal-ion doping in $LiFePO_4$: isovalent doping and aliovalent doping. The former is where both the metal ion and its substituent ion possess the same oxidation state, whereas the latter is where they differ. In the latter

case, the difference in charge is balanced with metal ion vacancies and/or electrons. Isovalent doping has been well researched and understood, whereas aliovalent doping is still a source of some disagreement.[154]

Isovalent doping can increase the energy density of $LiFePO_4$ by replacing Fe^{2+} with another divalent metal ion, thereby exploiting a different electrochemical couple. Mn^{2+} is one of the most promising isovalent dopants, as the Mn^{2+}/Mn^{3+} potential is greater than the Fe^{2+}/Fe^{3+} couple (4.1 compared to 3.45 V vs. Li/Li^+, Figure 3.6) whilst residing in the electrolyte stability window.[171] In contrast, the Co^{2+}/Co^{3+} and Ni^{2+}/Ni^{3+} couples exceed this window. This is discussed in greater detail in Chapter 6, which concerns $LiMnPO_4$.

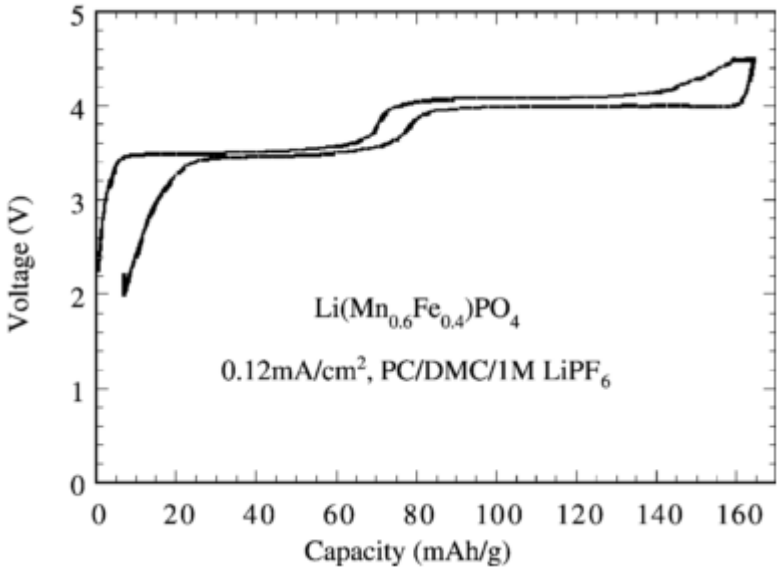

Figure 3.6 - The cycling performance of Mn-doped $LiFePO_4$. Reprinted from "Yamada, A. *et al.* Olivine-type cathodes: Achievements and problems. *J. Power Sources* 119–121, 232–238 (2003)", Copyright 2003, with permission from Elsevier.[171]

Chung *et al.* first reported aliovalent doping of Mg^{2+}, Al^{3+}, Zr^{4+}, Ti^{4+}, Nb^{5+} and W^{6+} in $LiFePO_4$, where they postulated the ions replaced Li^+ within the material.[172] This generated vacancies in the material according to formula **a** (Equation 3.3), resulting in a compound with chemical formula **b**.[173] These dopants therefore stabilise solid-solutions of Li_xFePO_4. and increase ionic conductivity, whilst also generating electrons associated with those vacancies, potentially increasing electrical conductivity. Moreover, the inclusion of these dopants has also been shown to increase unit cell

volume and reduce lithium diffusion activation barriers, thereby improving rate performance.

$$\text{a) } [V'_{Li}] = (n-1)\left[M^{(n-1)\cdot}\right] \quad \text{b) } Li_{1-ny}M_y^{n+}FePO_4$$

Equation 3.3 – a) The mechanism of lithium vacancy generation V'_{Li} with inclusion of metal ion M with oxidation state *n* in Kröger-Vink notation. b) The resultant compound with an addition of *y* M^{n+} dopant ions.[173]

However, this claim has been disputed, with other researchers suggesting that trace carbon was responsible for the improved extra conductivity.[174] It has also been postulated that doping $LiFePO_4$ with aliovalent ions is energetically unfavourable, and should not therefore be possible.[154] Despite this, over 10% aliovalent substitution has been achieved within $LiFePO_4$,[175] although the improved conductivity could be attributed to highly conductive surface impurity phases in some cases.[175] Hence there is still much debate about the source of the effects of dopants.

It should be noted that any beneficial effect of dopants by this method is intrinsically limited, as the cathode contains fewer Li^+ cations as a result. Moreover, the dopant ion will block Li^+ diffusion channels if they are immobile. This can be avoided if the dopant replaces a different ion in the structure, i.e. Fe^{2+} or PO_4^{3-}. Fe-site dopants include Mg^{2+},[176] Al^{3+},[176] and a number of oxidation states of V,[177,178] whereas anions such as F^- and Cl^- replace PO_4^{3-}.[179] Fe-site dopants have been found to improve Li^+ mobility by widening the 1D diffusion channels,[180] but can also increase electronic conductivity by reducing the Li_xFePO_4 band gap.[181]

3.2.5. Mechanism and Effects of Vanadium Doping

Vanadium has been extensively investigated as a dopant in the $LiFePO_4$ structure, although there is still no clear consensus on the precise mechanism of substitution. The vast majority of publications claim substitution on the iron site.[177,178,180–189] This was claimed often with no explanation of the compensating vacancy mechanism, even when the V oxidation state was 3+ or 4+. The most convincing description of Fe-site substitution is provided by Omenya *et al.*, where an XRD study showed V^{3+} replaced Fe^{2+}, generating Fe vacancies.[177] A separate DFT study supports V occupation of the Fe site on energetic grounds.[181] In a later report, the same authors found attempted substitution of V on Li sites in fact generated the structure $Li_{1-3y}Fe_y[Fe_{1-y}V_y]PO_4$,

where V occupies Fe sites, and Fe is displaced onto an Li site. P-site substitution has also been reported,[183] although attempts by the authors to reproduce this result were unsuccessful.[177]

Generally, incorporation of vanadium has produced an improved electrochemical performance in $LiFePO_4$, although there is still some debate regarding the mechanism responsible. Optimal performance of V-doped $LiFePO_4$ when impurity phases such as $Li_3V_2(PO_4)_3$ or VO_2 are present has been observed by several authors.[177,178,186,187] It is thought that the increased ionic or electronic conductivity of these phases gave increased performance. In contrast, others claim that the impurity phases inhibits performance, and only vanadium successfully incorporated in the lattice has the desired effect.[180] Computational studies suggest that vanadium incorporation reduces the band gap in $LiFePO_4$, and improves Li^+ diffusion kinetics by volume expansion of the diffusion channels.[181]

3.2.6. Effects of Niobium Doping

In a similar manner to vanadium, niobium has been suggested to occupy multiple sites in the $LiFePO_4$ structure. The first mechanism found is substitution on the Li site, with Li vacancies generated.[173,190] Meethong *et al*. found the primary effect of Li site occupation was an increase in the lithium miscibility of the Li_xFePO_4 and $Li_{1-x}FePO_4$ phases, which could increase the utilisation of the faster solid-solution diffusion mechanism.[173] Substitution on the iron site gave reduced charge transfer resistance and increased crystal lattice volume, boosting ionic and electronic conductivity.[191] Modelling studies supported this, showing that Nb^{5+} on an Fe^{2+} site (generating Li vacancies) is the most stable doping mechanism.[192]

3.2.7. Previous Continuous Hydrothermal Synthesis Efforts

Xu *et al.* employed CHFS to produce phase-pure $LiFePO_4$ using a precursor ratio of 1:1:3 $FeSO_4$:H_3PO_4:LiOH, in subcritical and supercritical conditions.[193] They found larger particles were produced in the supercritical case (productivity rate of 0.3 g h^{-1} assuming 100% yield). Hong *et al.*, on the other hand, found supercritical water solvent (100 nm, variable morphology) gave smaller particles than subcritical water solvent (> 1 µm, rhomboid morphology).[194] The size and morphology observed varied

significantly with synthesis conditions (productivity rate of 0.5 g h^{-1} assuming 100% yield), and a 40 s residence time was necessary to achieve pure $LiFePO_4$. A relatively short residence time (12 s) was required by Aimable *et al.* using a 1:1:3.75 Fe:P:Li ratio.[195] The electrochemical performance of these materials was generally poor, however, with the best high-rate performance (*ca*. 88 m A h g^{-1} at 10C) recorded by Hong *et al*.[196] There is also commercial research ongoing by Hanwha Corporation, Korea.[197]

Within the CMTG at UCL, there has been a preliminary investigation into the continuous hydrothermal synthesis of $LiFePO_4$.[198] An optimal Fe:P:Li ratio of 1:1:3.45 was used to produce pure $LiFePO_4$, and degassing the precursor solutions prevented ferric impurities (as the dissolved O_2 was removed). Incorporating fructose and using a Fe:P:Li ratio of 1:1.5:3.45 generated phase-pure $LiFePO_4$ with a thin carbon coating (Figure 3.7a). The crystallites had rounded morphology, and formed fused agglomerates (Figure 3.7b).

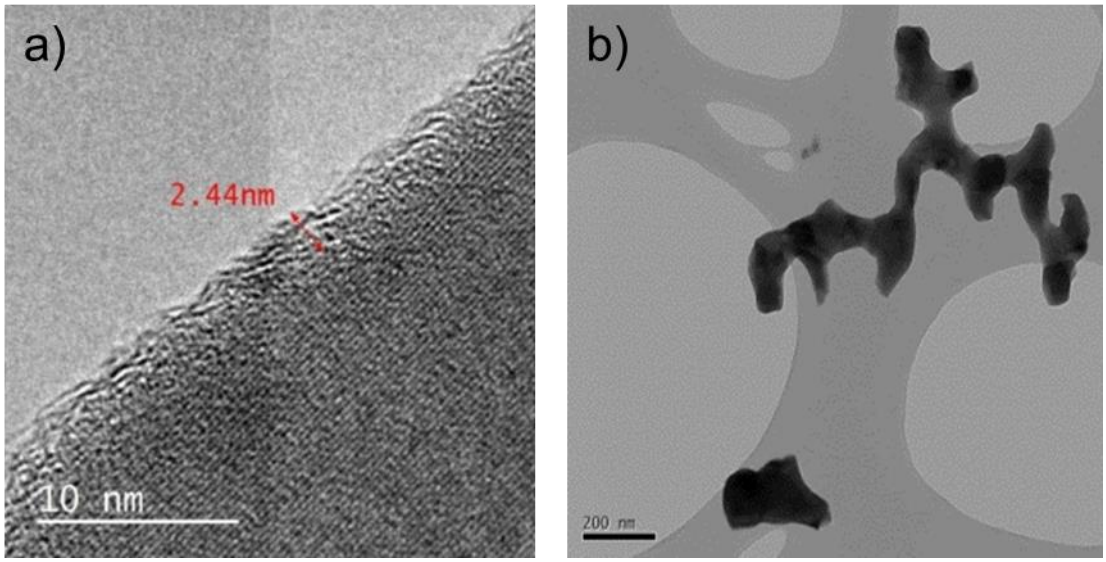

Figure 3.7 a) The 2.4 nm thick graphitic coating and b) The morphology of the synthesised $LiFePO_4$/C from TEM analysis. Reproduced with permission from O. Y. Wu's PhD thesis.[198]

An optimal carbon coating of about 8 wt% C was observed, although the electrochemical performance was not exceptional at low C-rate (150 mA h g^{-1} at C/10). The capacity at high discharge rates was substantial (120 mA h g^{-1}); however, the tests were conducted with a constant charge rate of C/5 for all discharge rates, which will improve high-rate performance (Figure 3.8).

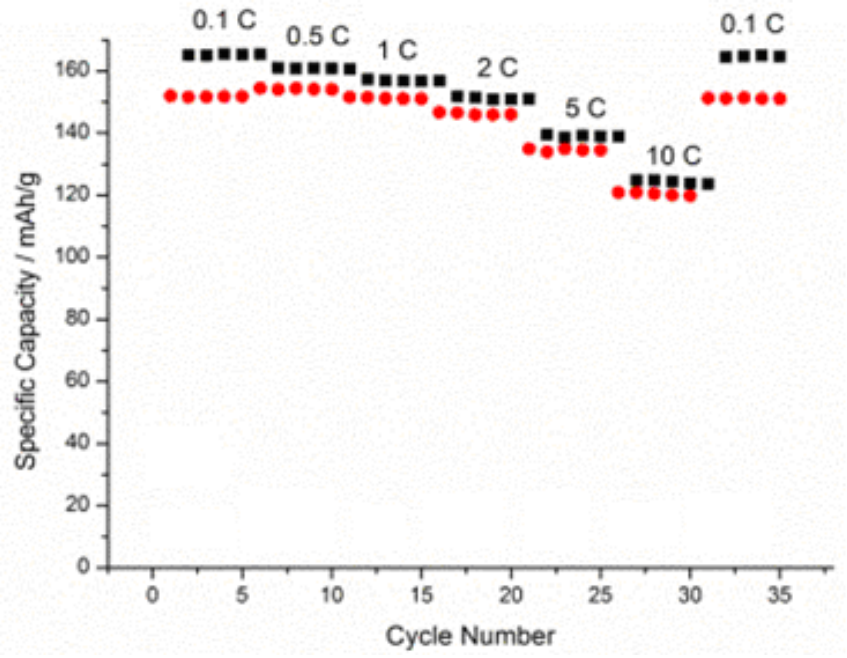

Figure 3.8 - Electrochemical tests of $LiFePO_4$/C with the C-rates, charge capacity (black squares) and discharge capacity (red circles) indicated. The electrode formulation ratio was 74:14:12 (active material:carbon:binder). Reproduced with permission from O. Y. Wu's PhD thesis.[198]

3.3. Experimental

This section describes the reactor configuration and conditions used to produce the pure and doped $LiFePO_4$ products. There is also a brief discussion regarding post-sample processing and analysis.

Pilot-scale synthesis was conducted using a single configuration as described in Figure 3.9, giving a reaction temperature of 335 °C and a residence time of 6.5 s. The fructose (99%, Alfa Aesar, Heysham, UK), iron sulfate (99+%, Alfa Aesar, Heysham, UK), vanadyl sulfate (17-23% V, Acros Organics, Loughborough, UK), ammonium niobate(V) oxalate pentahydrate ($C_4H_4NNbO_9 \cdot 5H_2O$, 99.99%, Sigma-Aldrich Ltd., Dorset, UK) and phosphoric acid (85-88% wt%, Sigma Aldrich, Steinheim, Germany) were pumped using P2, and LiOH (99+%, Fisher Scientific, Loughborough, UK) using P3.

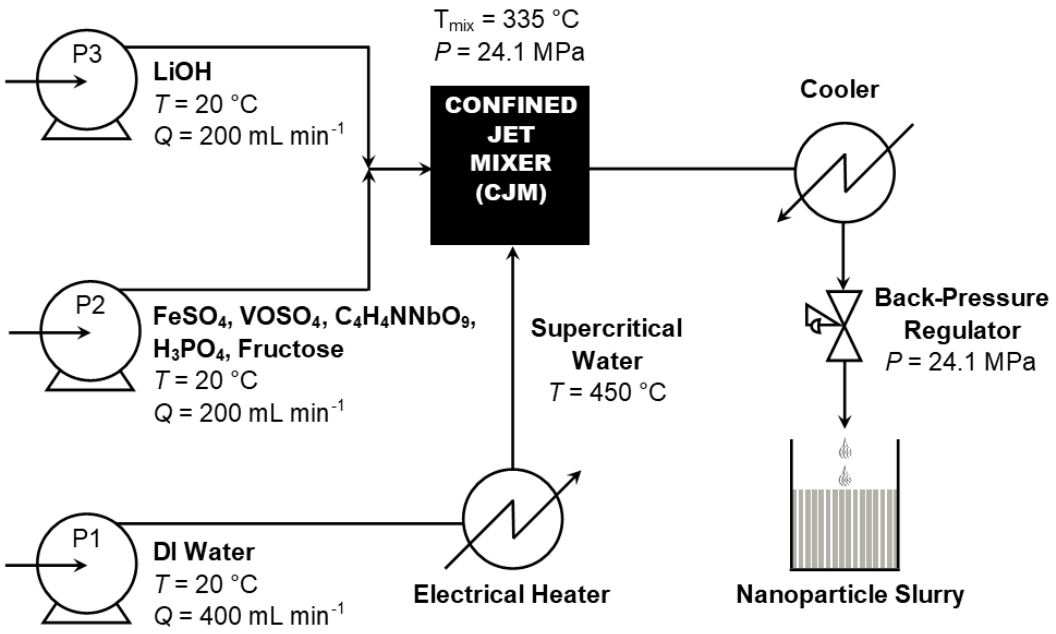

Figure 3.9 – A schematic of the Pilot-Scale apparatus including the precursors used to generate the $LiFePO_4$-based products.

The slurry was allowed to settle (1 h) and the supernatant siphoned off. Centrifugation (4500 rpm for 5 minutes) further concentrated the slurry to a wet paste. This paste was repeatedly centrifuged (3 × 4500 rpm for 10 minutes) after redispersion in D.I. water to remove aqueous impurities. The cleaned paste was further concentrated with centrifugation (4500 rpm over 30 minutes) and freeze-dried by slowly heating from 60 °C to 25 °C, over 24 h under vacuum of < 13 Pa as further described in Section 2.1.3.3. The freeze-dried powder was subsequently heat-treated from ambient temperature up to 700 °C with a heating rate of 5 °C min^{-1}, and held for at this temperature for 3 h under a flow of Ar gas.

Powder XRD patterns of the as-prepared and heat-treated samples in Section 3.4.1 were obtained on set-up **a** in Section 2.1.4.1, using Cu-Kα radiation (λ = 1.54 Å) in the 2θ range 5 to 60° with a step size of 0.05° in 2θ and a count time of 4 s. Additionally, higher-quality XRD patterns of heat-treated samples in Section 3.4.1 were collected using set-up **c** in Section 2.1.4.1, using Mo-Kα radiation (λ = 0.71 Å) over the 2θ range 2 – 60° with a step size of 0.5° and step time of 87 s. Rietveld analysis was performed using MAUD software.[132]

Powder XRD patterns of the as-prepared and heat-treated samples in Section 3.4.2 were obtained on set-up **b** in Section 2.1.4.1, using Mo-Kα radiation (λ = 0.71 Å) over the 2θ range 2 – 40° with a step size of 0.5° and step time of 10 s. Rietveld analysis was performed using MAUD software.[132]

ICP-AES analysis was conducted using the set-up described in Section 2.1.4.9. Briefly, 0.1 g of as-prepared sample was dissolved in 3 mL of gently heated 69% HNO_3 overnight. The resulting solution was diluted with 10 mL 1% HNO_3, and 1 ml of the resultant solution was diluted into 100 mL of 1% HNO_3, and diluted again by a factor of 2 (with 1% HNO_3). This heavily diluted solution was analysed using the ICP-AES apparatus. Li, Fe, V and P standard solutions were provided by the ICP technician.

Electrodes of the active material were fabricated by ball-milling 80 wt% heat-treated sample, 10 wt% carbon (carbon black, Super P™, Alfa Aesar, Heysham, UK) and 10 wt% PVDF (PI-KEM, Staffordshire, UK) in NMP solvent for 1 h. The PVDF was dissolved in NMP (Sigma Aldrich, St. Louis, USA) by stirring at room temperature prior to ball-milling. The resultant ink was cast on aluminium foil using a doctor blade (PI-KEM, Staffordshire, UK), and subsequently dried in an oven set to 80 °C. 16 mm diameter circular electrodes were cut from the sheet and pressed (1.5 tons cm^{-2} pressure). The active mass loadings of these electrodes were 2.1-3.7 mg cm^{-2} for the V-doped $LiFePO_4$ tests, aside from those which were used to calculate diffusion coefficient, which were *ca.* 3 mg cm^{-2}. For the Nb-$LiFePO_4$ tests, all electrodes were in the range 2.8 – 4.0 mg cm^{-2}.

CVs and C-rate tests (Section 2.1.5) were performed at different scan rates/currents within this chapter. For the CVs, scan-rates of 0.05, 0.1, 0.2, 0.5, 1 and 2 mV s^{-1} were used. For C-rate testing, generally C-rates of 0.5C, 1C, 2C, 5C and 10C were employed (where 1C = 170 mA g^{-1}) between voltage limits of 4.2 V and 2.0 V, unless otherwise indicated.

3.4. Results and Discussion

3.4.1. Vanadium-Doped $LiFePO_4$

3.4.1.1. Aims

As mentioned previously, vanadium doping has been shown to dramatically improve the performance of $LiFePO_4$. An array of vanadium-doped $LiFePO_4$ samples were prepared in an attempt to find an optimal dopant concentration, and to achieve high rate performance by combining doping with nanosizing and carbon coating. The reactivity and site occupation of the V dopant was also explored.

3.4.1.2. Physical Characterisation

$LiFePO_4$/C (pure and V-doped) samples were successfully synthesised as grey powders, and are given the following nomenclature: LFP1 and LFP2 are pure $LiFePO_4$/C, LFVP(x) [x = 2.5, 5, 10, and 20] are vanadium-doped samples, where x is the nominal vanadium at% (as a proportion of total transition metal content). The concentrations of precursors were varied according to Table 3.2, to give the desired molar ratios of Fe:V while keeping overall transition metal concentration at 0.25 M. The LiOH and H_3PO_4 concentrations were held constant at 0.8625 M and 0.375 M, respectively. Heat-treatment of these powders produced black powders, and are named ΔLFP1, ΔLFP2 and ΔLFVP(x), respectively. Molar yields of these samples were in the range 50 – 70 mol%.

Table 3.2 – The concentration of precursors used to generate the pure $LiFePO_4$ and V-doped $LiFePO_4$ samples. Carbon loadings were calculated using CHN analysis.

Sample	[$FeSO_4$] / M	[$VOSO_4$] / M	at% V	[Fructose] / M	As-prepared carbon loading / wt%	Heat-treated carbon loading / wt%
LFP1	0.25	0	0	0.75	11.2	9.1
LFP2	0.25	0	0	0.875	17.5	12.7
LFVP(2.5)	0.24375	0.00625	2.5	0.65	4.3	3.7
LFVP(5)	0.2375	0.0125	5	0.65	5.1	3.7
LFVP(10)	0.225	0.025	10	0.65	4.4	3.9
LFVP(20)	0.20	0.05	20	0.65	4.7	3.2

The nature of the as-prepared and heat-treated carbon coatings was investigated with Raman spectroscopy. As-prepared sample LFVP(10) displayed very broad disordered carbon (D) and graphitic carbon modes (G) (Figure 3.10a). In contrast, the heat-treated sample ΔLFVP(10) displayed clear features due to the surface carbon, with sharper disordered carbon (D) and graphitic carbon modes (G) (Figure 3.10b). This indicated the heat-treated carbon coating should be reasonably conductive due to the significant proportion of graphitic carbon.

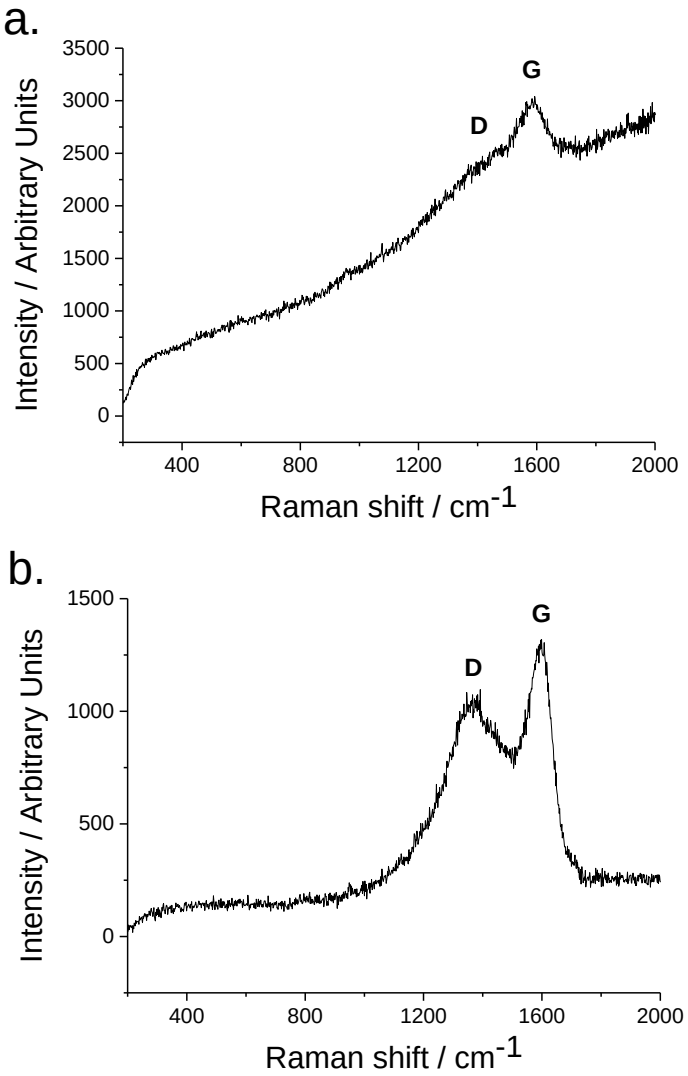

Figure 3.10 – a) The Raman spectrum of sample LFVP(10), showing very weak disordered carbon (D) and graphitic carbon modes (G). b) The Raman spectrum of sample ΔLFVP(10), displaying sharper disordered carbon (D) and graphite carbon modes (G).

The $LiFePO_4$ olivine structure was observed exclusively in all as-prepared samples from XRD patterns (PDF Card No. 01-070-6684, Figure 3.11). Significant peak broadening and shift to higher 2θ values was observed with increased vanadium incorporation, indicating a distortion of lattice parameters and increased crystallographic strain was induced by the presence of the dopant.

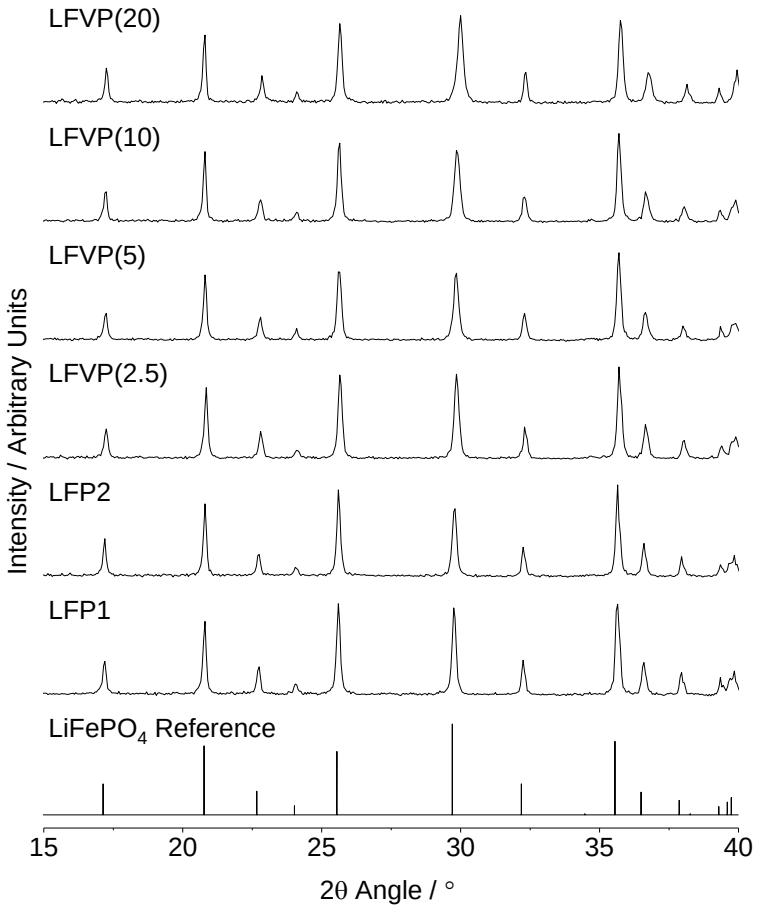

Figure 3.11 – XRD patterns (Cu-Kα radiation) of an $LiFePO_4$ reference (PDF Card No. 01-070-6684), the pure $LiFePO_4$ samples LFP1 and LFP2, and the vanadium-doped $LiFePO_4$ samples prior to heat-treatment. Reprinted from reference 199.

Rietveld refinement of these diffraction patterns confirmed a reduction in unit cell volume with increasing V dopant (Table 3.3, Figure 3.12 d), and an approximately linear change in lattice parameters (consistent with Vegard's Law, Table 3.3, Figure 3.12a-c) which matched those previously observed in V-doped $LiFePO_4$, i.e. decreasing *a* and *b* lattice parameters and increasing *c* lattice parameter.[188] The goodness-of-fit parameter R_{wp} was very high for these refinements due to the relatively poor quality of the diffraction data, so these parameters should only be used to qualitatively compare these samples. Plots of the fits are included in Chapter 11 Appendix I.

Table 3.3 – The lattice parameters and goodness-of-fit parameters of the as-prepared samples found from Rietveld analysis. Adapted from reference 199.

Sample	*a* / Å	*b* / Å	*c* / Å	*V* / Å^3	R_{wp}	χ^2
LFP(1)	10.3181(10)	6.0000(6)	4.6926(5)	290.51(9)	22.6	1.25
LFP(2)	10.3221(11)	6.0015(6)	4.6945(6)	290.82(9)	24.5	1.39
LFVP(2.5)	10.3142(10)	5.9937(6)	4.6958(6)	290.29(9)	21.0	1.11
LFVP(5)	10.3090(11)	5.9901(7)	4.6961(6)	289.99(10)	22.5	1.20
LFVP(10)	10.3019(11)	5.9807(7)	4.6991(6)	289.52(10)	22.6	1.21
LFVP(20)	10.2771(13)	5.9569(8)	4.7014(7)	287.82(12)	24.3	1.34

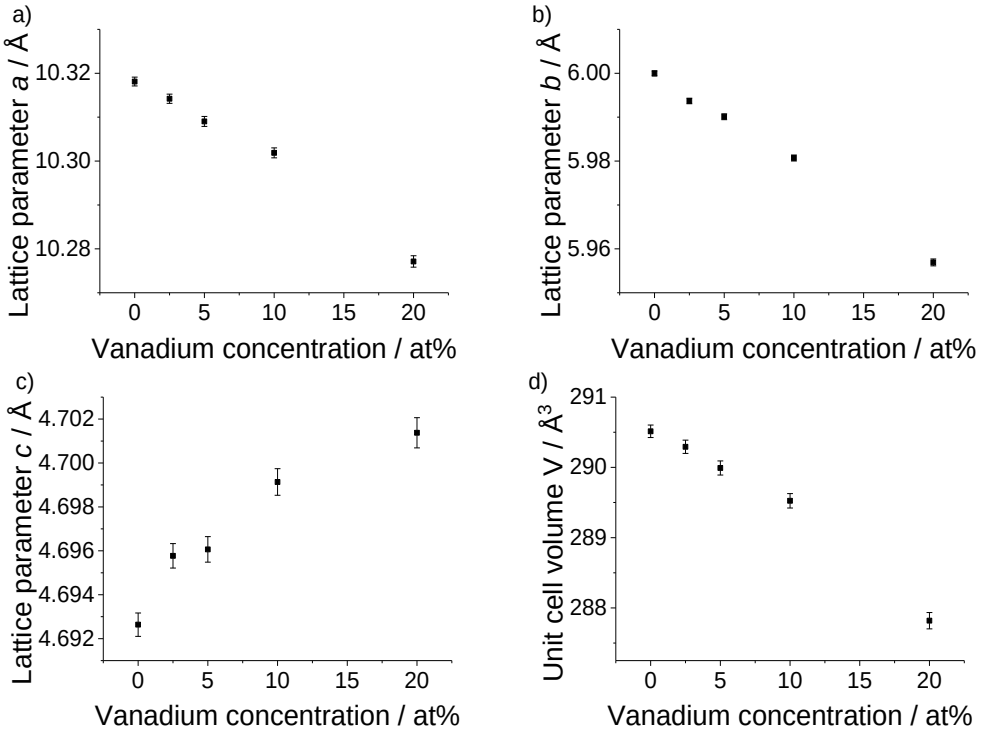

Figure 3.12 – The effect of vanadium concentration (in at%) on a) the *a* lattice parameter (in Å), b) the *b* lattice parameter (in Å), c) the *c* lattice parameter (in Å) and d) the unit cell volume *V* (in Å^3) of the as-prepared samples. Errors calculated from the fit are included as error bars.

After heat-treatment, the pure olivine phase (PDF Card No. 01-070-6684) was observed exclusively in all cases by XRD aside from ΔLFVP(10) and ΔLFVP(20), where a minor $LiV(P_2O_7)$ phase (PDF Card No. 01-085-2381) was observed (Figure 3.14). Pyrophosphates are commonly formed from reaction of phosphates in reducing conditions, so it was unsurprising that the impurity phase contained this ion.[200] The relative ratios of the elements contained were confirmed using ICP-AES (discussed later, Figure 3.18c), and showed the degree of V incorporation matched that of the precursors. The high V doping degree (*ca*. 20 at%) in the as-prepared material matches the maximum achieved using low-temperature $LiFePO_4$ synthesis.[189] The segregation

observed after heat-treatment suggested the heavily doped phases were metastable, and were only accessible due to the low synthesis temperature employed (335 °C). This was consistent with a study on the solubility of V in $LiFePO_4$ with reaction temperature.[189] The ability to make metastable solid solutions *via* CHFS with solubilities above the expected values has been observed in the Ce-Zr-Y-O and Ce-Zn-O fluorite structure phase diagrams previously.[128,201]

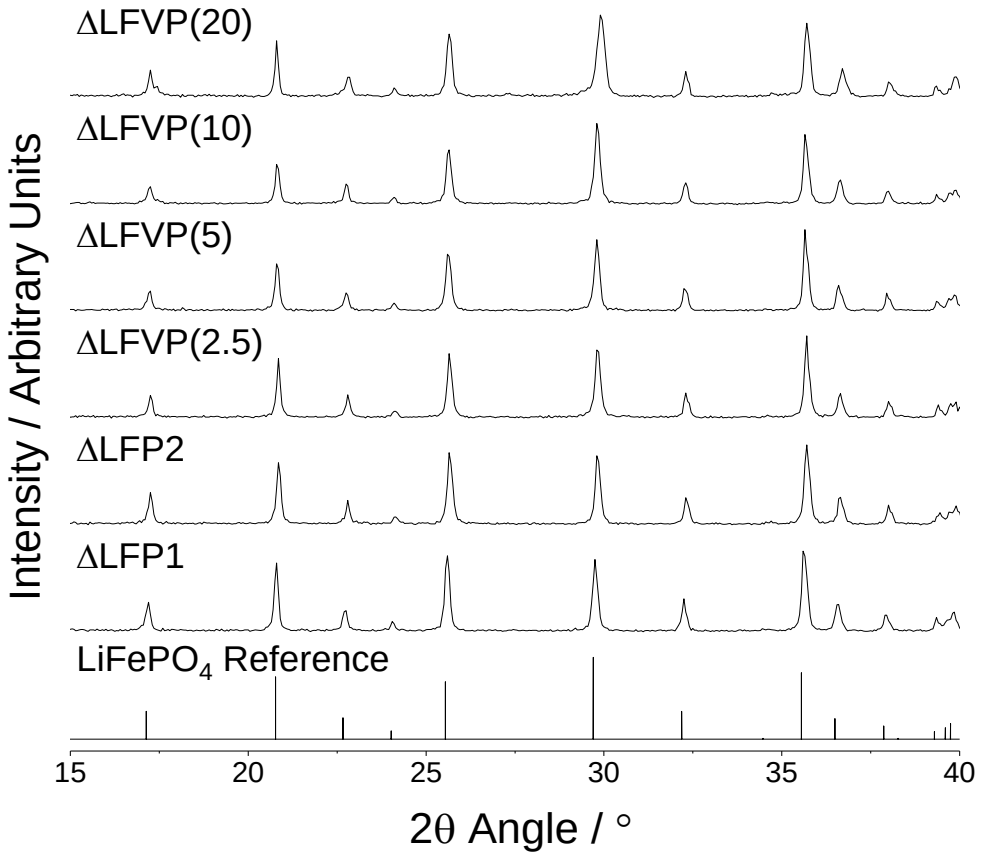

Figure 3.13 – XRD patterns (Cu-Kα radiation) of an $LiFePO_4$ reference (PDF Card No. 01-070-6684), the pure $LiFePO_4$ samples ΔLFP1 and ΔLFP2, and the vanadium-doped $LiFePO_4$ samples after heat-treatment. Reprinted from reference 199.

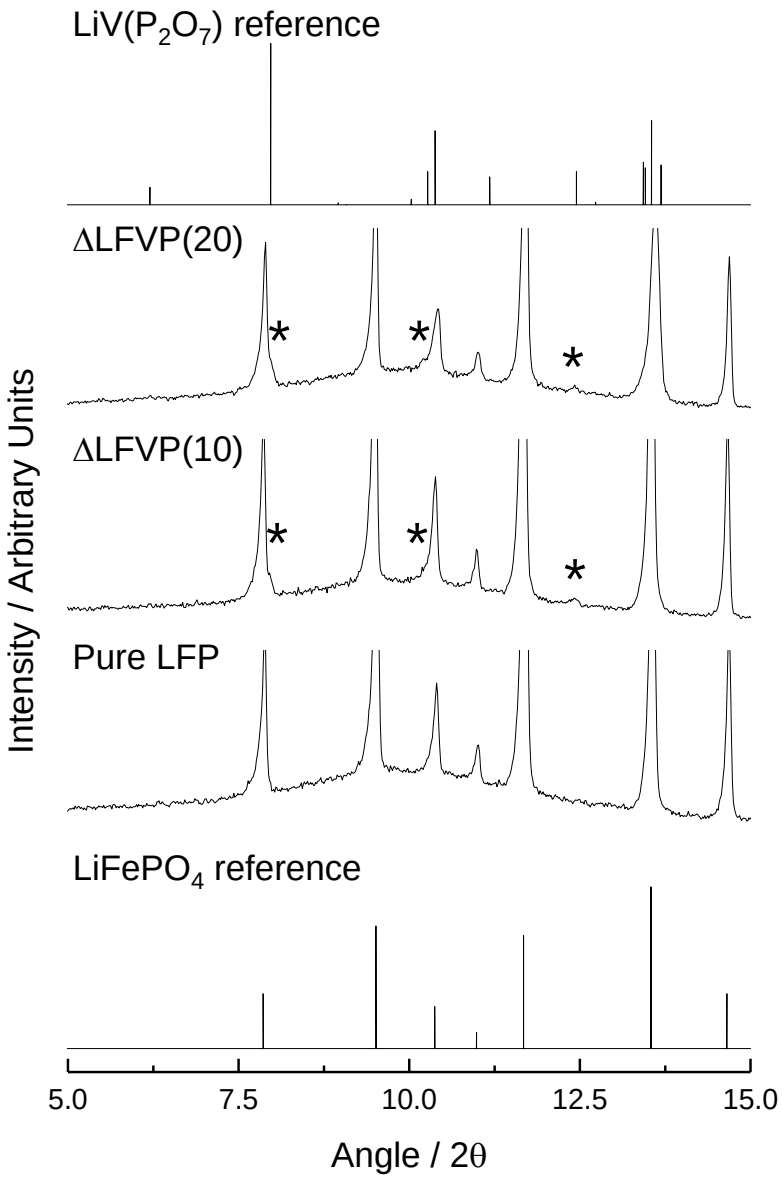

Figure 3.14 – High-quality XRD patterns (Mo-Kα radiation) of ΔLFVP(10) and ΔLFVP(20) with $LiFePO_4$ and $LiVP_2O_7$ reference patterns, with the $LiVP_2O_7$ phase indicated with asterisks. Truncated *y*-axes were employed in the experimental data to highlight the impurity peaks. Reprinted from reference 199.

Rietveld refinement was employed to extract lattice parameters and particle diameters (D) of the heat-treated samples from X-Ray diffraction patterns (Fits shown in Chapter 11, Appendix I, and parameters displayed in Table 3.4) collected using conditions described in Section 2.1.4.1.

Table 3.4 – The lattice parameters, particle diameter D and goodness-of-fit parameters of the heat-treated samples found from Rietveld analysis. Adapted from reference 199.

Sample	*a* / Å	*b* / Å	*c* / Å	*V* / Å^3	D / nm	R_{wp}	χ^2
ΔLFP(1)	10.32407(14)	6.00399(9)	4.69447(7)	290.990(13)	200	4.48	1.34
ΔLFVP(2.5)	10.32274(16)	6.00371(10)	4.69564(8)	291.011(14)	205	4.87	1.40
ΔLFVP(5)	10.32068(15)	6.00194(9)	4.69686(7)	290.943(13)	187	4.75	1.33
ΔLFVP(10)	10.32383(12)	6.00127(7)	4.69766(6)	291.049(10)	242	4.24	1.18
ΔLFVP(20)	10.30233(33)	5.9763(2)	4.70006(16)	289.381(29)	240	7.45	1.98

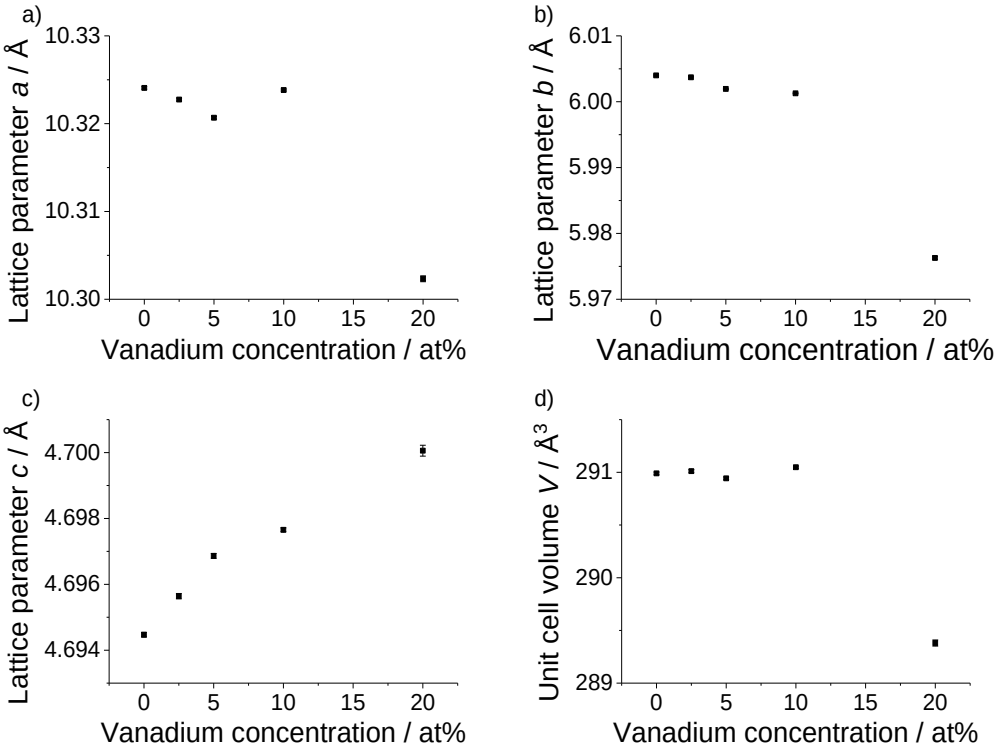

Figure 3.15 – The effect of vanadium concentration (in at%) on a) the *a* lattice parameter, b) the *b* lattice parameter, c) the *c* lattice parameter and d) the unit cell volume *V* of the heat-treated samples. Errors calculated from the fit are included as error bars. Reprinted from reference 199.

The particle sizes extracted from Rietveld refinement suggested an average particle size of ~200 nm for most of the heat-treated samples, although this increased to ~240 nm for ΔLFVP(10) and ΔLFVP(20), and suggested the vanadium dopant increased particle size. The lattice parameters of the heat-treated samples varied systematically with vanadium dopant (in a similar manner to the as-prepared samples); however, the magnitude of variation was decreased compared to before heat-treatment, and implied some of the structural discrepancies were due to defects which were reduced with annealing. The variation in lattice parameters implied successful incorporation of vanadium in the $LiFePO_4$ lattice. This was supported by energy-dispersive X-Ray spectroscopy (EDS) analysis, which indicated a consistent dispersion of V atoms

within particles of sample ΔLFVP(5). In contrast, ΔLFVP(10) displayed the slight phase-separation observed previously with XRD analysis with the growth of a V-rich phase on the particle surface. This impurity phase had an approximate V:P elemental ratio of 1:2, consistent with the postulated $LiV(P_2O_7)$ phase.

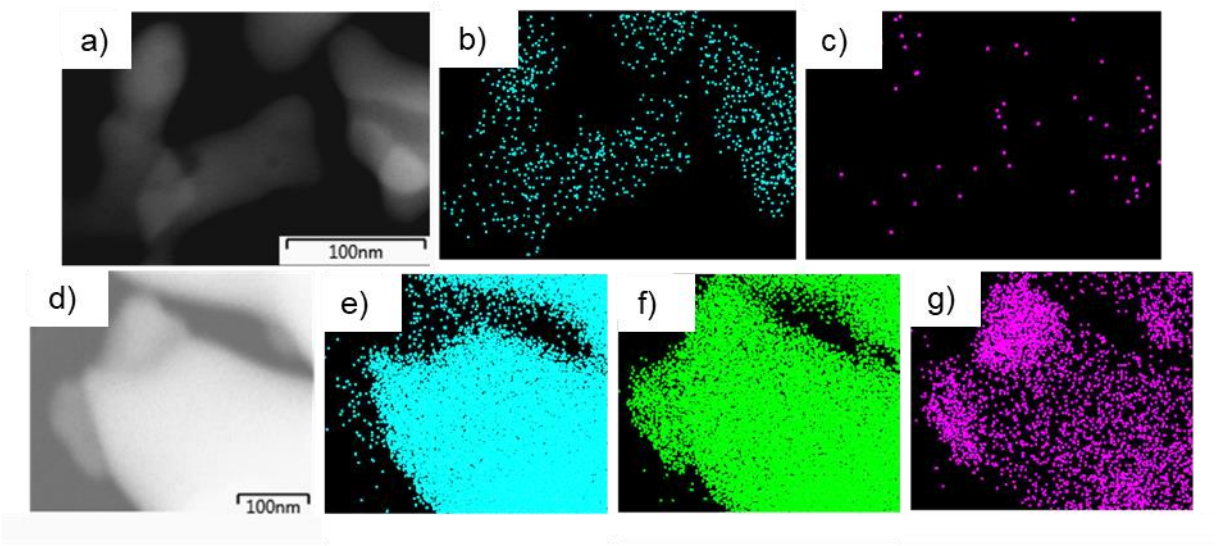

Figure 3.16 – EDS analysis of V-doped $LiFePO_4$ samples. a) A darkfield image of sample ΔLFVP(5) with b) the Fe-Kα (blue) and c) V-Kα (purple) signals from the same sample area. d) A darkfield image of sample ΔLFVP(10) with e) the Fe-Kα (blue), f) the P-Kα (green) and g) V-Kα signals (purple) from the same sample area. Adapted from reference 199.

While XRD and EDS analysis suggested homogenous doping in the olivine structure, it did not provide the location of V in the olivine structure. It was important, therefore, to ascertain the nature of the coordination environment of V, and to relate that to possible occupation sites in the $LiFePO_4$ lattice. ΔLFVP(2.5) was analysed using extended X-Ray absorption spectroscopy (EXAFS) data (V K-edge) to provide insights into local V coordination environment.[202] The presence of defects in the sample caused a breakdown in the fitting of the second and third coordination shells, so the analysis was limited to the first coordination shell. This revealed two distinct V-O bond lengths present in the sample; 49 ± 5 % of V-O bonds were of length 1.68 ± 0.012 Å, and 50 ± 8 % of V-O bonds were of length 2.01 ± 0.016 Å (Figure 3.17, Table 3.5). XAS data reduction and EXAFS modelling were performed on Horae Athena and Excurve 9.273, respectively, by Glen Smales and Husn Islam (UCL).[202,203]

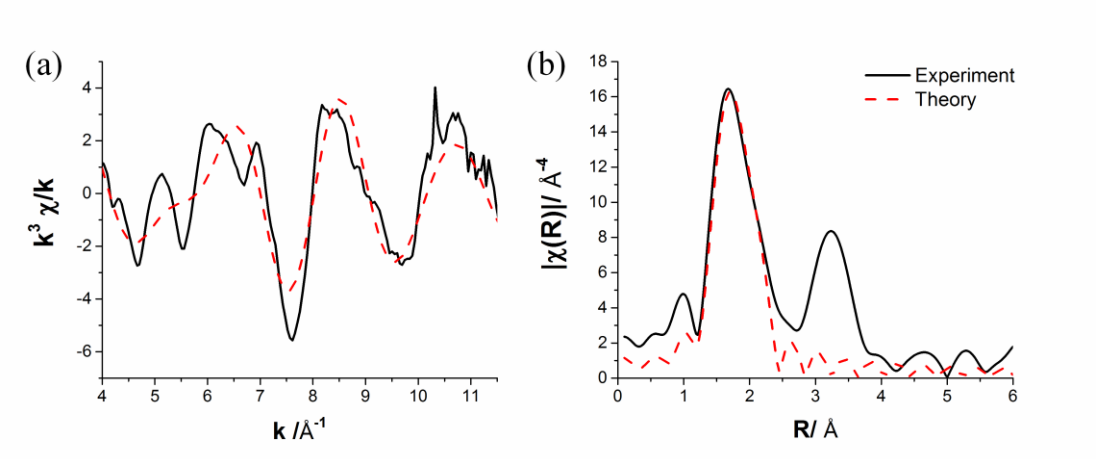

Figure 3.17 – The a) EXAFS and b) Fourier Transform analysis of ΔLFVP(2.5) at the vanadium K-edge (*ca.* 5465 eV) performed at the B18 beamline, Diamond Light Source using ion chambers to measure incident and transmitted beams. Reprinted from reference 199.

Table 3.5 – The results of EXAFS analysis, revealing V-O bond lengths and their errors, their relative abundancy and their errors, the Debye-Waller factor and the goodness-of-fit parameter (R_{ex}). Adapted from reference 199.

	R / Å	Relative Composition / %	$2\sigma^2$	R_{ex}
V-O bonds	1.68 ± 0.012 2.01 ± 0.016	49.27 ± 5.4 50.73 ± 7.6	0.00625 ± 0.00133	55

In isolation, the bond lengths are not enough to suggest which sites V occupies within the $LiFePO_4$ lattice. Density functional theory (DFT) analysis was employed by Prof. F. Cora and R. Dedigama (UCL) to explore different substitution mechanisms of V using hybrid-exchange functionals with periodic boundary conditions. The details of the computation were identical to those utilised within a study of V-doped aluminophosphates.[204,205] Vanadium oxidation states of 2 and 3 in the Li sites, 2, 3, 4 and 5 in the Fe site and 4 and 5 in the P sites were considered as possibilities in either $LiFePO_4$ or $FePO_4$. Full geometry optimisations were performed where possible for these configurations, and supercells of different sizes (4 and 16 LFP formula units) were considered to investigate the effect of V dopant concentration.

With respect to vacancy compensation mechanisms, isovalent defects (V^{2+}/Fe^{2+} in $LiFePO_4$, V^{3+}/Fe^{3+} in $FePO_4$, V^{5+}/P^{5+} in $FePO_4$ and $LiFePO_4$) did not need an additional compensating defect. In contrast, added defects were required to charge-balance aliovalent replacements: V^{4+} and V^{5+} in the Fe site by Li^+/Fe^{3+} or Li and Fe vacancies; V/Li^+ by Fe vacancies and V^{4+}/P^{5+} in $LiFePO_4$ by converting a Fe^{2+} to Fe^{3+}.

Some V oxidation states were not stable and underwent internal redox transformations; V^{4+}/P^{5+} with a Fe^{3+} defect in $LiFePO_4$ converted to the isovalent arrangement of V^{5+} and Fe^{2+}. Replacing Fe^{3+} with V^{5+} oxidised an O^{2-} ion to an O^{1-} radical adjacent to the charge-balancing defect (Fe vacancy or Li^{+}/Fe^{3+}) and V^{5+} reduced to V^{4+}. Vanadium was not stable on an Li site in any oxidation state or compensation mechanism. Equilibrium V-O bond distances for all stable configurations are shown in Table 3.6.

Table 3.6 – V-O bond distances calculated by DFT for different V oxidation states, modes of incorporation and concentrations of V ions in LFP. This includes a) V in $LiMnPO_4$ for comparison; b) Li in Fe site compensating defect; c) interstitial Li and Fe vacancy compensating defect. Adapted from reference 199.

Oxidation state of V	Site	Conc. (%)	Supercell Formula	**<V-O>**
2+	Fe	12.5	$Li_8Fe_7VP_8O_{32}$	**2.1593**
		12.5	$Li_1Fe_7VP_8O_{32}$	**2.1543**
		100	$Li_4V_4P_4O_{16}$	**2.1570**
3+	Fe	12.5	$Fe_7VP_8O_{32}$	**2.0514**
	(a)	12.5	$Mn_7VP_8O_{32}$	**2.0426**
		100	$V_4P_4O_{16}$	**2.0467**
4+	Fe (b)	12.5	$Li_1Fe_6VP_8O_{32}$	**1.9542**
	(c)	12.5	$Li_1Fe_6VP_8O_{32}$	**1.9552**
5+	P	12.5	$Fe_8P_7VO_{32}$	**1.7060**
		6.25	$Fe_{16}P_{15}VO_{64}$	**1.7045**
		12.5	$Li_8Fe_8P_7VO_{32}$	**1.7075**
		100	$Fe_4V_4O_{14}$	**1.7115**
		100	$Li_4Fe_4V_4O_{16}$	**1.7123**
			EXAFS	**1.68**
				2.01

The calculated V-O bond lengths appeared to be little affected by concentration or the compensating defect; only oxidation state appeared to have a noticeable effect. Therefore, the bond lengths observed were diagnostic of both oxidation state and site occupation. Only two local environments described in Table 3.6 corresponded to the measured bond lengths from the EXAFS analysis; V^{3+}/Fe^{3+} and V^{5+}/P^{5+}. According to the quantification of these bond lengths from EXAFS, V^{3+} in octahedral Fe sites and V^{5+} in tetrahedral P sites were present in a ratio of *ca.* 40:60. It is worth noting that the impurity phase $LiVP_2O_7$ also had an average V-O bond length close to 2.01 Å (2.00

Å),[206] so this phase may also have been responsible for the observed bond lengths (although it was not observed by XRD for this sample).

ICP-AES was used to determine the effect of vanadium content on the other constituents of $LiFePO_4$. There appeared to be a slight deficiency of phosphorous in all compounds (due to the > 1 molar ratio of Li/P and Fe/P observed in the pure $LiFePO_4$ compound, Table 3.7). The elemental ratios of sample LFVP(2.5) agreed with the suggestion of V ions on Fe and P sites, as phosphorous was deficient, and there was a corresponding decrease in Fe content with the addition of V compared to the pure LFP sample. However, increasing the dopant concentration further led to an equal reduction in Fe, and implied compensatory Li vacancy formation with Fe substitution (Figure 3.18a-c). This has also been suggested for other highly vanadium-substituted samples.[189]

Table 3.7 – Elemental ratios of the pure $LiFePO_4$ and V-doped $LiFePO_4$ samples found from ICP-AES analysis (normalised to phosphorous). Adapted from reference 199.

Sample	Li/P	Fe/P	V/P	P/P
LFP1	1.05	1.04	0.00	1.00
LFVP(2.5)	1.01	1.00	0.03	1.00
LFVP(5)	0.97	0.96	0.05	1.00
LFVP(10)	1.01	0.94	0.09	1.00
LFVP(20)	0.92	0.85	0.19	1.00

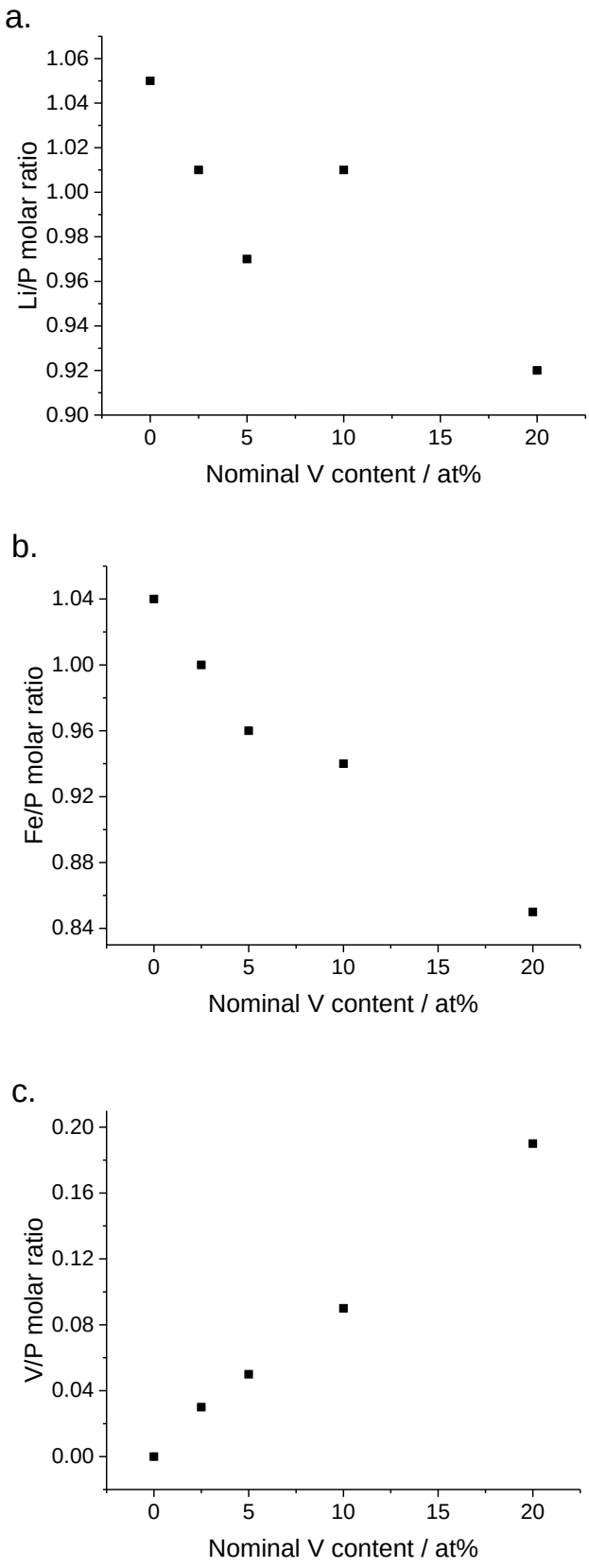

Figure 3.18 – Ratios of elements found from ICP-AES analysis normalised to phosphorous for the V-doped $LiFePO_4$ samples, displaying: a) Li, b) Fe and c) V, plotted against nominal V content in at%.

TEM (Figure 3.19a-e) and FE-SEM images (Figure 3.20) of the heat-treated samples showed the particles all formed agglomerated networks of crystallites. The fused nature of the crystallites made particle size distributions impossible for these samples; however, it was generally observed that the longest axis of the particles was between 100 – 300 nm for all samples, with a minor population of particles above 0.5 µm in size. This is consistent with the average particle sizes estimated from Rietveld refinement (Table 3.4). It can be seen that when the vanadium content was increased to 10 and 20 at%, there was a general shift towards larger platelet morphology (Figure 3.19a-e, Table 3.4), which was further evidenced from the relative transparency of these plates observed in SEM (Figure 3.20) for sample ΔLFVP(20). The presence of carbon in the samples was confirmed by CHN analysis (Table 3.2), and a consistent carbon coating (approximately 1.7 nm thick) was observed in high-resolution TEM analysis (Figure 3.19f).

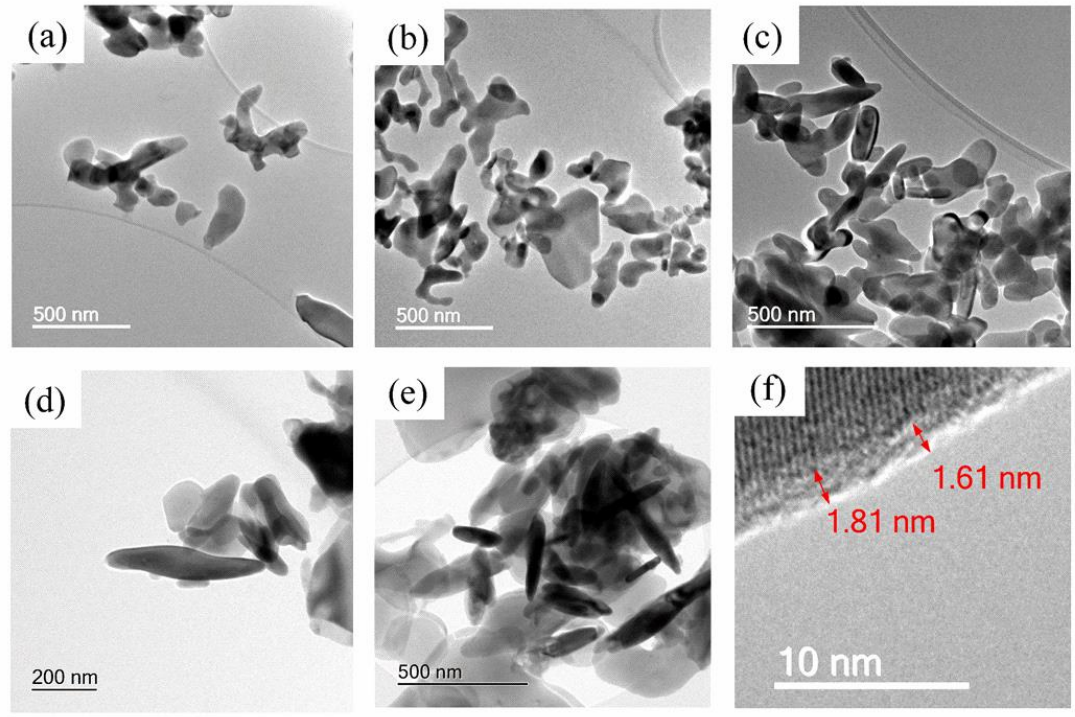

Figure 3.19 – TEM micrographs of a) ΔLFP2, (b) ΔLFVP(2.5), (c) ΔLFVP(5), (d) ΔLFVP(10) and (e) ΔLFVP(20). (f) The continuous carbon coating on sample ΔLFVP(20) (the amorphous-type layer on the surface of the particle) which is approximately 1.7 nm thick. Reprinted from reference 199.

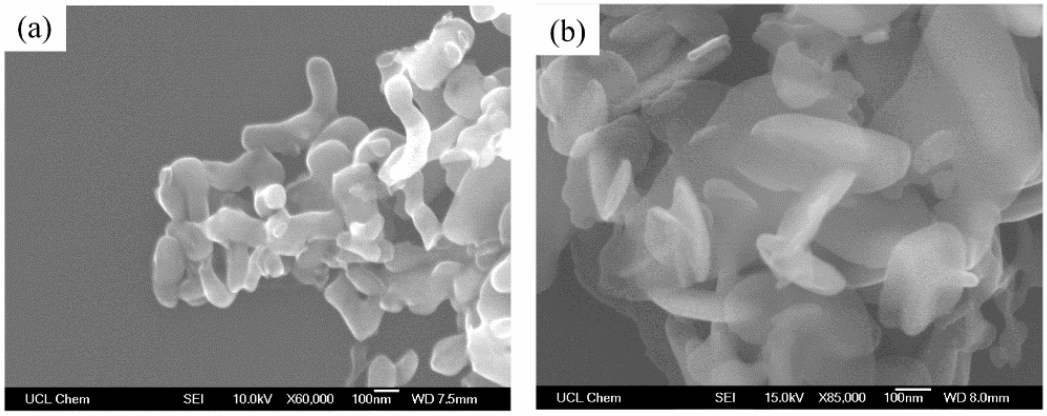

Figure 3.20 – SEM micrographs of (a) ΔLFP2, which displayed rounded morphology and (b) ΔLFVP(20), which possessed platelet morphology. Reprinted from reference 199.

3.4.1.3. Electrochemical Characterisation

CV tests were employed to understand the reversible and irreversible electrochemical processes occurring upon charge/discharge. The Fe^{2+}/Fe^{3+} couple at 3.45 V was observed in all samples (Figure 3.21), and no additional electrochemistry could be specifically ascribed to the $LiV(P_2O_7)$ impurity, although the electrochemical activity of the $LiV(P_2O_7)$ phase is beyond the testing voltage window (4.2 – 4.8 V).[207] For sample ΔLFVP(10) an additional irreversible charge process was observed at 2.15 V (Figure 3.21), but was not observed in subsequent cycles. The peak discharge current increased with increasing vanadium doping from ΔLFP2 (−520 mA) to 2.5 and 5 at% V (−650 mA), but then decreased for higher V-dopant levels. As the peak discharge current is a crude indicator of the kinetics of the lithiation reaction, this implied that ΔLFVP(2.5) and ΔLFVP(5) possessed optimal kinetics within these samples.

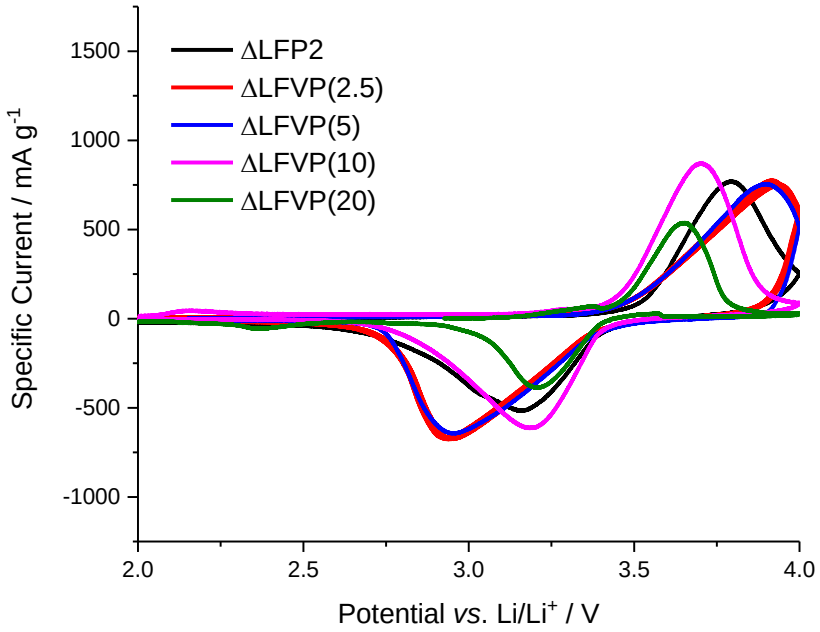

Figure 3.21 – Cyclic Voltammetry of the pure $LiFePO_4$ and heat-treated V-doped samples (scan rate 0.5 mV s^{-1}) between 2 – 4 V.

In an attempt to quantify the improvement in charge/discharge kinetics within samples ΔLFP2, ΔLFVP(2.5) and ΔLFVP(5), the CV data was analysed using the Randles-Sevcik equation (Equation 2.5, Section 2.1.5.3). The current at potential scan rates of 0.05, 0.1, 0.2, 0.5, 1 and 2 mV s^{-1} was measured, and the peak discharge currents plotted against $v^{1/2}$ (the square root of scan rate, Figure 3.22). The gradients can be related to Li^+ diffusion coefficients within the electrodes, which were 1.0×10^{-10}, 1.6×10^{-10} and 2.1×10^{-10} cm^2 s^{-1} for ΔLFP2, ΔLFVP(2.5) and ΔLFVP(5) respectively. These results were not "true" diffusion coefficients, but allowed comparisons to be made between electrodes of similar composition and mass loading. Therefore, enhanced Li^+ diffusion kinetics were observed with increased V doping up to 5 at%.

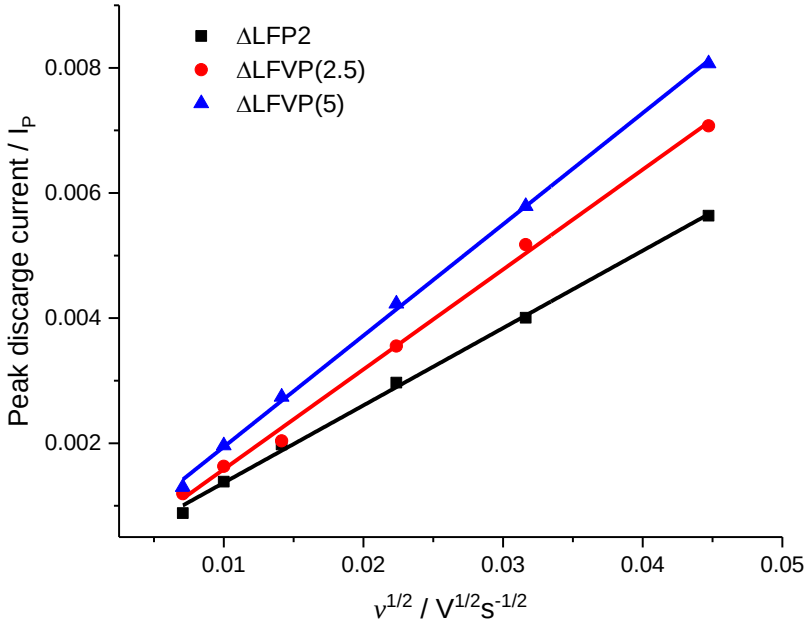

Figure 3.22 – Randles-Sevcik analysis of ΔLFP2, ΔLFVP(2.5) and ΔLFVP(5), plotting the peak discharge current I_P against the square root of scan rate, $v^{1/2}$, where the gradient can be related to the Li^+ diffusion coefficient according to Equation 1.15. Reprinted from reference 199.

Within C-rate testing, a sharp decline in discharge capacity with dopant concentration was observed at low C-rates above 2.5 at% V-doping (Figure 3.23a). As the V-dopant did not appear to be active, and the active Fe^{2+} species decreased with V-doping, the maximum capacity was reduced significantly for the highly V-doped compounds. This has been observed previously by other authors.[188] The high-rate performance displayed a different trend; increasing the V-dopant to 5 at% gave a significant increase in discharge capacity, and any further substitution resulted in a decrease in performance. The lack of additional electrochemistry was verified from first cycle charge/discharge plots, where only the Fe^{2+}/Fe^{3+} plateau at 3.45 V was evident (Figure 3.23b, Figure 3.24, Figure 3.25). Furthermore, the influence of the V dopant could be most clearly seen in the overpotentials of charge and discharge; they decreased from ΔLFP2 to ΔLFVP(5), then increased again for sample ΔLFVP(20) (Figure 3.23b, Figure 3.24, Figure 3.25). It is suggested that the appearance of the impurity phase had a deleterious influence on high-rate cathode performance, and was responsible for the reduced performance above 5 at% V. It is important to note that there was carbon present in all samples, and therefore the trends in performance could be unambiguously attributed to the V dopant. The highest capacity observed at 10C (130 mA h g^{-1}) for the 5 at% V sample compares extremely favourably with a performance review of other $LiFePO_4$

electrodes in literature (Figure 3.26), where the only electrodes which surpass ΔLFVP(5) for the 10C discharge capacity contain significantly more carbon (17 and 30 wt%, respectively).

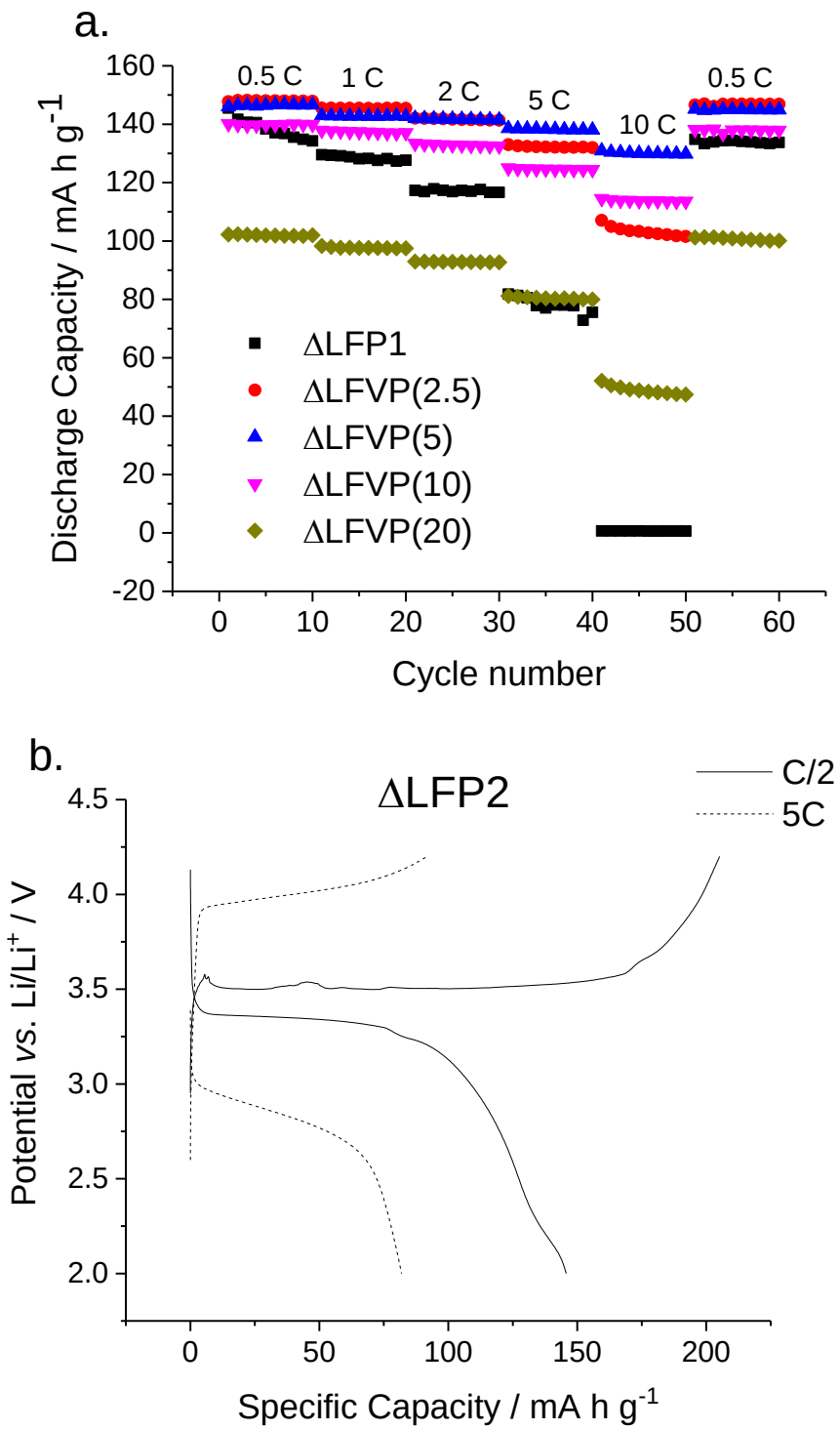

Figure 3.23 – a) C-rate testing of the pure $LiFePO_4$ and V-doped $LiFePO_4$ compounds, with the charge/discharge rate indicated above the discharge capacities. b) The first cycle of charge discharge at C/2 (solid line) and 5C (dotted line) for sample ΔLFP2.

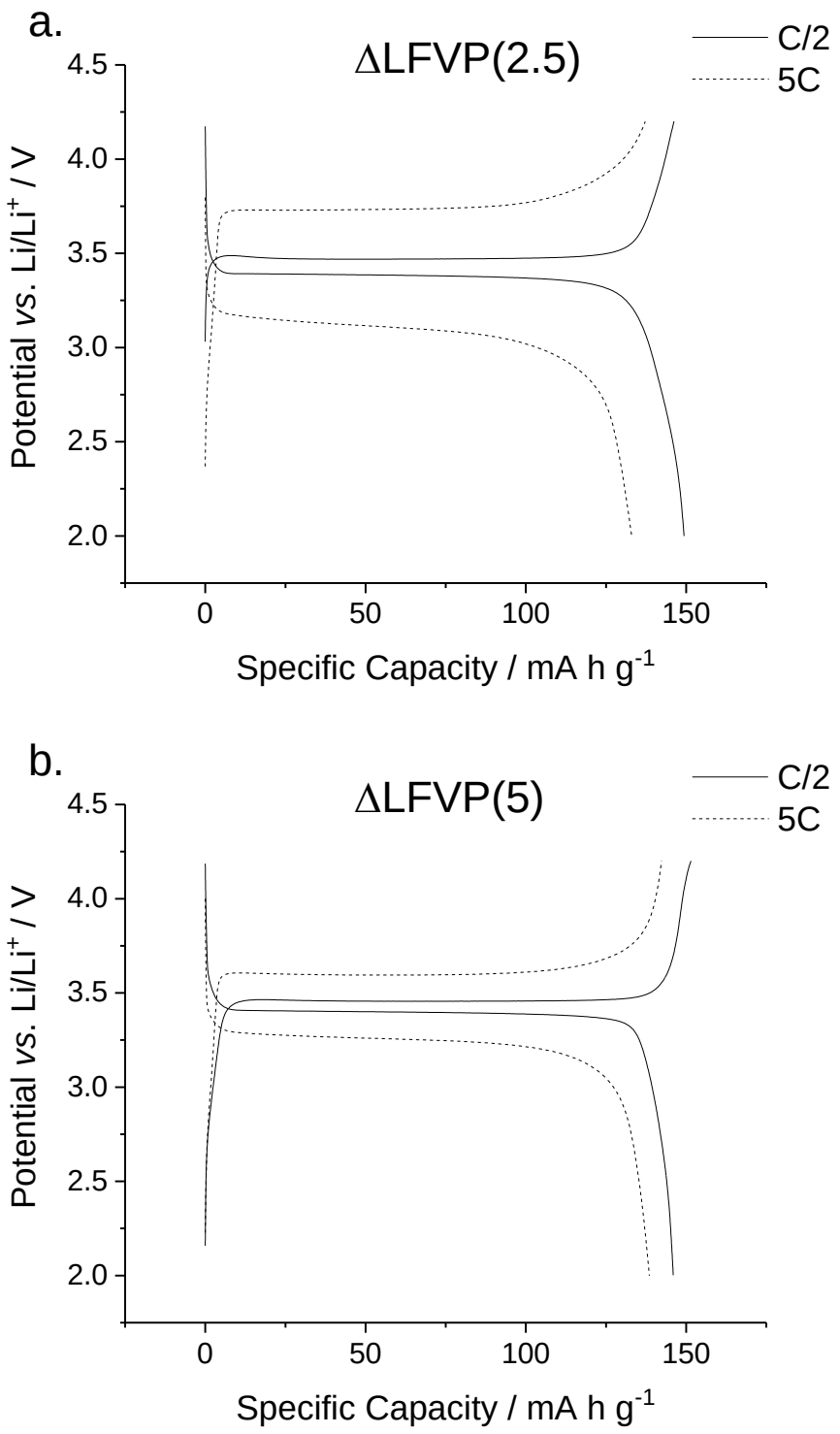

Figure 3.24 – a) The first cycle of charge discharge at C/2 (solid line) and 5C (dotted line) for sample ΔLFVP(2.5). b) The first cycle of charge discharge at C/2 (solid line) and 5C (dotted line) for sample ΔLFVP(5).

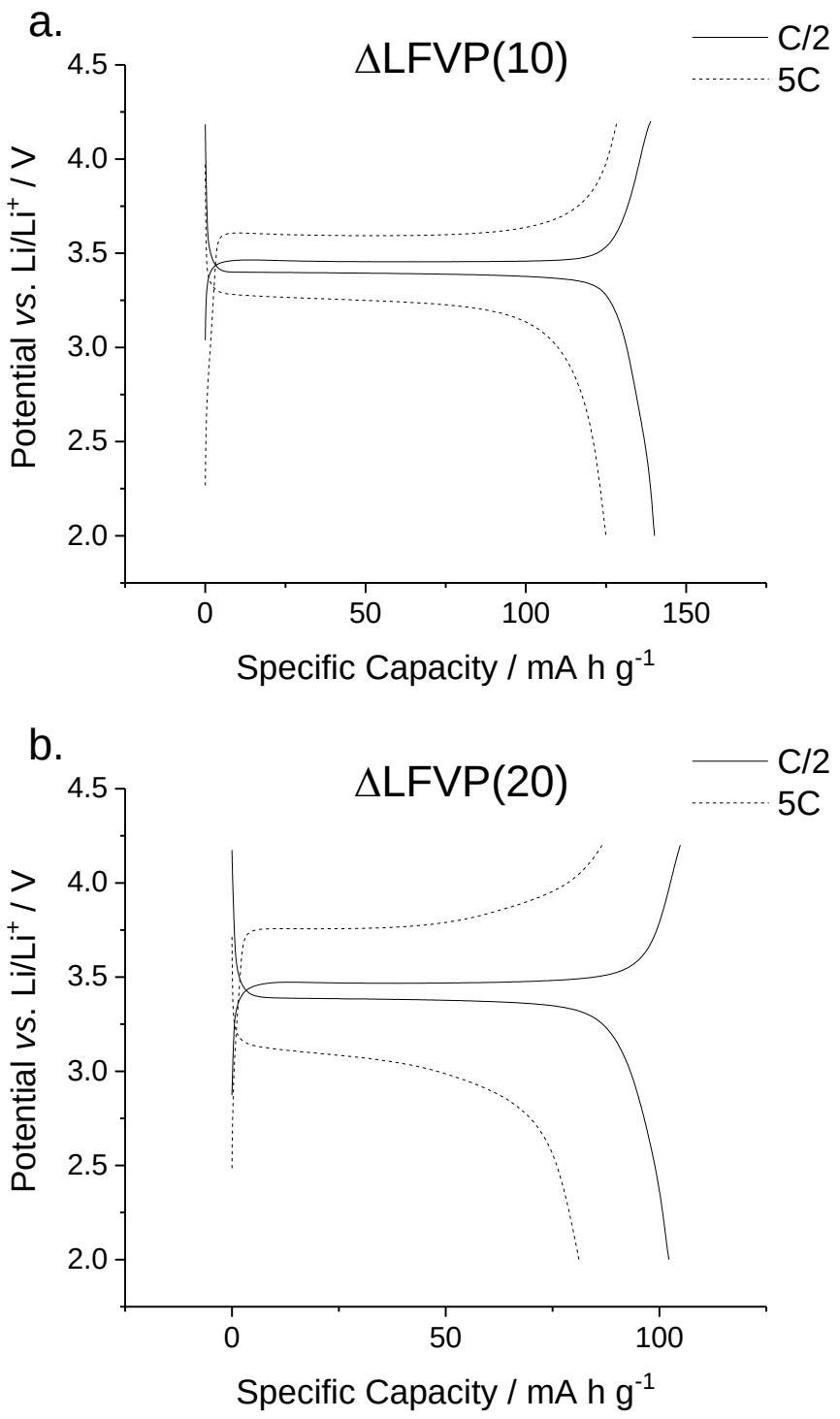

Figure 3.25 – a) The first cycle of charge discharge at C/2 (solid line) and 5C (dotted line) for sample ΔLFVP(10). b) The first cycle of charge discharge at C/2 (solid line) and 5C (dotted line) for sample ΔLFVP(20).

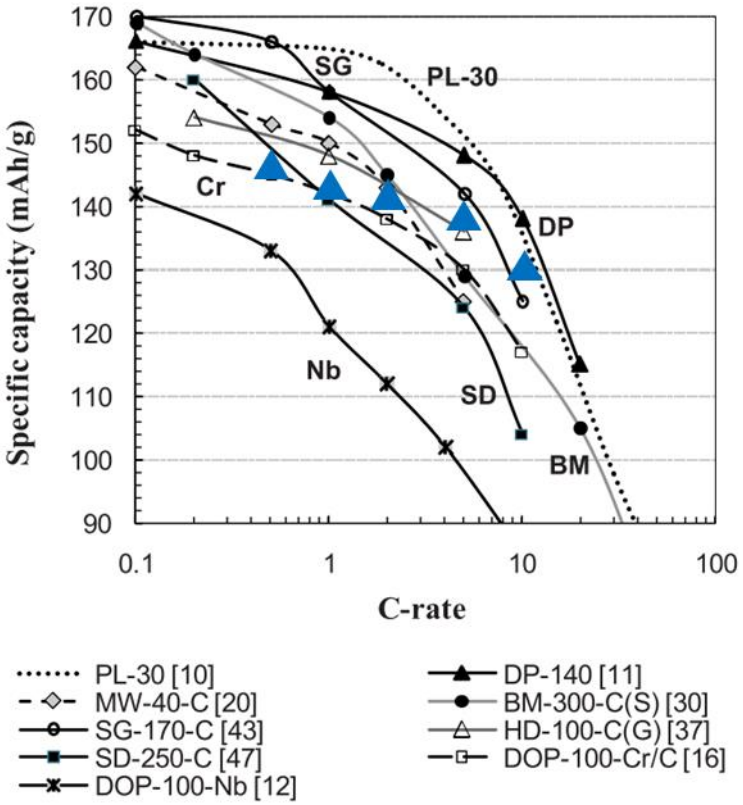

Figure 3.26 – A summary of the best-performing $LiFePO_4$ electrodes from a literature review, with the results from the best performing sample, ΔLFVP(5), shown with blue triangles. Adapted with permission from "Zhang, W.-J. Comparison of the Rate Capacities of $LiFePO_4$ Cathode Materials. J. Electrochem. Soc. 157, 1040–1046 (2010).". Copyright 2010 Electrochemical Society.[170]

In order to assess the stability of the electrodes, long-term cycle stability tests were performed (1000 cycles at 0.88C) for the best sample, ΔLFVP(5). It displayed excellent capacity retention of >96% over 200 cycles and >70% over 1000 cycles (Figure 3.27).

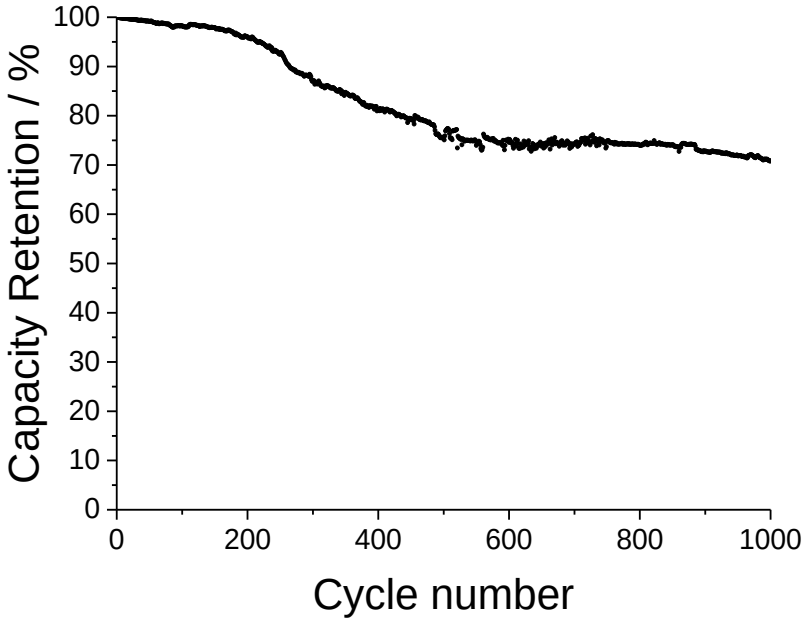

Figure 3.27 – Long-term stability test of ΔLFVP(5) at 0.88 C for 1000 cycles, where the capacity was normalised to the first discharge capacity. Adapted from reference 199.

3.4.1.4. Conclusions

A high-performance, carbon-coated vanadium-doped $LiFePO_4$ cathode was successfully synthesised *via* a continuous hydrothermal pilot-scale process. The synergistic combination of nano-sizing, carbon-coating and doping dramatically improved the cathode rate capability, with ΔLFVP(5) achieving a high discharge capacity of 130 mA h g^{-1} at a 10C discharge rate, which matches or indeed surpasses the highest performances achieved in the literature for $LiFePO_4$-based materials.[170] Moreover, as these samples were produced at a scale of a 6 kg per day, this holds promise for future development of large-scale cells and is discussed in Chapter 4 .

A combination of experimental and computational techniques suggested the vanadium dopant was found on both Fe and P sites within the structure. This had numerous effects, including distorting the lattice parameters and possibly introducing Li^+ vacancies within the structure. It is suggested that the shorter diffusion distance (determined by the *b* lattice parameter) and/or Li^+ vacancy inclusion is responsible for the increase in performance, although further analysis such as EXAFS, neutron diffraction and muon spectroscopy are necessary to determine the V dopant and location effect. Muon spectroscopy is discussed in Chapter 5.

3.4.2. Nb-doped $LiFePO_4$ investigation

3.4.2.1. Aims

Following the success of the V-doping study, it was important to determine if similar effects could be seen with other dopants. As Nb-doping had also been shown to improve discharge capacity at high rates in $LiFePO_4$,[172] and possesses similar chemistry to V as they share the same periodic table group, it was a natural candidate for investigation. The Nb-doped materials were made as nanoparticles and carbon-coated in an analogous manner to the previous section. The samples were centrifuged and cleaned by a masters' student, (Ekaterina Blagovidova), and all electrodes and cells were fabricated and tested by the same student.

3.4.2.2. Physical Characterisation

Nb-doped $LiFePO_4$ samples were successfully synthesised using the Pilot-Scale CHFS process as grey powders at a production scale of 0.25 kg h^{-1}. In an analogous manner to the V-doped $LiFePO_4$ experiments in Section 3.4.1, the concentrations of precursors were varied according to Table 3.8 to generate doped compounds of the nominal formula $LiFe_{1-x}Nb_xPO_4$. The LiOH, H_3PO_4 and fructose concentrations were 0.8625 M, 0.375 M, and 0.65 M, respectively. These samples were given the nomenclature LFNP(*x*), where *x* is the Nb at% relative to total transition metal content (Fe + Nb) in the precursor solution. Heat-treatments produced black powders, which were analogously named ΔLFNP(*x*), and the carbon contents were calculated using CHN analysis (Table 3.8). Molar yields were in the range 50 – 70 mol%.

Table 3.8 – The molar concentrations of the Fe and Nb precursors used to generate the samples. The carbon coating wt% was calculated using CHN analysis. Adapted from reference 208.

Sample Name	$FeSO_4.7H_2O$ / mM	$C_4H_4NNbO_9.5H_2O$ / mM	C / wt.%
ΔLFNP(0.01)	249.975	0.025	4.8
ΔLFNP(0.1)	249.750	0.250	5.5
ΔLFNP(0.5)	248.750	1.250	7.3
ΔLFNP(1.0)	247.500	2.500	2.9
ΔLFNP(1.5)	246.250	3.750	4.3
ΔLFNP(2.0)	245.000	5.000	2.5

ICP-AES was employed to measure the concentrations of Li, Fe and P within the Nb-doped samples, where sample LFP1 was included in the data set from the previous section for comparison. Unfortunately, Nb was not measurable by ICP-AES as it did not produce a stable signal in the plasma; however, all other elements could readily be

measured. Similar to the V-doped $LiFePO_4$, there was a slight deficiency of P within all samples, and both the Li and Fe content decreased uniformly with increasing Nb content. Sample LFNP(0.5) had Li/P and Fe/P ratios of 0.89 and 0.9, respectively, and was considered an anomalous result. In general, the molar ratios of both Li and Fe decreased by an approximately equal amount to the Nb added in the reagents, which suggested it could occupy either site. A combined EXAFS and DFT study on these materials would be suitable future methods for discerning the doping mechanism of Nb in $LiFePO_4$, i.e. which site it occupies in the lattice.

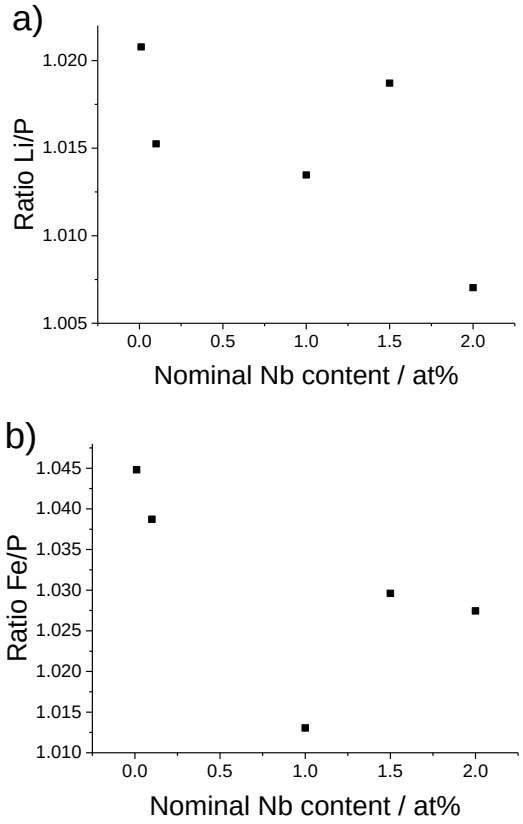

Figure 3.28 – The elemental ratios a) Li/P and b) Fe/P as a function of nominal Nb dopant content from ICP-AES analysis.

XRD patterns of the heat-treated samples all closely resembled the pure $LiFePO_4$ olivine structure (PDF Card No. 01-070-6684, Figure 3.29a), although a very minor impurity peak was present in some samples, indicated by an asterisk. A high-quality XRD pattern of sample ΔLFNP(1.0) (using set-up **c**, Section 2.1.4.1) revealed this peak more clearly (Figure 3.29b). This was tentatively suggested to be $Fe_2P_2O_7$ (similar to PDF Card No. 00-076-1672), and may reflect the overall lithium deficiency observed in these compounds. This was also observed in Chapter 6 and is discussed in

further detail there. Rietveld refinement revealed the variation of lattice parameters (and unit cell volume) was almost identical between samples, i.e. uniform expansion and contraction (Table 3.9, Figure 3.30, Chapter 11 - Appendix I). There was no overall shift in lattice parameters with composition, implying the differences in parameters observed may be random variance, perhaps caused by the inevitable inhomogeneity of the heating zone in the tube furnace. This was in direct contrast to the claims of Ma *et al.*, where they observed an expansion of the (1 0 1) interplanar distance with increased Nb incorporation.[209] However, it must be noted that they did not perform Rietveld refinement, instead relying on the 2θ shift of the (1 0 1) peak, so their observed variance could easily be due to 2θ error rather than a shift in lattice parameters.

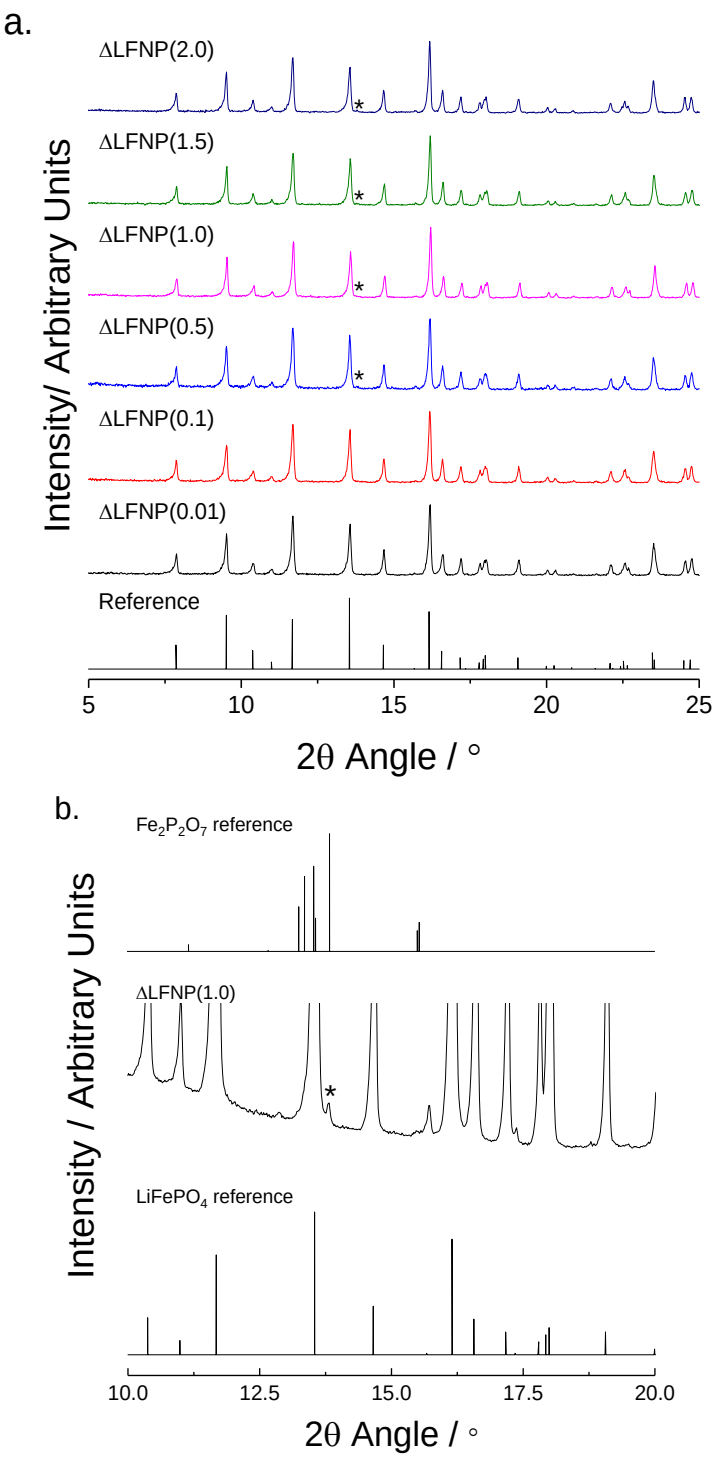

Figure 3.29 – a) XRD patterns (Mo-Kα radiation) of the Nb-doped $LiFePO_4$ samples, including an $LiFePO_4$ reference pattern (PDF Card No. 01-070-6684). b) A high-quality XRD pattern (Mo-Kα radiation, capillary mode) of the ΔLFNP(1.0) sample with a truncated *y*-axis, showing the presence of a minor impurity peak (indicated by an asterisk), and the suggested impurity phase $Fe_2P_2O_7$ (PDF Card No. 00-076-1672). Adapted from reference 208.

Table 3.9 – The lattice parameters of the heat-treated Nb-doped samples calculated from Rietveld refinement. Sample ΔLFP1 is included as a reference. Adapted from reference 208.

Sample	*a* / Å	*b* / Å	*c* / Å	*V* / Å^3	R_{wp}	χ^2
ΔLFP1	10.32413(13)	6.00392(8)	4.69445(7)	290.897(12)	4.02	1.21
ΔLFNP(0.01)	10.3283(4)	6.0066(3)	4.6974(2)	291.42(4)	17.2	1.14
ΔLFNP(0.1)	10.3303(5)	6.0082(3)	4.6976(2)	291.57(4)	17.6	1.23
ΔLFNP(0.5)	10.3290(5)	6.0070(3)	4.6969(2)	291.43(4)	17.1	1.03
ΔLFNP(1.0)	10.3137(4)	5.9971(2)	4.6899(2)	290.08(4)	15.5	1.05
ΔLFNP(1.5)	10.3251(4)	6.0026(2)	4.6951(2)	290.99(4)	16.3	1.10
ΔLFNP(2.0)	10.3329(4)	6.0074(2)	4.6691(2)	291.69(4)	15.6	1.09

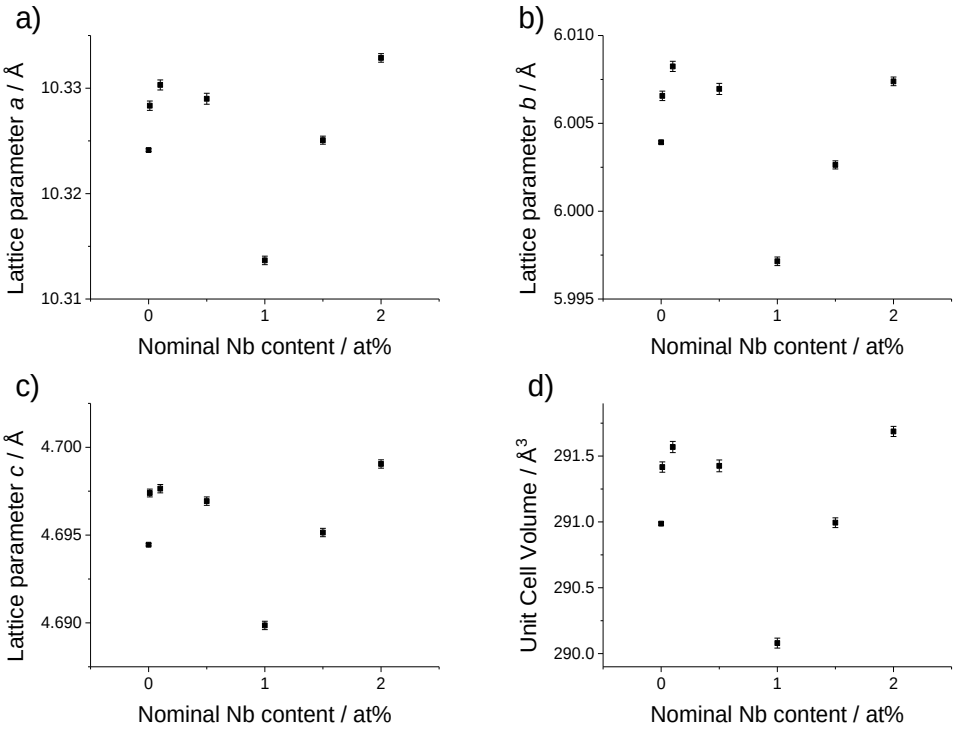

Figure 3.30 – The effect of Nb concentration (in at%) on a) the *a* lattice parameter, b) the *b* lattice parameter, c) the *c* lattice parameter and d) the unit cell volume *V* of the heat-treated samples. Errors calculated from the fit are included as error bars.

In a similar manner to the EDS investigation of V-doped $LiFePO_4$ in Section 3.4.1, a uniform dispersion of Nb within the particles was observed from EDS analysis of sample ΔLFNP(2.0), with no obvious Nb-rich phases (Figure 3.31). This is consistent with homogeneous doping, although techniques such as EXAFS would be required to add further weight to this suggestion.

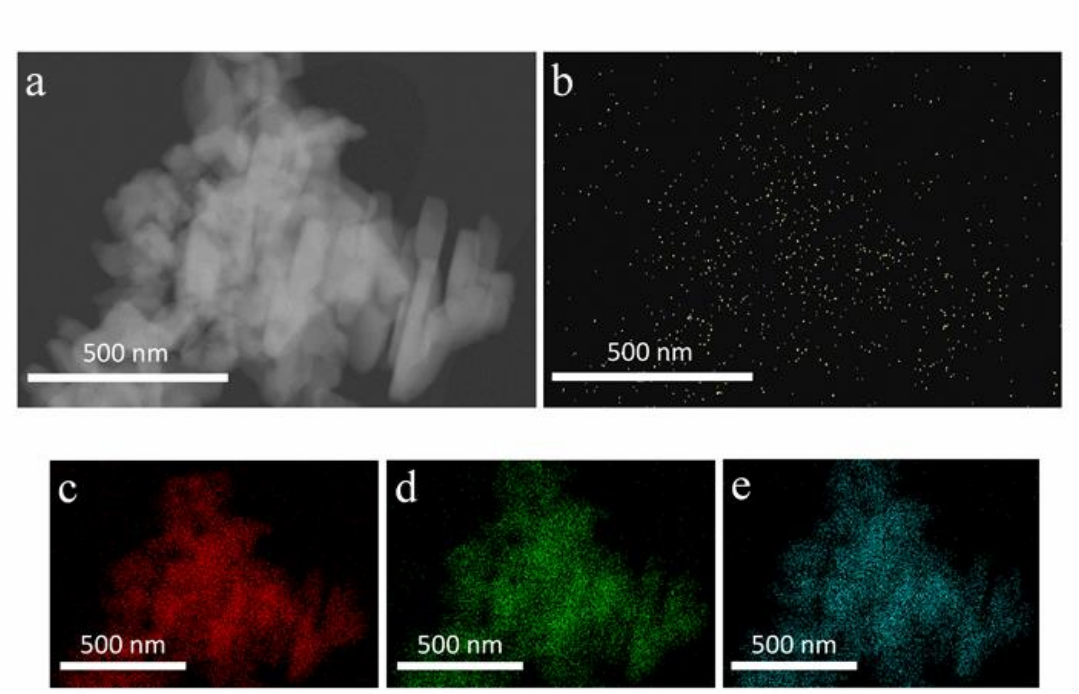

Figure 3.31 – EDS imaging of sample LFNP(2.0), displaying a) the darkfield image, b) the Nb-Kα signals (yellow), c) the Fe-Kα signals (red), d) the O-Kα signals (green) and e) the P-Kα signals (blue). Adapted from reference 208.

FE-SEM analysis indicated the Nb-doped $LiFePO_4$ exhibited similar particle size and morphology to those observed for pure $LiFePO_4$ in the previous section (Section 3.4.1.2), adopting a fused crystallite morphology. The majority of particles possessed long axis lengths between 100 – 300 nm, with a minority of particles > 0.5 µm. Therefore, Nb-doping did not appear to significantly affect crystallite size or morphology.

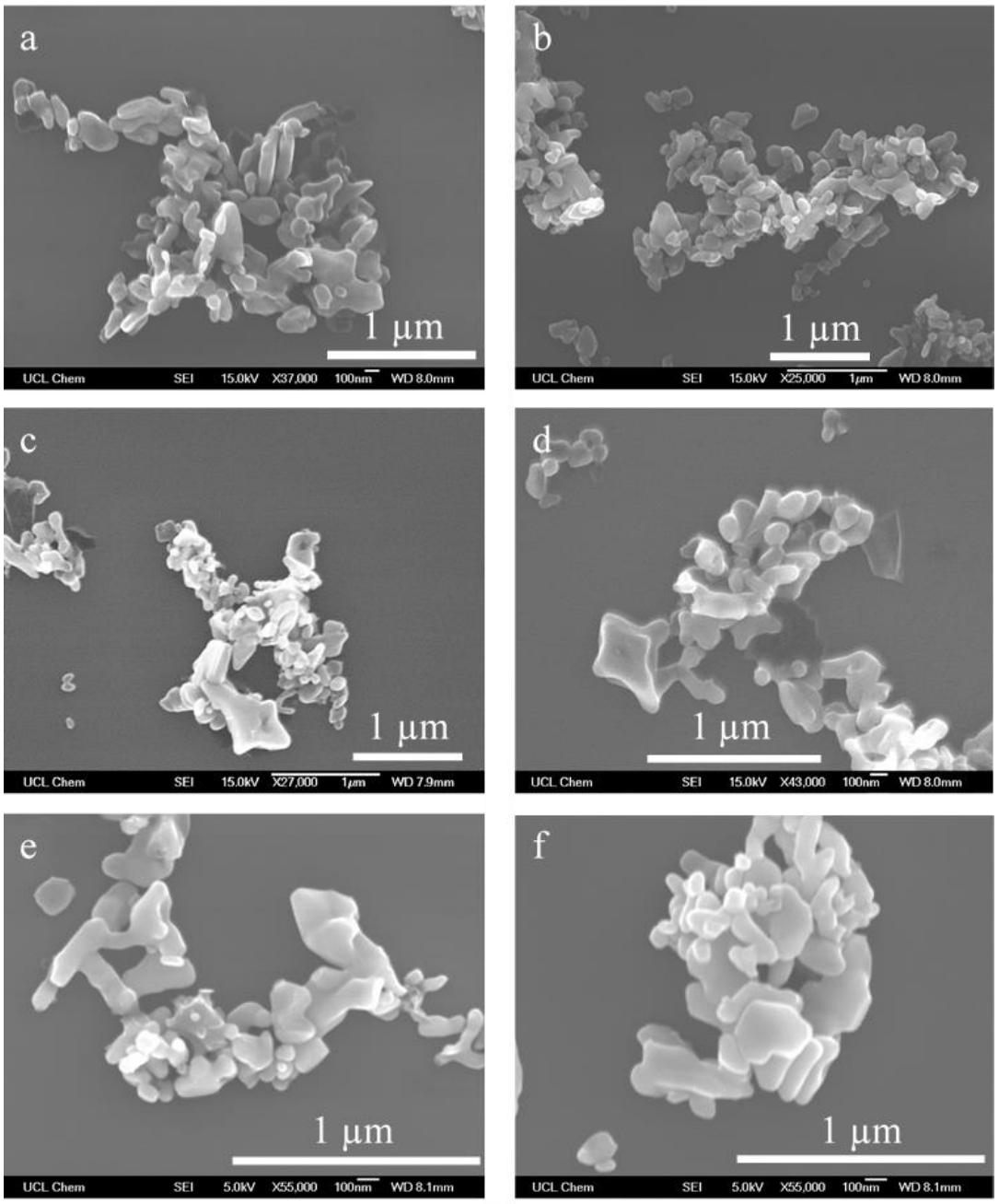

Figure 3.32 – FE-SEM images of samples a) ΔLFNP(0.01); b) ΔLFNP(0.1); c) ΔLFNP(0.5); d) ΔLFNP(1.0); e) ΔLFNP(1.5); f) ΔLFNP(2.0). Adapted from reference 208.

The heat-treated samples ΔLFNP(*x*) showed a more varied carbon coating degree compared to the V-doped study (in the range 2.5 to 7.3 wt%) (Table 3.8). TEM images of ΔLFNP(1.0) revealed a continuous coating approximately 3.5 nm thick (Figure 3.33a), which is thicker than the coating observed in the V-doped LFP study, and reflects the higher carbon content of ΔLFNP(1.0). Raman spectroscopy analysis of the heat-treated samples consistently showed D-bands (1350 cm^{-1}) and G-bands (1600 cm^{-1}, Figure 3.33b), which implied successful graphitisation.

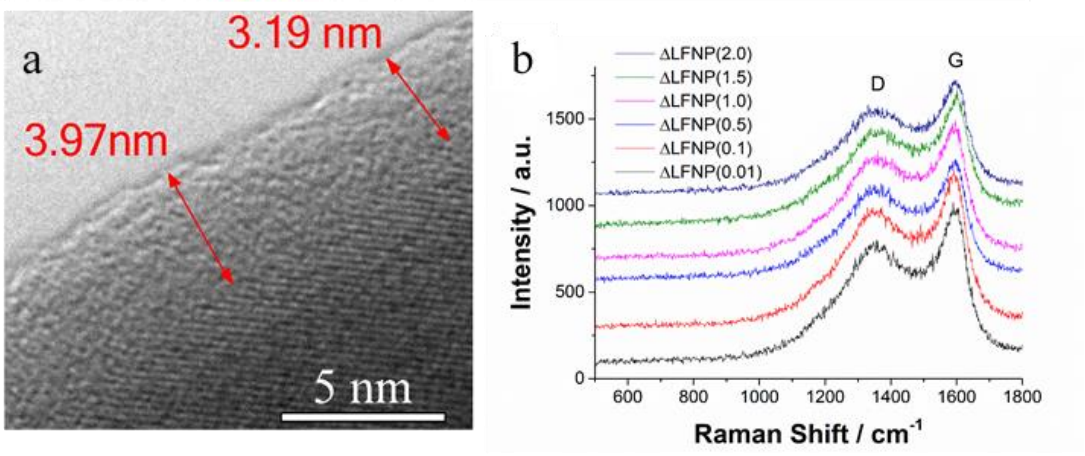

Figure 3.33 – a) A TEM micrograph image of ΔLFNP(1.0) showing a continuous carbon coating; b) Raman spectra of the heat-treated samples, with the D and G modes indicated. Adapted from reference 208.

Cyclic voltammetry showed the reversible Fe^{2+}/Fe^{3+} redox couple at 3.45 V (Figure 3.34a), and no additional activity with the inclusion of Nb. The peak discharge currents were generally higher for the more highly doped samples 1.5 at%, which demonstrated improved delithiation kinetics with Nb addition. A CV profile for pure $LiFePO_4$, ΔLFP(1), was included for reference; although it displayed greater peak discharge current compared to ΔLFNP(0.01)-ΔLFNP(0.5), it did also have a thicker carbon coating (9.1 wt% *vs.* a range of 2.5 – 7.3 wt%). To clarify the improvement in charge/discharge kinetics, the Randles-Sevcik equation (Equation 1.15, Section 2.1.5.3) was used to compare samples ΔLFP(1), ΔLFNP(1.0), ΔLFNP(1.5), and ΔLFNP(2.0) (Figure 3.34b). In a similar manner to the V-doped $LiFePO_4$ section, the diffusion coefficients obtained depend on the mass loading and electrode architecture. Therefore, these values are only used to compare the diffusion kinetics of samples within this study, which were all made in the same way. The calculated diffusion coefficients of the doped samples were very similar; 2.0×10^{-10}, 2.2×10^{-10}, and 1.9×10^{-10} cm^2 s^{-1} for ΔLFNP(1.0), ΔLFNP(1.5), and ΔLFNP(2.0), respectively. This displayed an increase in the diffusion coefficients compared to the pure LFP sample from Section 3.4.1.3 (ΔLFP2, 1.0×10^{-10} cm^2 s^{-1}), but suggested that further Nb-doping of $LiFePO_4$ beyond 1 at% did not significantly improve performance.

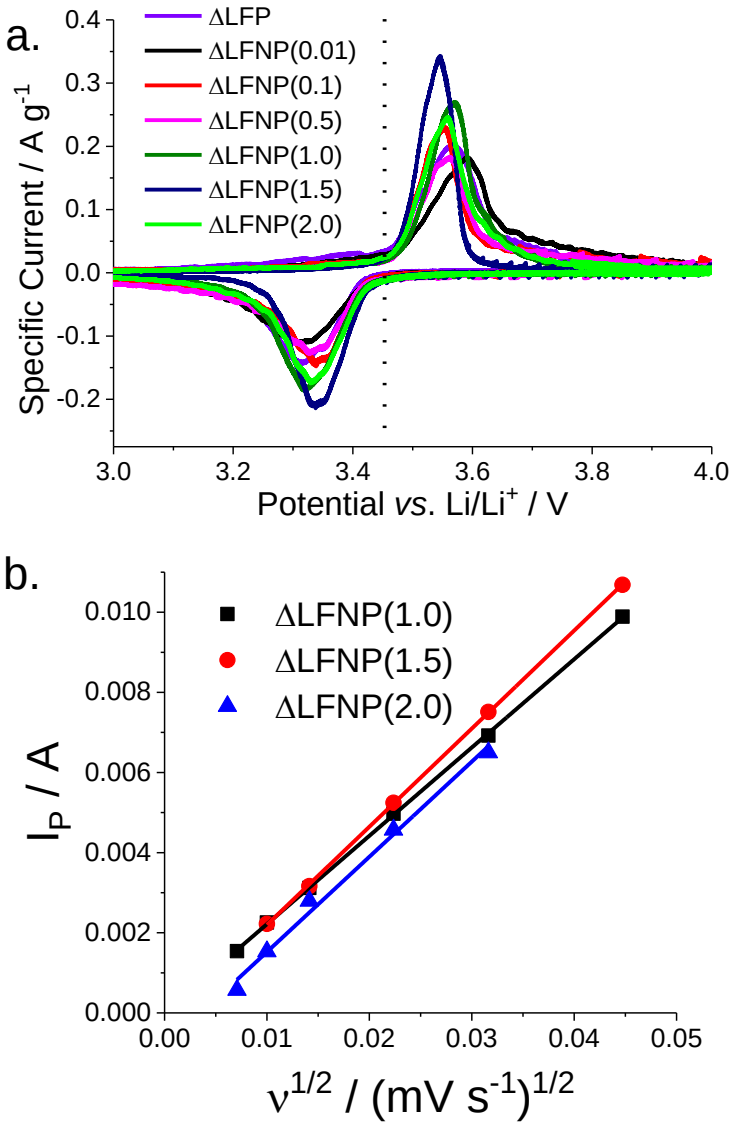

Figure 3.34 – CV results at 0.05 mV s^{-1} scan rate for all heat-treated samples, including ΔLFP(1) sample from previous work; b) linear fits obtained from the peak discharge current (I_P) versus square root of scan rate ($\nu^{1/2}$) for samples ΔLFNP(1.0), ΔLFNP(1.5), and ΔLFNP(2.0) (sample:carbon:binder wt% ratio 80:10:10). Adapted from reference 208.

Constant current tests of these electrodes revealed that Nb-doping improved rate capability up to 1 at% Nb, and made little difference with further substitution, which was consistent with the Randles-Sevcik analysis. The best performing sample ΔLFNP(1.0) displayed a capacity of 110 mA h g^{-1} at 10C (Figure 3.35a), which surpassed capacities generally obtained for $LiFePO_4$ made *via* continuous hydrothermal methods,[193–195] although it was inferior to the V-doped $LiFePO_4$ discussed in Section 3.4.1.3. Electrodes with higher added carbon content (sample:carbon:binder wt% ratio 75:15:10) were fabricated to examine the impact on

overall performance. Interestingly, a reduced variation in performance with Nb content was observed (Figure 3.35b). In this case, the lowest dopant concentration (ΔLFNP(0.01)) was the best of these samples, which implied the additional electrode conductivity provided by the increased carbon nullified the effect of the Nb dopant.

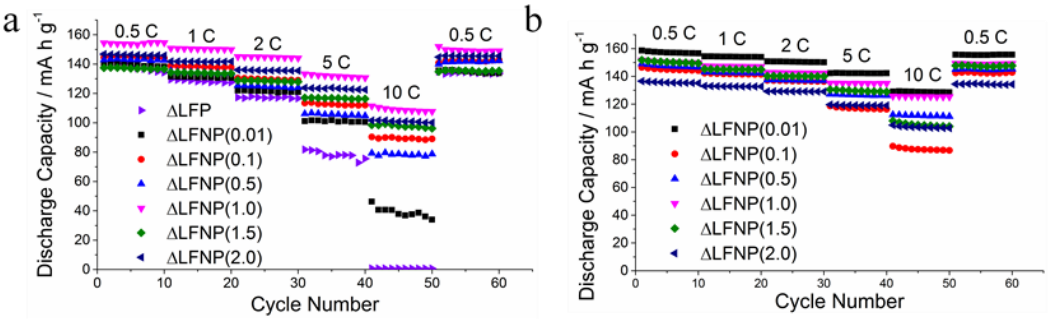

Figure 3.35 - C-rate tests for all electrodes with sample:carbon:binder wt% ratios of a) 80:10:10 (including ΔLFP(1) from Section 3.4.1) and b) 75:15:10. Adapted from reference 208.

The charge/discharge profile of ΔLFNP(1.0) at 0.5C and 10C only showed activity due to the Fe^{2+}/Fe^{3+} couple, and was consistent with the CV analysis (Figure 3.36a). The capacity retention of all samples supported the limited benefit of additional Nb substitution beyond 1 at% Nb for the 80:10:10 sample:carbon:binder ratio electrodes, where the retention of ΔLFNP(1.0), ΔLFNP(1.5), and ΔLFNP(2.0) was approximately equal (Figure 3.36b). In contrast, the electrodes with higher carbon loadings generally displayed higher capacity retentions with increasing C-rate, and a narrower variation between electrodes (Figure 3.36c). Excellent capacity retention (range 96 to 98 %) was also observed in long term stability testing at a 1C charge/discharge rate (range of 100 to 200 cycles) for the 80:10:10 electrodes (Figure 3.36d). This suggested that Nb-doped $LiFePO_4$ is suitable for long-life, high power applications.

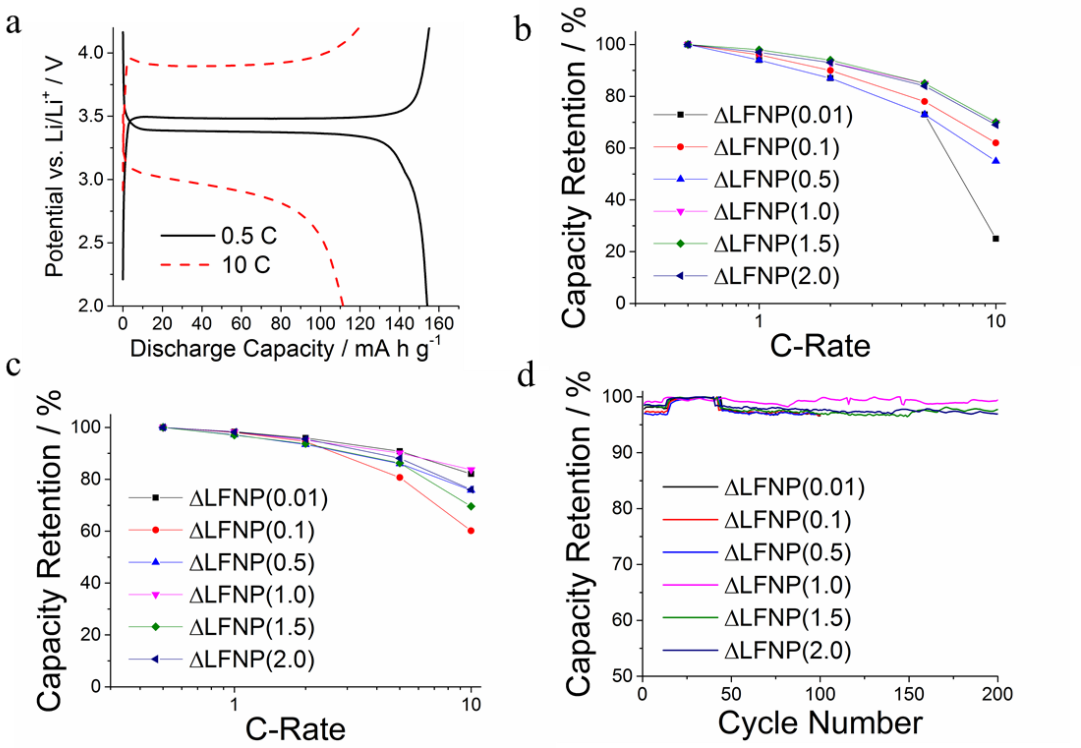

Figure 3.36 - a) A voltage *vs.* capacity plot of ΔLFNP(1.0) (80:10:10 electrode) at 0.5C and 10C. Capacity retention test data for all electrodes with S:C:B wt% ratios of: b) 80:10:10 and c) 75:15:10. 100% capacity was the capacity of each electrode at 0.5 C. d) Capacity retention at a charge and discharge rate of 1C for 80:10:10 electrodes of ΔLFNP(0.01), ΔLFNP(0.1), and ΔLFNP(0.5) for 100 cycles and ΔLFNP(1.0), ΔLFNP(1.5), and ΔLFNP(2.0) for 200 cycles. The capacity retention was relative to the highest capacity recorded during these cycles. Adapted from reference 208.

3.5. Conclusions and Further Work

Nb-doping was found to have a similar effect to V-doping within $LiFePO_4$; increasing the high-rate performance of the material. Results from EDS analysis and XRD were consistent with homogenous doping of Nb within the $LiFePO_4$ structure. An optimal dopant concentration of 1 at% Nb was found; no significant benefit was observed by increasing it above this value. Experiments conducted with additional carbon in the electrode removed the benefit of the Nb dopant, and it is tentatively suggested that the its main influence is to increase the electronic conductivity of the $LiFePO_4$ phase, the effect of which is masked by added carbon.

While this was an interesting case study and proved that dopant systems in $LiFePO_4$ can be made *via* CHFS, the performance of V-doped $LiFePO_4$ was superior to Nb-doped $LiFePO_4$. Therefore, the best-performing V-doped $LiFePO_4$ sample was chosen

for scaled-up synthesis and potential fabrication at the pouch-cell level, and is discussed in the next section.

Possible future work concerning doped $LiFePO_4$ species made *via* CHFS could include looking at a much wider array of dopants (specifically aliovalent dopants). This could identify other substituents which may surpass the performance observed with the V-doped $LiFePO_4$. Furthermore, a large combined synchrotron XRD and EXAFS study could be performed on these materials, and could better establish the doping mechanisms operating in $LiFePO_4$. Combined with the electrochemical characterisation, a much greater understanding of the effects of dopants in the $LiFePO_4$ system could be achieved.

4. Scale-up and Full-Cell development of V-doped $LiFePO_4$

4.1. Aims

This section aims to develop the optimal cathode material from the previous chapter, 5 at% V-doped $LiFePO_4$, and produce a great enough quantity of nanomaterial for testing at pouch-cell level, which typically requires 100 g minimum of active cathode material for preliminary testing. This includes full-cell testing of the material against a silicon anode, which presents additional challenges compared to standard half-cell testing.

4.2. Background

In order to make a functioning cell for a device, full-cell testing is necessary. Rather than charging and discharging the material *vs.* Li metal (half-cell testing), a suitable complimentary anode/cathode must be paired with the cathode/anode in question. This is in large part due to safety concerns regarding the use of an Li anode, which forms dendrites upon repeated cycling and can cause a short circuit.[210] This effectively renders the cell useless, but can also cause fires and explosions. Therefore, alternative anodes (such as graphite) have been developed, which safely intercalate or alloy with Li^+ to prevent dangerous dendrite growth. However, the specific capacity of graphite (372 mA h g^{-1}) is far lower than that of Li metal (3860 mA h g^{-1}), so higher-capacity alternatives are being pursued to enhance the overall storage capability of the cell.

One such example is the Si anode, which possesses a high theoretical capacity of 3579 mA h g^{-1}.[107,211–215] Such a high capacity is achieved as 3.75 equivalents of Li alloys into the Si anode according to the reaction below:

$$4\,[3.75\,Li + Si] \rightarrow Li_{15}Si_4$$

Equation 4.1 – The alloying reaction of Li with Si during lithiation.

However, there are numerous problems observed with this anode with electrochemical cycling. Firstly, there is a very large expansion/contraction with lithiation/delithiation (280 vol%),[102] which can cause microstructural fracturing of the Si particles. This can result in reduced capacity with cycling due to the formation of "dead zones" of inactive Si, and Li isolation within Si particles. In addition, this expansion causes irreversible

lithium loss due to continuous solid-electrolyte interphase (SEI) formation during cycling.[102]

Continuous formation of SEI or oxidation of electrolyte within a full cell will directly lead to loss of capacity.[216,217] This is due to the finite amount of active Li^+ or electrolyte within the cell, which, if it is consumed by such side-reactions, will steadily reduce to the point where the total charge/discharge capacity is affected. These problems can be somewhat overcome by a variety of strategies; water scavengers,[218] electrolyte additives,[219] and electrode coatings can reduce SEI formation and side reactions, thereby extending the lifetime of the full cell. Such additives were employed in this chapter within V-doped $LiFePO_4$ cathode / Si anode full cells.

4.3. Experimental

4.3.1. Synthesis conditions

A large-scale repeat of the 5 at% V-doped sample from Section 3.4.1 was performed, keeping the precursor concentrations and pump flow-rates identical. In precursor pump 2, 0.2375 M $FeSO_4$, 0.0125 M $VOSO_4$, 0.375 M H_3PO_4 and 0.65 M Fructose were fed into the CJM at 200 mL min^{-1}. Likewise, pump 3 provided 0.8625 M LiOH.

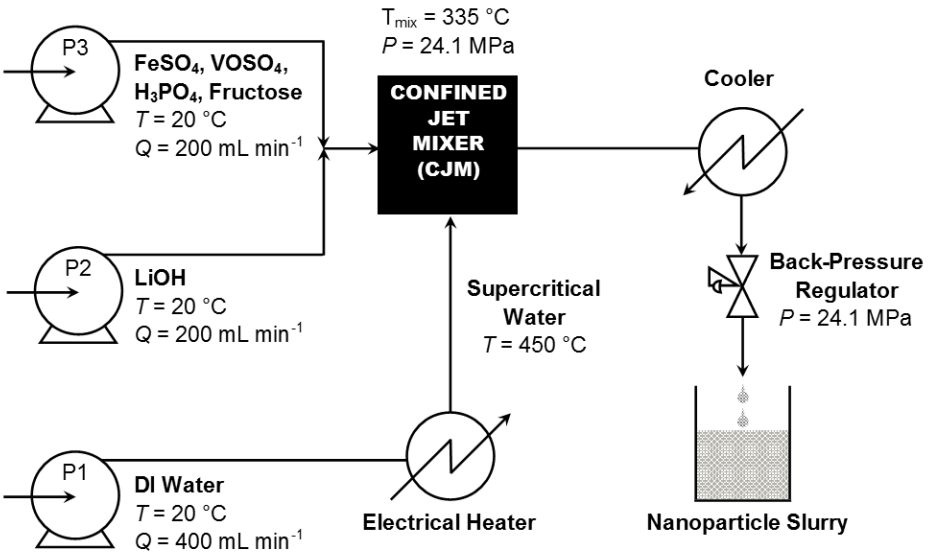

Figure 4.1 – A schematic of the reaction conditions for the scaled-up ΔLFVP(5) synthesis.

4.3.2. Sample Processing and Physical Characterisation

Approximately 90 L of product slurry was obtained from the reaction conditions, which was allowed to settle overnight and the supernatant discarded. The remaining concentrated sludge was concentrated *via* centrifuge (4500 rpm for 10 minutes) into 8 800 mL centrifuge pots, centrifuged, and dispersed in D.I. water 5 times. At this point, significant quantities of product did not settle, so the sample was freeze-dried according to Section 2.1.3.3. The supernatant conductivity was approximately 600 µS m^{-1}. The mass yield of product was 0.50 kg, which corresponded to a molar yield of approximately 50%. The powder was heat-treated according to the procedure in Section 2.1.3.4, producing a black powder. CHN analysis of this powder revealed a carbon-coating of 6.7 wt%.

The heat-treatment carbonisation step produced very large sintered agglomerates which proved difficult to break down. The material was lightly ball milled for 1 h in NMP solvent (sample:solvent mass ratio 1:1) at 400 rpm using a Retsch planetary ball mill (PM-200), which successfully reduced the particle size (D_{90}) from 650 µm to 22 µm.

XRD patterns of the heat-treated, scaled-up sample was collected using set-up **c** in Section 2.1.4.1, using Mo-Kα radiation (λ = 0.709 Å) over the 2θ range 2 – 60° with a step size of 0.5° and step time of 100 s. Rietveld analysis was performed using MAUD software.[132]

4.3.3. Electrode processing

4.3.3.1. Composite anode formulation

The Si-based anodes were prepared according to the following steps. Micron-sized Si (> 99%, Elkem Bremanger) was combined with the binder polyacrylic acid (PAA, Sigma Aldrich) molecular weight = 450 k, y ≥ 99.5%) and acetylene black (Alfa Aesar, 99.9%) and few-layer graphene (FLG, XG Sciences M Grade, > 99.9%).

Firstly, PAA (24 g) was mixed with 176 g of D.I. water (giving a 12 wt% PAA solution) in a 500 mL Nalgene® beaker. This slurry was mixed with a Primix Homodisper (Model 2.5, 500 rpm, 120 mins), and was subsequently stirred (Primix

medium shear impeller blade, 250 rpm, 120 mins) to give a clear solution. Na_2CO_3 was added to the solution (12.4 g, Fisher Chemical, > 99.5 %) and hand-stirred to dissolve. Na^+ partially neutralised the PAA carboxyl groups to elongate the polymer configuration and improve the binding interaction. The resultant Na-PAA solution was allowed to rest overnight to produce a clear solution.

A mixture of conductive carbons was generated by mixing FLG (10.0 g), acetylene black (5.0 g), and D.I water (136.4 g). The suspension was stirred using the Primix Homodisperser (500 rpm), and was subsequently ultrasonicated using a Hielscher sonic probe (Model UP400S), employing 0.5 s sonication cycles, 60% amplitude for two 7 min periods.

Si powder (20.0 g) was combined with the carbon mix described above (46.45 g) and stirred using the Primix Homodisperser (1000 rpm for 30 minutes followed by 500 rpm for 30 minutes). This slurry was ultrasonicated to break down agglomerates, and subsequently 33.33 g of partially neutralized Na-PAA solution (described above) was added to form a composite slurry. This slurry was dispersed (Primix Homodisper Model 2.5, 30 mins) and 30 mL aliquots were further dispersed according to the following protocol: two slower dispersions (10 m s^{-1}, 30 s) followed by a more intense one (25 m s^{-1}, 30 s) in a Filmix mixing vessel.

The dispersed slurry was degassed in a glove-box antechamber under vacuum, and cast onto 10 μm thick Cu foil (Oak Mitsui), using a doctor blade on an RK Instruments K Coating Proofer. The resultant spread was dried on a hot plate set to 80 °C, and was vacuum dried (7 mBar, 12 h, 70 °C). Electrodes were therefore generated with compositional ratio 70:14:16 (Silicon: Na-PAA: carbon additives). The anodes were fabricated by Dr. Melanie Loveridge (WMG).

4.3.3.2. Cathode Formulation

The cathode was formulated with a 80:10:10 wt % ratio of V-LFP:PVDF:Carbon from the scaled-up ΔLFVP(5) sample with acetylene black (99.9%, Timcal C65) and PVDF (Grade 5130, Solvay) dissolved in NMP (Sigma Aldrich). The cathode was formulated thus:

144 g ΔLFVP(5) and 16.6 g acetylene black were first mixed in a HIVIS high torque mixer (10 rpm, 10 mins). Meanwhile, to produce 8 wt% binder solution, 80 g PVDF powder was dissolved in 920 g NMP with T2F Turbula mixing apparatus (WAB, Germany) for 12 hours. 208.1 g of the PDVF solution was added to the combined powders, which was mixed further (15 rpm, 30 mins). A further 50 g of NMP was added to decrease the solution viscosity, and was mixed further (15 rpm, 35 mins and 100 rpm, 30 mins). 70 g NMP was added and stirred under vacuum (100 rpm, 90 mins). The resultant slurry was high-shear mixed (8 m s^{-1}, 30 s, FilmixTM Model 56–50 Disperser), which had an overall solid content of 35 wt%.

The slurry was cast on Al foil using a reel-to-reel coater (MEGTEC) with increasing comma bar blade gaps in the range 50–240 μm. The coating production rate was 0.75 m min^{-1}, and the coating was dried using a three-zone heater with temperatures of 100, 120 and 110 °C. This produced coating densities in the range 24 – 95 g m^{-2}.

4.3.4. Coin Cell Preparation and Electrochemical Characterisation

4.3.4.1. Two-electrode cells

V-doped $LiFePO_4$ half-cell tests were performed in 2032-type coin cells as described in Section 2.1.5.2. Specific current tests in the range 0.05 and 9 A g^{-1} were performed between voltage limits of 4.3 V to 2.0 V vs. Li/Li^+, and a C-rate test (C/2) was performed on selected half-cells using a GAMRY battery tester (INTERFACE1000, GAMRY, Scientific & Medical Products Ltd., Cheshire, UK).

4.3.4.2. Three-electrode Cells

Stainless steel Swagelok® hardware and perfluoroalkoxy (PFA) ferrules were assembled to form the three-electrode cells. A ½" T-piece union with a plastic insert (MicroPlas Mouldings Ltd) was used as the cell body (Figure 4.2). Two 0.5" stainless steel plungers were employed as anode and cathode supports, which were orientated to face each other. The Si anode, V-doped $LiFePO_4$ cathode and separators (Whatman GFA) were cut into 12 mm diameter discs using a punch (MicroPlas Mouldings Ltd). The discs were selected so that the capacity of the anode was in ~10% excess of the cathode capacity. The anode/cathode discs were placed on the ends of the opposing supports and aligned in the centre of the T-union. 60 μL of electrolyte was dispensed

with a precision micropipette into the body of the T-union. The electrolyte employed was LP30, 1 M $LiPF_6$ in 1:1 ethylene carbonate (EC): dimethyl carbonate (DMC), with 10 wt% fluoroethylene carbonate (FEC) and 5 wt% vinylidene carbonate (VC) additives. Li foil (12 mm) and an additional separator disc were attached to the end of the top plunger, and inserted until in contact with the separator between the anode/cathode. All nuts and ferrules were fitted and hand tightened. These 3-electrode cells were assembled and tested by Dr. Melanie Loveridge (Warwick Manufacturing Group, WMG).

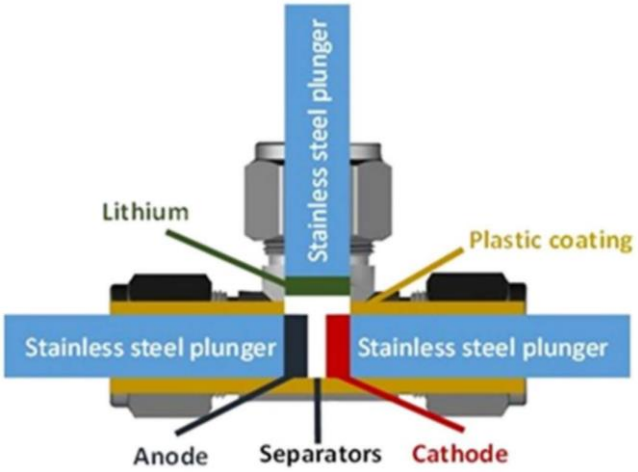

Figure 4.2 – A schematic of the 3-electrode cell assembled from Swagelok components.

4.3.4.3. Cycling procedure

A Biologic VMP3 multi-potentiostat unit was connected to the 3-electrode cell and used to make electrochemical measurements. The 3-electrode cell was charged at a C-rate of C/20 (relative to Si content), and was subsequently cycled at C/5. The charge limit was a cathodic potential 3.95 V vs. Li/Li^+, and the discharge limit was an anodic potential of 1.50 V vs. Li/Li^+.

4.4. Results and Discussion

XRD analysis confirmed the large-scale V-doped $LiFePO_4$ sample possessed the pure olivine structure (Figure 4.3), with no additional peaks present. An overlay of the large-scale product with the initial product (Section 3.4.1.2) diffraction pattern shows good consistency between samples, and is reflected in the relatively similar lattice parameters found from Rietveld refinement (Table 4.1).

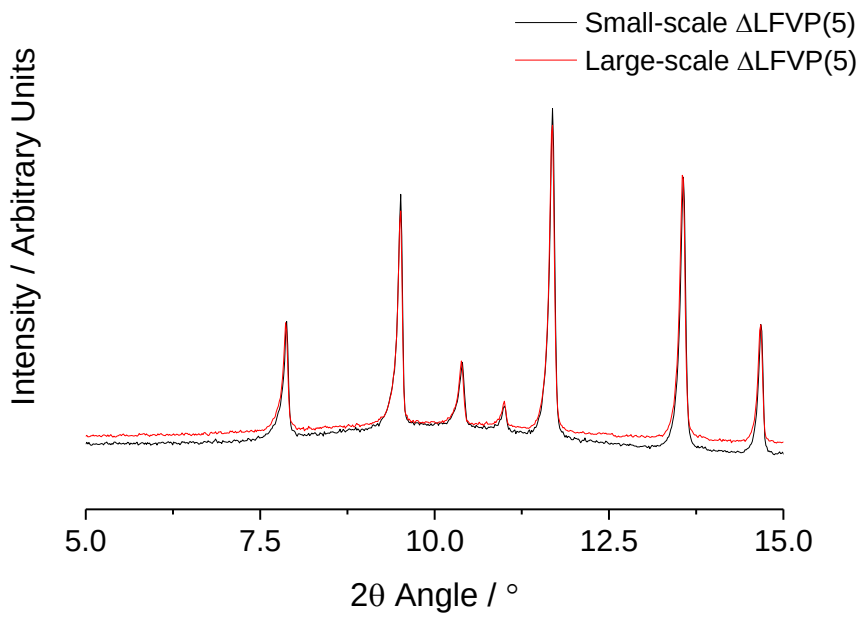

Figure 4.3 – Comparison of the XRD patterns (Mo-Kα radiation) of the small-scale and large-scale ΔLFVP(5) sample.

Table 4.1 – Comparison of the lattice parameters for the small-scale and large-scale ΔLFVP(5) samples from Rietveld refinement.

Sample	*a* / Å	*b* / Å	*c* / Å	*V* / Å^3	R_{wp}	χ^2
Small-scale	10.32068(15)	6.00194(9)	4.69686(7)	290.943(13)	4.75	1.33
Large-scale	10.32766(10)	6.00442(6)	4.69633(5)	291.227(9)	3.75	2.17

A combination of CHN analysis and TEM also confirmed a carbon coating was present (6.64 wt%) where the carbon was found as a surface layer approximately 5 nm thick (Figure 4.4), although there was some evidence of additional small carbonaceous particles.

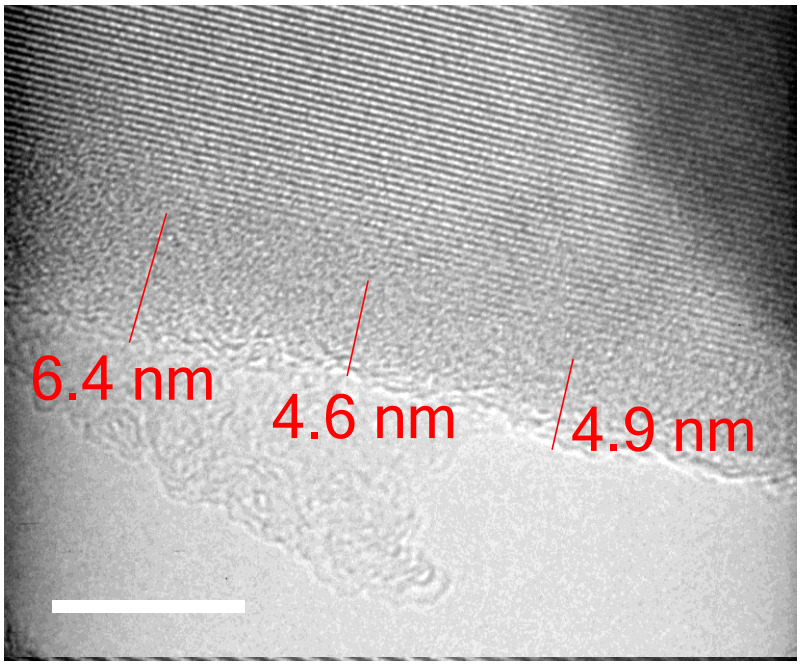

Figure 4.4 – A TEM microscopy image, showing the presence of a uniform carbon coating on the large-scale ΔLFVP(5) particle surface. Adapted from reference 220.

FE-SEM micrographs of the large-scale sample were used to compare particle size and morphology with the original small sample, and indeed they tended to form agglomerated networks of approximately 100 – 300 nm size particles as was observed previously (Figure 4.5 and Section 3.4.1.2). Again, there was significant variation of size and morphology within the sample, with some evidence of larger, μm-scale particles.

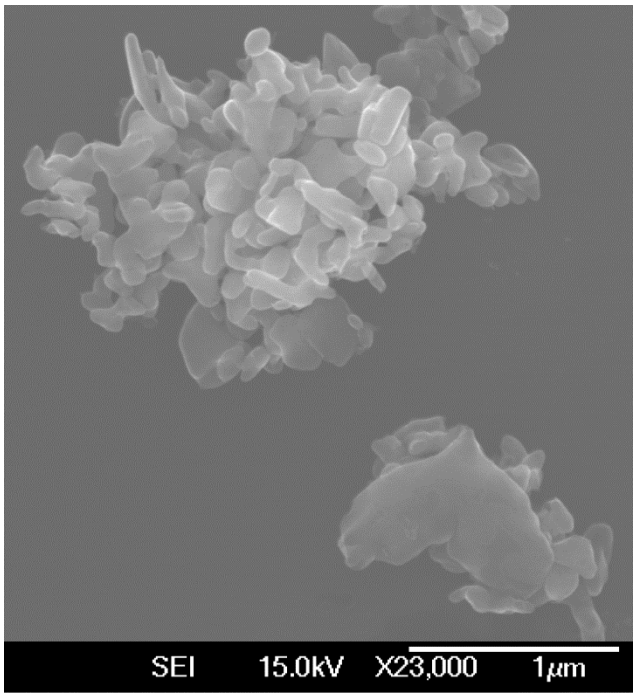

Figure 4.5 – An SEM images of the large-scale ΔLFVP(5) (which had been heat-treated at 700 °C for 3 hours). Adapted from reference 220.

The rate performance of the scaled-up ΔLFVP(5) sample was assessed using half-cell C-rate tests (Figure 4.6). The variable coating thickness provided by the reel-to-reel coater enabled the comparison of electrodes of different mass loading, ranging from 1.65 g cm^{-2} to 5.9 g cm^{-2}. The capacities observed for the electrodes decreased with increasing active material loading, and was more pronounced as the C-rates increased. This was most likely a result of diffusion-limited mass transfer of Li^+ ions within the electrode, which would limit performance with thicker electrodes. As observed previously, the discharge capacity of the cells fell from 158 mA h g^{-1} to < 130 mA h g^{-1} for C-rates in the range 0.3C to 8.8C. Extremely high capacity retention was observed, with the best performing electrode still delivering 125 mA h g^{-1} at a high C-rate of 8.8C, which is similar to the best performance seen in Section 3.4.1.3 (130 mA h g^{-1} at 10C), and suggests the beneficial electrochemical effect of the vanadium dopant is reproducible.

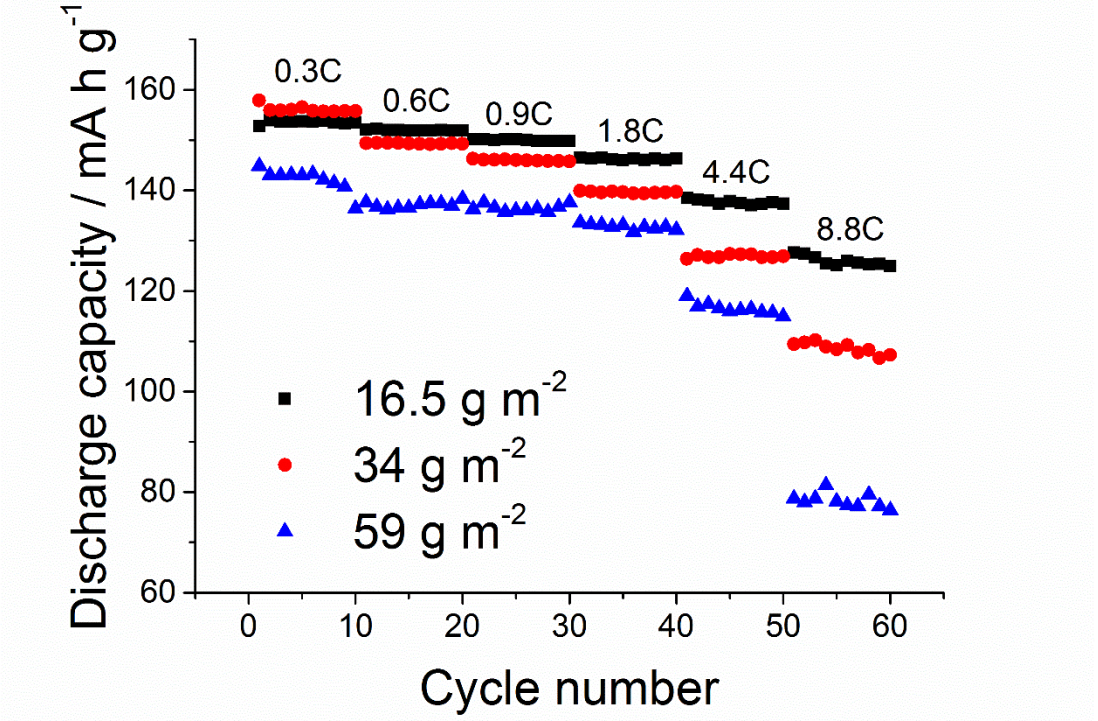

Figure 4.6 – Half-cell cycling tests of the large-scale ΔLFVP(5) electrodes in a half cell, comparing electrodes of different thicknesses. Adapted from reference 220.

However, in a full cell, the coulombic efficiency (C.E) of the charge/discharge reaction should be as close to 100% as possible. To achieve > 65% capacity retention over 1000 charge and discharge cycles, a C.E. of > 99.96% is required, and therefore C.E. is an important metric in full cell assessment. In a half cell, a C.E. < 100% does not impact cell performance as the oversized Li anode provides replacement lithium. A GAMRY battery tester (which provides a more accurate measure of C.E.) was employed to cycle a half-cell of the large-scale ΔLFVP(5) electrode (Figure 4.7). It can be seen that the C.E. is significantly below 100%, and only asymptotes to ~98.5% after multiple cycles. The effect of coulombic efficiency was observed in the full cell tests (Figure 4.8); the cell capacity substantially decreased (20% capacity retention over 50 cycles). Full cells were assembled and tested by Dr. Melanie Loveridge (WMG). To achieve good full-cell performance, the coulombic efficiency of the ΔLFVP(5) material must be increased.

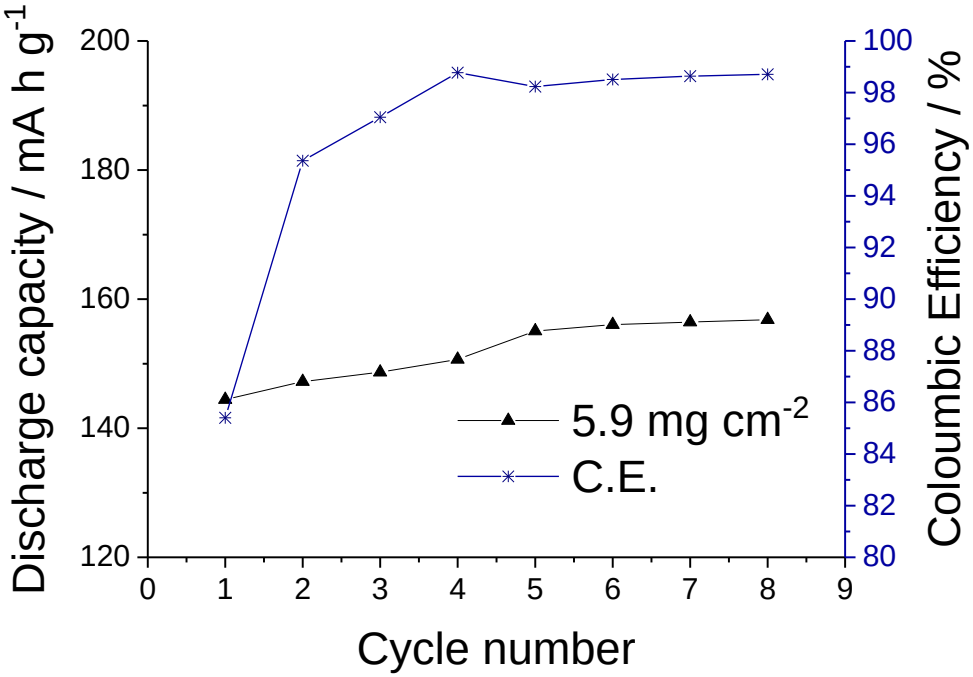

Figure 4.7 – Capacity retention and coulombic efficiency vs. cycle number for a large-scale ΔLFVP(5) half-cell made using a GAMRY battery tester.

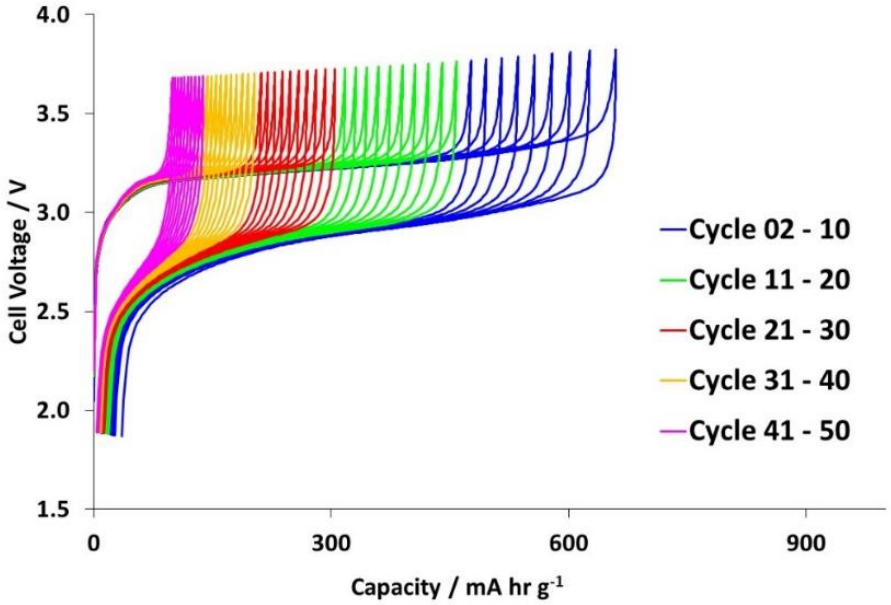

Figure 4.8 – Voltage vs. capacity plots for a large-scale ΔLFVP(5) – Si three electrode full-cell. Adapted from reference 220.

4.5. Conclusions and Further Work

The synthesis of ΔLFVP(5) was successfully reproduced, and displayed almost identical half-cell electrochemical performance after scaled-up electrode manufacture.

However, full-cell assessment of large-scale ΔLFVP(5) revealed rapid capacity decay. The most likely reason for the observed loss in capacity was the inferior cathodic coulombic efficiency, and may be a result of side-reactions occurring on the cathode surface. It is suggested that the nanoparticulate nature of the sample was responsible for the electrolyte consumption (due to the higher surface area of the cathode), or possibly incomplete decomposition of the carbon coating, resulting in active species on the particle surface which degraded the electrolyte. Therefore, it is suggested that further surface modifications should be explored for nanosized $LiFePO_4$, i.e. changing the nature of the surface carbon coating, to provide a stable electrode surface which prevents side reactions. This could be achieved by heat-treatments at higher temperatures, or using longer heat-treatment times, to achieve a less reactive carbon coating. Another method for generating a different carbon coating could be to use a different carbonaceous precursor, such as sucrose.

It is also suggested that further exploration of electrolyte additives may improve this coulombic efficiency by minimising detrimental side-reactions during cycling. This would be crucial for enabling full-cells of other nanosized electrode materials made *via* CHFS, where low coulombic efficiencies are commonly observed .[221,222] If this can be achieved, V-doped $LiFePO_4$ made *via* CHFS could be scaled-up into pouch cells, and therefore this should be the focus of future research.

5. Investigating Li^+ Diffusion in Doped $LiFePO_4$ with Muon Spectroscopy

In Chapter 3, the beneficial impact of V- and Nb-doping within $LiFePO_4$ was established. However, beyond observing an increase in delithiation/lithiation kinetics, the data obtained was insufficient to unambiguously determine how the dopant improved performance. The two most probable possibilities are generation of Li^+ vacancies (and stabilisation of the Li_xFePO_4 solid-solution), and increased electronic conductivity. Muon Spectroscopy was performed in this chapter to investigate the intrinsic Li^+ diffusion within the pure and doped $LiFePO_4$ materials to elucidate the improved performance.

5.1. Background

Muons are elementary particles (belonging to the lepton family) which are in many ways analogous to electrons; they possess a charge of -1 e and spin ½. However, they are much heavier than electrons (~$207m_e$),[223] and are unstable; they undergo radioactive decay to form an electron, a muon neutrino and an electron antineutrino (Equation 5.1), where the muon has a mean lifetime of 22 μs.[224] In an analogous manner, antimuons decay to form positrons with an electron neutrino and an antimuon neutrino.[225]

$$\text{a.}\quad \mu^- \rightarrow e^- + \bar{\nu}_e + \nu_\mu$$
$$\text{b.}\quad \bar{\mu}^+ \rightarrow e^+ + \bar{\nu}_\mu + \nu_e$$

Equation 5.1 – a) Muon decay and b) antimuon decay.

Within muon spectroscopy, the spin and short life-time of the muon is exploited to investigate numerous properties of solid-state materials. When an antimuon beam interacts with a sample, the antimuons are preferentially implanted on sites of high electronegativity, i.e. they typically form a formal bond with oxyanions (μ^+-O^{2-}), which prevents μ^+ diffusion.[226,227] This effectively "embeds" the antimuons in the sample, where their nuclear spin interacts with local magnetic moments until they decay. N.B.: "Antimuons" are referred to as "muons" throughout the rest of this chapter in line with the convention in this area. Because the muon decays into three particles, the direction of emission of the daughter positron is the same as the nuclear spin direction of the parent muon at the time of decay. Therefore, the positron emission

(which can be easily detected) can be used to infer muon spin. When the muons are implanted in the sample, their spin is polarised antiparallel to the direction of the muon beam, which is a direct result of the method of generation. If their spins are not affected by the sample, they will decay to form positrons which are primarily detected by the back detector, B (Figure 5.1a) according to the expected angular distribution of emitted positrons given the initial muon spin (Figure 5.1b).

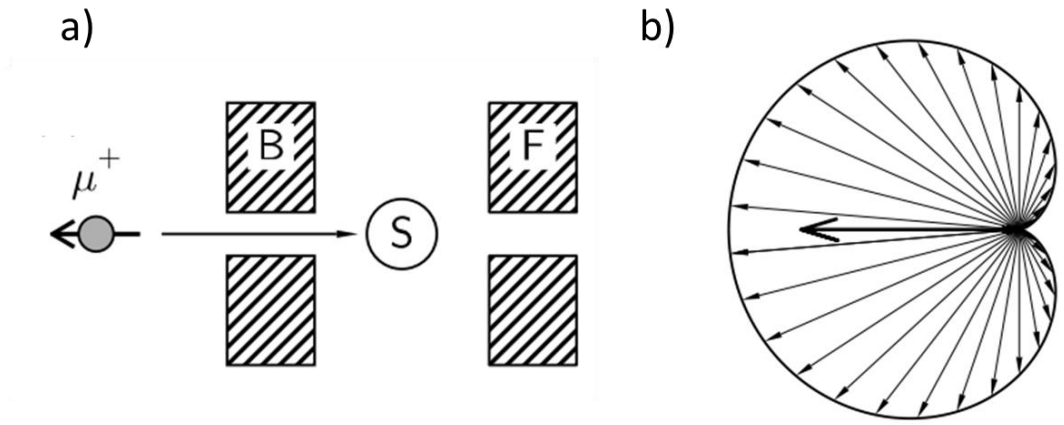

Figure 5.1 – a) a schematic of muon implantation in a sample, with the spin antiparallel to the direction of insertion, and b) the angular distribution of emitted positrons, with the muon spin direction indicated with the largest arrow. Adapted with permission from "Blundell, S. J. Spin-polarized muons in condensed matter physics. *Contemp. Phys.* **40,** 175–192 (1999).". Copyright 2010 Taylor & Francis.

However, the local nuclear magnetic fields contained within the sample (e.g. the unpaired electrons of Fe^{2+} in $LiFePO_4$) cause the muon spins to precess. If the internal magnetic field (B) is assumed constant (and transverse), the relative proportion of positrons detected by the forwards and backwards detectors follows a sinusoidal relationship as a function of time (Figure 5.2b, known as the asymmetry function). The decay rate of muons into positrons is exponential with time, therefore the number of positrons detected by forwards, $N_F(t)$, and backwards, $N_B(t)$, detectors varies according to Figure 5.2a.

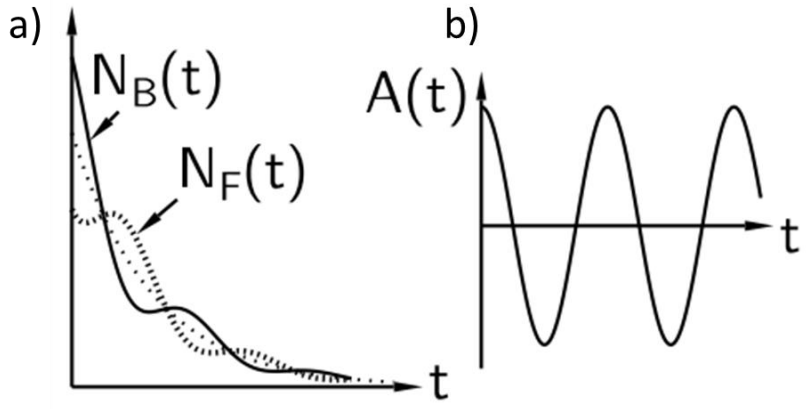

Figure 5.2 – a) the number of positrons detected by the forwards and backwards detectors, $N_B(t)$ and $N_F(t)$ respectively, in a uniform transverse magnetic field. b) the asymmetry function, A(t). Adapted with permission from "Blundell, S. J. Spin-polarized muons in condensed matter physics. *Contemp. Phys.* **40,** 175–192 (1999).". Copyright 2010 Taylor & Francis.

However, in a typical inorganic solid the magnetic field is rarely homogenous. Indeed, there is likely to be a range of local field strengths and directions, and in a powder sample the individual crystallites will be randomly orientated with respect to the initial muon spin direction (assuming no preferred orientation effects). If a muon implants in a site with magnetic field B and angle θ between its spin and the field, the normalised positron decay asymmetry G(t) (Equation 5.2a) will vary according to Equation 5.2b. If the orientation of the magnetic field is random, the average of this over all directions yields Equation 5.2c. Finally, if the local magnetic field strength distribution is assumed to be Gaussian with a mean of zero and a standard deviation of Δ/γ_μ, where Δ is the local field distribution and γ_μ is the gyromagnetic ratio of the muon, this yields Equation 5.2d. Finally, the average of this function over the multiple magnetic field strengths present in the sample (Figure 5.3a) yields the Kubo-Toyabe function, which has a characteristic form shown in Figure 5.3b.

$$\text{a) } G(t) = A(t)/A_{max}$$

$$\text{b) } G(t) = \cos^2\theta + \sin^2\theta\cos(\gamma_\mu Bt)$$

$$\text{c) } G(t) = {}^1/_3 + {}^2/_3\cos(\gamma_\mu Bt)$$

$$\text{d) } G(t) = {}^1/_3 + {}^2/_3\, e^{-\Delta^2 t^2/2}(1 - \Delta^2 t^2)$$

Equation 5.2 – a) the normalised asymmetry function in terms of the asymmetry function A(t) and the maximum observed asymmetry A_{max}, b) the normalised positron asymmetry function, G(t), c) G(t) averaged over all directions and d) G(t) assuming a Gaussian distribution of local fields.

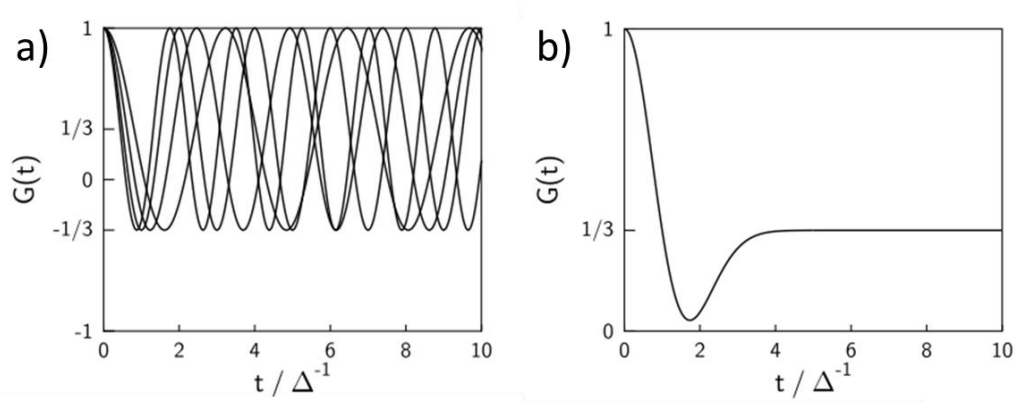

Figure 5.3 – a) The asymmetry function G(t) as a function of time for different values of local magnetic field, B, and b) the averaging of the terms from a) to yield the Kubo-Toyabe function. Adapted with permission from "Blundell, S. J. Spin-polarized muons in condensed matter physics. *Contemp. Phys.* **40,** 175–192 (1999).". Copyright 2010 Taylor & Francis.

However, in a sample where diffusion is possible (such as Li^+ diffusion or μ^+ diffusion), this will cause similar dephasing which can also be described by the dynamic Kubo-Toyabe function. By applying various external longitudinal fields, this modifies the overall Kubo-Toyabe function as shown in Figure 5.4, and allows the static internal magnetic field and the dynamic diffusion effects to be separated, as their respective Kubo-Toyabe functions possess very different behaviours under an applied field.[228]

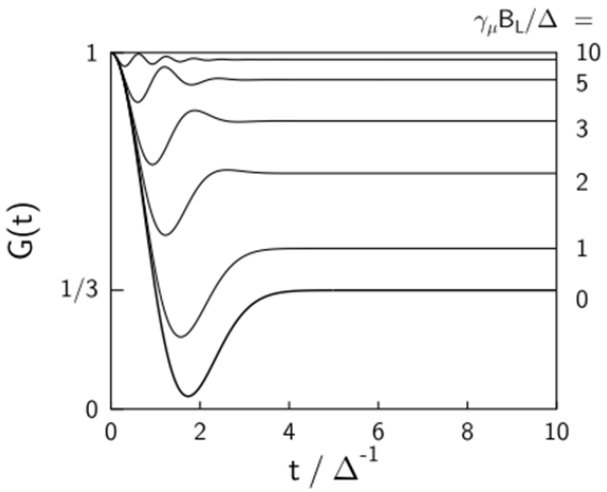

Figure 5.4 – The Kubo-Toyabe function with different applied longitudinal magnetic fields. Adapted with permission from "Blundell, S. J. Spin-polarized muons in condensed matter physics. *Contemp. Phys.* **40,** 175–192 (1999).". Copyright 2010 Taylor & Francis.

Therefore, Li^+ diffusion adjacent to an embedded muon will perturb its spin which can be described by the dynamic Kubo-Toyabe function. In practice, Keren's analytic generalization of the Abragam function (which combines the dynamic Kubo-Toyabe function with an additional relaxation term) provides a better fit to experimentally measured $LiFePO_4$ samples, and is used within this chapter. This function is therefore able to decouple the effect of the local nuclear environment from those caused by Li^+ or μ^+ diffusion by comparing depolarisation at multiple longitudinal fields, and the Li^+ hopping rate can be extracted (assuming localisation of μ^+ on oxyanions). This method has successfully calculated the Li-ion diffusion coefficients in $LiCoO_2$,[226] bulk $LiFePO_4$,[229–231] and nano-$LiFePO_4$.[232]

Indeed, muon spectroscopy (μSR) is particularly useful for investigating Li^+ diffusion within $LiFePO_4$. Sugiyama *et al.* established that Muon Spectroscopy probes the self-diffusion of Li^+ within the host lattices of the battery materials – there are inevitably defects in the material (e.g. Schottkey defects) which will give a concentration of Li^+ vacancies, which adjacent Li^+ can diffuse into, even within a "fully lithiated" material.[230] No applied potential driving force is required in such a case, which is in contrast to other techniques, such as impedance spectroscopy.

The diffusion coefficient D_{Li} has been difficult to measure experimentally due to the two-phase lithiation/reaction mechanism in $LiFePO_4$. Experimental values range from 10^{-16} to 10^{-7} cm^2 s^{-1},[147,164,233–236] whereas computational studies are in much closer

agreement (E_a values of 270-550 meV).[153,154] Muon spectroscopy has successfully obtained consistent D_{Li} values which reside within the experimental range, but are also closely match the computed values ($3.6 \times 10^{-10} – 6.3 \times 10^{-10}$ cm^2 s^{-1}, corresponding to E_a ~ 100 meV).

5.2. Experimental Details of Muon Spectroscopy

The μSR experiments were conducted at the ISIS pulsed muon and neutron source on the EMU instrument.[237] The data were analysed using the Windows Muon Data Analysis (WIMDA) program.[238] Sample ΔLFP1 was selected as a control sample, and doped samples ΔLFVP(5) and ΔLFNP(1.0) were selected for analysis, as they were the optimal samples within each doping study. These samples were prepared for analysis by transferring approximately 1 g into Ti cavities with a Ti foil window. Ti was chosen as a sample holder material as Ti interacted very weakly with muons, and therefore gave a simple background feature which could be easily subtracted in the analysis.

Spin-polarised positive muons were implanted into the ΔLFP1, ΔLFNP(1.0) and ΔLFVP(5) samples, where they occupied interstitial sites for a mean lifetime of 2.2 μs before decay. The muon spin direction was affected by the local magnetic field in the implantation site. The asymmetry in the count rate of the positrons, A(t), was measured in two arrays of detectors on opposite sides of the sample. In order to probe the lithium diffusion behaviour in the three samples, measurements were collected in 20 K steps in the temperature ranges 100 – 140 K and 220 – 400 K, and in 10 K steps in the temperature range 150 – 210 K for all samples. At each temperature, multiple magnetic field measurements were made. The Li^+ diffusion was investigated in this study with μSR with zero applied field (ZF) and varying strengths of applied longitudinal field (LF) at 5, 10 and 20 G. Representative muon decay asymmetry spectra at 290 K for sample LFP at 0 and 20 G are shown in Figure 5.5.

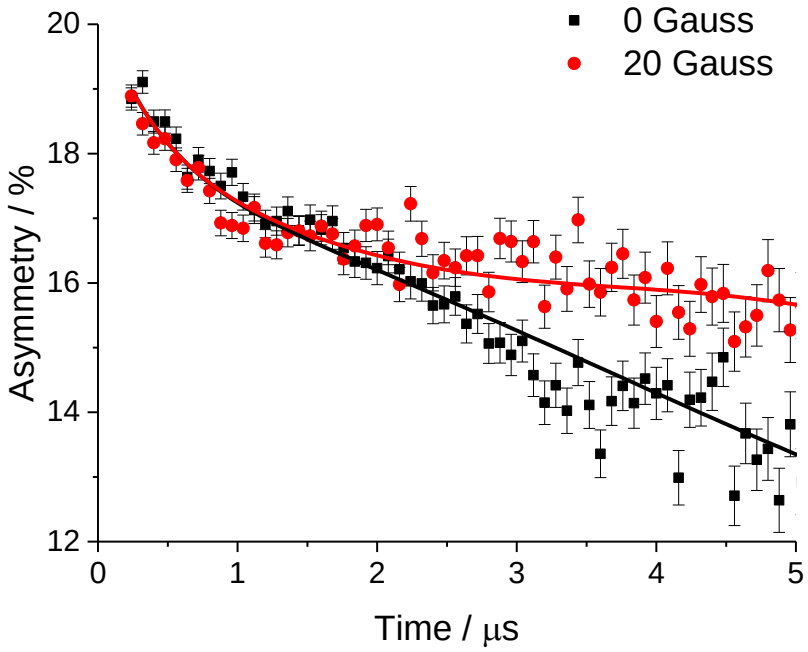

Figure 5.5 – Representative muon decay asymmetry, showing the raw data with the fit overlaid, as a function of time at various magnetic fields.

The spectra arose from a combination of a rapid interaction with the paramagnetic iron moments, and a slower interaction with the ^6Li, ^7Li and ^{31}P nuclear magnetic moments. This allowed Li^+ diffusion to be extracted in a similar manner to previous μSR studies of $LiFePO_4$.[231,232] The data sets were fitted using four different parameters. Firstly, an exponential relaxing function, accounting for the rapid interaction with iron electronic magnetic moments. Secondly, a baseline asymmetry, accounting for weak interactions with Ti and C present in the sample holder and sample, respectively. Thirdly, Keren's analytic generalization of the Abragam function was applied, which has previously been altered to describe fluctuations due to Li^+ or μ^+ diffusion (assuming a Gaussian distribution of local fields).[231] This function was chosen due to the increased relative speed of computation of the Keren function compared to the Kubo-Toyabe function used in previous studies.[229] Finally, an additional exponentially decaying function was added, to account for interactions with minor ferric impurities. By fitting with these parameters, the muon fluctuation rate (ν_{Li}) due to Li^+ diffusion and the local field distribution (Δ), could be extracted. Errors in the values extracted were also estimated by the fitting software.

5.3. Results and Discussion

The behaviour of Δ was similar to that reported previously for $LiFePO_4$, i.e. a steady decrease with increasing temperature, although the values for Δ were consistently lower for the doped samples (Figure 5.6). The reduction in Δ seen in the doped samples cannot be definitively attributed, but could originate from an altered occupation of muon stopping sites or increased Li vacancies.

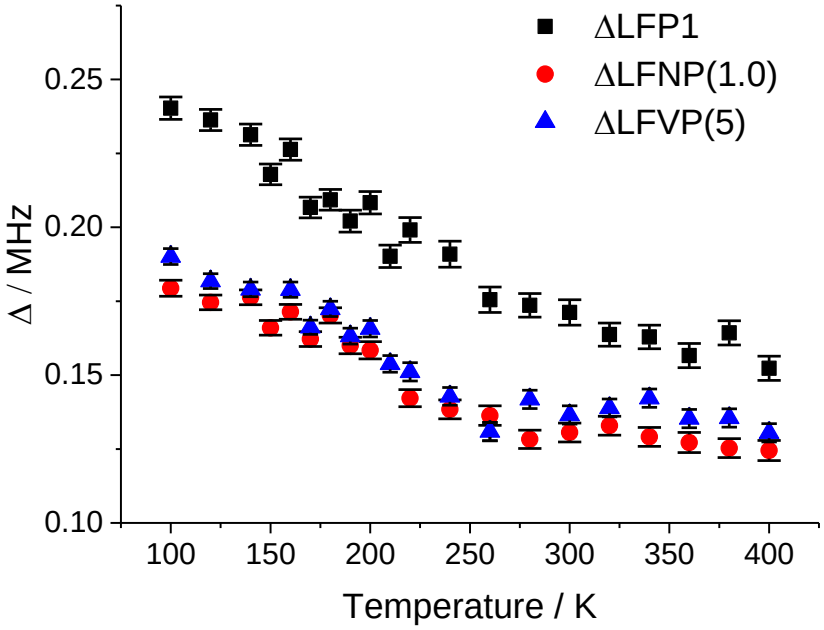

Figure 5.6 – The local field distribution (with error bars) as a function of temperature for samples ΔLFP1, ΔLFNP(1.0) and ΔLFVP(5).

All samples showed a characteristic increase and then decrease in ν_{Li} with temperature, although the magnitude of ν_{Li} was about 10% of that reported in the literature for $LiFePO_4$ samples previously (Figure 4).[230–232] This may have been due to the significant embedding of muons in the carbon shell, which would have detracted from the overall measured diffusion rate but would not contribute to the observed fluctuation rate. For ΔLFP1 and ΔLFNP(1.0), an increase in ν_{Li} with increasing T in the range *ca.* 180 – 250 K and a decrease thereafter was observed (Figure 4a-b). However, ΔLFVP(5) exhibited a marked difference in behaviour; a rapid increase of ν_{Li} in the range 170-210 K, followed by a rapid decay above 210 K to a lower value of ν_{Li} (0.03 MHz, Figure 4c). This implied Li^+ diffusion was too rapid to affect the muon lifetime above this temperature, as has been previously noted.[231]

As Li^+ diffusion in $LiFePO_4$ has been shown to occur exclusively along the b-axis,[157] the hopping length is approximately $b/2$. D_{Li} can be estimated from $b^2\nu_{Li}/4$, and extrapolating ν_{Li} against 1/T afforded a value for the Li-ion diffusion coefficient at room temperature (Figure 5.8). Diffusion coefficients of 1.5×10^{-10}, 2.1×10^{-10} and 2.3×10^{-10} $cm^2\ s^{-1}$ were estimated for ΔLFP1, ΔLFNP(1) and ΔLFVP(5), respectively (Table 5.1). However, the error in this estimation was high due to the weak overall signal, such that μSR could not differentiate the room temperature diffusion coefficients of these samples, although the diffusion coefficient values were consistent with those obtained by μSR for $LiFePO_4$ previously.[229,231,232] The activation energies of Li^+ diffusion (calculated from the gradient of diffusion coefficient against 1/T) were also consistent with previous analyses; E_a was in the range 70 – 100 meV for all samples.[229,231,232] However, the relative errors were too large quantitatively differentiate the three samples.

Table 5.1 – The calculated diffusion coefficients and gradients from μSR.

Sample	D_{Li} @ 300 K / $cm^2\ s^{-1}$	E_a / meV
ΔLFP1	$1.8 \pm 2 \times 10^{-10}$	70 ± 10
ΔLFNP(1)	$2.1 \pm 20 \times 10^{-10}$	100 ± 18
ΔLFVP(5)	$2.3 \pm 6 \times 10^{-10}$	100 ± 30

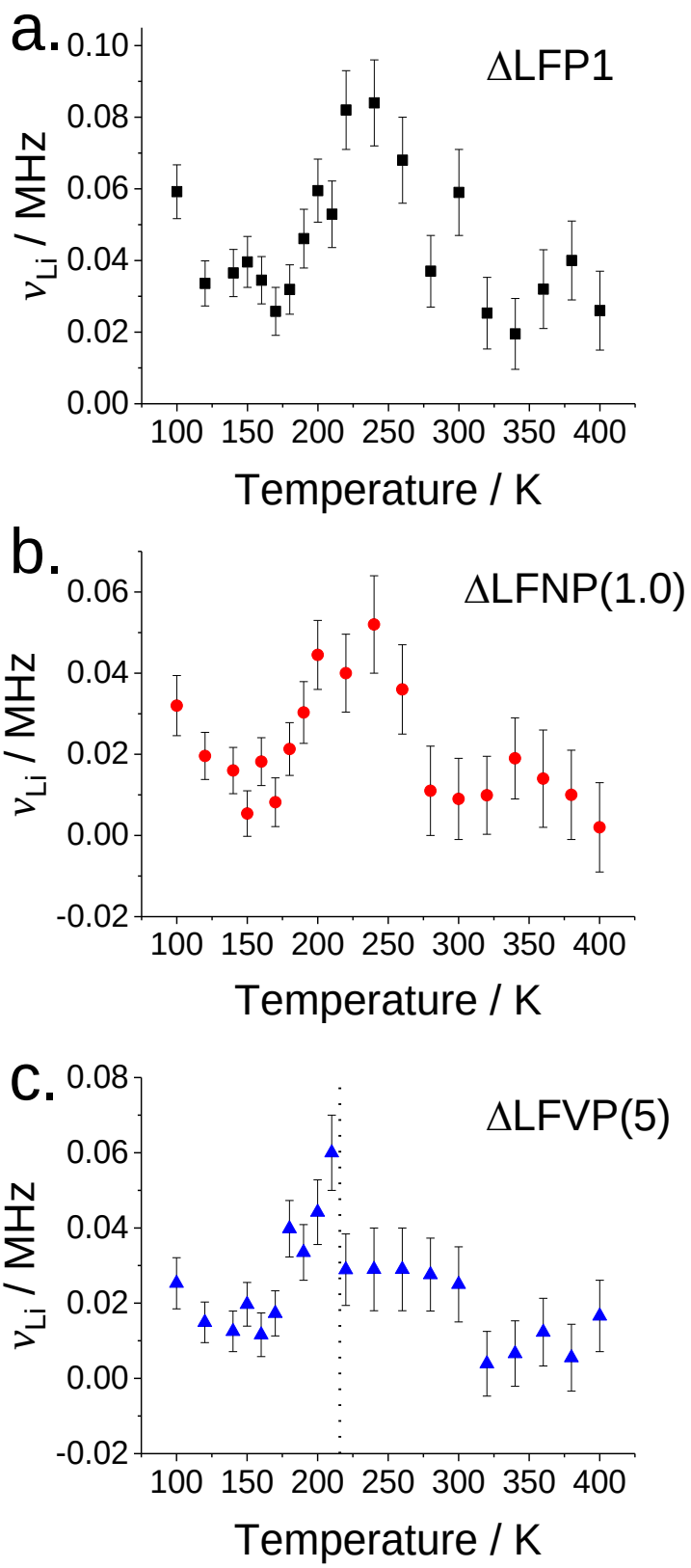

Figure 5.7 – Plots of muon fluctuation rates ν_{Li} vs Temperature for a) ΔLFP1, b) ΔLFNP(1.0) and c) ΔLFVP(5).

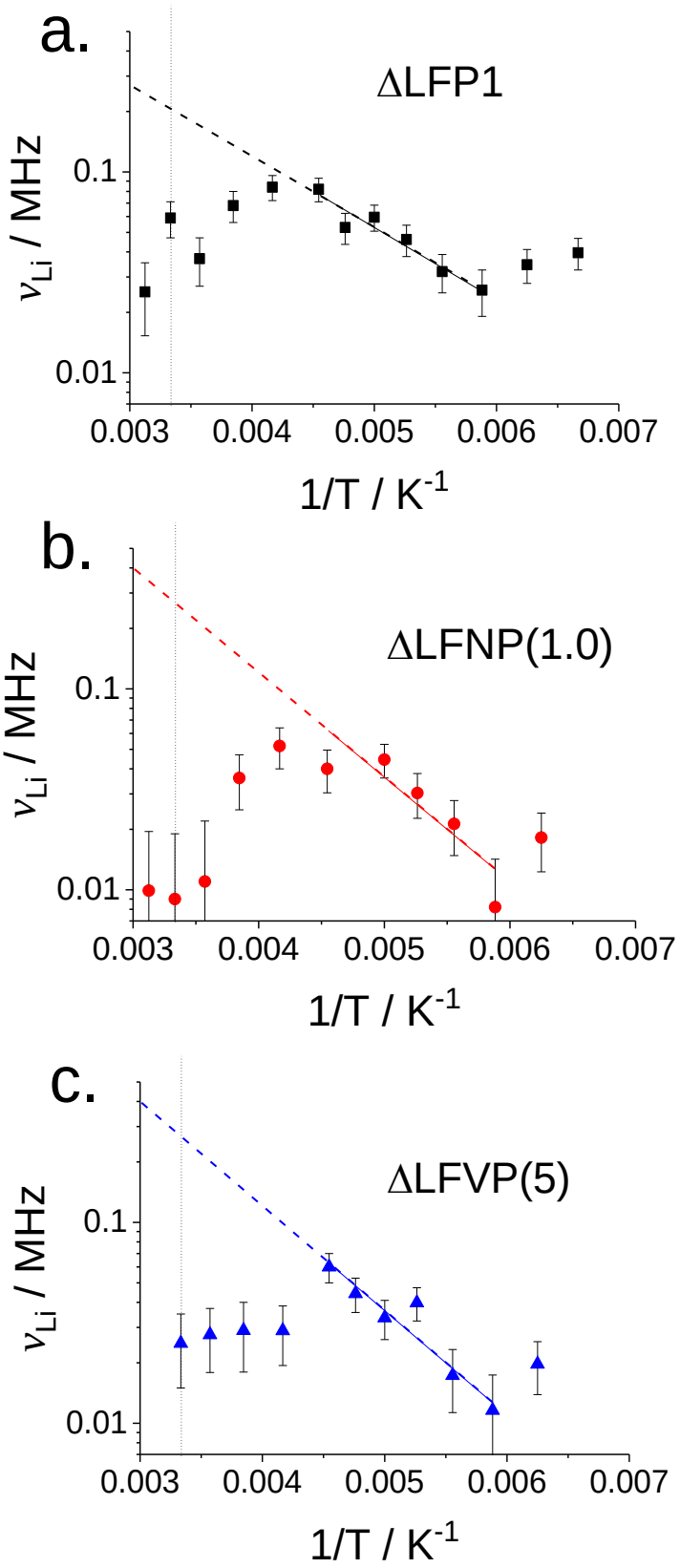

Figure 5.8 – Extrapolations of the muon fluctuation rate ν_{Li} to room temperature on a log plot (indicated by the dotted line) for a) ΔLFP1, b) ΔLFNP(1.0) and c) ΔLFVP(5).

5.4. Conclusions and Further Work

Li^+ diffusion within carbon-coated $LiFePO_4$ and the doped analogues discussed in Chapter 3 have been characterised with muon spectroscopy for the first time. While the diffusion coefficients and activation energies obtained were in-keeping with previous muon studies, the errors in the analysis were too great to differentiate between the pure and doped samples. It is suspected that a significant proportion of muons embedded in the carbon coating, reducing the signal-to-noise ratio and leading to corresponding errors in the Li^+ hopping rate. Normally an effective way to reduce the errors in the data points is to repeat the experiment and collect more data at each temperature. However, this is impractical given each sample already required 24 h for analysis, and longer periods of time are not available on muon beamlines.

Encouragingly, there were indications that the V-doped sample may have enhanced diffusion kinetics; the sudden reduction in the ν_{Li} signal observed above 210 K implied rapid Li^+ diffusion, although this is inconclusive evidence in isolation. It is suggested that further muon studies on doped samples without carbon coatings would give better signal-to-noise ratio, and allow accurate comparison between samples. This may be difficult to achieve *via* CHFS given the presence of carbon in the synthesis is necessary to reduce V^{4+} to V^{3+} (Section 3.4.1), but could be achieved by other, well-established solution-based routes, such as microwave synthesis.[189]

6. A Combinatorial Co-doping study of Fe and V in $LiMnPO_4$

6.1. Aims

$LiMnPO_4$ is a high energy density cathode material (due to its relatively high operating voltage of 4.1 V), but typically suffers from poor electrochemical performance due to its low electronic conductivity, and large structural distortions upon charge/discharge. Given that V-doping in $LiFePO_4$ produced a significant improvement in electrochemical performance in Chapter 3, the effect of V within the isostructural $LiMnPO_4$ material was investigated. It is suggested that the V dopant could increase the Li-diffusion coefficient and the electronic conductivity of $LiMnPO_4$. Furthermore, it is hypothesised the co-inclusion of an isovalent dopant (Fe^{2+}) with the V^{3+} aliovalent dopant may bring separate benefits to the performance of $LiMnPO_4$, which could combine synergistically in a manner hitherto previously unseen. Therefore, to assess the relative merits of each dopant (both separately and together), a 17-sample array of Fe-doped, V-doped and V, Fe-codoped $LiMnPO_4$ was synthesised and characterised.

6.2. Background

6.2.1. Structure, Stability and Properties

After the successful reversible Li extraction from $LiFePO_4$, Padhi *et al*. attempted to replicate these results with $LiMnPO_4$.[91] They were unable to see any Li extraction, and this observation was repeated by Okada *et al*., even with a high charge voltage of 5.2 V.[239] It was found that substitution with Fe was required to achieve extraction, with a voltage plateau observed at 4.1 V vs. Li/Li^+.[91,240] Yamada *et al*. suggested that > 20% replacement of Mn with Fe was required to observe any cycling behaviour in $LiMn_{1-x}Fe_xPO_4$, due to large polarisation (i.e. high overpotentials) caused by the transition between Mn^{2+} and the Jahn-Teller distorted Mn^{3+} ion, and the reduced conductivity of the $LiMnPO_4$ phase.[240] The $LiMnPO_4$ band gap is 2 eV compared to 0.3 eV for $LiFePO_4$, corresponding to observed electronic conductivities of 10^{-10} S cm^{-1} and a range of $10^{-7} – 10^{-10}$ S cm^{-1} respectively.[241] Furthermore, DFT calculations suggest the vacancy formation energy in $LiMnPO_4$ is 0.19 eV greater than $LiFePO_4$, resulting in reduced Li^+ diffusion kinetics.[242]

$LiMnPO_4$ possesses the same crystal symmetry as $LiFePO_4$ and a very similar unit cell, albeit with differing lattice parameters (Table 6.1). However, when $LiMnPO_4$ is delithiated a greater volume change is observed compared to $LiFePO_4$ (due to the Jahn-Teller distortion observed when Mn^{2+} converts to Mn^{3+}). This greater volume expansion/contraction (~10%) is partially responsible for the sluggish lithiation/delithiation kinetics (and greater overpotentials of the charge/discharge reaction) due to the reduced coherence at the $LiMnPO_4/MnPO_4$ boundary.

Table 6.1 – The lattice parameters of $LiMnPO_4$ and the delithiated $MnPO_4$ phase adapted from reference 240. The lattice parameters of the delithiated phase were estimated by extrapolation from delithiated $Mn_{1-x}Fe_xPO_4$ phases.

Material	Lattice Parameter *a*/Å	Lattice Parameter *b*/Å	Lattice Parameter *c*/Å	Unit Cell Volume *V*/Å^3
$LiMnPO_4$	6.13	10.45	4.75	304
$MnPO_4$ (predicted)	5.92	9.625	4.78	273

In a similar manner to $LiFePO_4$, the strong P-O bonds prevent oxygen evolution reaction of the $LiMnPO_4$ structure at elevated temperature (290 J g^{-1}), as evidenced by comparatively low heat evolution in comparison to alternative cathode materials $LiCoO_2$ (1000 J g^{-1}) and $LiNiO_2$ (1600 J g^{-1}). However, the delithiated phase of $LiMnPO_4$ ($Li_{1-x}MnPO_4$) has been shown to be thermally unstable. This is because $Li_{1-x}MnPO_4$ exists as two phases ($LiMnPO_4$ and $MnPO_4$) at room temperature, and at elevated temperatures $MnPO_4$ decomposes according to Equation 6.1. The presence of Mn may influence this, as it is thought to catalyse the decomposition of P_2O_7 to PO_4.[243]

$$2MnPO_4 \rightarrow Mn_2P_2O_7 + \frac{1}{2}O_2$$

Equation 6.1 – The decomposition of $MnPO_4$ to form $Mn_2P_2O_7$.

6.2.2. Reactivity and Performance

Since the initial experiments,[91,239,240] Li has been successfully removed and re-inserted into the pure $LiMnPO_4$ structure, which is thought to diffuse along the b-axis to enter/exit the structure in an analogous manner to $LiFePO_4$. Typically, this has been achieved by similar strategies that proved successful for $LiFePO_4$; nanosizing, carbon coating, and doping. However, the performance of $LiMnPO_4$ is still very much limited, and typically only achieves significant capacity with very small particles (< 50 nm) and/or a high proportion of carbon in the electrode (typically > 20%, Table 6.2). This

additional carbon will reduce the volumetric capacity of the electrode and prevents $LiMnPO_4$ from becoming a viable alternative to other candidate materials. Table 6.2 summarises recent efforts towards pure $LiMnPO_4$ cathode materials, including particle sizes and carbon loadings within the electrode.

Table 6.2 – A summary of electrode carbon content, particle sizes and specific capacities achieved for $LiMnPO_4$ from a selection of literature reports.

Electrode carbon loading / wt%	Particle Size/ nm	Specific Capacity / mA h g^{-1}	Reference
39	100 – 200	89 at C/20	[244]
25	17	153 at C/100, 62 at C/2	[245]
30	20	145 at C/20, 113 at 1C	[246]
22.8	200 × 20 sheets	160 at C/10, 80 at 5C	[247]
26	200 × 20 sheets	170 at C/10, 122 at 5C	[248]
10	10 - 20	165 at C/40, 66 at 1C	[249]

6.2.3. The role of dopants in $LiMnPO_4$

6.2.3.1. Isovalent dopants

A wide variety of dopants within the $LiMnPO_4$ system have been attempted; these include isovalent substitution of Mn^{2+} with divalent Mg,[246,250–254], Fe,[246,252,255,256] Co,[252,253,257] and Ni,[246,253] among others. These were generally found to reduce the polarisation (overpotentials) of charge/discharge and enable greater capacities with doping degrees typically < 20 at%. The main effects of these dopants were to stabilise the discharged $MnPO_4$ structure, as the substituent ions effectively buffered the Jahn-Teller distorted Mn^{3+} ions. This reduced the structural rearrangement on charge/discharge, but additionally improved the coherence of the $LiMnPO_4/MnPO_4$ boundary, which furthermore improved the lithiation/delithiation kinetics. Divalent Fe, Co and Ni had the additional advantage of redox activity when doped into the $LiMnPO_4$ system, with redox potentials of 3.45, 4.8 and 5.2 V *vs.* Li/Li^+ respectively. However, exploiting the potentials at > 4.5 V typically incurred significant electrolyte decomposition, so it is not practical to utilise the redox capability of Co and Ni with current commercial electrolytes. Therefore, substitution of Co, Ni and inert dopants (such as Mg) will inevitably reduce the maximum obtainable capacity of the host $LiMnPO_4$, which suggests Fe may be the ideal candidate for divalent doping. Indeed, Fe was proposed as the best divalent dopant among Fe, Mg, Ni and Zn by Wang *et al*. at the 10 at% doping level (Figure 6.1).[246]

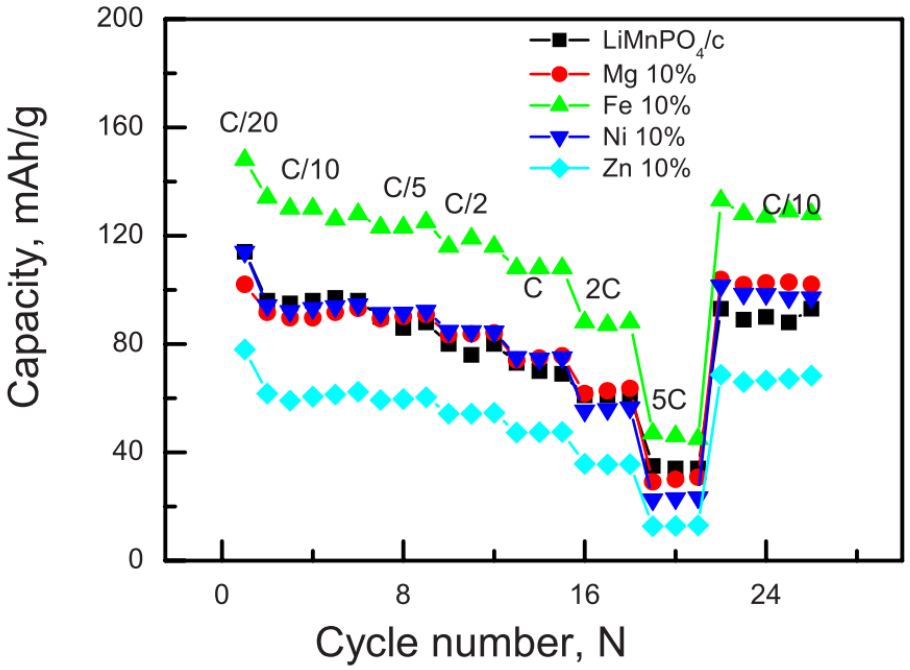

Figure 6.1 – The discharge capacities of various $LiMnPO_4$ based samples investigating the effect of isovalent Fe^{2+} substitution. Reprinted with permission from "Wang, D. *et al.* Improving the Electrochemical Activity of $LiMnPO_4$ Via Mn-Site Substitution. *J. Electrochem. Soc.* **157,** A225" (2010). Copyright 2010 Electrochemical Society.[246]

For this reason, significant research efforts have concentrated on Fe-doped $LiMnPO_4$ ($LiMn_{1-x}Fe_xPO_4$). As previously stated, initial studies found that > 20 at% substitution with Fe (x > 0.2) was required to obtain any measurable Li extraction from $LiMn_{1-x}Fe_xPO_4$.[240] This has been radically improved in recent years, with efforts focussing at approximate doping values of x ~ 0.2. For example, Martha *et al.* developed $LiMn_{0.8}Fe_{0.2}PO_4$/C composite cathodes which attained 162 mA h g^{-1} at C/10 and > 90 mA h g^{-1} at 10C.[258] Dai *et al.* synthesised $LiMn_{0.75}Fe_{0.25}PO_4$/graphene composites with capacities of 155 mA h g^{-1} at 0.5C, and 65 mA h g^{-1} at an extremely high rate of 100C, and represents the best high-rate performance of these materials in literature, although the cathode contained 36 wt% C and would have a correspondingly low volumetric capacity.[259] In contrast, Oh *et al.* developed micron-sized $LiMn_{0.85}Fe_{0.15}PO_4$, and while it did not obtain such impressive specific capacities, it did achieve a high volumetric capacity of 370 mA h cm^{-3} and is more likely to be suitable for a practical device.[260]

6.2.3.2. Aliovalent doping

Within $LiMnPO_4$, aliovalent dopants such as Cr,[261] Zr,[250,251] V,[252,262–264] and Gd,[252,263] have all been attempted to improve the electrochemical performance. The results were not consistent between authors; for example, Lee *et al*. found a positive benefit to Zr^{4+} inclusion, in contrast to Shiratsuchi *et al*.[250,251] However, it has been generally found that these dopants also increase electrochemical performance. In the case of Zr and Cr, this was attributed to a reduction in polarisation, although no further analysis was undertaken to ascertain why this was the case. In contrast, V and Gd were shown to improve performance by distorting the $LiMnPO_4$ structure to lengthen and weaken the Li-O bonds, which resulted in higher ionic conductivity.[263] Furthermore, the V-dopant was shown to increase the electronic conductivity of both the electrode and V-doped $LiMnPO_4$ material compared to pure $LiMnPO_4$.[264]

Similar to $LiFePO_4$, vanadium has been found to substitute on both the Mn and P sites within the $LiMnPO_4$ structure.[265,266] Gutierrez *et al*. established that V^{3+} occupies Mn sites using a combined EXAFS and XRD study. Mn vacancies were generated as a charge-balancing mechanism, and gave the structural formula $LiMn_{1-3x/2}V_x\square_{x/2}PO_4$ (where □ represents a Mn vacancy) according to Equation 6.2.

$$Mn_{Mn}^{x} \rightarrow V_{Mn}^{\cdot} + \frac{1}{2}\square_{Mn}''$$

Equation 6.2 – The doping mechanism of V into $LiMnPO_4$ according to Gutierrez *et al.* in Kröger-Vink notation. Mn_{Mn}^{x} represents a Mn atom occupying a Mn site with zero net charge. $V_{Mn}^{\cdot}$ represents a V atom occupying a Mn site with a single positive charge. $\square_{Mn}''$ represents a Mn vacancy with a double negative charge.

It was found that up to 20 at% V could be incorporated in the $LiMnPO_4$ lattice by using low-temperature, microwave-assisted synthesis (300 °C), without generating impurity phases, although heating above 525 °C generated the $Li_3V_2(PO_4)_3$ LISICON phase and $LiVP_2O_7$ (as observed in Section 3.4.1.2 in V-doped $LiFePO_4$). Testing of these samples resulted in significant increases in discharge capacity deriving from the 4.1 V Mn^{3+}/Mn^{2+} couple (100 *vs.* 8 mA h g^{-1} for the 20 at% V-doped and pure samples respectively at C/20 charge/discharge rate). Moreover, heat-treating the 20 at% doped sample to 525 °C (i.e. keeping olivine phase purity) improved this capacity to 150 mA h g^{-1}, which was very close to the theoretical capacity (assuming the V^{3+}/V^{4+} couple

was active). The researchers suggested in their report that the main benefit of the V-dopant was to increase the covalency of the Mn-O bonds, improving the kinetics of the Mn^{2+}/Mn^{3+} transition.[265] In contrast, the work of Clemens *et al*. found that V^{5+} can substitute on the P site, generating the compound $LiMn(PO_4)_{1-x}(VO_4)_x$ from another combined EXAFS and XRD study.[266] This effectively shrank all lattice parameters (and the unit cell volume), and increased the electronic conductivity by 1 – 2 orders of magnitude within the samples tested (between $0 < x < 0.2$), although unfortunately no Li-ion testing was performed on these materials.

Aside from the work of Gutierrez *et al*., more highly doped compounds (typically > 5 at% V) often contained a highly electronically and ionically conductive $Li_3V_2(PO_4)_3$ impurity phase. The presence of this phase usually increased performance, and has been manually added to $LiMnPO_4$ to form $LiMnPO_4$:$Li_3V_2(PO_4)_3$ composite cathodes for this purpose.[264,267,268] This idea was extended to make "core-shell" structures by Zhang *et al*., with a shell of $Li_3V_2(PO_4)_3$ on the surface of $LiMnPO_4$, which significantly reduced the polarisation of the $LiMnPO_4$ phase, although there was a significant excess of the shell phase ($LiMnPO_4$: $Li_3V_2(PO_4)_3$ = 27 : 73 weight ratio).[268]

6.2.3.3. Co-doping studies within $LiMnPO_4$

There are relatively few reports of 2 or more dopants within $LiMnPO_4$, although all those reported generally show benefit compared to singly-doped compounds. In the case of purely isovalent substitution, it has been found that a combination of Fe and Mg dopants (either 1 at% or 5 at%) improved electrochemical performance more than Fe on its own (10 at%).[269,270] In an Mg^{2+}/Zr^{4+} co-doping study, it was found a combination of Mg and Zr (10 and 2 at% respectively) gave the lowest polarisation (and greatest capacity) compared to simple binary compounds.[251]

6.3. Experimental Details of the Synthesis of Doped $LiMnPO_4$ compounds

Amorphous carbon-coated iron- and vanadium-doped lithium manganese phosphate samples were synthesised using the Pilot-Scale CHFS reactor set-up described in Section 2.1.1.1, and a schematic (including precursors) is provided in Figure 6.2. The first precursor solution (fed in *via* P2) consisted of: $MnSO_4 \cdot H_2O$ (99+%, Sigma Aldrich, Steinheim, Germany), $FeSO_4 \cdot 7H_2O$ (99+%, Alfa Aesar, Heysham, UK),

$VOSO_4 \cdot 5H_2O$ (17-23% V, Acros Organics, Loughborough, UK), 0.375 M H_3PO_4 (85-88 wt%, Sigma Aldrich, Steinheim, Germany) and fructose (99%, Alfa Aesar, Heysham, UK) in D.I. water. The composition of this solution was varied such that the sum of [Mn], [Fe] and [V] was 0.25 M and the concentration of fructose was fixed throughout at 0.65 M (described in full in Table 6.3). The second solution, fed in *via* P3, was 0.8625 M $LiOH \cdot H_2O$ (99+%, Fisher Scientific, Loughborough, UK) in D.I. water for all experiments.

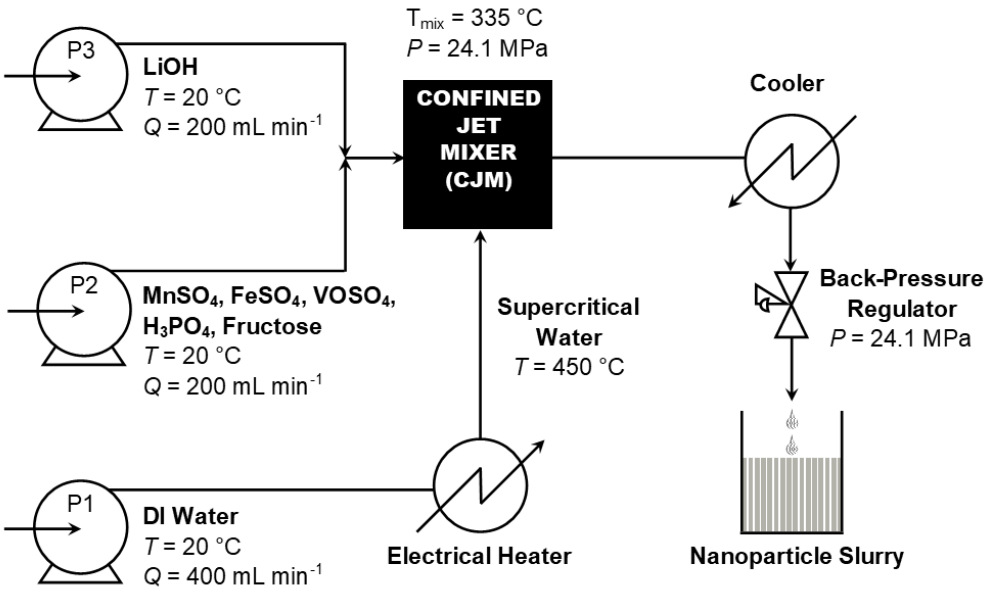

Figure 6.2 – A schematic of the Pilot-Scale CHFS process and reaction conditions used to make the doped $LiMnPO_4$ array of samples.

Table 6.3 – The concentration of metal salt precursors used to generate the sample array, and the carbon content of the heat-treated samples measured by CHN analysis.

Sample	$[MnSO_4]$	$[FeSO_4]$	$[VOSO_4]$	Carbon content after heat-treatment / wt%
ΔLMP	0.25	0	0	2.47
ΔLMFVP(0,2.5)	0.24375	0	0.0063	5.77
ΔLMFVP(0,5)	0.2375	0	0.0125	5.01
ΔLMFVP(0,10)	0.225	0	0.025	4.44
ΔLMFVP(0,15)	0.2125	0	0.0375	6.27
ΔLMFVP(0,20)	0.2	0	0.05	5.89
ΔLMFVP(5,15)	0.2	0.0125	0.0375	1.55
ΔLMFVP(10,10)	0.2	0.025	0.025	5.04
ΔLMFVP(15,5)	0.2	0.0375	0.0125	3.03
ΔLMFVP(2.5,0)	0.24375	0.00625	0	4.84
ΔLMFVP(5,0)	0.2375	0.0125	0	3.21
ΔLMFVP(10,0)	0.225	0.025	0	3.30
ΔLMFVP(15,0)	0.2125	0.0375	0	3.86
ΔLMFVP(20,0)	0.2	0.05	0	3.72
ΔLMFVP(1.25,1.25)	0.24375	0.00313	0.00313	3.01
ΔLMFVP(2.5,2.5)	0.2375	0.00625	0.00625	3.78
ΔLMFVP(5,5)	0.225	0.0125	0.0125	5.06

Both the metal salt and LiOH solutions were pumped to meet with supercritical water at 450 °C as described in Section 2.1.1.1 (Pilot-Scale reactor). The reaction temperature was *ca.* 335 °C with a residence time of *ca.* 6.5 s, and the product slurry was collected in a plastic container open to the atmosphere at a production rate of 800 mL min^{-1}.

The slurry was allowed to settle (1 h) and the supernatant siphoned off. Centrifugation (1500 rpm for 5 minutes) further concentrated the slurry to a wet paste, which was dialysed in D.I. water until the conductivity of the paste was reduced below 150 μS m^{-1}. The cleaned paste was further concentrated with centrifugation (4500 rpm over 30 minutes) and freeze-dried by slowly heating from −60 °C to 25 °C, over 24 h under vacuum of < 13 Pa as further described in Section 2.1.3.3. The freeze-dried powder was subsequently heat-treated from ambient temperature up to 700 °C with a heating rate of 5 °C min^{-1}, and held for at this temperature for 3 h under a flow of Ar gas.

Powder XRD patterns of the as-prepared and heat-treated samples were obtained using set-up **a** (Section 2.1.4.1) using Cu-Kα radiation (λ = 1.54 Å) in the 2θ range 5 to 60° with a step size of 0.05° in 2θ and a count time of 4 s. Rietveld analysis was performed using MAUD software.[132] The $Fe_2P_2O_7$ impurity phase was identified using set-up **b**

(Section 2.1.4.1) Mo-Kα radiation (λ = 0.709 Å) over the 2θ range 10 - 18° with a step size of 0.5° and step time of 20 s.

ICP-AES analysis was conducted using the set-up described in Section 2.1.4.9. 50 mg of the as-prepared samples were dissolved in 1.5 mL of conc. HCl (analytical grade, 36.5-38.0%, Sigma-Aldrich, Dorset, UK), and the resultant solution diluted with 12.5 mL 1% HNO_3. 1 mL of the resulting solution was further diluted into 100 mL of 1% HNO_3 to produce the solutions analysed by ICP-AES. Standards were prepared by dissolving Li, Mn, Fe, V, and PO_4 precursors in 100 ml of 1% HNO_3 to give a stock solution with concentrations of 800, 4000, 4000, 800 and 8000 ppm of the respective elements. This stock solution was diluted further into 100 ml 1% HNO_3 to give standard solutions (Table 6.4). The effect of HCl in the analysed solutions was considered negligible due to the heavy dilution (0.04 % HCl). The precursors used were: $LiOH{\cdot}7H_2O$ (99+%, Fisher Scientific, Loughborough, UK), $Mn(CH_3COO)_2{\cdot}4H_2O$ (≥ 99%, Aldrich, Dorset, UK), $FeSO_4{\cdot}7H_2O$ (99+%, Alfa Aesar, Heysham, UK), NH_4VO_3 (99%, Sigma-Aldrich, Dorset, UK) and $(NH_4)_3PO_4$ (≥ 99.0%, Fluka, Dorset, UK).

Table 6.4 – The concentrations (in ppm) of the various chemical species used to make the ICP-AES standards

Chemical Species	Blank / ppm	Standard 1 / ppm	Standard 2 / ppm	Standard 3 / ppm	Standard 4 / ppm
Li	0	2	4	6	8
Mn	0	10	20	30	40
Fe	0	10	20	30	40
V	0	2	4	6	8
PO_4	0	20	40	60	80

The Li-ion battery cathodes were prepared by mixing each heat-treated sample with conductive agent with Super P™ carbon and PVDF to give an active material:carbon:binder mass ratio of 75:15:10 for all electrodes. This included the surface carbon coating, which was between 2.5 to 6.3 wt% across all samples (Table 6.3). The PVDF was stirred in NMP for at least 1 h at room temperature until it was fully dissolved. This solution was combined with the sample and carbon, and ball-milled for 1 h; the product slurry was cast on Al foil and dried in an oven set to 70 °C. 16 mm diameter circular electrodes were punched out of the dried sheet, and pressed

(1.5 tons cm^{-2}). The mass loadings of all electrodes were in the range 2.2 – 2.7 mg cm^{-2}.

For rapid assessment across the compositional range, standard 2032 coin cells (referred to as Batch 1 cells, Hohsen, Japan) were assembled in a dry room with a dew point of < −40 °C. Li discs were employed as anodes (PI-KEM, Staffordshire, UK), and the separator (Celgard) was saturated with 1 M $LiPF_6$ in 1:1 ethylene carbonate/ethyl methyl carbonate, with 1 wt% vinylidene carbonate additive, supplied by BASF, Ludwigshafen, Germany. Subsequent cell assembly of key electrodes (referred to as Batch 2 cells) was conducted in the standard manner described in Section 2.1.5.2.

Electrochemical measurements were performed using an Arbin Instruments battery tester at 20 °C as described in Section 2.1.5. The areas of electrochemical activity were investigated by cyclic voltammetry in the range 2.0 to 4.5 V *vs*. Li/Li^+ at a 0.05 mV s^{-1} scan rate. The Batch 1 cells were subjected to a constant current, constant voltage (CCCV) test regime, with voltage limits of 2.0 and 4.5 V *vs*. Li/Li^+. This meant C-rates of C/2, 1C, 2C and 5C were applied on charge and discharge (where 1C value was calculated with an assumed specific capacity of 170 mA h g^{-1}), but an additional holding voltage of 4.5 V was employed at the end of the charge step. This voltage was held until the measured current dropped below 3% of the charge rate. The specific current and specific capacity was calculated based on the mass of active material (i.e. pure or doped $LiMnPO_4$) for each printed electrode. Long-term cycling tests were performed subsequently at C/10, using the same holding voltage regime. Additional slower CCCV rates (with the same holding voltage protocol) were performed on the Batch 2 cells at charge/discharge C-rates of C/10, C/5, C/2, 1C, 2C, 5C.

6.4. Results and Discussion

6.4.1. Physical Characterisation

Given the separate beneficial effects previously observed in $LiMnPO_4$ by the inclusion of Fe and V dopants separately, the relative merits of these dopants were assessed with a range of binary and tertiary compounds. $LiMnPO_4$ and the Fe and V codoped derivatives $LiMn_{1-x-y}Fe_xV_yPO_4$ were synthesised, where *x* and *y* are the nominal

percentages of iron and vanadium, respectively. The metal at% was assumed to be identical to those present in the precursor, which were normalised to total transition metal content. The pure $LiMnPO_4$ sample was named LMP, and the iron/vanadium doped samples were named LMFVP(*x*,*y*). Firstly, binary compounds were compared to explore the separate effects of the dopants in the system (where either *x* or *y* is equal to zero). The possible synergistic effect of both dopants employed together in the ternary system (*x* and *y* are both non-zero) was also evaluated. Given the large amount of interest in the high theoretical energy density possible with high Mn content, the compositions attempted were limited to the Mn-rich portion of phase diagram (as highlighted in Figure 6.3a). 17 samples with nominal compositions as shown in Figure 6.3b were all synthesized with an amorphous carbon coating generated in process by the decomposition of fructose as previously described in Chapter 3. Molar yields of the products were in the range 45 – 60 mol%. It was hoped that the analysis of this large array would allow the identification and exploration of hitherto unseen trends in crystal structure and performance.

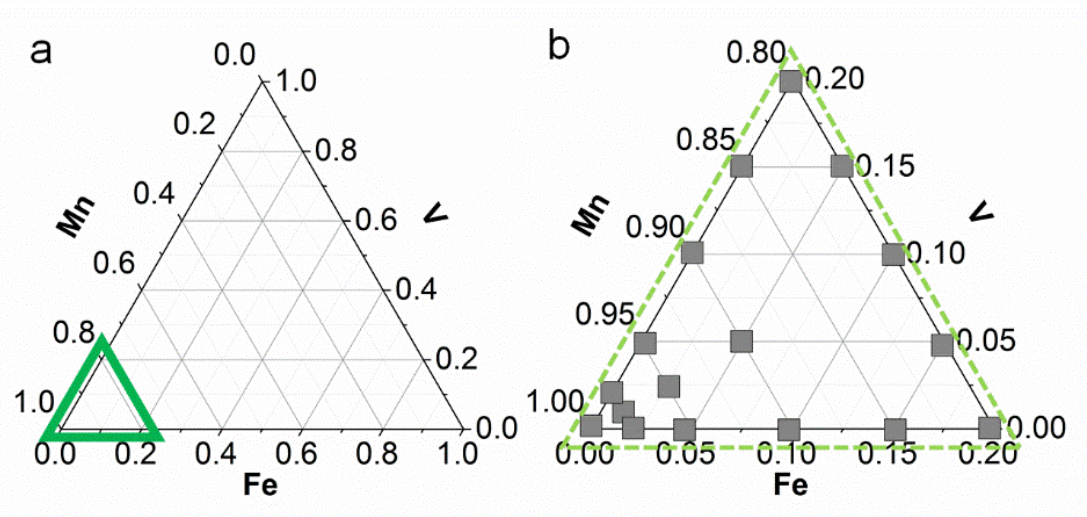

Figure 6.3 – a) The Mn-Fe-V olivine phase diagram, indicating the specific region of interest for high-energy cathode materials. b) The compositions of the doped samples attempted within the region of interest. Adapted from reference 271.

The as-prepared samples were heat-treated in argon to give the corresponding samples named ΔLMP and ΔLMFVP(*x*,*y*), which converted the amorphous surface carbon to graphitic carbon, which was confirmed with Raman spectroscopy (Figure 6.4 and Figure 6.5). In the as-prepared samples, a very weak G band was evident, but the spectrum was dominated by a very broad feature across the entire range of analysis.

This implied a great degree of disorder in the amorphous carbon shell. Heat-treatment did produce clear D and G modes, which are indicators of graphitic carbon. The symmetric stretching vibration of PO_4 at 950 cm^{-1} was also observed. The as-prepared samples were grey-blue or grey-pink powders, and heat-treatment produced black powders.

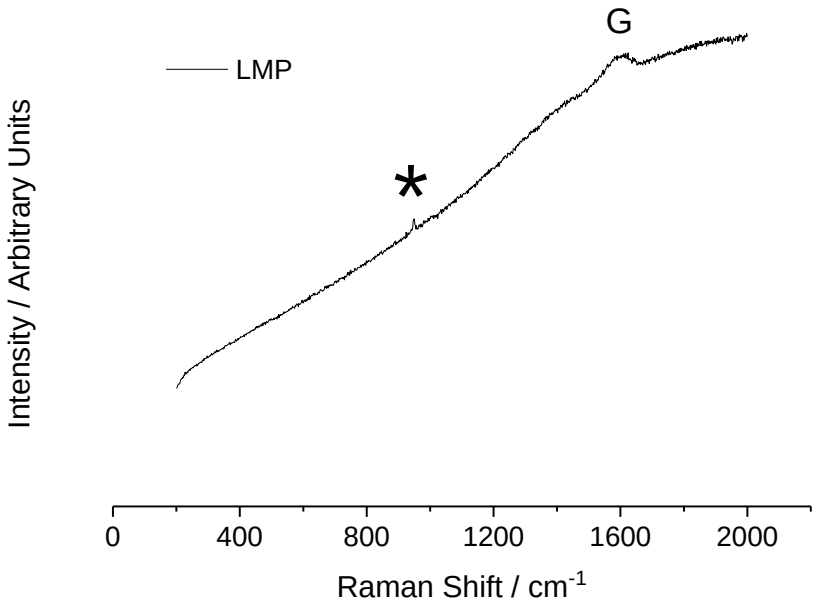

Figure 6.4 – The Raman spectrum of the as-prepared $LiMnPO_4$ sample, displaying the PO_4 band (*) and the graphitic carbon band (G). Adapted from reference 271.

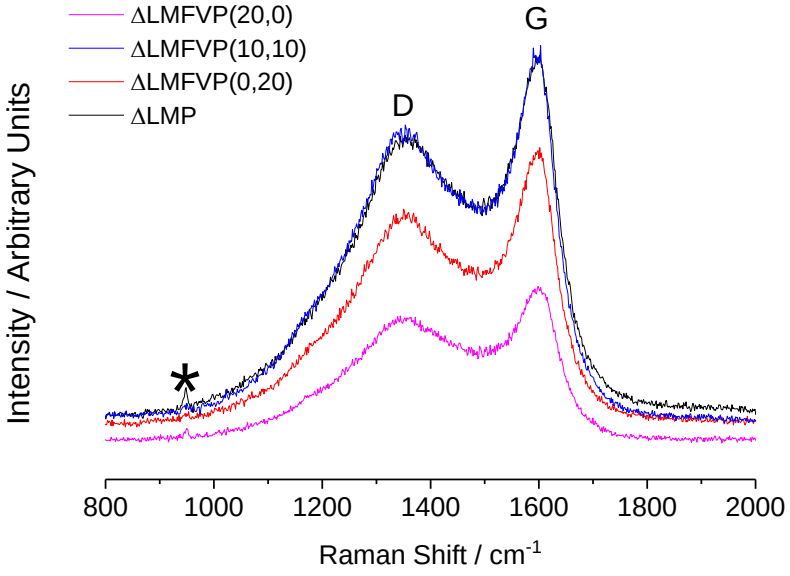

Figure 6.5 – The Raman spectrum of the heat-treated samples ΔLMP, ΔLMFVP(0,20), ΔLMFVP(10,10) and ΔLMFVP(20,0), showing the PO_4 band (*), the graphitic carbon band (G) and the disordered carbon band (D). Adapted from reference 271.

XRD patterns (Cu-Kα radiation, set-up **a** in Section 2.1.4.1) of the as-prepared samples could all be matched exclusively to the pure olivine $LiMnPO_4$ structure (PDF Card No. 01-074-0375, Figure 6.7a, Figure 6.8a, Figure 6.9a). The peaks broadened and shifted with increasing vanadium content (Figure 6.7b) in the Mn-V binary compounds, which indicated increasing distortion of the lattice parameters and lattice strain. As discussed later in this section, the likely oxidation state of V within this compound is V^{3+}, and therefore these crystallographic changes could be induced by local distortion in the olivine lattice by the smaller ionic radius of V^{3+} compared to Mn^{2+} (0.64 Å vs. 0.83 Å respectively),[86] leading to shorter average Me-O bond lengths and a contraction in unit cell volume. Furthermore, the defects associated with V^{3+} inclusion on an Fe^{2+} site (suggested to be Li^{+} vacancies from the ICP-AES data discussed later in this chapter) will also contribute to lattice parameter shifts and crystallographic distortion. EDS mapping confirmed that V was included homogenously into the structure in the most heavily V-doped as-prepared sample LMFVP(0,20) (Figure 6.6), with no secondary phases evident. In contrast, the Fe dopant caused comparatively reduced shift with no broadening (Figure 6.8b) in the Mn-Fe binary compounds, which reflects the greater similarity of Fe^{2+} and Mn^{2+} ionic radii (0.78 vs 0.83 Å respectively) and the absence of charge-compensating defects with Fe substitution.[86] The ternary (Fe and V co-doped) samples exhibited behaviours entirely in-keeping with those suggested by the binary solutions, i.e. small 2θ shifts with the Fe dopant, and larger 2θ shifts with peak broadening from the V dopant (Figure 6.9b). These consistent shifts implied that the two dopants had uniform effects on the crystal structure, and achieved homogenous doping throughout the structure. The obvious distortion of the unit cell suggested the lattice parameters of these samples should be explored with Rietveld refinement.

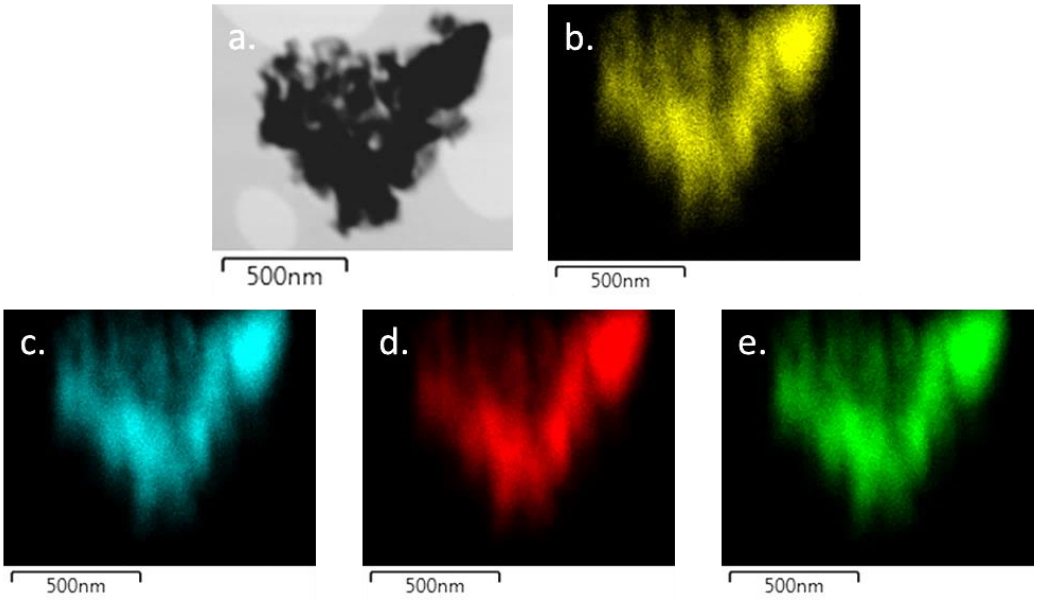

Figure 6.6 – EDS mapping of sample LMFVP(0,20), showing a) the darkfield image, b) the V-Kα signals (yellow), c) the Mn-Kα signals (blue), d) the O-Kα signals (red) and e) the P-Kα signals (green).

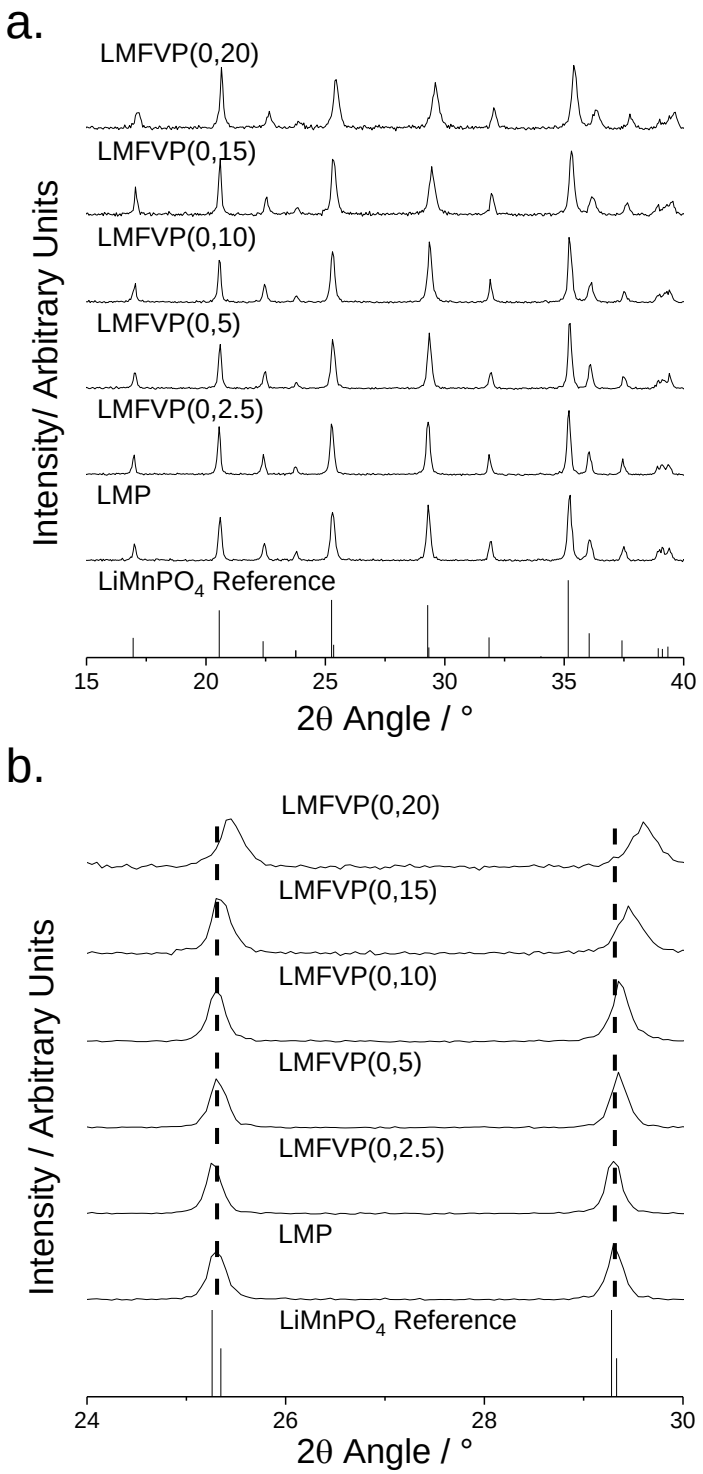

Figure 6.7 – a) X-ray diffraction patterns of the V-doped $LiMnPO_4$ samples, including a reference $LiMnPO_4$ diffraction pattern (PDF Card. No. 01-074-0375), and samples LMP, LMFVP(0,2.5), LFMVP(0,5), LMFVP(0,10), LMFVP(0,15) and LMPVP(0,20). b) A magnification of the diffraction plots in the 2θ range 24 – 28°, showing shifts in the peaks. Adapted from reference 271.

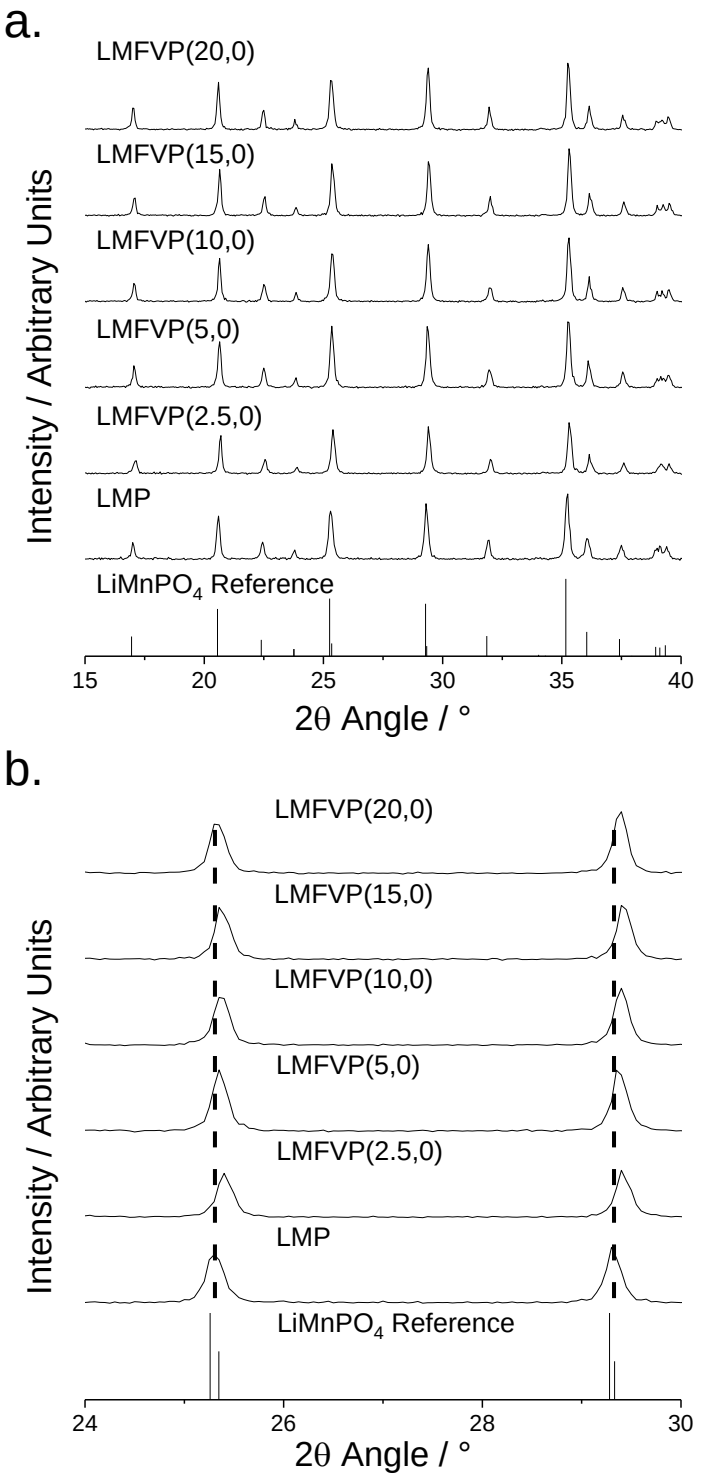

Figure 6.8 – a) X-ray diffraction patterns of the Fe-doped $LiMnPO_4$ samples, including a reference $LiMnPO_4$ diffraction pattern (PDF Card. No. 01-074-0375), and samples LMP, LMFVP(2.5,0), LFMVP(5,0), LMFVP(10,0), LMFVP(15,0) and LMFVP(20,0). b) A magnification of the diffraction plots in the 2θ range 24 – 28°, showing shifts in the diffraction peaks. Adapted from reference 271.

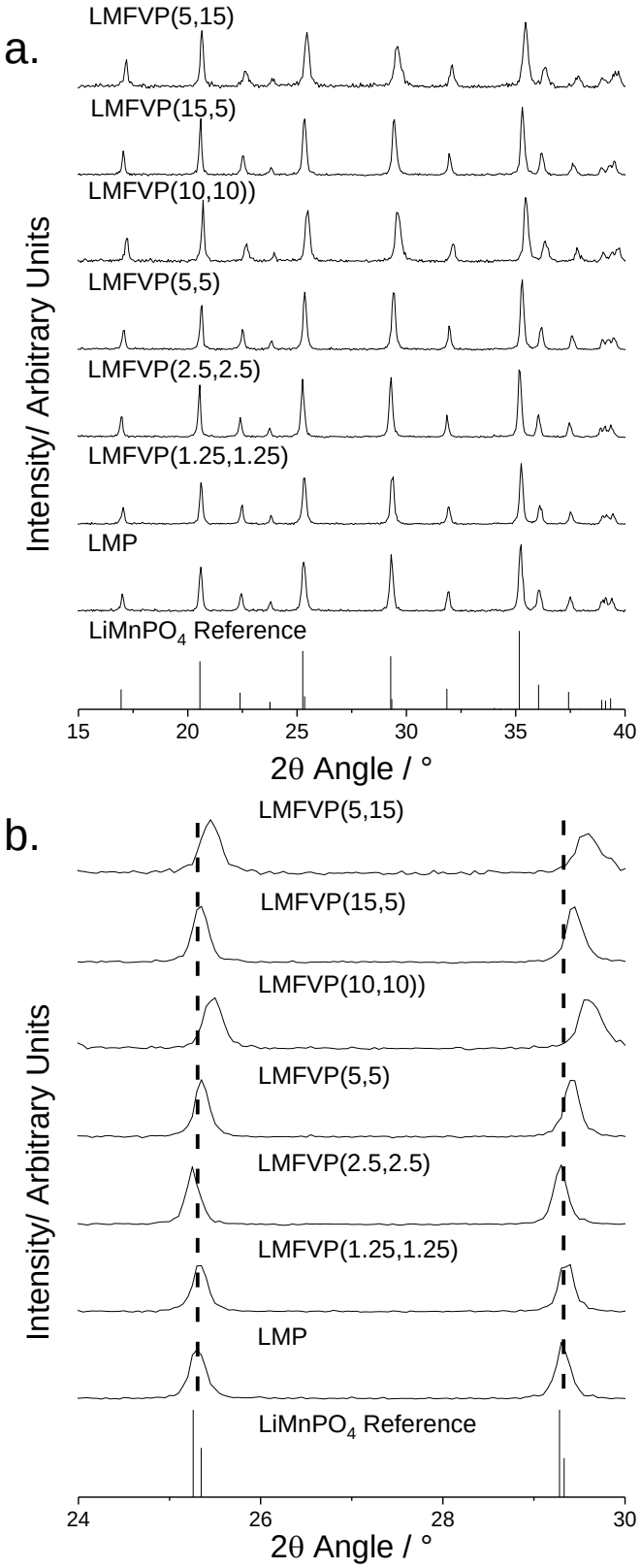

Figure 6.9 – a) X-ray diffraction patterns of the V and Fe co-doped $LiMnPO_4$ samples, including a reference $LiMnPO_4$ diffraction pattern (PDF Card. No. 01-074-0375), and samples LMP, LMFVP(1.25,1.25), LFMVP(2.5,2.5), LMFVP(5,5), LMFVP(15,5) and LMFVP(5,15). b) A magnification of the diffraction plots in the 2θ range 24 – 28°, showing shifts in the diffraction peaks. Adapted from reference 271.

Rietveld refinement revealed consistent trends in the relationship between lattice parameters and sample composition (Figure 6.10a-d, Table 6.5). Plots of the fits are included in Chapter 11 - Appendix I. Increasing incorporation of both Fe and V dopant gave a smooth reduction of the *a* and *b* lattice parameters across the entire range of samples. However, increasing V incorporation increased the *c* parameter, whereas Fe incorporation decreased it. This was consistent with the change in lattice parameters observed in the $LiMn_{1-x}Fe_xPO_4$ solid solution reported previously,[240] but also the shifts reported by Gutierrez *et al*. in V-doped $LiMnPO_4$.[265] Moreover, this effect mirrored the changes observed in Section 3.4.1.2 when V was incorporated into $LiFePO_4$. It is suggested, therefore, that V mainly substituted on the Fe site, as opposed to the P site, in these samples (which gave a reduction in *c* parameter with increased V doping). However, EXAFS analysis of these samples is required to fully confirm this hypothesis.

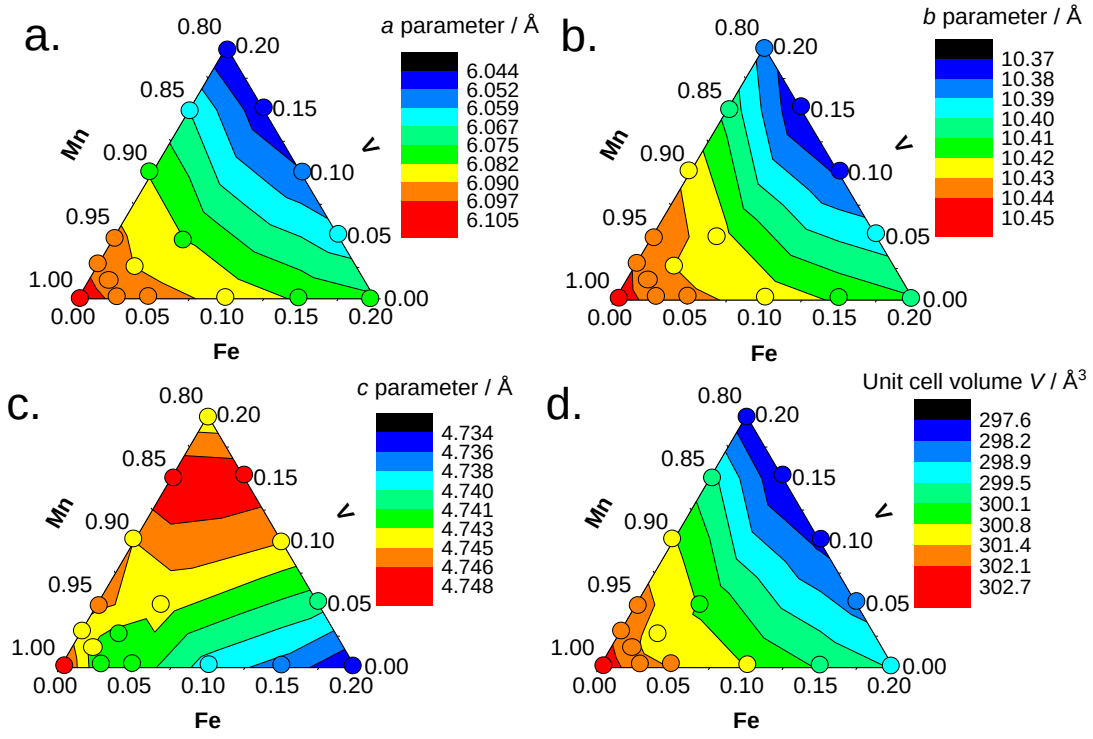

Figure 6.10 – A 2D contour plot of the lattice parameters extracted from Rietveld analysis, showing a) the *a* lattice parameter, b) the *b* lattice parameter, c) the *c* lattice parameter and d) the unit cell volume *V* as a function of composition. Coloured circles are included to show the value of the individual data points which were used to create the contour plots. Adapted from reference 271.

Table 6.5 – The lattice parameters and unit cell volume (with errors in parentheses) derived from Rietveld refinement, including the figures of merit, for the array of doped samples. Adapted from reference 271.

Sample	*a* / Å	*b* / Å	*c* / Å	V / Å^3	R_{wp}	χ^2
LMP	6.1044(7)	10.449(1)	4.7473(6)	302.8(1)	21.97	1.07
LMFVP(0,2.5)	6.0941(6)	10.439(1)	4.7439(5)	301.79(9)	20.27	1.07
LMFVP(0,5)	6.0914(7)	10.438(1)	4.7452(6)	301.7(1)	21.13	1.06
LMFVP(0,10)	6.0814(8)	10.427(1)	4.7448(7)	300.9(1)	22.11	1.15
LMFVP(0,15)	6.067(1)	10.405(2)	4.748(1)	299.7(2)	21.68	1.11
LMFVP(0,20)	6.044(1)	10.383(2)	4.744(1)	297.7(2)	20.15	1.02
LMFVP(5,15)	6.046(1)	10.367(2)	4.748(1)	297.6(2)	21.97	1.10
LMFVP(10,10)	6.052(1)	10.376(2)	4.7465(9)	298.1(2)	23.09	1.10
LMFVP(15,5)	6.0618(7)	10.393(1)	4.7402(6)	298.6(1)	20.43	1.06
LMFVP(2.5,0)	6.0950(7)	10.435(1)	4.7419(7)	301.6(1)	23.00	1.11
LMFVP(5,0)	6.0928(6)	10.431(1)	4.7424(5)	301.4(1)	20.92	1.05
LMFVP(10,0)	6.0877(6)	10.426(1)	4.7388(6)	300.8(1)	23.49	1.18
LMFVP(15,0)	6.0810(6)	10.417(1)	4.7372(6)	300.08(9)	21.40	1.07
LMFVP(20,0)	6.0759(6)	10.410(1)	4.7345(5)	299.45(9)	21.24	1.10
LMFVP(1.25,1.25)	6.0938(6)	10.435(1)	4.7431(6)	301.6(1)	20.85	1.06
LMFVP(2.5,2.5)	6.0899(5)	10.430(1)	4.7425(5)	301.22(9)	19.99	1.06
LMFVP(5,5)	6.0811(6)	10.420(1)	4.7435(6)	300.6(1)	21.34	1.09

As stated previously, the heat-treatment of the samples was necessary to graphitise the surface carbon. However, upon heat-treatment, the same limitation in vanadium solubility previously observed in $LiFePO_4$ and $LiMnPO_4$ was encountered. A $Li_3V_2(PO_4)_3$ impurity phase was found in the heat-treated samples ΔLMFVP(0,15) and ΔLMFVP(0,20) (match to PDF Card No. 01-072-7074), which was not observed in the as-prepared compounds (Figure 6.11). An additional broad feature at ~ 31° 2θ was also observed in samples with 5 – 15 at% V, and may correspond to a pyrophosphate phase (discussed in detail later in this chapter). The Fe dopant was stable in the $LiMnPO_4$ olivine structure in the range explored, consistent with previous literature reports, as no impurity peaks were observed upon heat-treatment. EDS analysis of sample ΔLMFVP(0,20) confirmed the segregation of a V-rich phase (Figure 6.12).

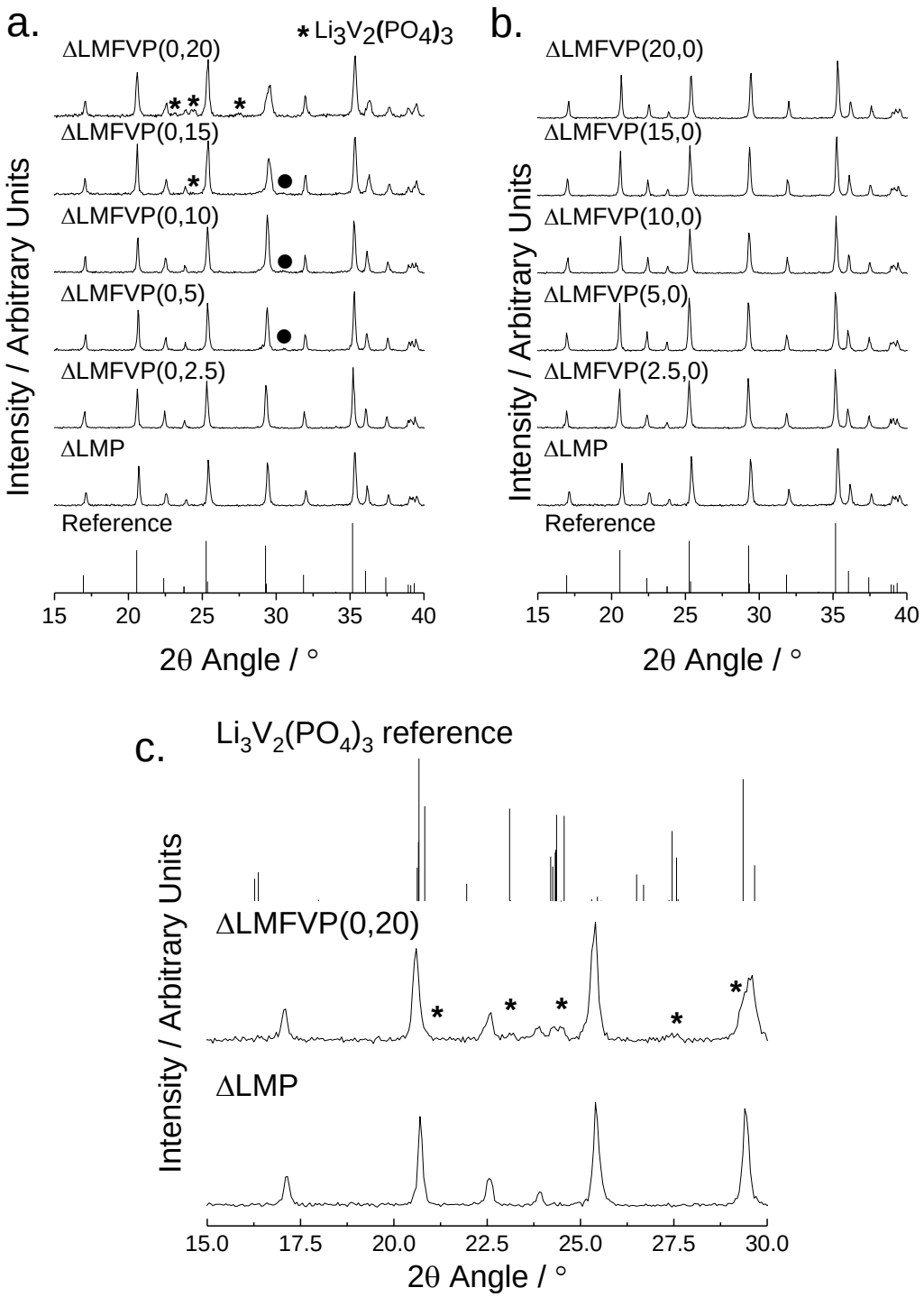

Figure 6.11 – XRD patterns of a) the heat-treated V-doped $LiMnPO_4$ samples (including the pure LMP sample), b) the heat-treated Fe-doped $LiMnPO_4$ samples (including the pure LMP sample) and c) a magnified plot of ΔLMFVP(0,20) with ΔLMP and a $Li_3V_2(PO_4)_3$ reference, with the $Li_3V_2(PO_4)_3$ impurity phase peaks indicated with asterisks. An additional impurity phase is marked with ●. The $LiMnPO_4$ reference used was PDF card No. 01-074-0375. Adapted from reference 271.

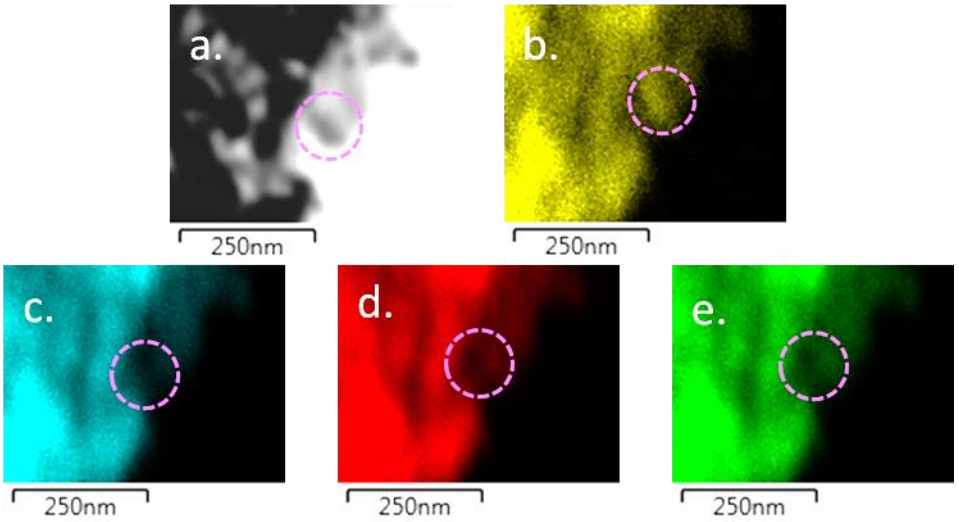

Figure 6.12 – EDS mapping of sample ΔLMFVP(0,20), showing a) the darkfield image, b) the V-Kα signals (yellow), c) the Mn-Kα signals (blue), d) the O-Kα signals (red) and e) the P-Kα signals (green). A pink dashed circle is added to highlight the presence of a V-rich phase. Adapted from reference 271.

For samples with a mixture of Fe and V dopants, broad diffraction peaks for samples ΔLMFVP(5,5), ΔLMFVP(10,10) and ΔLMFVP(15,5) indicated the potential presence of a pyrophosphate phase ($M_2P_2O_7$, where M = Fe or Mn) phase (Figure 6.17b). This was revealed with greater clarity using Mo-Kα radiation using set-up **b** in Section 2.1.4.1 (Figure 6.17b, matches to PDF Card. No. 01-076-1762 and 01-077-1423). The impurity peaks were very similar to those observed in Section 3.4.2.2, and suggested a $Fe_2P_2O_7$ impurity phase. It may be possible that some form of solid solution ($Fe_{2-x}Mn_xP_2O_7$) has been generated for these samples. Indeed, the relative similarities of crystal structures of both pyrophosphates (Figure 6.13 - Figure 6.15) suggest a solid solution may be possible. Both form layers of $P_2O_7^{4-}$ ions separated by metal ion layers along the (0 0 1) plane, and the orientation of the pyrophosphate ions is identical between the structures (Figure 6.13 and Figure 6.14). The main difference between the two phases is within the metal ion layer; in $Mn_2P_2O_7$, the Mn-ions are coordinated to six oxyanions in distorted octahedron geometry, and each octahedron edge-shares with three other octahedra (Figure 6.15 and Figure 6.16). In $Fe_2P_2O_7$, the structure distorts to effectively break one of the edge-sharing connections on each metal ion polyhedra (broken along the [-1 1 0] direction, Figure 6.16). This reduced oxyanion sharing lowers the coordination of the Fe-ions to FeO_5 in a distorted square-based pyramid geometry. Therefore, it is conceivable that a solid solution exists between these two materials, with increasing disconnection between metal polyhedra as Fe replaces Mn.

As mentioned, $Mn_2P_2O_7$ has been observed to segregate from Li-deficient $LiMnPO_4$ previously, so elemental analysis should reveal if the co-doped samples are Li deficient.

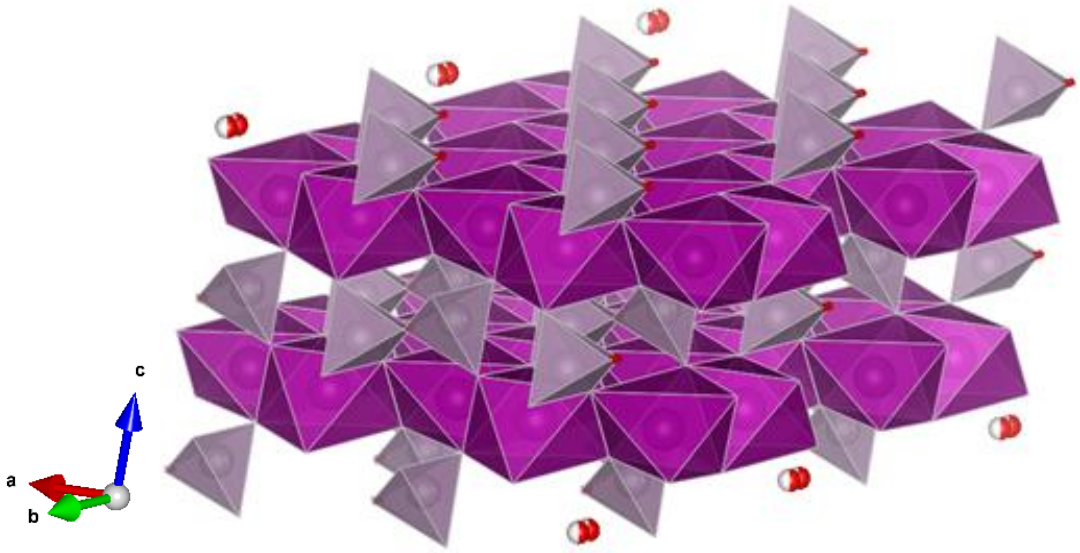

Figure 6.13 – The crystal structure of $Mn_2P_2O_7$ with the [-1 1 0] direction normal to the page, with P_2O_7 polyhedra in grey and MnO_6 octahedra in purple. The image was created using VESTA software from PDF Card. No. 01-077-1423.[90]

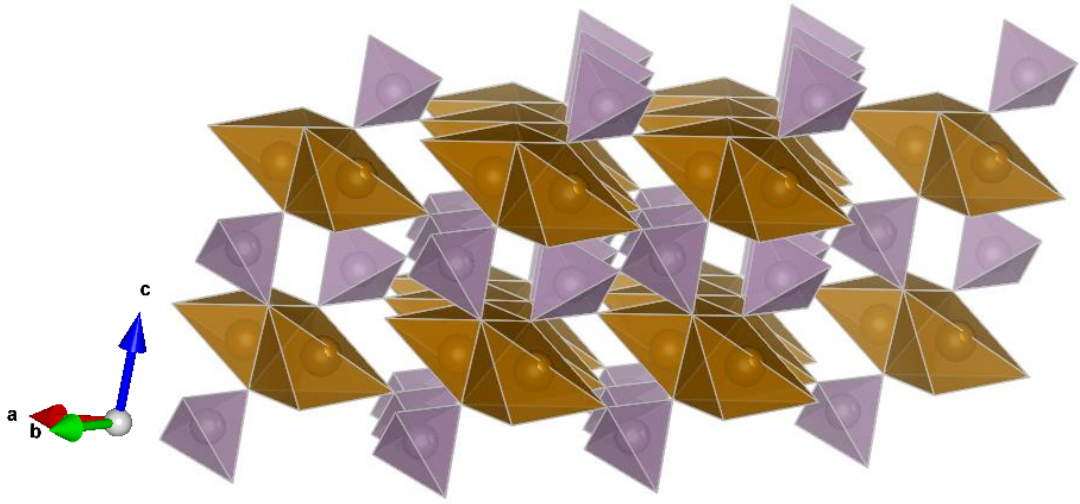

Figure 6.14 – The crystal structure of $Fe_2P_2O_7$ with the [-1 1 0] direction normal to the page, with P_2O_7 polyhedra in grey and FeO_5 polyhedra in brown. The image was created using VESTA software from PDF Card. No. 01-076-1762.[90]

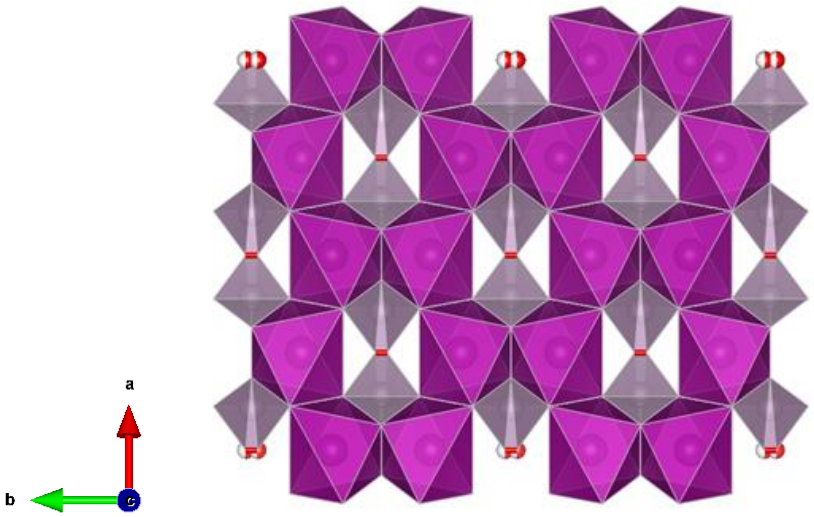

Figure 6.15 – The crystal structure of $Mn_2P_2O_7$ with the [0 0 1] direction normal to the page, with P_2O_7 polyhedra in grey and MnO_6 octahedra in purple. The image was created using VESTA software from PDF Card. No. 01-077-1423.[90]

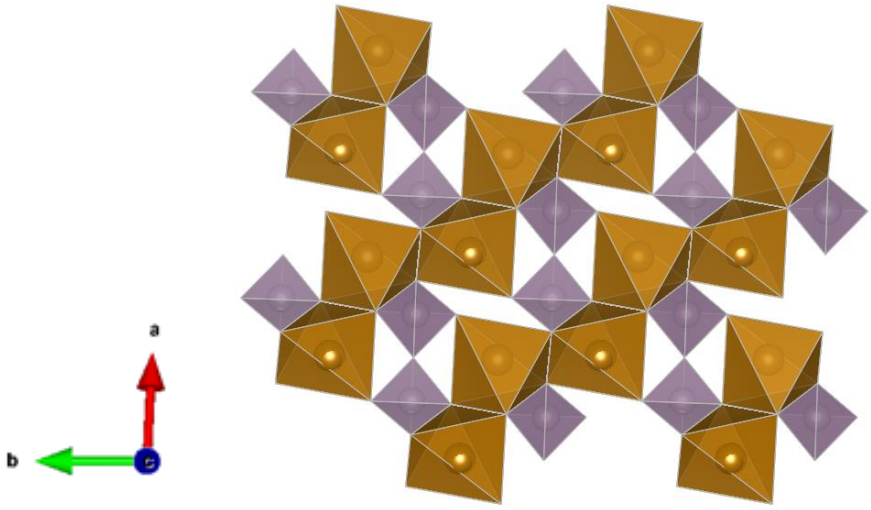

Figure 6.16 – The crystal structure of $Fe_2P_2O_7$ with the [0 0 1] direction normal to the page, with P_2O_7 polyhedra in grey and FeO_6 polyhedra in brown. The image was created using VESTA software from PDF Card. No. 01-076-1762.[90]

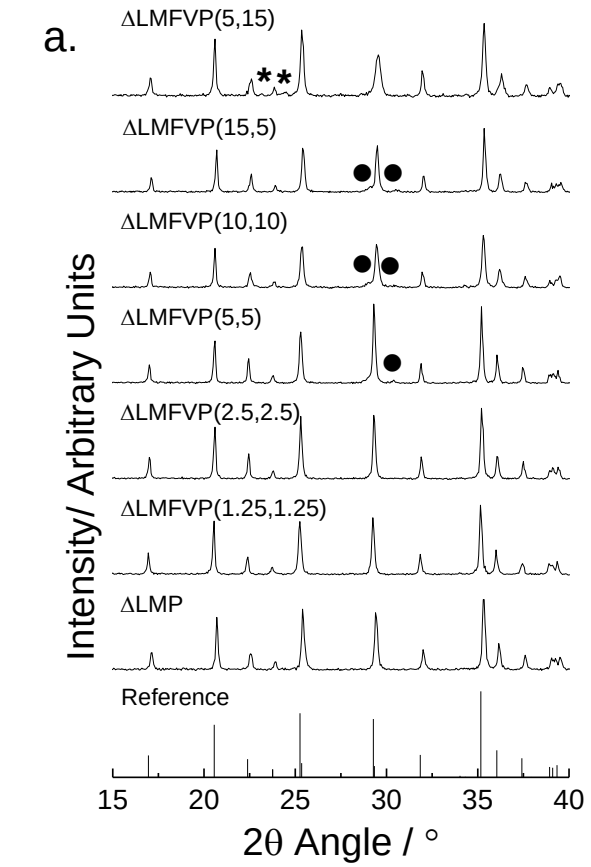

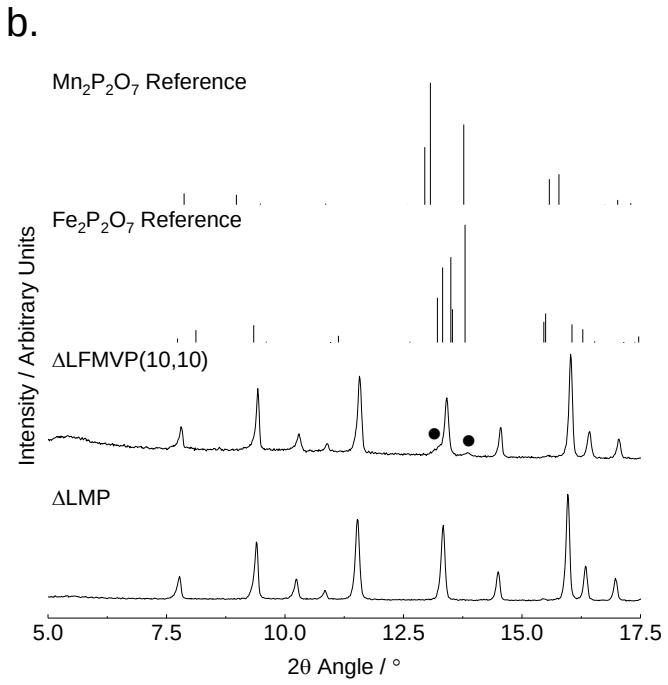

Figure 6.17 – a) XRD patterns of the V and Fe co-doped, heat-treated $LiMnPO_4$ samples, with PDF Card No. 01-074-0375 used as a reference. The $Li_3V_2(PO_4)_3$ impurity phase peaks are marked with asterisks, and the pyrophosphate impurity phase with a circle. b) High-quality XRD patterns of the pure, heat-treated $LiMnPO_4$ phase with the ΔLMFVP(10,10) sample, showing matches to pyrophosphate impurity phases. Adapted from reference 271.

ICP analysis was utilised to determine the elemental ratios of the elements contained within the samples. All samples appeared to be phosphorous deficient, and this was reasonably invariant as a function as composition. Therefore, a P content of 0.9 was assumed for all samples for the purpose of normalisation. The elemental composition of the 16 samples analysed was in broad agreement with the ratios employed as precursors (Table 6.6). There was a small discrepancy between the predicted and calculated Mn:V ratios for the V-doped samples; the Mn content and V contents were lower and higher than expected, respectively. This suggested partial Mn vacancy generation (as observed by Gutierrez *et al.*) as a defect compensation mechanism, which would explain the deficit. In addition, the Li content decreased uniformly with increasing V concentration (Table 6.6, Figure 6.18), in an analogous manner observed in Section 3.4.1.2 with the V-doped $LiFePO_4$ samples, whereas Li content was essentially invariant with Fe content. This is in contrast to the report of Gutierrez *et al*, who found the Li content was invariant with vanadium dopant concentration, and suggested that Li^+ vacancy generation is the dominant charge balancing mechanism within these samples. However, further structural analysis such as EXAFS is required to better understand the doping effect of V within this system.

Table 6.6 – The elemental composition of the sample array found from ICP-AES. The relative compositions were normalised to phosphorous, assuming a constant phosphorous deficiency of 10 at%.

Sample	Li/P	Mn/P	Fe/P	V/P	P/P
LMP	0.91	0.98	0.00	0.00	0.90
LMFVP(0,5)	0.91	0.94	0.00	0.05	0.90
LMFVP(0,10)	0.87	0.90	0.00	0.10	0.90
LMFVP(0,15)	0.77	0.86	0.00	0.17	0.90
LMFVP(0,20)	0.74	0.76	0.00	0.24	0.90
LMFVP(5,15)	0.77	0.77	0.04	0.20	0.90
LMFVP(10,10)	0.83	0.78	0.09	0.13	0.90
LMFVP(15,5)	0.87	0.83	0.14	0.07	0.90
LMFVP(2.5,0)	0.92	1.04	0.03	0.00	0.90
LMFVP(5,0)	0.93	0.99	0.05	0.00	0.90
LMFVP(10,0)	0.91	0.94	0.10	0.00	0.90
LMFVP(15,0)	0.91	0.89	0.14	0.00	0.90
LMFVP(20,0)	0.92	0.86	0.19	0.00	0.90
LMFVP(1.25,1.25)	0.92	1.01	0.02	0.01	0.90
LMFVP(2.5,2.5)	0.93	1.00	0.02	0.02	0.90
LMFVP(5,5)	0.85	0.92	0.05	0.05	0.90

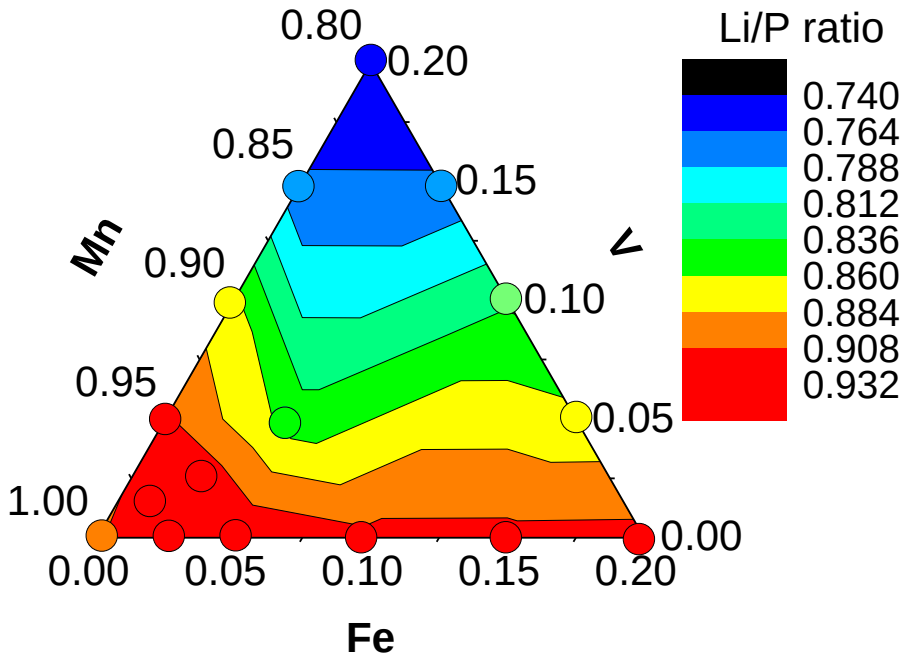

Figure 6.18 – The Li/P ratios of the sample array found from ICP-AES, plotted against nominal composition. The individual data points are marked with circles, with the value of the data point indicated by the colour of the circle.

For the samples with low dopant concentrations, ΔLMFVP(1.25,1.25) and ΔLMFVP(2.5,2.5), no impurity phases were obvious. In contrast, sample ΔLMFVP(5,15), which possessed the highest vanadium content of the doped samples, contained the $Li_3V_2(PO_4)_3$ impurity observed in the Mn-V binary system. This clearly demonstrated a consistent phase behaviour across the phase-space upon heat treatment; the Mn-V binary compositions and high V-content tertiary compounds gave $Li_3V_2(PO_4)_3$ impurities, whereas low V-content phases formed a pyrophosphate impurity phase.

FE-SEM analysis was used to ascertain changes in particle size and/or morphology with composition. All samples appeared to be formed of agglomerated particles approximately 100 – 300 nm across the long axis, with occasional larger agglomerates > 0.5 µm. In contrast to the V-doped $LiFePO_4$, no noticeable morphological change was observed with V-doping. However, Fe-doping appeared to increase the faceting of the particles (Figure 6.19b) whereby sample ΔLMFVP(20,0) appeared more cuboid-like, and therefore doping possibly altered the relative surface energies of the olivine samples. In addition, TEM analysis was employed to confirm the presence of a carbon coating *ca.* 1 – 1.5 nm thick on the $LiMnPO_4$ surface (Figure 6.20b). Analysis of the lattice planes evident within the particles revealed a d-spacing of 2.36 Å, which was consistent with the (0 0 2) lattice planes (d = 2.37 Å).

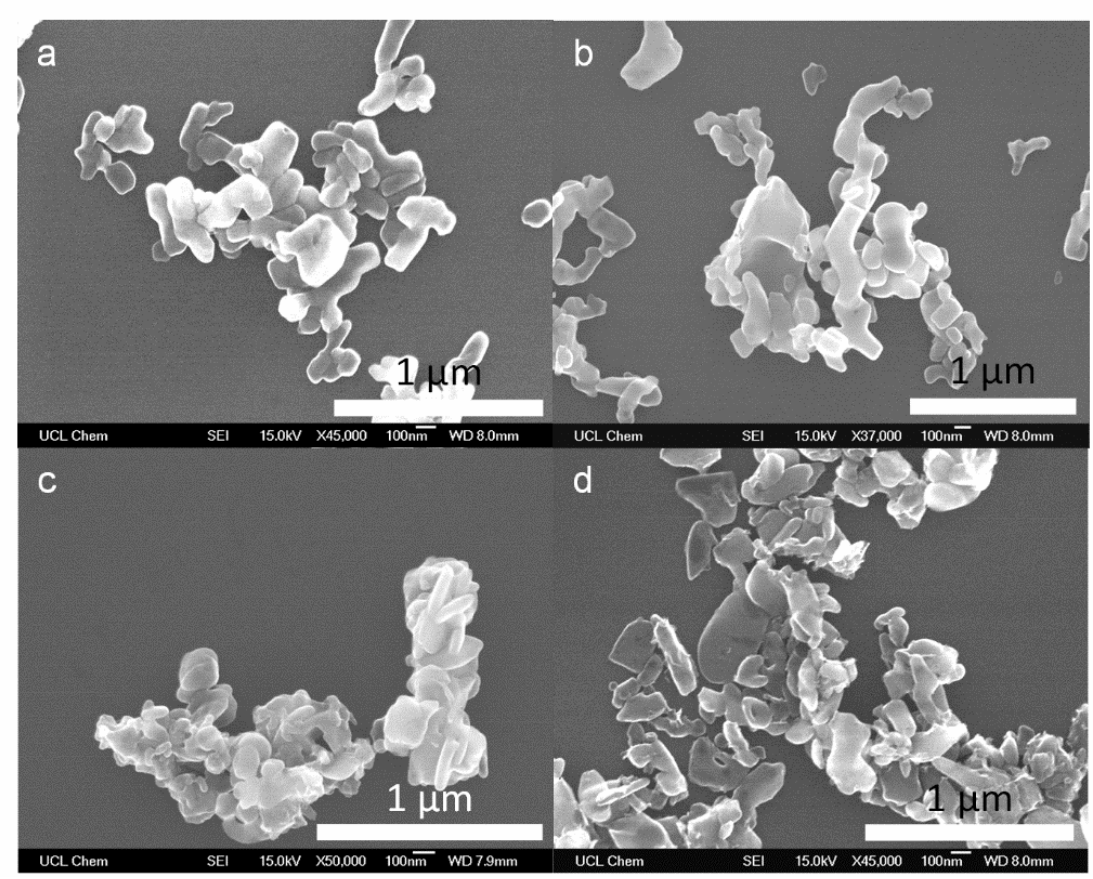

Figure 6.19 – SEM micrographs of a) ΔLMP, b) ΔLMFVP(20,0), c) ΔLMFVP(0,20) and d) ΔLMFVP(10,10). Adapted from reference 271.

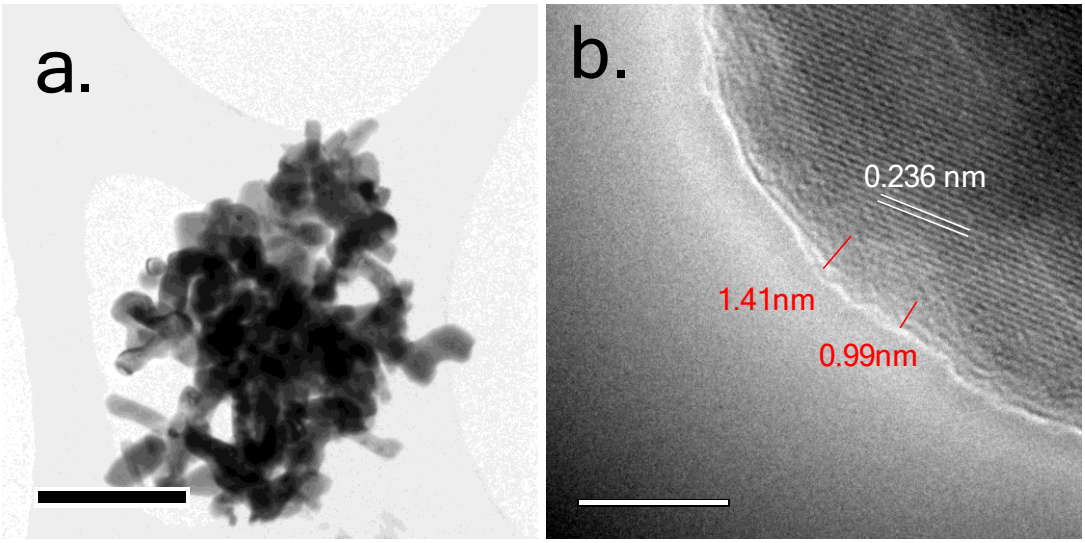

Figure 6.20 – TEM images of sample ΔLMP, where a) displays a representative cluster of particles and b) is a higher magnification image of the particle surface, with a carbon coating and lattice planes clearly visible. Adapted from reference 271.

6.4.2. Electrochemical Characterisation

All 17 heat-treated samples were processed into electrodes as described in Section 2.1.5.1 and made into Li-ion half-cells. Cyclic voltammetry (CV) tests were first conducted (scan rate 0.05 mV s^{-1}) to establish the redox processes occurring within the electrodes. The expected Mn^{2+}/Mn^{3+} redox couple was observed in all samples at 4.1 V vs. Li/Li^+ (Figure 6.21), with a sharper discharge peak compared to charge peak in all samples. This is in agreement with the relative kinetics previously observed in $LiMnPO_4$, i.e. the charge process is typically slower than the discharge process due to the effects of Jahn-Teller distorted Mn^{3+} ions. All samples within the Mn-Fe binary system, i.e. from sample ΔLMP to sample ΔLMFVP(20,0), showed the gradual emergence and growth of the Fe^{2+}/Fe^{3+} couple as the iron content increased beyond 5 at% (Figure 6.21a-f). Despite the reduced amount of active Mn species, the Mn^{2+}/Mn^{3+} redox couple peak discharge current increased with iron dopant (from *ca*. 50 mA g^{-1} to 100 mA g^{-1}) up to 10 at% Fe doping, and suggested that the inclusion of iron improved delithiation kinetics and/or increased the maximum Li extraction possible from the $LiMn_{1-x}Fe_xPO_4$ solid solution.

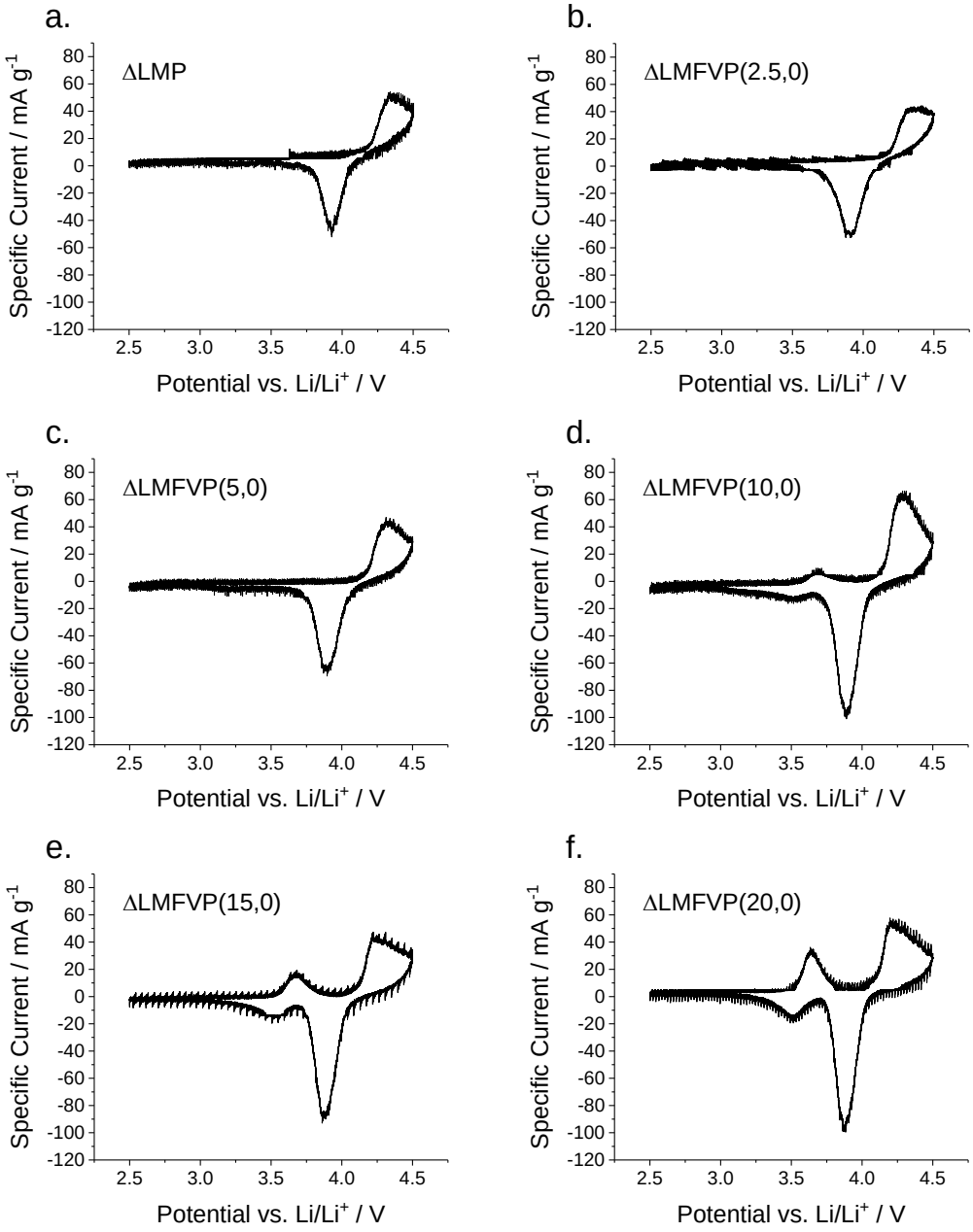

Figure 6.21 – Cyclic voltammograms of samples a) ΔLMP, b) ΔLMFVP(2.5,0), c) ΔLMFVP(5,0), d) ΔLMFVP(10,0), e) ΔLMFVP(15,0) and f) ΔLMFVP(20,0) at a scan-rate of 0.05 mV s^{-1}. Identical *y* axis scales were employed to facilitate comparison of peak discharge current. Adapted from reference 271.

The samples with high vanadium content (and with the minor $Li_3V_2(PO_4)_3$ impurity phase identified by XRD) displayed minor redox couples at 3.6, 3.7 and 4.1 V, which was consistent with the electrochemistry of the impurity phase (Figure 6.22e-f).[268] The current peak intensities of the Mn^{2+}/Mn^{3+} couple were almost invariant with V content, which implied it had a smaller effect on Li^+ diffusion dynamics compared to Fe doping (Figure 6.22), and/or that the maximum delithiation capability did not change as a

function of V content. The samples which possibly contained minor pyrophosphate impurity phase, ΔLMFVP(5,0) and ΔLMFVP(10,0), did not display any additional electrochemical features.

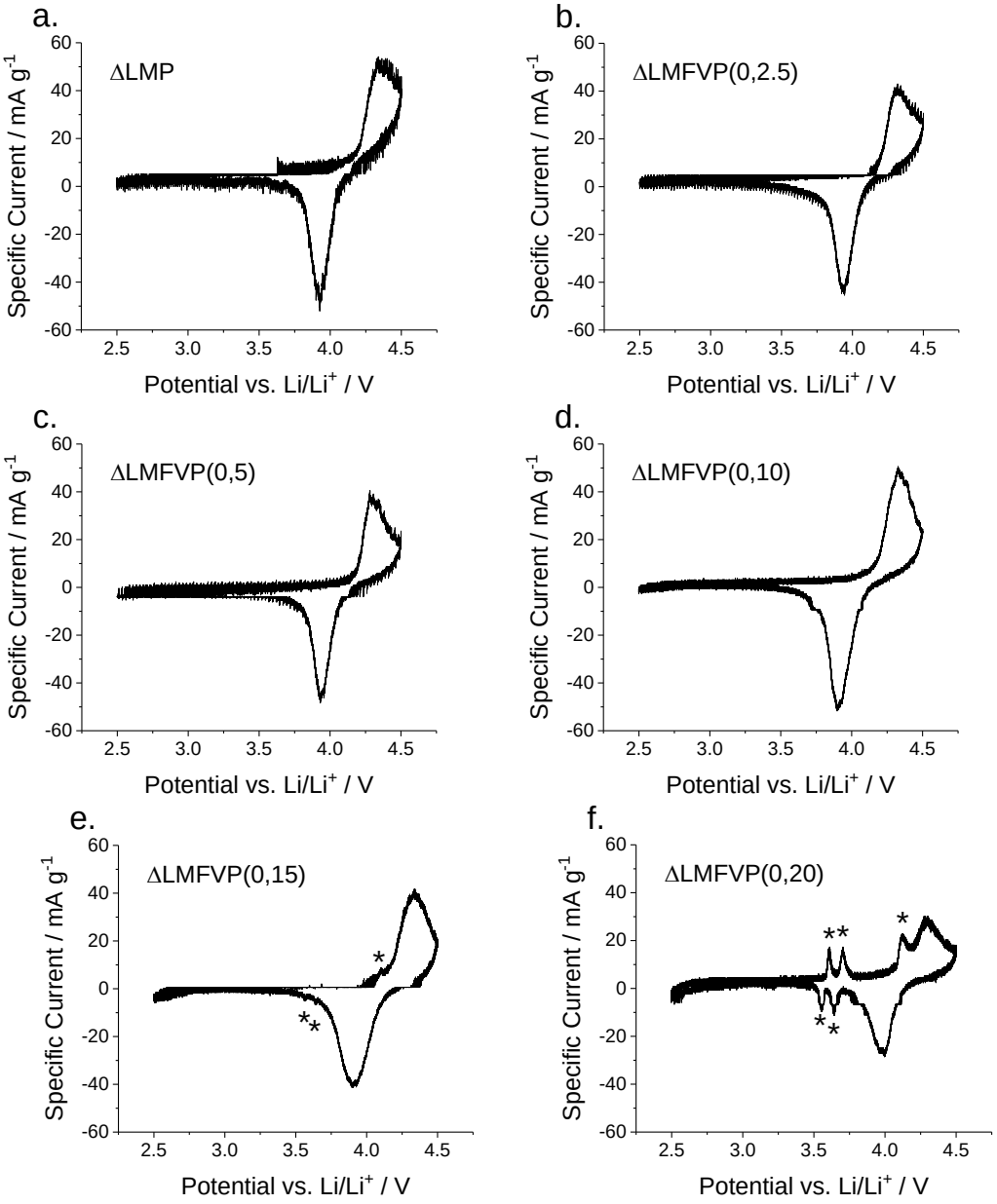

Figure 6.22 – Cyclic voltammograms of samples a) ΔLMP, b) ΔLMFVP(0,2.5), c) ΔLMFVP(0,5), d) ΔLMFVP(0,10), e) ΔLMFVP(0,15) and f) ΔLMFVP(0,20) at a scan-rate of 0.05 mV s^{-1}. Additional redox activity due to the $Li_3V_2(PO_4)_3$ phase is marked with asterisks. Identical *y* axis scales were employed to facilitate comparison of peak discharge current. Adapted from reference 271.

The minor pyrophosphate phase did not display any electrochemical activity in the co-doped samples where it was present (samples ΔLMFVP(5,5), ΔLMFVP(10,10) and ΔLMFVP(15,5), Figure 6.23d,f,g), consistent with ΔLMFVP(0,5) and ΔLMFVP(0,10). Within the co-doped samples, the electrochemistry observed

reflected the composition of the precursors. Characteristic redox peaks of $Li_3V_2(PO_4)_3$ were evident in the CV of the V-rich sample ΔLMFVP(5,15) (Figure 6.23e), whereas the Fe^{2+}/Fe^{3+} couple was observed in samples ΔLMFVP(10,10) and ΔLMFVP(15,5) (Figure 6.23f-g). The peak discharge currents appeared to be largely invariant with composition, aside from the larger current observed in sample ΔLMFVP(15,5) (Figure 6.23g). An anomalous feature was observed at ~4 V for ΔLMFVP(5,5) (Figure 6.23d), but was not observed on subsequent cycles and was assumed to be an electrolyte impurity side-reaction.

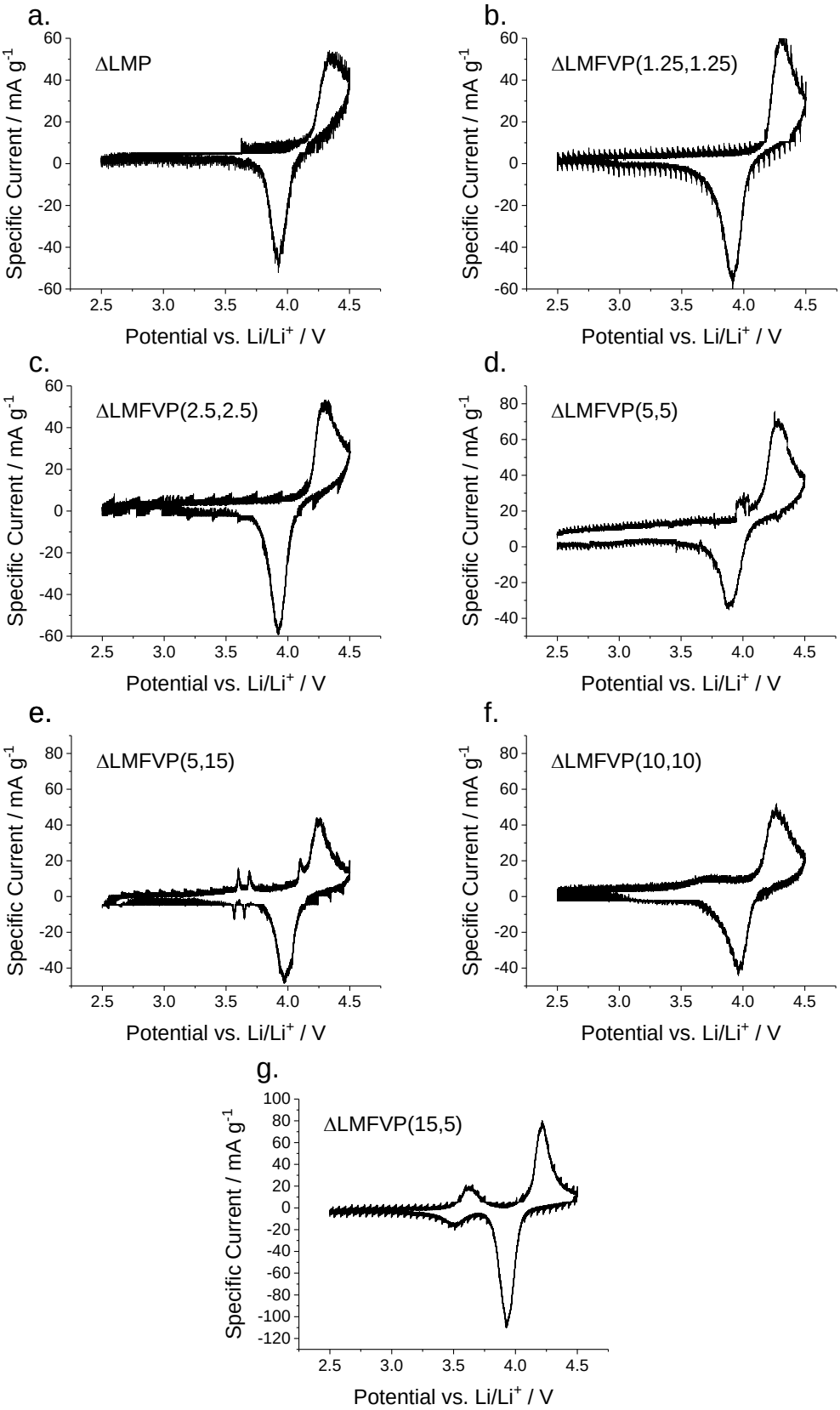

Figure 6.23 – Cyclic voltammograms of samples a) ΔLMP, b) ΔLMFVP(1.25,1.25), c) ΔLMFVP(2.5,2.5), d) ΔLMFVP(5,5), e) ΔLMFVP(5,15), f) ΔLMFVP(10,10) and g) ΔLMFVP(15,5) at a scan-rate of 0.05 mV s^{-1}. Variable *y*-axis scales were employed within these plots. Adapted from reference 271.

Constant current, constant voltage tests were employed to determine the ability of the samples to respond to current load. The nature of the testing employed relatively rapid charge/discharge currents to quickly determine the samples of greatest interest (i.e. C/2 and higher), with slower testing reserved for these samples (i.e. C/10 and C/5). The discharge capacities at C/2, 1C, 2C and 5C were all plotted as a function of composition as a heat map (Figure 6.24a-d). It can be seen that uniform variation in capacity was observed as a function of composition for all four C-rates, where inclusion of the Fe dopant gave the most significant increase in discharge capacity (compared to the pure $LiMnPO_4$ sample). In contrast, V-doping gave little improvement to discharge capacity.

However, inspecting the charge/discharge curves of key samples ΔLMP, ΔLMFVP(0,20), ΔLMFVP(10,10) and ΔLMFVP(20,0) revealed a more nuanced picture (Figure 6.25 – Figure 6.28). While the capacities of the iron-doped samples were greater than the V-doped samples, especially at a low C-rate testing of C/10 (Figure 6.29), they experienced greater polarisation with increasing charge/discharge rates, i.e. the overpotentials were increased relative to those observed in the ΔLMFVP(20,0). This is in agreement with the findings of Gutierrez *et al.* and Wang *et al*. who also observed decreased overpotentials with V-doping and the presence of $Li_3V_2(PO_4)_3$. The effects of this can clearly be seen when considering energy density as a function of discharge rate (Figure 6.30). The difference between the energy densities at low C-rates was stark, and clearly showed that the iron dopant makes the greatest positive impact. However, when the C-rate increased, the V-doped samples, ΔLMFVP(10,10) and ΔLMFVP(0,20), retained a greater proportion of energy density than of ΔLMFVP(20,0). This suggested that the Fe dopant enabled greater maximum extraction of Li from the $LiMnPO_4$ structure, and hence improved low rate performance. The V dopant and $Li_3V_2(PO_4)_3$ impurity, in contrast, reduced the overpotential of the Mn^{2+}/Mn^{3+} conversion to give greater capacity retention with increasing charge/discharge rate (Figure 6.29). As hypothesised, the two dopants provided separate beneficial effects to improve the performance of the $LiMnPO_4$ cathode materials.

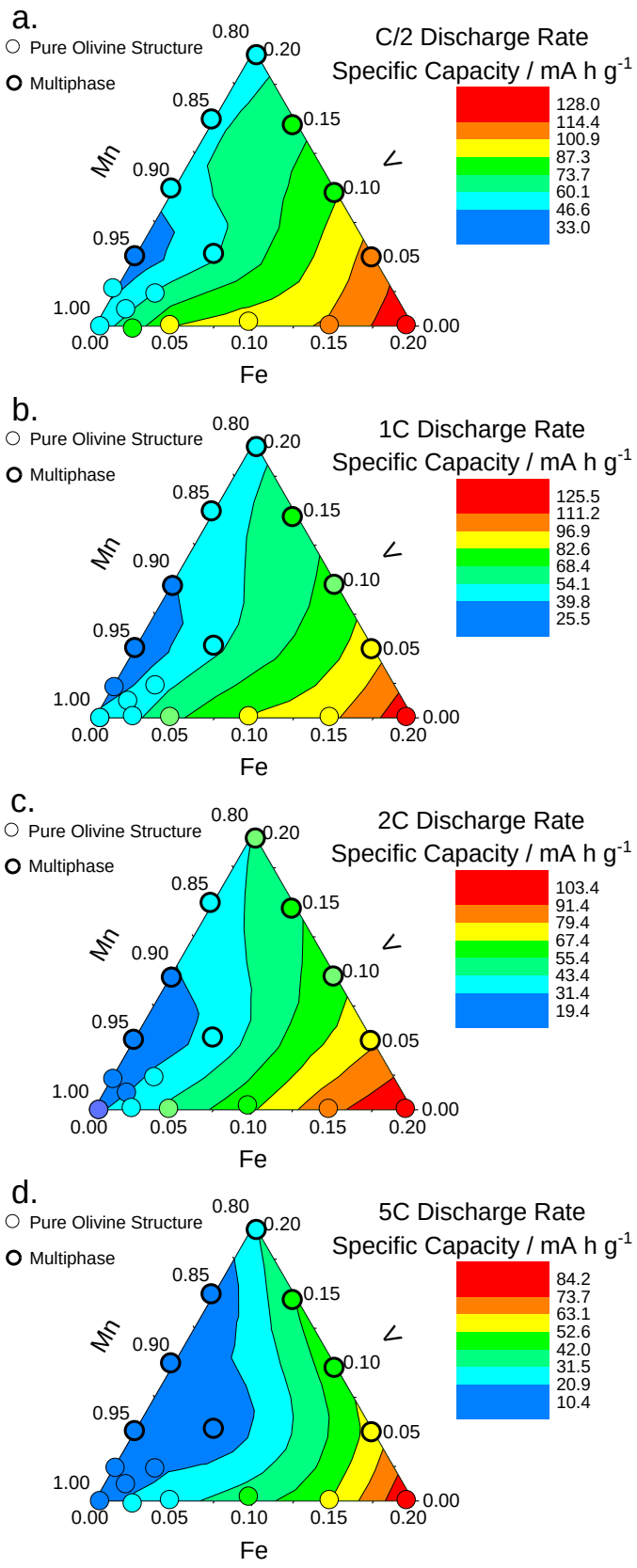

Figure 6.24 – The discharge capacities observed for all samples plotted as a function of composition at discharge rates of a) C/2, b) 1C, c) 2C and d) 5C. The capacities for each composition were indicated by the colour of the circles. The impure samples were indicated with a dark border. Adapted from reference 271.

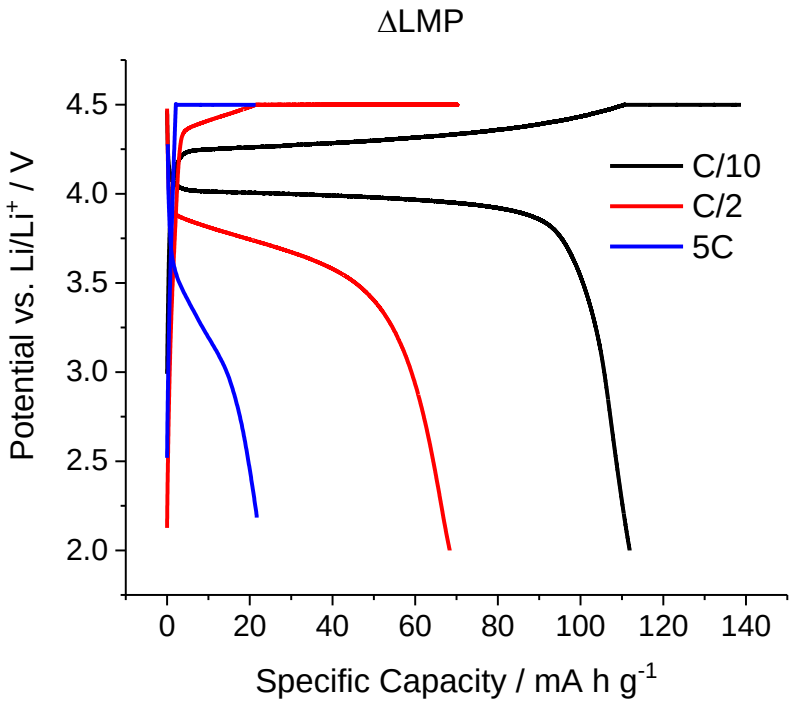

Figure 6.25 – The charge/discharge curves for sample ΔLMP at rates of C/10 (first cycle), C/2 (fifth cycle) and 5C (fifth cycle).

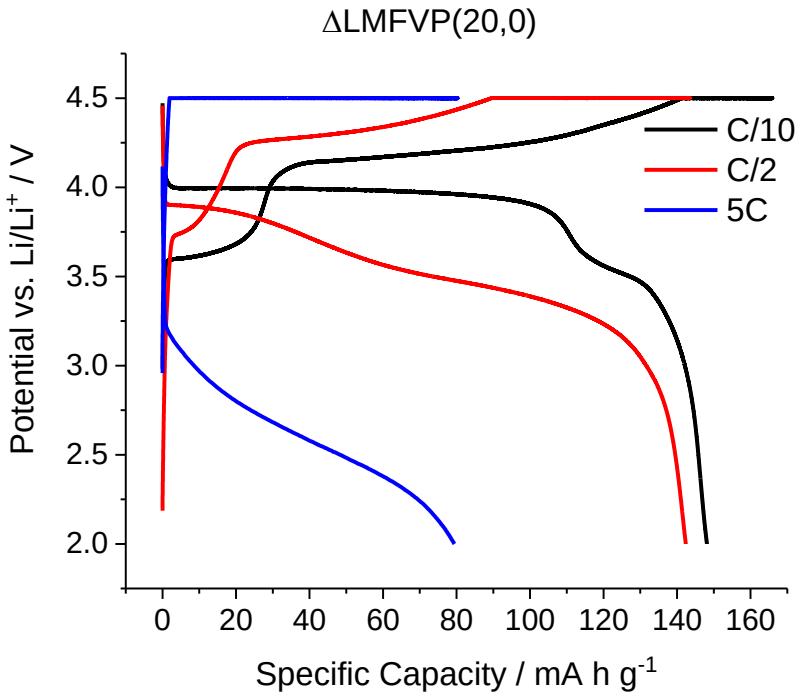

Figure 6.26 – The charge/discharge curves for sample ΔLMFVP(20,0) at rates of C/10 (first cycle), C/2 (fifth cycle) and 5C (fifth cycle).

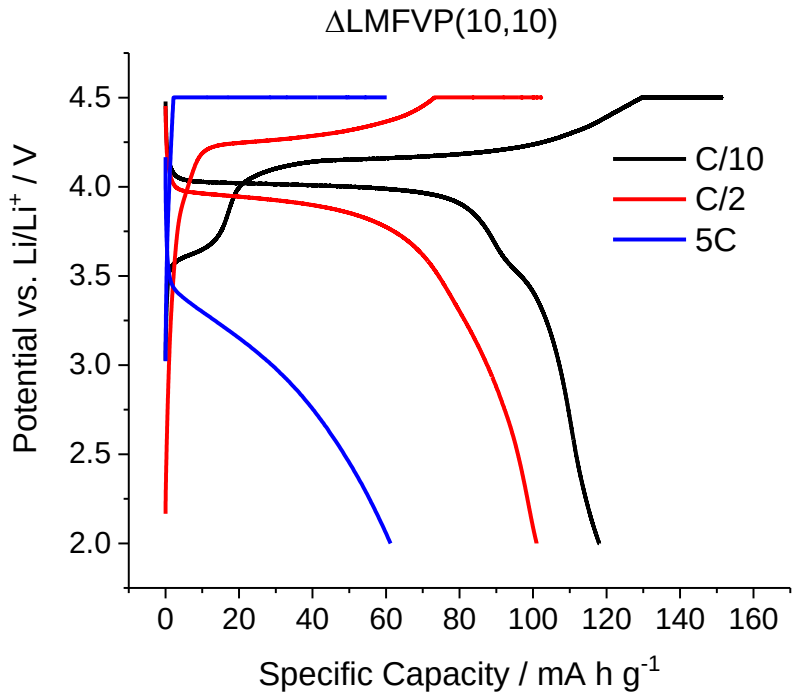

Figure 6.27 – The charge/discharge curves for sample ΔLMFVP(10,10) at rates of C/10 (first cycle), C/2 (fifth cycle) and 5C (fifth cycle).

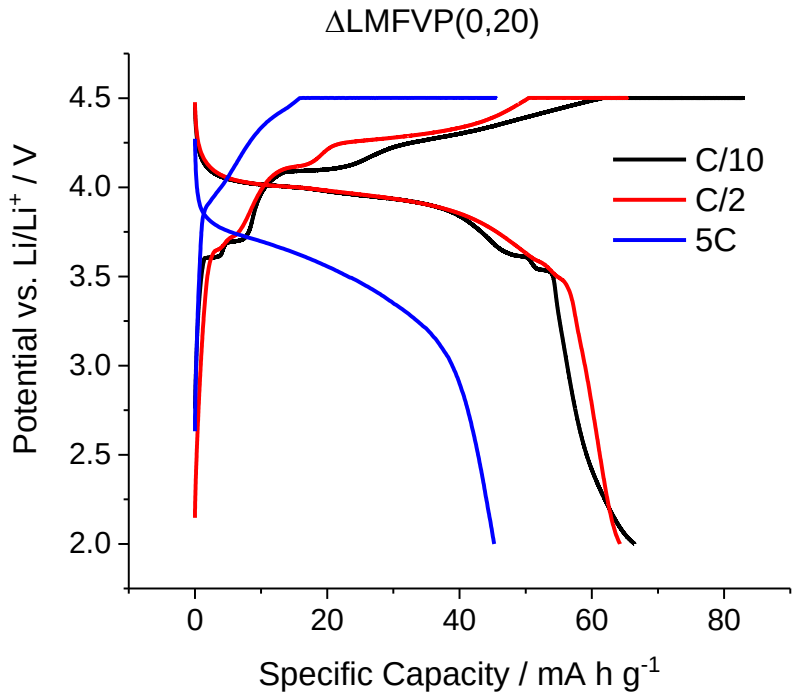

Figure 6.28 – The charge/discharge curves for sample ΔLMFVP(0,20) at rates of C/10 (first cycle), C/2 (fifth cycle) and 5C (fifth cycle).

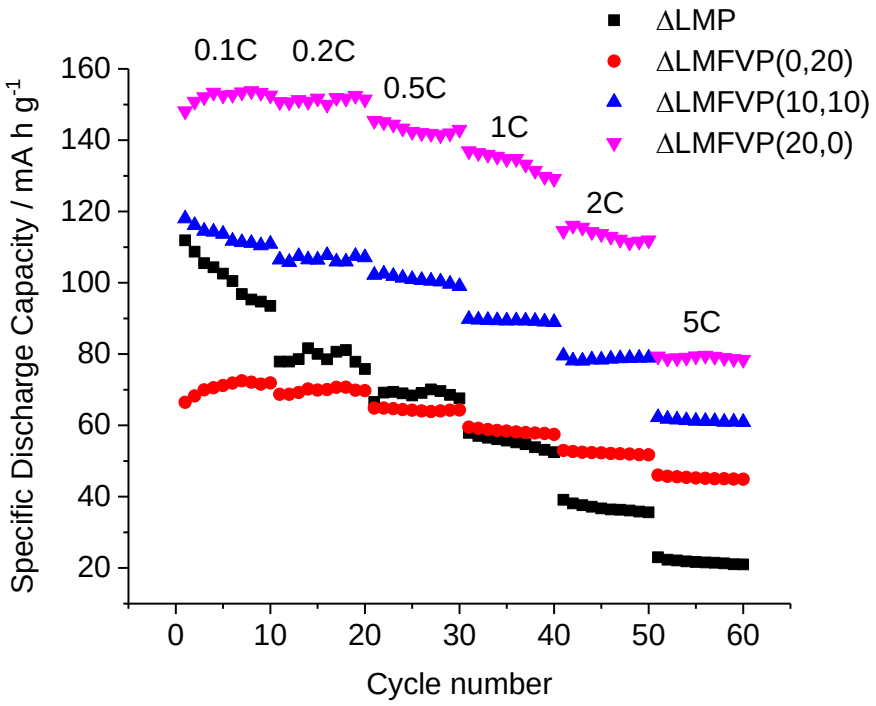

Figure 6.29 – The discharge capacities of ΔLMP, ΔLMFVP(0,20), ΔLMFVP(10,10) and ΔLMFVP(20,0) at C-rates in the range 0.1C – 5C.

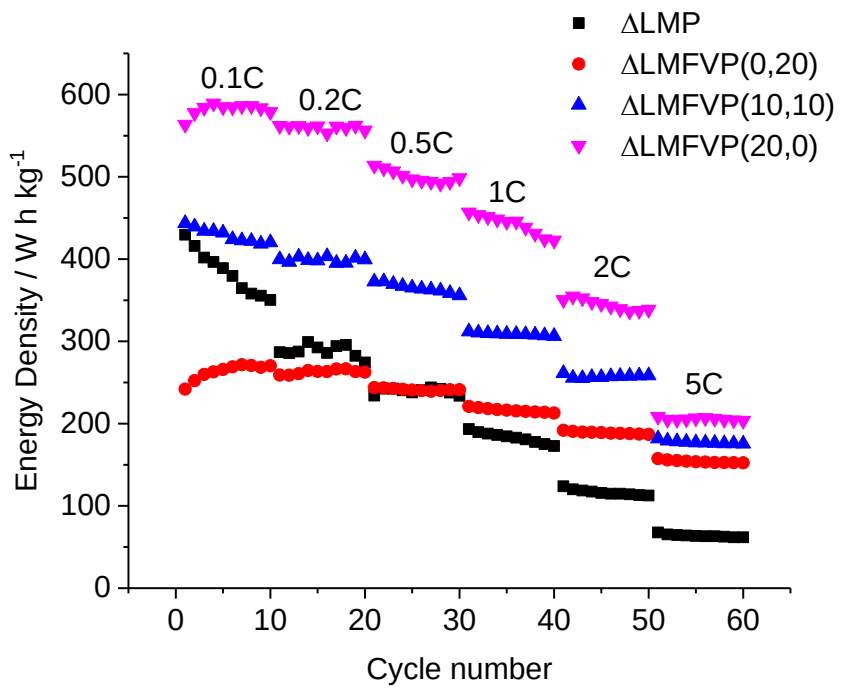

Figure 6.30 – The energy densities of ΔLMP, ΔLMFVP(0,20), ΔLMFVP(10,10) and ΔLMFVP(20,0) at C-rates in the range 0.1C – 5C.

The best performing sample within the range explored ($LiMn_{0.8}Fe_{0.2}PO_4$) achieved a discharge capacity of 153 mA h g^{-1} at C/10 discharge rate, and between 80 – 85 mA h

g^{-1} at 5C discharge rate (between the two batches). A stable coulombic efficiency of ~98% was also observed, which is similar to that observed for ΔLFVP(5) (Figure 6.21, Chapter 4). While a commercial electrode would typically require a lower carbon content than those employed in this study (15 vs. 5 wt%), this was still comparatively low compared to similar $LiMnPO_4$ materials reported previously. A long-term cycling test at C/10 for 200 cycles for ΔLMFVP(20,0) showed 70% capacity retention (Figure 6.32), which would have to be improved if ΔLMFVP(20,0) is to be employed in a commercial device.

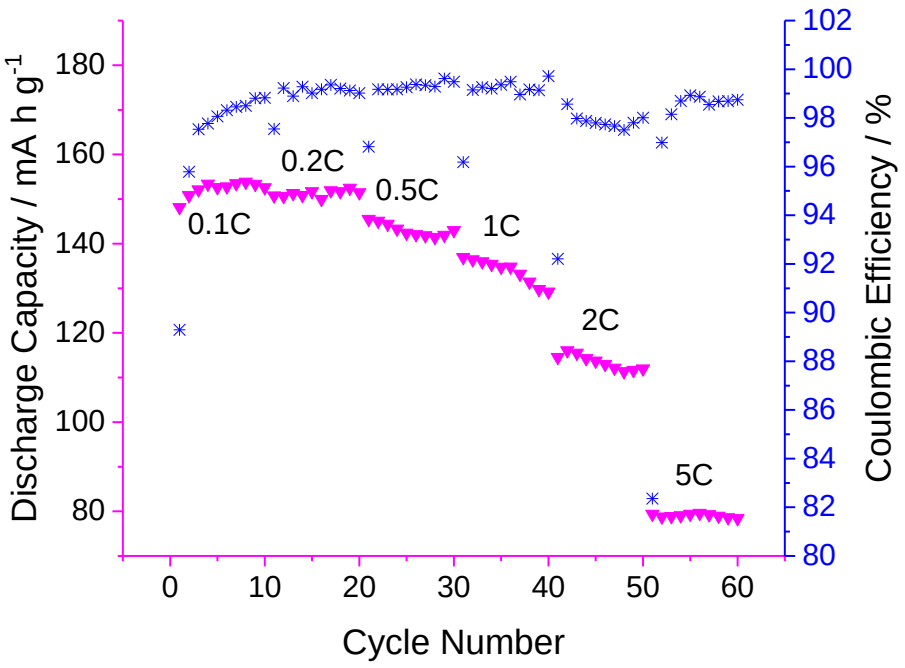

Figure 6.31 – The discharge capacities of ΔLMFVP(20,0) at C-rates between 0.1C – 5C (pink triangles) with the coulombic efficiency (blue asterisks) for each cycle.

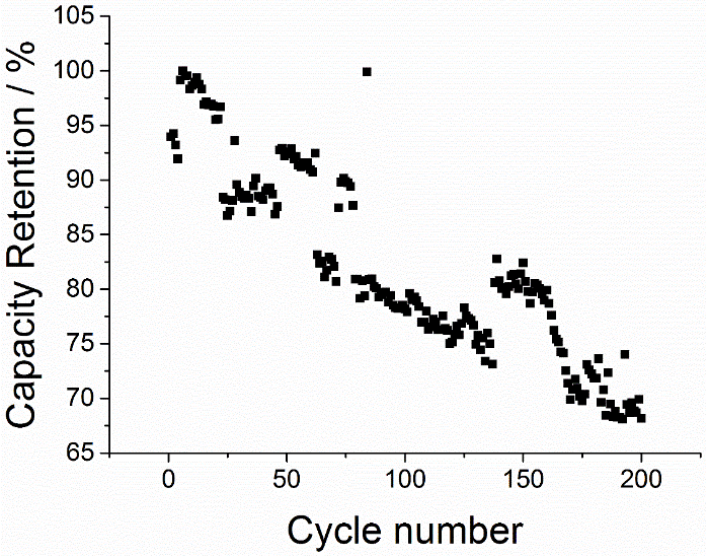

Figure 6.32 – The capacity retention of ΔLMFVP(20,0) over 200 cycles at a charge/discharge rate of C/10. Adapted from reference 271.

6.5. Conclusions and Further Work

The CHFS Pilot-Scale process was utilised to systematically synthesise and analyse an array of Fe- and V-doped $LiMnPO_4$ samples in a high-throughput manner. It was found that Fe improved the maximum attainable capacity of $LiMn_{1-x-y}Fe_xV_yPO_4$ cathodes, whereas doping with V or generating the $Li_3V_2(PO_4)_3$ impurity phase reduced the overpotentials observed with charge/discharge, confirming they impart different effects on the $LiMnPO_4$ cathodic behaviour. The optimal composition within the array analysed achieved a high energy density of 580 W h kg^{-1} at a discharge rate of C/10, which is 83% of the theoretical of $LiMnPO_4$, and represents a step forward in the development of this material as a commercial high energy cathode material and compares favourably with other high-performance $LiMnPO_4$ materials from literature.

Further work on this co-doped system could include a combined EXAFS/XRD study to investigate the location of the V dopant within $LiMnPO_4$, and to confirm the generation of Li vacancies. Furthermore, it is suggested that further synthesis and doping studies should be conducted to achieve a compromise between the two dopants; by fixing the Mn:Fe ratio at 4:1, and including greater proportions of V, a reasonably high-energy cathode with high rate performance could be achieved. As it stands, the current optimal cathode is suitable only for low-power applications, and further work

is needed to improve electrolyte stabilities and coulombic efficiencies to advance this material to the battery pack level and commercialisation.

In conclusion, these results clearly highlight the benefit of analysing multiple doped compounds across a compositional array, and suggest that this method should be employed within other doped systems. In light of this, the next chapter aims to investigate $LiNi_xMn_yCo_zO_2$ compounds in a similar manner.

7. Synthesis and Evaluation of High Energy-Density $LiCoO_2$ and Ni, Mn doped variants

7.1. Aims

$LiCoO_2$ (LCO) and the doped compounds $LiNi_xMn_yCo_zO_2$ (NMC) are amongst a range of commercial cathode materials that are of interest for high energy density applications, such as electric vehicle batteries. Their high energy density stems from their relatively high tap density (5.1 g cm^{-3}) compared to $LiFePO_4$ (3.6 g cm^{-3}) and their high operating voltage (~4 V vs. Li/Li^+). However, these are generally made *via* solid-state processes with high reaction temperatures and long reaction times. Therefore, there is significant commercial interest in the scalable production of LCO and NMC at lower temperatures and reaction times. LCO has been made previously *via* CHFS, albeit with large Li excesses, whereas the synthesis of NMC has never been reported by this method. This chapter concerns the attempted continuous hydrothermal synthesis of these compounds, and preliminary electrochemical evaluation.

7.2. Background

The LCO phase was first reported as a Li-ion battery cathode by Mizushima *et al*. in 1980.[89] It was very rapidly developed by SONY to be incorporated in the first commercially successful Li-ion cell in the 90s, and used a graphite anode and LCO cathode.[272] Many commercial cells are still based upon LCO, or the related NMC compounds, and this introduction summarises the reactivity of these phases.

7.2.1. Structure and Reactivity

LCO and NMC both possess the layered, α-$NaFeO_2$ structure (trigonal crystal system) with space group $R\bar{3}m$, which can be understood as a cubic closed-packed array of oxide ions with alternating layers of Co^{3+} and Li^+ (Figure 7.1). Upon charge, the Li^+ is removed from the LCO structure, but in contrast to LFP and LMP, this occurs in the solid-state regime, i.e. Li is uniformly removed from between the LCO layers, rather than forming discrete lithiated and delithiated phases. To balance the charge, Co^{3+} converts to Co^{4+}.

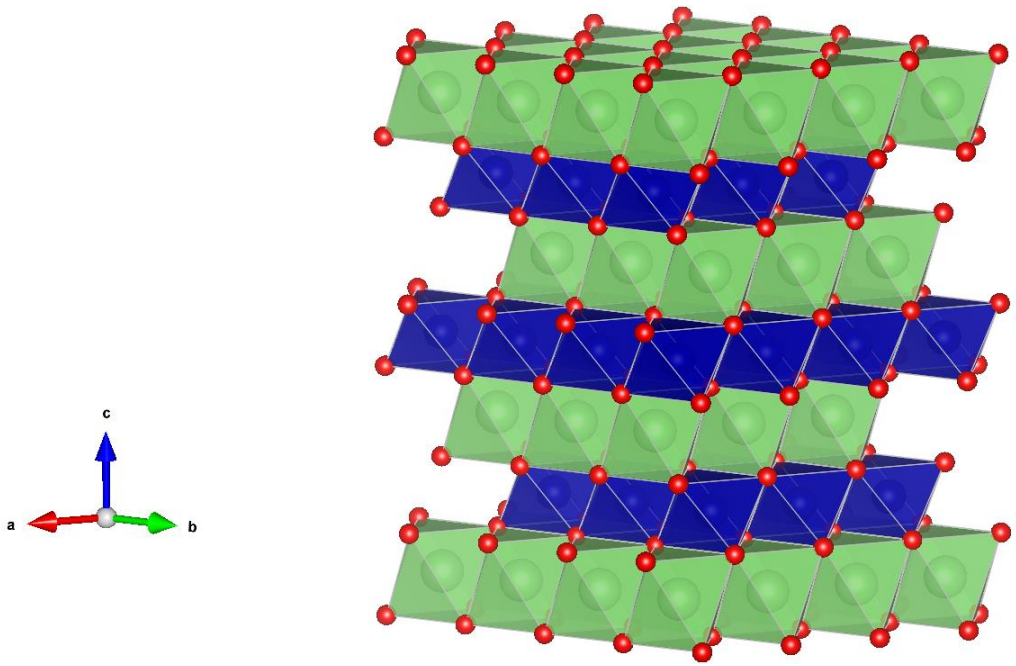

Figure 7.1 – The structure of $LiCoO_2$ viewed along the [1 1 0] axis, with the (0 0 1) planes visible (the plane normal is parallel to the *c*-axis). The CoO_6 octahedra are blue, and the LiO_6 octahedra are green, with oxygen atoms represented as red balls. The structure was generated from PDF Card No. 01-070-2685 using VESTA software.[90]

It has been found by the original researchers and others that Li cannot be fully removed from the LCO structure without irreversible structural changes taking place;[89] the cubic close-packed oxide structure re-organises to a hexagonal close packed structure, and results in capacity fade with repeated cycling.[273] This limited the initial discharge capacity to 140 mA h g^{-1} ($Li_{0.5}CoO_2$ as the charge product). Working within the original 0.5 Li per formula unit limit, the lattice parameters and unit cell volume are remarkably consistent with charge and discharge (Table 7.1). There is only a 2% volume change overall, and this small change is partially responsible for the highly reversible intercalation chemistry of this phase (Table 7.1).

Table 7.1 – The lattice parameters and unit cell volume of the unit cells of $LiCoO_2$ and the partially delithiated $Li_{0.5}CoO_2$ phase. [89]

Structural formula	*a* parameter / Å	*c* parameter / Å	Unit cell volume *V* / Å^3
$LiCoO_2$	2.816	14.08	83.5
$Li_{0.5}CoO_2$	2.807	14.42	84.9

As part of a separate investigation, the compounds $LiNiO_2$ and its doped analogue $LiNi_{0.5}Mn_{0.5}O_2$ were explored as Li-ion battery cathodes. $LiNiO_2$ is isostructural with $LiCoO_2$, but cannot be used as a cathode in its pure form for a variety of reasons.

Firstly, stoichiometric $LiNiO_2$ may not exist, as many researchers claim the stable structure incorporates an excess of Ni within the Li layers, generating the compound $Li_{1-x}Ni_{1+x}O_2$.[274–276] Additionally, upon significant Li extraction the remaining structure is unstable to O_2 gas evolution, which is a significant safety concern.[277] The $LiNi_{0.5}Mn_{0.5}O_2$ material, in contrast, can be fully delithiated, and Mn is therefore thought to stabilise the α-$NaFeO_2$ structure during charge and discharge. XPS confirmed the oxidation states found in $LiNi_{0.5}Mn_{0.5}O_2$ are Ni^{2+} and Mn^{4+}, as opposed to Ni^{3+} and Mn^{3+}.[278] Therefore, Mn remains electrochemically inactive upon charge, and Ni^{2+} is oxidised to Ni^{4+}. Mn does not, however, reduce the presence of Ni within the Li layers, which is suspected to impact the rate performance of these materials in a similar manner to antisite defects in $LiFePO_4$.[279]

The addition of Co to $LiNi_{0.5}Mn_{0.5}O_2$ (forming NMC compounds) was found to have dual benefits; it reduces the presence of Ni in the Li layers,[280] and the electronic conductivity increases an order of magnitude between $LiNi_{0.5}Mn_{0.5}O_2$ and $LiNi_{0.4}Mn_{0.4}Co_{0.2}O_2$.[281] XPS studies confirm the common oxidation states found in lithiated NMC are Ni^{2+}, Co^{3+} and Mn^{4+}, although there is a small amount of Ni^{3+} and Mn^{3+} present.[282] In NMC compounds, the Ni constituent has the greatest capacitive contribution, and Co only contributes at higher electrochemical potentials. Mn, in an analogous way to $LiNi_{0.5}Mn_{0.5}O_2$, is electrochemically inactive, but stabilises the structure with repeated cycling.[273] NMC based materials have a slight advantage over LCO, in that they can be charged/discharged at higher potentials of 4.3 – 4.4 V (thus increasing the average discharge voltage), and a greater proportion of Li can be extracted before irreversible structural changes occur, increasing capacity (Figure 7.2). Increasing both voltage and capacity results in increased energy density with respect to LCO, and NMCs have hence been used in high energy density applications, such as the Chevy Volt electric vehicle.[283]

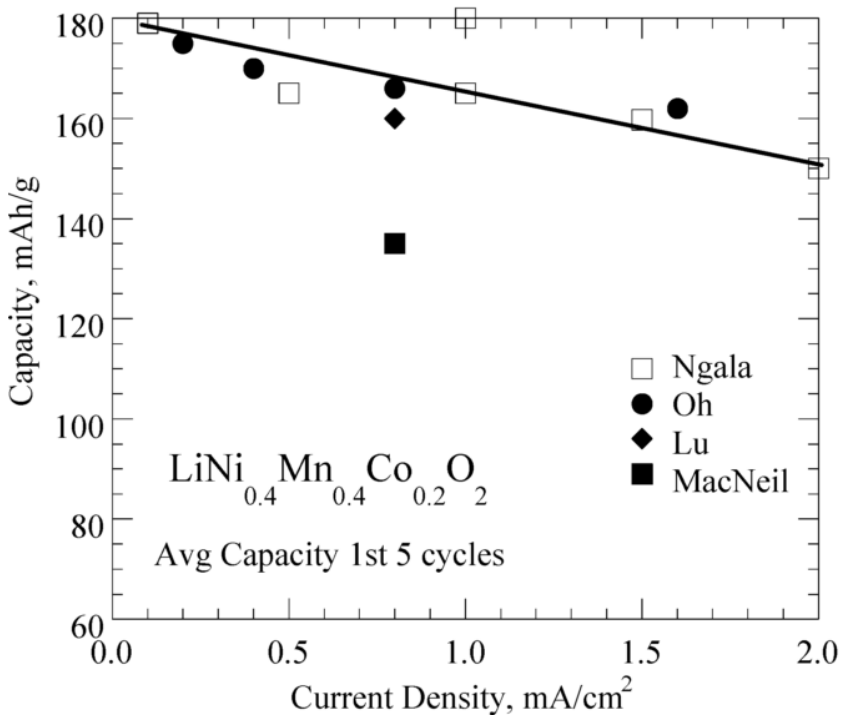

Figure 7.2 – A plot displaying the different capacities achieved by NMC compounds at different current densities. Reprinted with permission from Whittingham, M. S. Lithium batteries and cathode materials. *Chem. Rev.* **104,** 4271–4301 (2004). Copyright 2004 American Chemical Society.[273]

7.2.2. Previous Continuous Hydrothermal Synthesis Efforts

The first continuous hydrothermal synthesis of LCO was reported by Kanamura *et al.* in the early 2000s.[60] Reaction conditions of 20:1:1 $LiOH:Co(NO_3)_2:H_2O_2$ were employed at a 400 °C mixing point temperature with a residence time of 12 s to achieve the LCO phase. The H_2O_2 was required to oxidise Co^{2+} to Co^{3+}, and was included in the supercritical water feed to decompose H_2O_2 to O_2 gas before meeting the Co and Li precursors. Minor, semi-crystalline impurities were observed, and the authors suggested their structure was defective, i.e. there was significant amount of Co within the Li layer. The same authors found in a later study that lower synthesis temperatures of 300 – 350 °C were insufficient to generate LCO, forming Co_3O_4 instead.[284] The pure LCO formed in the later study had particle sizes in the range 0.6 – 1.0 µm, and achieved a discharge capacity of 120 mA h g^{-1}.

A more detailed study on the effect of reaction conditions on LCO formation in CHFS processes was performed by Shin *et al.*, who found that pure LCO could be formed independent of residence time (within the explored range of 7-58 s). As above, a high Li excess (10:1 Li:Co ratio) was required to drive the formation of LCO, and any

reactions in subcritical water produced Co_3O_4 as opposed to LCO. It was suggested that CoOOH formed as an intermediate product of the reaction, which was more rapidly decomposed in supercritical water, producing the desired LCO phase. In addition, the excess of LiOH was suggested to have a doubly beneficial effect; the greater Li content biased the formation of the lithiated phase, and the higher OH^- content catalysed the nucleation of nanoparticles according to Section 1.1.2.1. Again, the pure LCO phase produced in their report was a similar size to other reports, with a volume-weighted average of 0.55 µm particle size.

To date, there are no reports of the continuous hydrothermal flow synthesis of NMC-type materials, and therefore achieving this phase *via* CHFS would be a significant first. However, there are reports of batch supercritical hydrothermal synthesis of NMC, where stoichiometric Li:M ratios were used (where M are the combined Ni, Mn and Co transition metals) to generate the expected pure phase. This was achieved by using KOH as an additional base, raising OH^- concentration without requiring increased Li.[285] This suggests a similar strategy may be successful in the continuous synthesis of LCO and NMC, reducing the Li excess in the process and increasing the commercial viability of a CHFS-made route.

7.3. Experimental

The LCO and NMC samples synthesised in this chapter were produced using both the Low-Temperature and High-Temperature Lab-Scale CHFS processes (Section 2.1.1). Low-temperature experiments were conducted with flow rates of 80, 25 and 25 mL min^{-1} from P1, P2 and P3, respectively, to give a mixing point temperature of 378 °C (Figure 7.3). A full description of the Low-Temperature Lab-Scale process is given in Section 2.1.1.2. For these experiments, a 6-metre-long ¼" section of pipe (internal volume 18300 cm^3) was added in a heated oven section (temperature set to 450 °C, component O in Figure 7.3) to extend the effective residence time from 6.5 to 12 s.

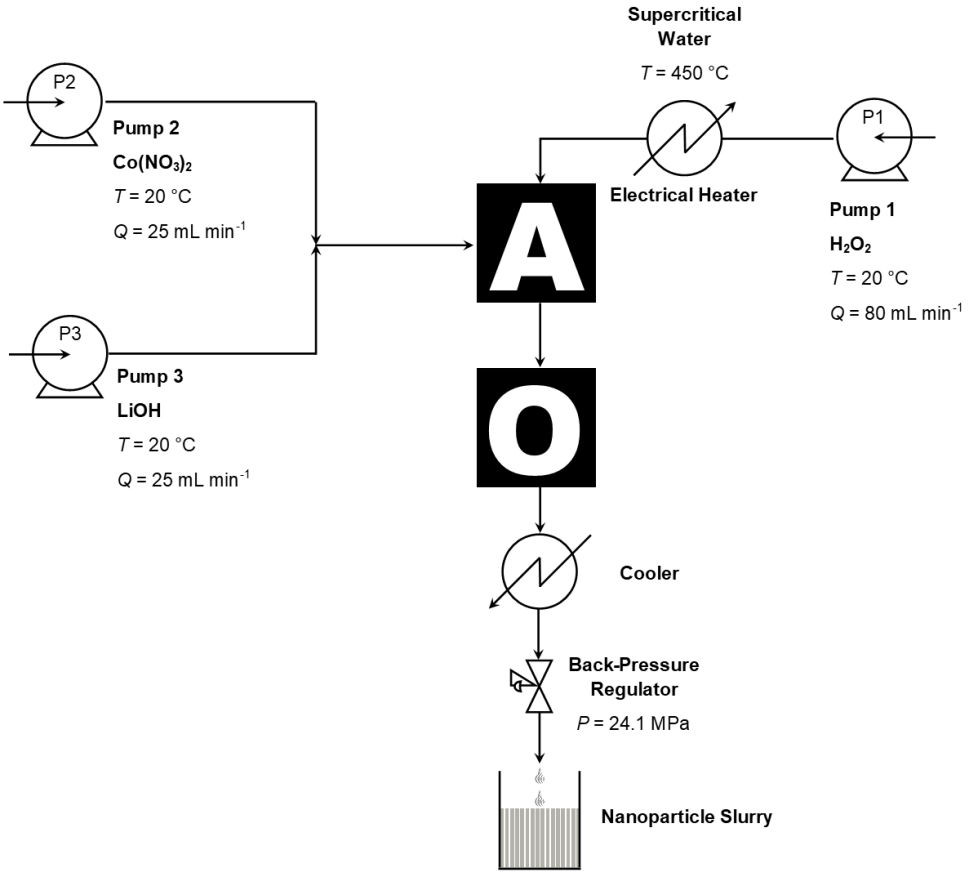

Figure 7.3 – The Low-Temperature Lab-Scale apparatus with additional oven attachment (position O). The Low-Temperature Lab-Scale mixer was employed in position A, as described in Section 2.1.2.1.

The high-temperature reactions, in contrast, were conducted using P1, P2 and P3 flow rates of 80, 5, 5 80, 7.5, 7.5 mL min^{-1}, giving mixing point temperatures of 402 °C and 391 °C, respectively (Figure 7.4). A full description of the High-Temperature Lab-Scale process is included in Section 2.1.1.3. For some experiments, a 6 m section of ¼" pipe (internal volume 18300 cm^3) was added in a heated oven section (temperature set to 450 °C) to extend the effective residence time from 1.0 to 5 s in position C.

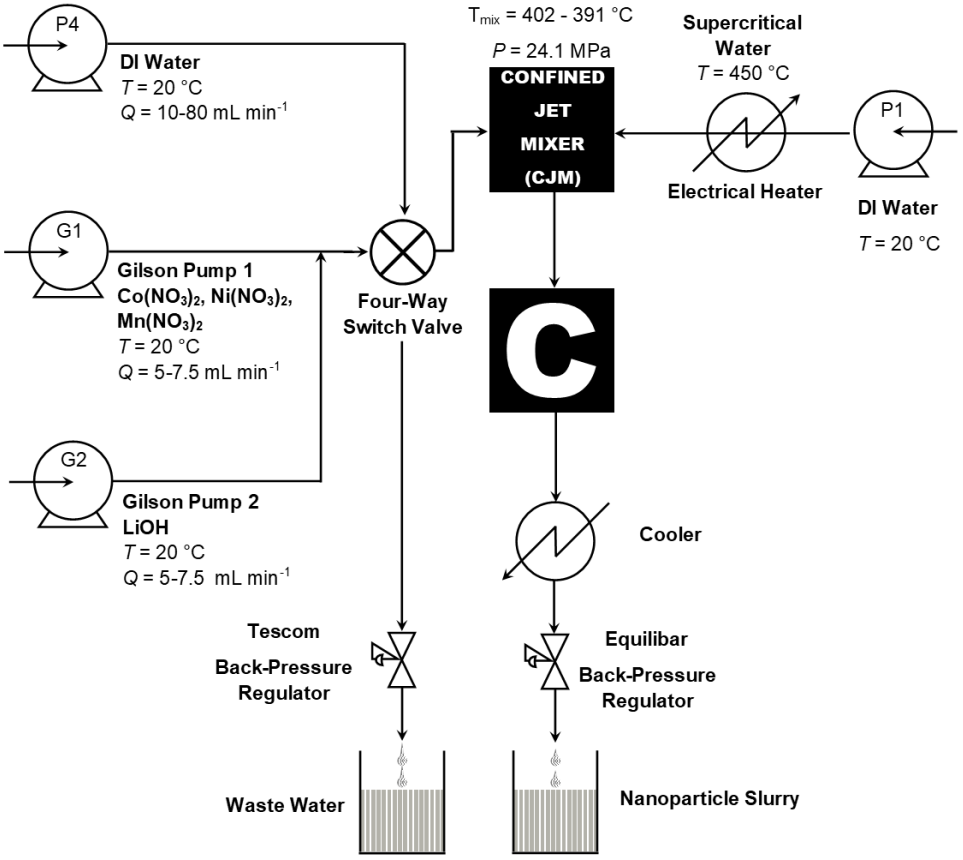

Figure 7.4 – The High-Temperature Lab-Scale apparatus with additional oven attachment (position O). The High-Temperature Lab-Scale mixer was employed as described in Section 2.1.2.1.

To oxidise the M^{2+} salts, H_2O_2 (30 wt%, Sigma-Aldrich, Dorset, UK) was dissolved in D.I. water and fed in *via* pump P1 (i.e. the supercritical water pump). The first precursor solution (fed in *via* pump P2) consisted of: $Co(NO_3)_2 \cdot 6H_2O$ (99%, Acros Organics, Loughborough, UK), $Mn(NO_3)_2 \cdot 4H_2O$ (98%, Alfa Aesar, Heysham, UK), $Ni(NO_3)_2 \cdot 6H_2O$ (98%, Alfa Aesar, Heysham, UK) in deionised (D.I.) water, with concentrations as described in Table 7.2. The second solution, fed in *via* pump P3, contained various concentrations of $LiOH \cdot H_2O$ (99+%, Fisher Scientific, Loughborough, UK) and KOH (86%, Fisher Scientific, Loughborough, UK) described in Table 7.2 in D.I. water for all experiments.

Table 7.2 – A summary of the reaction conditions and sample names used throughout this chapter.

Sample Name	T_{mix}	Oven	$[H_2O_2]$ / M	[Ni] / M	[Co] / M	[Mn] / M	[LiOH] / M	[KOH] / M
LT-LCO-1	378	Yes	0.1	0	0.1	0	0.1	0
LT-LCO-2	378	Yes	0.1	0	0.1	0	0.2	0
LT-LCO-5	378	Yes	0.1	0	0.1	0	0.5	0
LT-LCO-10	378	Yes	0.1	0	0.1	0	1	0
LT-LCO-20	378	Yes	0.1	0	0.1	0	2	0
HT-LCO-OVEN-5-0.1	402	Yes	0.1	0	0.1	0	0.5	0
HT-LCO-OVEN-5-0.5	402	Yes	0.1	0	0.5	0	2.5	0
HT-LCO-OVEN-10-0.5	402	Yes	0.1	0	0.5	0	5	0
HT-LCO-OVEN-5-1	402	Yes	0.1	0	1	0	5	0
HT-LCO-402-5-1	402	No	0.1	0	1	0	5	0
HT-LCO-391-5-1	391	No	0.1	0	1	0	5	0
HT-LCO-402-1.5-1	402	No	0.1	0	1	0	1.5	3.5
HT-LCO-402-1.3-1	402	No	0.1	0	1	0	1.3	3.7
HT-LCO-402-1.0-1	402	No	0.1	0	1	0	1	4
NMC 1/3 1/3 1/3	402	No	0.2	0.33	0.33	0.33	5	0
NMC 2/5 1/5 2/5	402	No	0.2	0.4	0.2	0.4	5	0
NMC 2/5 2/5 1/5	402	No	0.2	0.4	0.4	0.2	5	0
NMC 1/5 3/5 1/5	402	No	0.2	0.2	0.6	0.2	5	0
NMC 3/5 1/5 1/5	402	No	0.2	0.6	0.2	0.2	5	0

The product slurry was collected in a plastic container open to the atmosphere at a total flow rate of 130, 90 or 95 mL min^{-1} (depending on the flow-rates of the precursor solutions). The slurry was allowed to settle (1 h) and the supernatant siphoned off. Repeated centrifugation and washing with D.I. water was performed (3 × 4500 rpm for 5 minutes) until the conductivity of the supernatant was reduced below 100 µS m^{-1}. The resulting clean, wet paste was dried in a vacuum oven as further described in Section 2.1.3.3.

Powder XRD patterns of the samples were collected using set-up **b** in Section 2.1.4.1, collected in the range 2 – 30° 2θ, 0.5° steps, 5 s per step. Rietveld analysis was performed using MAUD (Material Analysis Using Diffraction) software.[132]

The Li-ion battery electrodes were prepared by mixing each sample with conductive agent (Super P™ carbon) and PVDF to give an active material:carbon:binder mass

ratio of 80:10:10 for all electrodes. The PVDF was stirred in NMP for at least 1 h at room temperature until it was fully dissolved. This solution was combined with the sample and carbon, and ball-milled for 0.5 h; the product slurry was cast on Al foil and dried on a hot-plate. 15 mm diameter circular electrodes were punched out of the dried sheet, and pressed (1.5 tons cm^{-2}). The mass loadings of all electrodes were in the range 2.6 – 3.9 mg cm^{-2}.

Li-ion cell assembly of electrodes was conducted in the standard manner described in Section 2.1.5.2. Electrochemical measurements were performed using an Arbin Instruments battery tester at 20 °C as described in Section 2.1.5. Cells were analysed using C-rate testing at C-rates of C/10, C/2, 1C, 2C, 5C and 10C. For LCO materials, the theoretical specific capacity was assumed to be 140 mA h g^{-1}, and for NMC materials it was assumed to be 200 mA h g^{-1}.

7.4. Results and Discussion

7.4.1. Physical Characterisation

Given the formation of $LiCoO_2$ appeared to require large LiOH excesses from previous continuous hydrothermal literature reports,[60,284,286] the preliminary set of experiments explored a variety of excesses of LiOH. The oven pipe section was included in the process to extend the residence time to 12 s. The concentrations were varied according to Table 7.3, and the samples labelled LT-LCO-*x*, where "LT" refers to "low temperature", "LCO" is the material, and "*x*" is the molar ratio of Li:Co used in process.

All products formed as black/brown slurries, which produced black/brown powders when dried. As predicted from literature accounts, the formation of the lithiated phase $LiCoO_2$ was indeed limited by LiOH excess in process, as evidenced by the increasing conversion of Co_3O_4 to $LiCoO_2$ with increasing Li:Co molar ratio (Table 7.3, Figure 7.5). All XRD diffraction patterns matched well to Co_3O_4 and $LiCoO_2$ diffraction patterns (PDF Card Nos. 01-071-0816 and 01-070-2685 respectively). The unidentified peaks within sample LT-LCO-20 were attributed to reaction by-products, as so little of this sample could be collected that it could not be comprehensively cleaned post-synthesis. The Co_3O_4:$LiCoO_2$ volume ratio was estimated from Rietveld

refinements of the two phases, and the yield estimated from the mass collected, volume ratios and densities of the products. The product became increasingly gassy with increased LiOH concentration, and led to occasional pressure fluctuations and sporadic product delivery (rather than as a continuous stream). This implies that significant product was trapped in the 6 m pipe addition, and occasionally became dislodged from the section to be collected. Therefore, the yields are only estimations, and the unusually low yield of LT-LCO-20 reflected the irregular release of nanoparticles from the reactor. The yields in Table 7.3 describe the cumulative yield of LCO and Co_3O_4.

Table 7.3 – The reaction conditions, yields and products of the reactions at lower temperature. All reactions used 0.1 M H_2O_2 and 0.1 M $Co(NO_3)_2$.

Sample Name	[LiOH] / M	Co_3O_4:$LiCoO_2$ volume ratio	Yield / %
LT-LCO-1	0.1	100:0	17
LT-LCO-2	0.2	95:5	33
LT-LCO-5	0.5	49:51	44
LT-LCO-10	1	31:69	56
LT-LCO-20	2	14:86	2

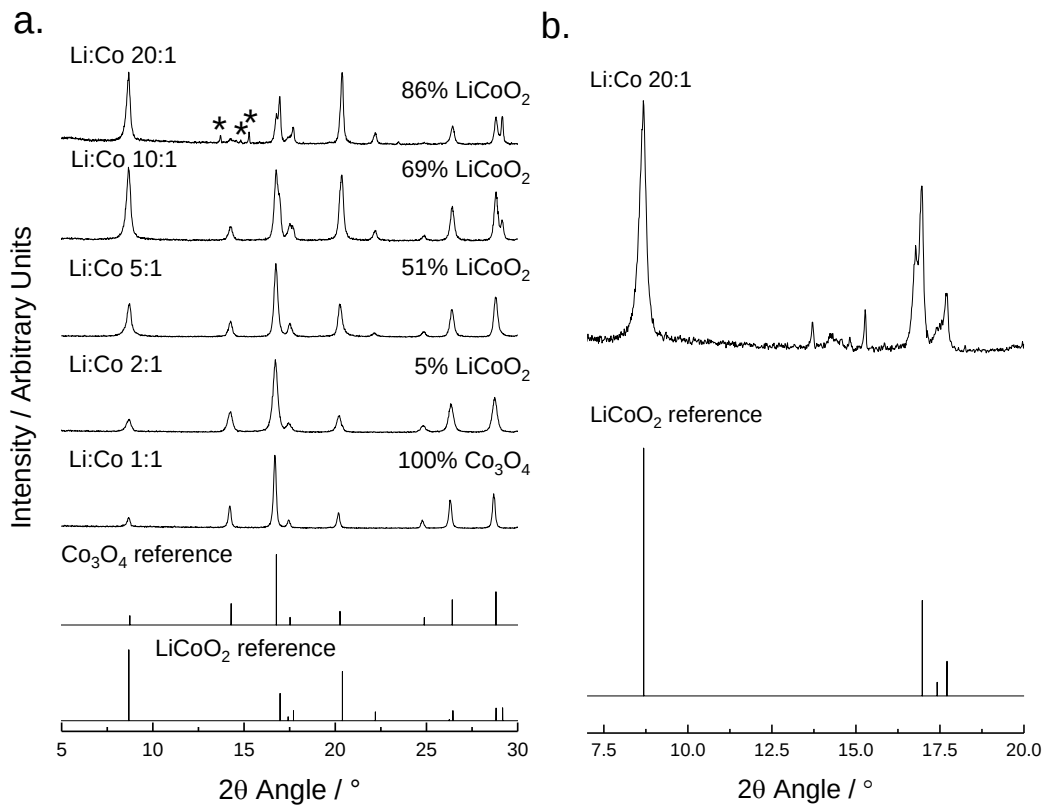

Figure 7.5 – a) XRD patterns of the attempted LCO syntheses made at mixing temperatures of 378 °C, showing the effect of increasing LiOH excess on the reaction products. Co_3O_4 and $LiCoO_2$ reference diffraction patterns were included for comparison (PDF Card Nos. 01-071-0816 and 01-070-2685 respectively). The unknown impurity phases (assumed to be reaction by-products) are indicated with asterisks. b) The XRD pattern of LT-LCO-20 between 7 – 20° 2θ, highlighting the impurity phases.

As previously observed from literature, it was clear that the formation of LCO was extremely kinetically limited, given the high temperatures and large excesses of LiOH required to form the pure phase. A new set of experiments was performed as described in Table 7.4, aiming to increase the reaction temperature by reducing the relative flow rates of the aqueous precursors relative to the supercritical water feed (which contained 0.1 M H_2O_2 in all experiments). The metal ion concentration, [Co], was also varied between experiments, as the overall concentration of the product was severely lowered in the output stream by reducing the P2 flow-rate from 25 mL min^{-1} to 5 mL min^{-1}. The reactions were named "HT-LCO-OVEN-*x*-*y*", where "HT" denotes it is a high temperature reaction at a 402 °C mixing point temperature, "LCO" is the target material, "OVEN" denotes that the additional 6 m oven coil was utilised to give an extended residence time of 5 s, "*x*" is the Li:Co ratio and "*y*" is the concentration of $Co(NO_3)_2$ precursor used.

Table 7.4 – A summary of the reaction conditions, products and yields from the high-temperature reactions using an extended residence time of 5 s.

Sample Name	$[Co(NO_3)_2]$ / M	[LiOH] / M	Product	Yield / %
HT-LCO-OVEN-5-0.1	0.1	0.5	No product	0
HT-LCO-OVEN-5-0.5	0.5	2.5	No product	0
HT-LCO-OVEN-10-0.5	0.5	5.0	Pure LCO	74
HT-LCO-OVEN-5-1	1.0	5.0	Pure LCO	53

The first two reactions, HT-LCO-OVEN-5-0.1 and HT-LCO-OVEN-5-0.5, did not yield any solid product, which again suggested significant amounts of product were deposited in the oven pipe section. It is also possible that the higher dilution of the precursors in the combined reaction stream (due to the lower P2 flow-rate) reduced the yield of the HT-LCO-OVEN-5-0.1 sample; the nucleation driving force is related to aqueous precursor concentration, so less solid may have nucleated at the reaction point, and could have re-dissolved in the cooling pipe section. However, the raised mixing temperature (378 °C to 402 °C) successfully generated phase-pure LCO at both 0.5 M and 1.0 M [Co], and is in agreement with literature studies claiming a reaction temperature of 400 °C is required to produce phase-pure LCO (Figure 7.6).

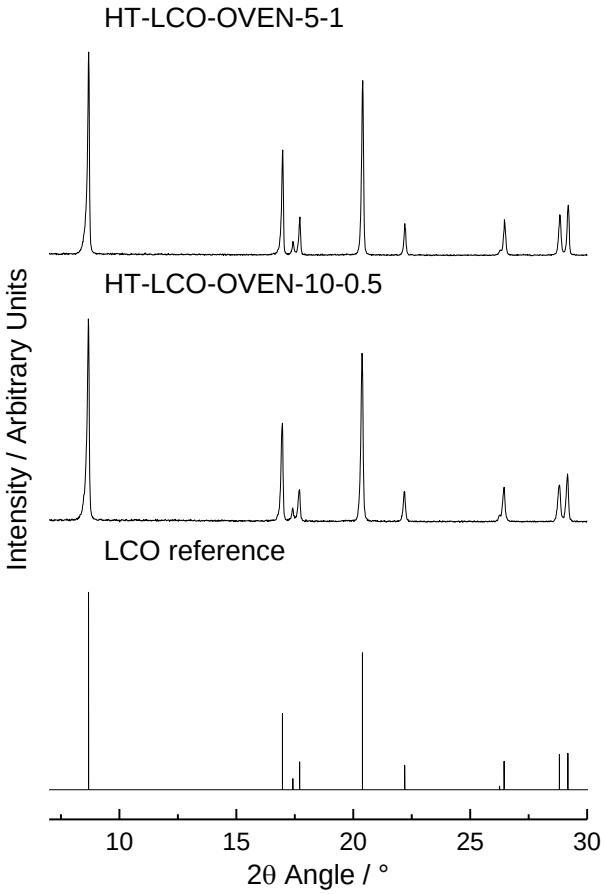

Figure 7.6 – XRD patterns (Mo-Kα radiation) of the LCO samples synthesised at a 402 °C mixing temperature with the extended residence time of 5 s. An LCO reference pattern is included for comparison (PDF Card No. 01-070-2685).

Given the LCO phase was successfully achieved, various strategies were implemented to improve the economy of the reaction. Firstly, all further experiments were conducted without the oven pipe section to determine whether the extended residence time was necessary to produce pure LCO. Secondly, it was important to ascertain whether the mass yield of the reaction could be increased (given the high degree of dilution required to achieve mixing point temperature of 402 °C). As the concentrations of $Co(NO_3)_2$ and LiOH were already very high, the other way to achieve higher mass yield is by increasing the relative P2 and P3 pump flow-rates. Therefore, an experiment where the P2 and P3 pump flow-rates were increased to 7.5 mL min^{-1} each (15 mL min^{-1} combined) was included, giving a reaction temperature of 391 °C (Table 7.5).

Furthermore, a very high excess of lithium has generally been employed to achieve the pure LCO phase *via* CHFS in other literature reports, so if this could be reduced

the economic feasibility of LCO formation will increase, as Li is an expensive metal. NMC has been synthesised previously without an excess of LiOH by using an excess of KOH instead, and suggests that a similar strategy may be effective in continuous synthesis.[285] Therefore, experiments were conducted replacing LiOH with KOH as detailed in Table 7.5.

As before, 0.1 M H_2O_2 was pumped *via* pump P1 in the supercritical water feed, and a summary of the reaction conditions is included in Table 7.5. Reactions were labelled HT-LCO-T-*x*-*y*, where "HT" refers to the high-temperature set-up used, "LCO" is the material, "T" is the mixing-point temperature, "*x*" is the Li:Co ratio and "*y*" is the concentration of $Co(NO_3)_2$ precursor used.

Table 7.5 – The concentrations of precursors, flow-rates, mixing point temperatures (T_{mix}), products and yields of the high temperature reactions. 1.0 M $Co(NO_3)_2$ was included in P2 in all experiments.

Sample Name	[LiOH] / M	[KOH] / M	$Q_{(P2+P3)}$ / mL min^{-1}	Tmix / °C	Product	Yield
HT-LCO-402-5-1	5.0	0	10	402	LCO	76
HT-LCO-391-5-1	5.0	0	15	391	LCO	78
HT-LCO-402-1.5-1	1.5	3.5	10	402	LCO/ Co_3O_4	44
HT-LCO-402-1.3-1	1.3	3.7	10	402	LCO/ Co_3O_4	48
HT-LCO-402-1.0-1	1.0	4.0	10	402	LCO/ Co_3O_4	48

The XRD data confirmed these samples were phase pure or semi-pure LCO (Figure 7.7 and Figure 7.8). The CHFS process residence time was 1.0 s and 1.1 s for HT-LCO-402-5-1 and HT-LCO-391-5-1 respectively, suggesting the longer residence time reported in literature (5 s or more) was not necessary to produce phase-pure LCO (Figure 7.7). Indeed, the data for HT-LCO-391-5-1 also showed that the reaction temperature can be slightly lower than 400 °C and still produce pure-phase LCO, increasing the mass yield of the reaction by 42%. Furthermore, the experiments where LiOH was substituted by KOH were successful in producing LCO, although trace CoO impurities were present (matches with PDF Card No. 01-071-1178, Figure 7.8). This suggested that the theory put forward by other researchers, that large Li excesses are necessary to produce LCO, is incorrect; an excess of base may be required, but LiOH can be stoichiometric with $Co(NO_3)_2$ to produce LCO.

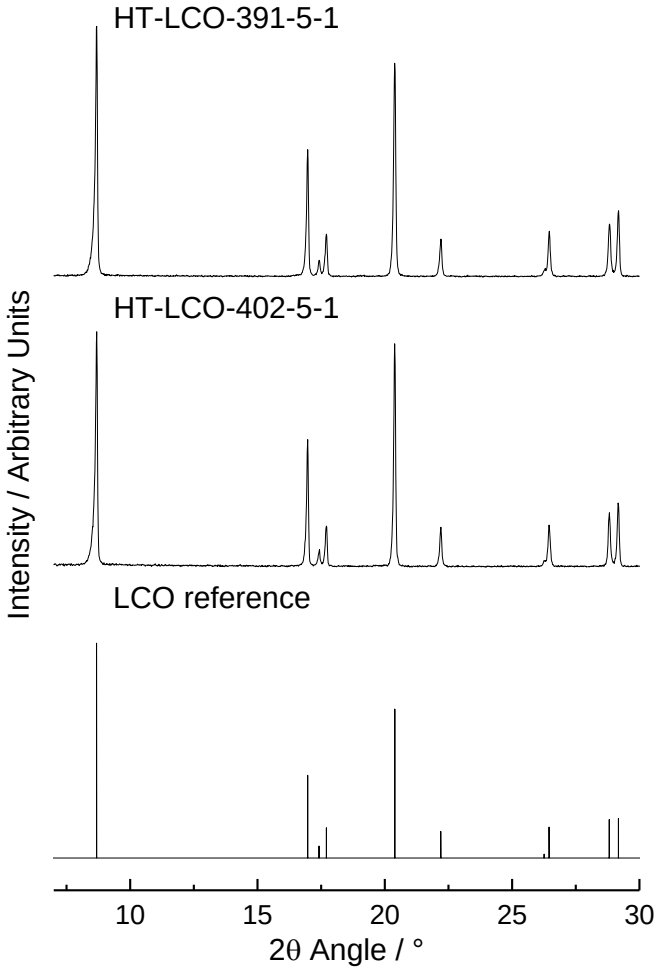

Figure 7.7 – XRD patterns (Mo-Kα radiation) of the high-temperature LCO samples, HT-LCO-402-5-1 and HT-LCO-391-5-1, made without the extended residence time. An $LiCoO_2$ reference pattern is included for comparison (PDF Card No. 01-070-2685).

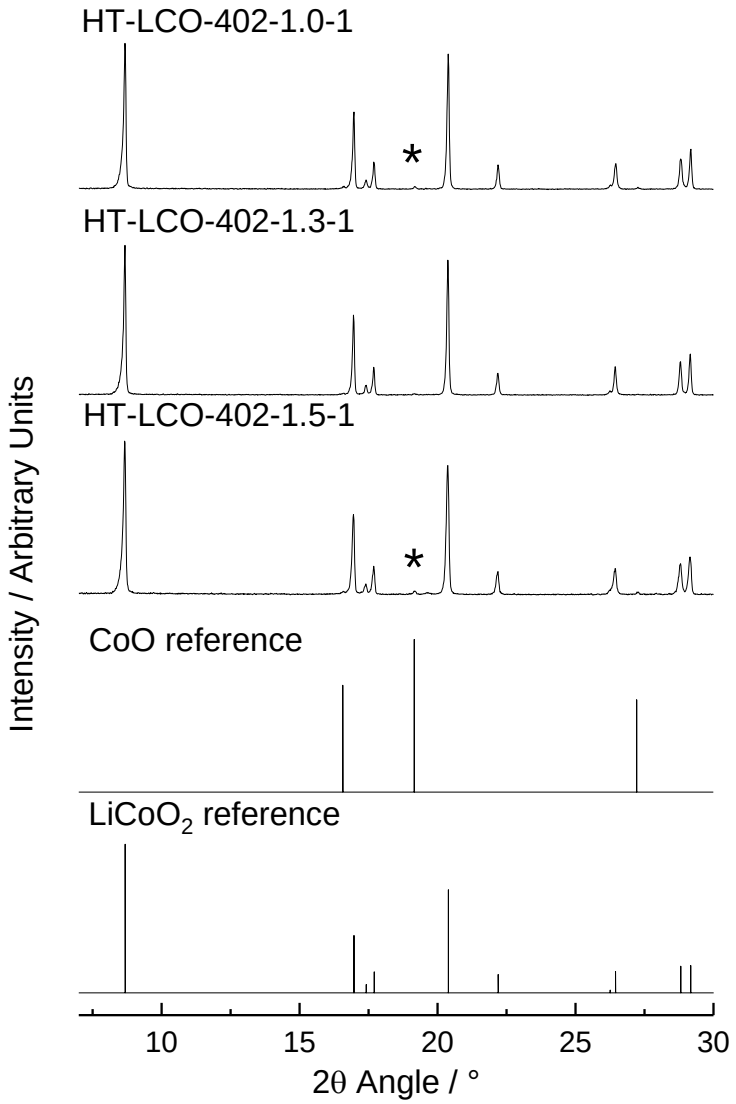

Figure 7.8 – XRD patterns (Mo-Kα radiation) of the LCO samples made with reduced LiOH concentrations. Trace CoO impurities are indicated with an asterisk. $LiCoO_2$ and CoO reference patterns are included for comparison (PDF Card Nos. 01-070-2685 and 01-071-1178 respectively).

While there are many reports of continuous hydrothermal synthesis of LCO, there are currently no reported syntheses of NMC by the same method. Therefore, the same successful reaction conditions which produced pure LCO (5 × Li excess, 1.0 M transition metal concentration, 402 °C mixing point temperature) were employed with five NMC compositions, as listed in Table 7.6. Samples were named "NMC *x y z*", where "*x*" is the Ni fraction, "*y*" is the Mn fraction and "*z*" is the Co fraction, where the fractions are as a function of total transition metal content. A H_2O_2 concentration of 0.2 M was fed through P1 for all reactions. Unfortunately, only NMC 1/5 3/5 1/5 possessed the pure NMC structure (ICSD Collect Code 171750); all other samples had a proportion of NiO impurity phase present (PDF Card No. 01-071-1179), with ratios

as described in Table 7.6. The ratios were estimated with Rietveld refinements of the XRD patterns, which are included in Chapter 11 - Appendix I. The amount of NiO observed was proportional to the Ni content of the precursors, as shown in Figure 7.10, indicating that Ni is only partially soluble (≤ 20 at%) in the NMC structure in these conditions. The yields of NMC phase in Table 7.6 were calculated using the NMC:NiO ratio.

Table 7.6 – The precursor concentrations, products and yields of the NMC materials. The concentration of LiOH in P3 was set to 5.0 M for all experiments. Sample names corresponded to the ratio of Ni, Mn and Co included as precursors.

Sample Name	$[Ni(NO_3)_2]$ / M	$[Mn(NO_3)_2]$ / M	$[Co(NO_3)_2]$ / M	NMC:NiO ratio	Yield / %
NMC 1/3 1/3 1/3	0.33	0.33	0.33	77:23	53
NMC 2/5 1/5 2/5	0.4	0.2	0.4	78:22	61
NMC 2/5 2/5 1/5	0.4	0.4	0.2	77:23	49
NMC 1/5 3/5 1/5	0.2	0.6	0.2	100:0	76
NMC 3/5 1/5 1/5	0.6	0.2	0.2	56:44	34

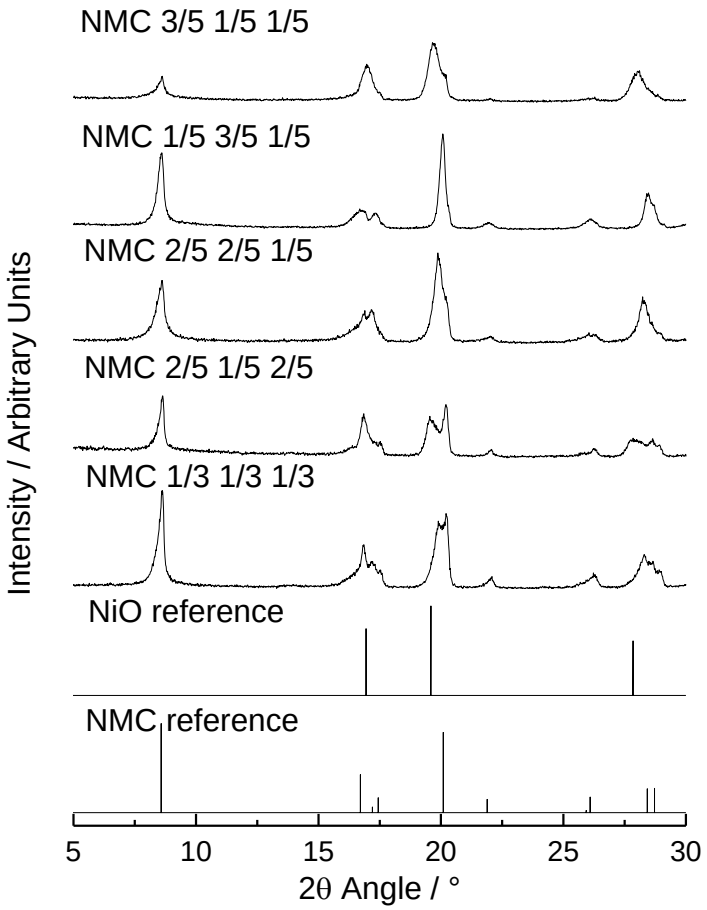

Figure 7.9 – XRD patterns (Mo-Kα radiation) of the NMC samples, with an NMC and NiO reference pattern included for comparison (ICSD Collect Code 171750, PDF Card No. 01-071-1179).

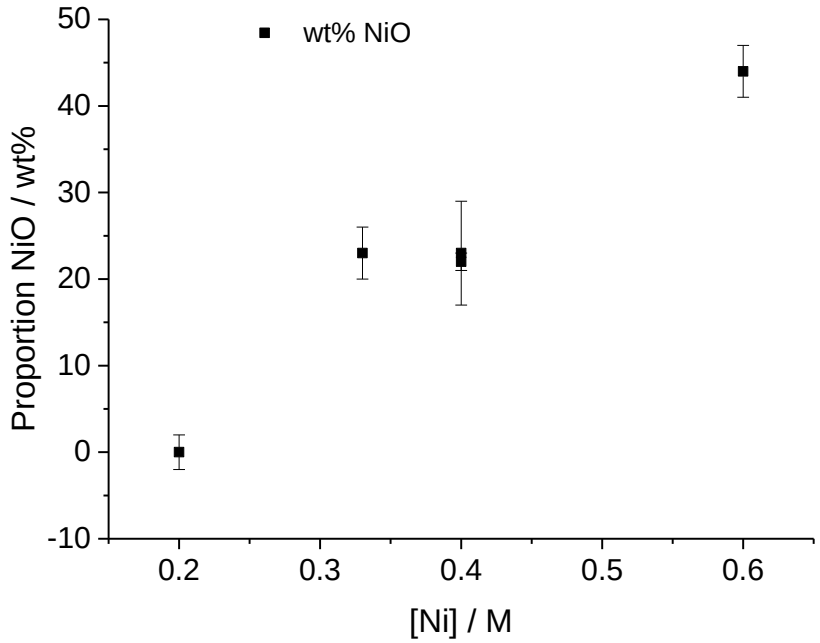

Figure 7.10 – The wt% of NiO calculated from Rietveld refinements of the XRD patterns from Figure 7.9.

7.4.1.1. Microscopy Analysis

A combination of FE-SEM and TEM imaging was used to investigate the particle size and morphology of the LCO and NMC particles produced by CHFS. FE-SEM revealed the LCO and NMC particles formed large agglomerates, with evidence of significant populations of particles on the 100 nm scale, but also larger, micron size particles (Figure 7.12). The largest particles tended to adopt hexagonal prism morphology, which reflected the crystal symmetry of the LCO/NMC unit cell. The large distributions observed suggested the elevated reaction temperatures enabled significant growth and ageing of the produced particles.

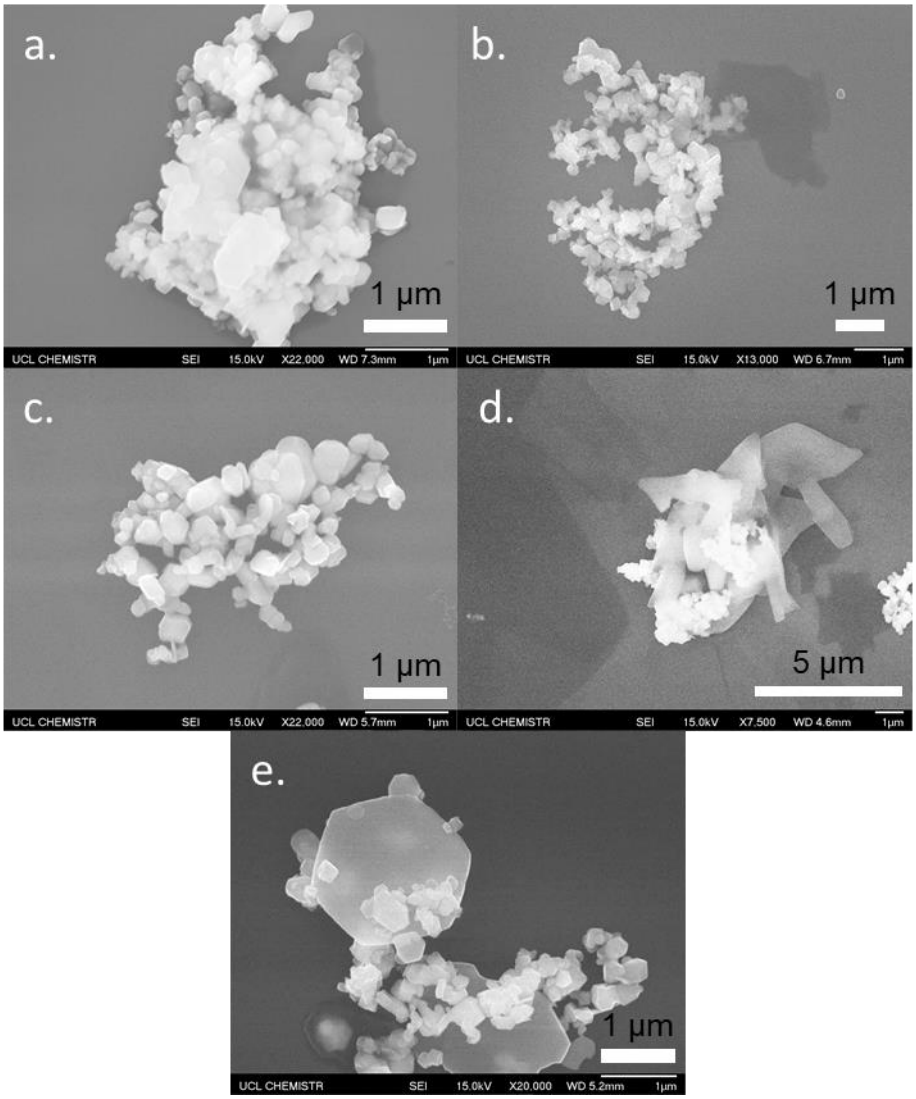

Figure 7.11 – FE-SEM images of samples a) LCO-OVEN-10-0.5, b) LCO-OVEN-5-1, c) LCO-402-5-1, d) LCO-391-5-1, e) NMC 1/5 3/5 1/5.

TEM analysis of sample NMC 1/5 3/5 1/5 revealed significant disorder was present in the crystal structure (Figure 7.12). Analysis of the (0 0 3) lattice planes revealed numerous defects resembling dislocations, which implies significant mixing between the transition metal and lithium layers. This may have consequences for electrochemical performance, as Li diffusion pathways may be obstructed by this disorder, and is discussed further in Section 7.4.2.

EDS analysis of sample NMC 1/5 3/5 1/5 confirmed the metal-ion ratios of Ni:Mn:Co were approximately equal to those included as precursors, and suggested equal conversion of all metal ions to NMC under the reaction conditions (Figure 7.13). Elemental mapping revealed most particles contained a homogenous distribution of

the three transition metals (Figure 7.14 and Figure 7.15), although there was evidence of minority phases closer in composition to $LiNi_{0.5}Mn_{0.5}O_2$ (Figure 7.14) and $LiCoO_2$ (Figure 7.15).

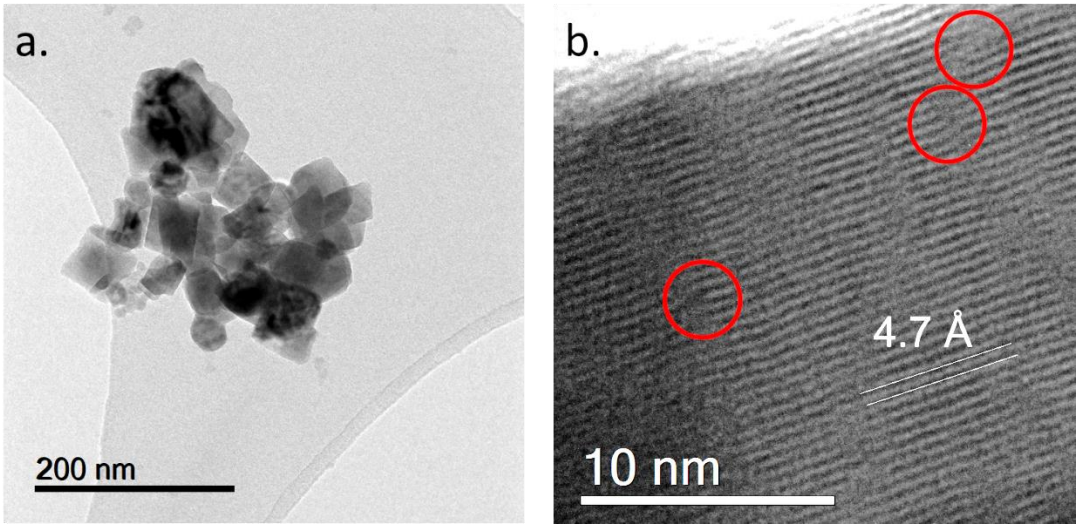

Figure 7.12 – TEM images of sample NMC 1/5 3/5 1/5, a) showing a typical particle agglomerate and b) lattice planes visible with d-spacing 4.7 Å, which corresponded to the (0 0 3) lattice spacing of NMC. There are also dislocation defects visible in the layers, highlighted by red circles, which implied significant disorder in the crystal.

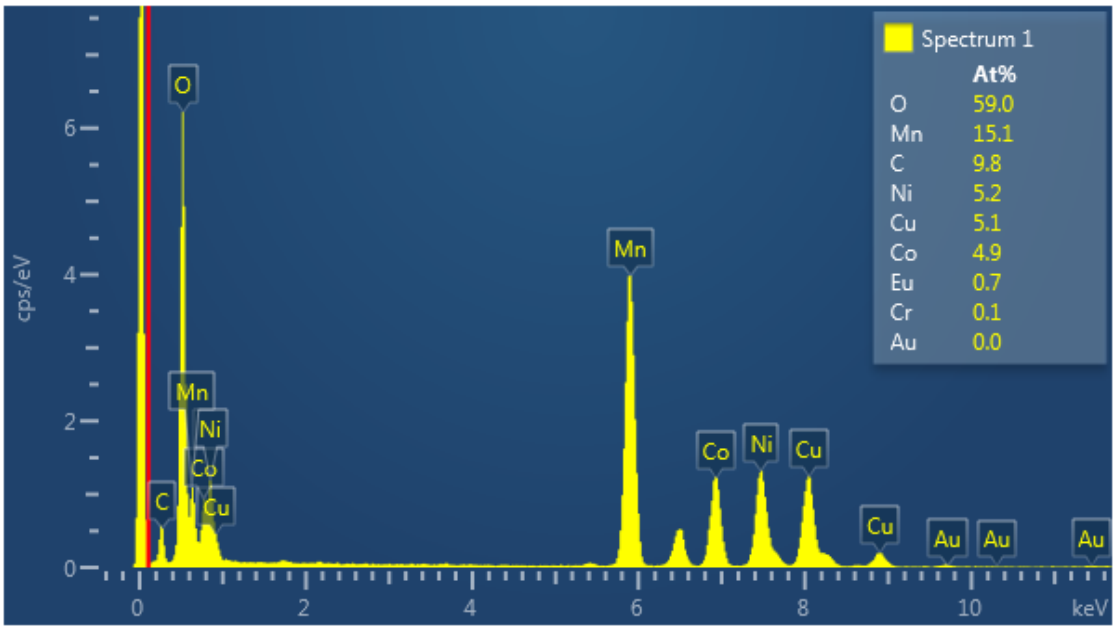

Figure 7.13 – The elemental spectrum from EDS analysis of sample NMC 1/5 3/5 1/5, with at% of the elements detected. The observed Ni:Mn:Co ratio was 1:2.9:0.94, which was similar to the theoretical ratio 1:3:1.

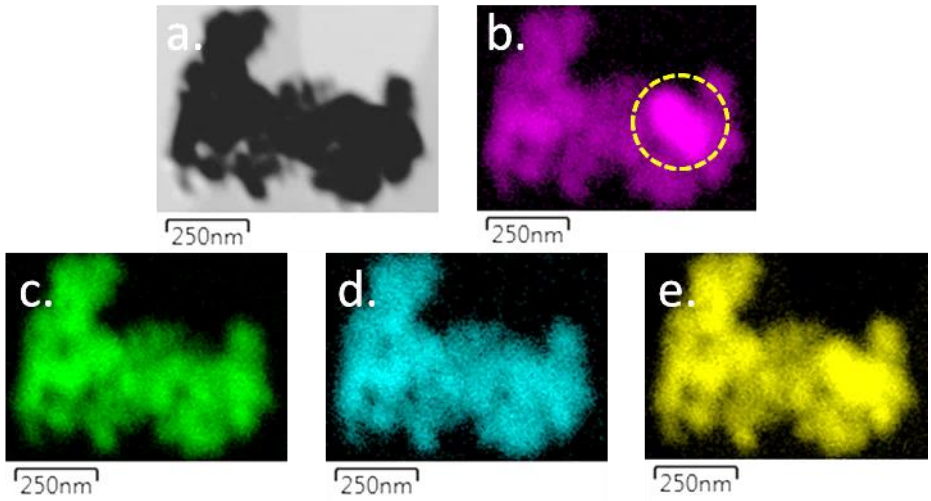

Figure 7.14 – EDS mapping of a cluster of NMC 1/5 3/5 1/5 particles, with a) the darkfield image, b) the Co-Kα signals, c) the Mn-Kα signals, d) the Ni-Kα signals, and e) the O- Kα signals. The region highlighted with a yellow dashed circle was Co-rich, which implied the presence of $LiCoO_2$.

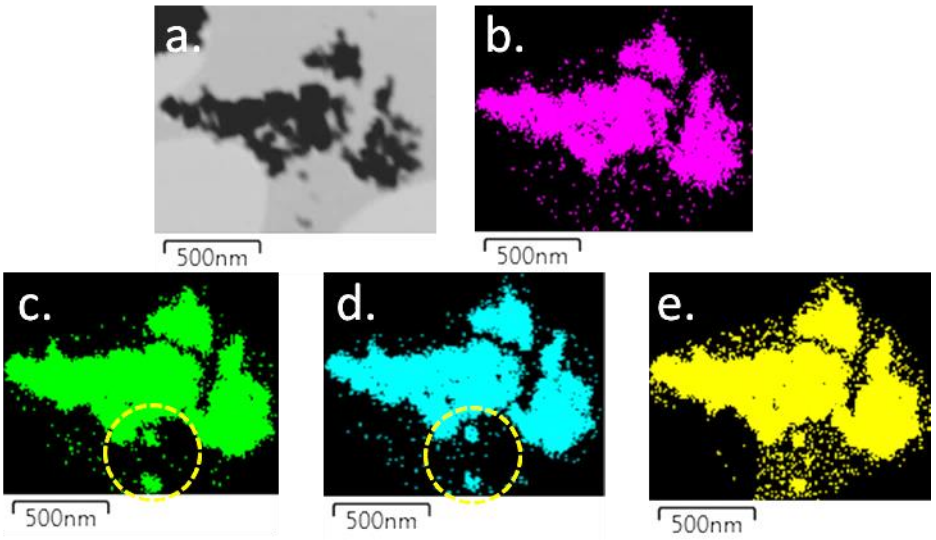

Figure 7.15 – EDS mapping of a cluster of NMC 1/5 3/5 1/5 particles, with a) the darkfield image, b) the Co-Kα signals, c) the Mn-Kα signals, d) the Ni-Kα signals, and e) the O- Kα signals. The region highlighted with a yellow dashed circle was Mn- and Ni-rich, which implied the presence of $LiNi_{0.5}Mn_{0.5}O_2$.

7.4.2. Electrochemical Testing

Samples HT-LCO-OVEN-5-1 and NMC 1/5 3/5 1/5 were selected for further electrochemical testing, as NMC 1/5 3/5 1/5 was the only pure NMC sample from the samples listed in Table 7.6. C-rate resting was performed on HT-LCO-OVEN-5-1, beginning with a low C-rate of C/10 and increasing to a high C-rate of 10 C. The material responded poorly to the increase in charge/discharge rate, achieving similar

capacities to other LCO materials made *via* CHFS in literature at C/10 but reduced to effectively zero at 1C (Figure 7.16). Inspection of the charge/discharge curves at C/10 and C/2 revealed large overpotentials developed in the material with increasing rate, and implied a high overall electrode resistance (Figure 7.17 and Figure 7.18). The capacity also degraded significantly with repeated cycling (100 mA h g^{-1} to 80 mA h g^{-1} within 10 cycles), which indicated an inherent instability in the LCO material itself. While the $LiCoO_2$ structure is more unstable than the $LiFePO_4$ structure, it was not obvious why such a degradation was observed, given much better capacity retention has been reported in literature for this material. It is suggested that there may be defects present in the lattice due to the low synthesis temperature and rapid reaction time, and that these defects were partially responsible for the poor performance. A large charge capacity was observed on the first cycle at C/10, implying significant side reactions within the cell, which perhaps indicated the presence of reactive species on the LCO surface.

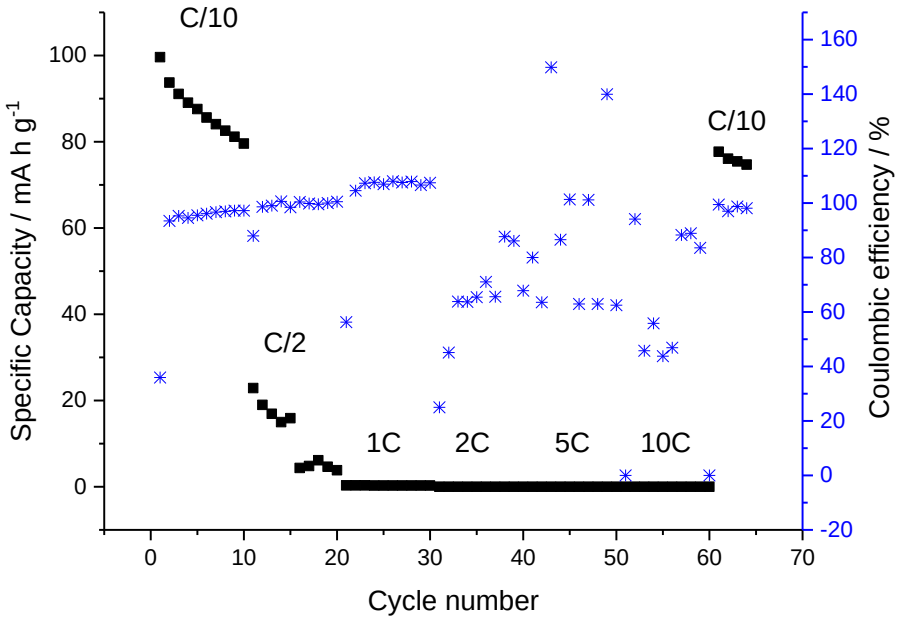

Figure 7.16 – C-rate testing of sample HT-LCO-OVEN-5-1 at C-rates of C/10, C/2, 1C, 2C, 5C and 10C, with discharge capacities indicated with black squares, and coulombic efficiencies indicated with blue asterisks.

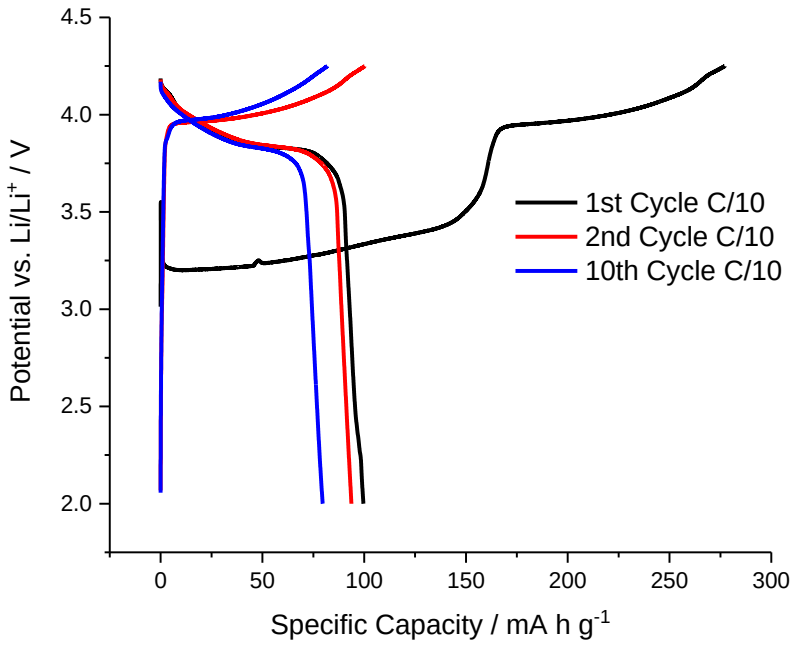

Figure 7.17 – Charge/discharge profiles of sample HT-LCO-OVEN-5-1 for the 1st, 2nd and 10th cycle at C/10.

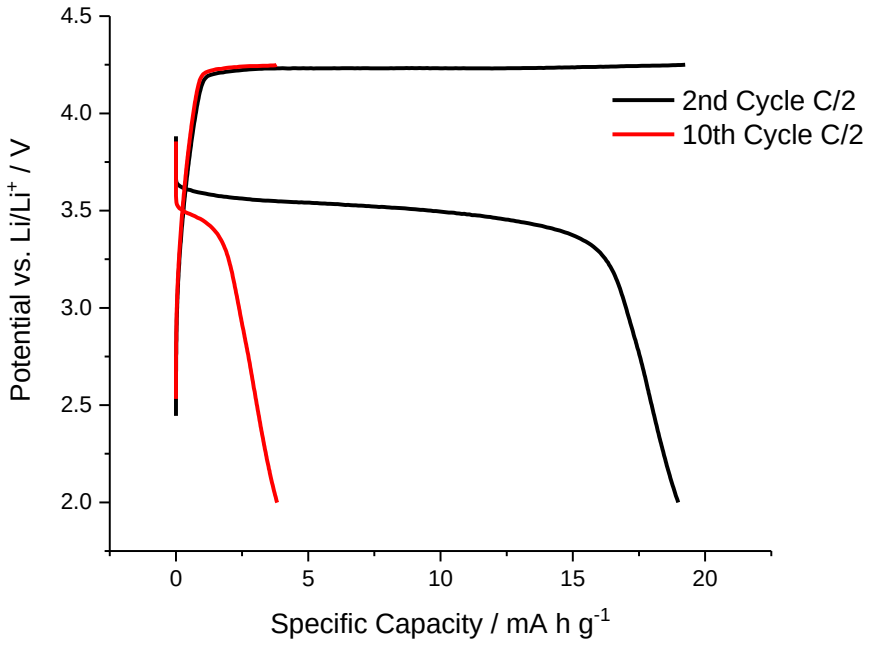

Figure 7.18 – Charge/discharge profiles of sample HT-LCO-OVEN-5-1 for the 2nd and 10th cycle at C/2.

In contrast, the NMC 1/5 3/5 1/5 sample showed a much lower overpotential and higher capacity at a C/2 charge/discharge rate (Figure 7.19 and Figure 7.20), although the capacity was significantly lower than those typically observed for NMC samples in literature. In addition, significant capacity fade was observed over ten cycles. It is

suggested that the disorder in the layered NMC structure reduced the maximum obtainable capacity, and that further synthesis efforts should seek to increase the crystallinity of the NMC phases made *via* CHFS.

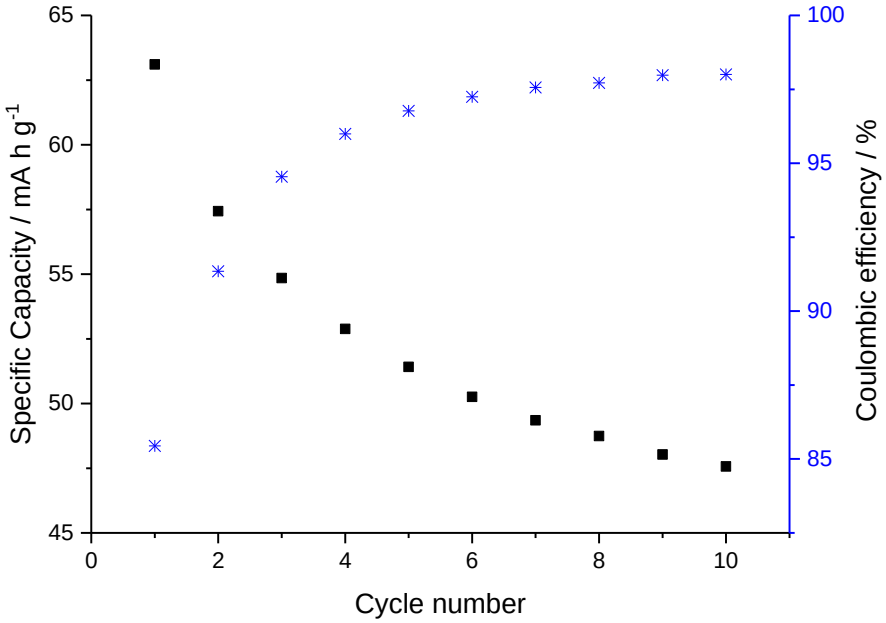

Figure 7.19 – The discharge capacities and coulombic efficiencies observed for sample NMC 1/5 3/5 1/5 at a charge/discharge rate of C/2.

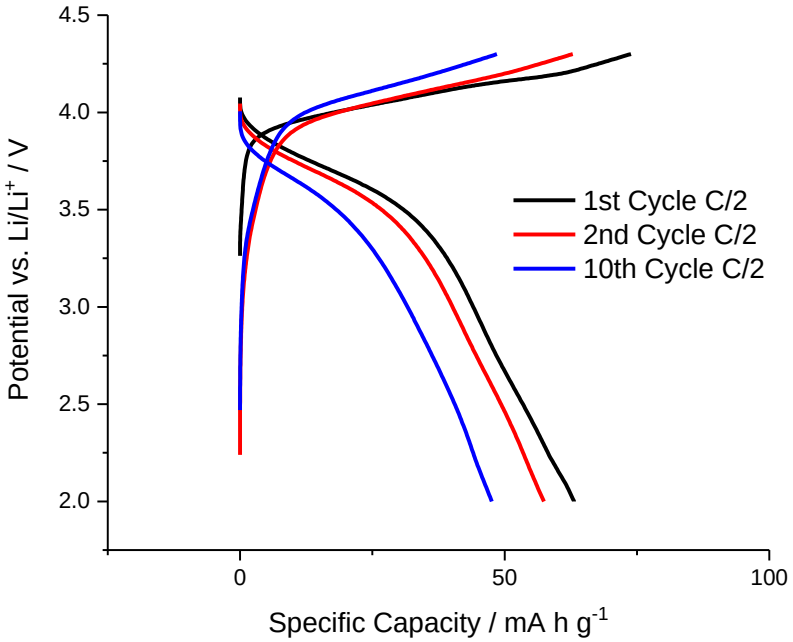

Figure 7.20 – Charge/discharge profiles of sample NMC 1/5 3/5 1/5 of the 1st, 2nd and 10th cycle at a charge/discharge rate of C/2.

7.5. Conclusions and Further Work

$LiCoO_2$ was successfully synthesised *via* CHFS with a reduced residence time, Li excess and temperature in comparison to other CHFS materials made in literature. This therefore represents a key step towards the commercialisation of this material made by such a low temperature, rapid technique. Various NMC compositions were also attempted, and the pure phase was successfully generated for the first time by this method, albeit with minor NiO impurities in most cases. Furthermore, while EDS revealed a good degree of transition metal ion homogeneity, there were still occasional regions with off-stoichiometry. These preliminary efforts suggest that CHFS may be a viable, low-temperature method for manufacturing NMC in the large scale. It is proposed that the main obstacle to phase purity is the relative stability of the NiO phase, and that higher temperatures may be required to fully incorporate Ni within the NMC structure across all compositions.

The electrochemical performance of the LCO and NMC materials synthesised in this chapter was not optimal with respect to rate performance and cycling stability. It is suggested that defects in the crystal structure, observed previously in LCO made *via* CHFS,[60] may cause the unsatisfactory performance. Therefore, further work could include the rapid heat-treatment of these compounds to remove these defects, whilst avoiding the evaporation of Li from the structure.

Further work could also include further synthesis at higher temperatures or longer residence times to increase crystallinity and discharge capacity. The former option would present logistical challenges, as the flow rates were already highly unbalanced to give the synthesis temperature of 402 °C. Furthermore, the mass yield of such a heavily unbalanced system would be very high, i.e. there would be significant water solvent waste. The only alternative would be to increase the supercritical water feed temperature, although this is not currently possible with the current CHFS set-up, as any increase in temperature will exceed the maximum temperature rating of the pipe at 240 bar pressure. However, it is plausible to design a CHFS system constructed of different components which would allow a significant increase in supercritical water temperature, and such a development could potentially enable other hard-to-obtain phases. Alternatively, a much longer residence time (on the order of minutes) could be

achieved by incorporating an extremely long (e.g. 50 m) pipe section in an oven after the CJM to potentially increase crystallinity of the LCO or NMC products. This would only be a practical solution if the overall flow-rate of the CHFS process could be significantly increased to avoid significant product build-up in the pipe.

Additionally, further electrode optimisation may also improve performance, i.e. by changing the active material:carbon ratio, or by changing the electrode preparation method. It is suggested that ball-milling may be too intensive to produce electrodes from layered materials (as layers can more easily slide over each other to cause defects), and therefore gentler methods (such as high shear mixing) should be explored as an alternative.

8. Synthesis of $MgCr_2O_4$ for Multivalent Battery Assessment

8.1. Aims

$MgCr_2O_4$ is a potential Mg-ion battery cathode material, and this section describes efforts to develop nano-sized $MgCr_2O_4$ samples *via* CHFS for Mg-ion battery testing. The kinetics of Mg-ion cells are typically sluggish; therefore, a range of particle sizes were attempted for potential future comparison. Achieving a $MgCr_2O_4$ sample which possesses phase purity, high crystallinity and small particle sizes is the goal of this chapter.

8.2. Background

8.2.1. Spinel Compounds for Multivalent Batteries

The main attraction of Mg-ion over Li-ion batteries is their higher theoretical energy density. Any reactions involving the Mg^{2+} ion are two-electron processes, rather than the one-electron processes involving Li^+, effectively doubling the charge transfer when these ions migrate between electrodes. In addition, Mg metal anodes have much greater volumetric capacity than commercial Li-ion graphite anodes (~3833 mA h cm^{-3} vs. ~800 mA h cm^{-3} respectively), and are also inherently safer than Li anodes as they do not form dendrites upon repeated cycling.[287,288]

Unfortunately, there are still many problems which prevent the commercialisation of multivalent-ion technology. Such issues include unstable electrolytes, unwanted degradation or solvent reactions/processes and poor cycle life. Specifically regarding Mg-ion cathode materials, the key issues are low operating voltages vs. Mg/Mg^{2+} (resulting in poor energy density),[288–290] sluggish ion mobility (resulting in low capacities and power capability),[289,291] and competing conversion reactions (resulting in capacity fade with repeated cycling).[292] Therefore, significant advances in cathode operating voltage and capacity are required to develop a successful Mg-ion cell which surpasses commercial Li-ion cells.

The first demonstration of an Mg-ion cell was performed by Aurbach in 2000, using an Mg anode and an $Mg_xMo_6S_8$ cathode.[288] While the magnesiation reaction of this

cathode has been shown to be highly reversible with good kinetics, the overall energy density was still well below the United States Advanced Battery Consortium (USABC) target for multivalent systems (77 vs. 908 W h kg^{-1}).[293] Therefore, the investigation of other compounds with greater potential energy density is paramount for enabling multivalent-ion batteries.

Possible high-capacity candidates for Mg-ion cathodes include MoO_3,[294,295] V_2O_5,[291,295,296] and spinel compounds with formula AB_2O_4 (where A is divalent and B is trivalent).[297–299] These structures generally have large interstitial sites for M^{2+} intercalation, or are layered structures which can incorporate these ions between metal oxide sheets. MoO_3 has already been shown to display relatively high Mg intercalation capacity (~200 mA h g^{-1}) with operating voltage of ~2.25 V, which offers a fivefold increase on energy density compared to $Mg_xMo_6S_8$.[292] However, the observed capacity is still well short of the theoretical (372 mA h g^{-1}), which is typically ascribed to poor ion diffusion kinetics. In addition, partial irreversibility of Mg intercalation and capacity fade are commonly observed for this compound. However, the high potential capacity of this cathode means that it is still of high academic interest.

V_2O_5 has also demonstrated reversible Mg-ion intercalation, and possesses a relatively high theoretical energy density (660 W h kg^{-1}). Unfortunately, V_2O_5 has often displayed slow reaction kinetics, and observed capacities have varied substantially between different reports. This is suspected to be due to the role of intercalated water in the V_2O_5 layers, making an assessment of the relative merits of V_2O_5 difficult.[300,301] However, nanosizing of V_2O_5 has generally proven a successful method for increasing performance despite the disparity between reports.[295]

More recently, novel multivalent cathode materials based on spinel compounds were proposed from a computational study.[297] These compounds possessed the chemical formula AB_2O_4, where A = Mg, Ca or Zn and B = Ti, V, Mn, Fe, Cr, Co and Ni, and operated according to Equation 8.1. The A^{2+} ion occupies tetrahedral sites in the spinel structure, and diffuses within the 3D diffusion network in an analogous way to Li within $LiMn_2O_4$ spinel.[302] According to theoretical calculations, these compounds generally have energy densities which surpass those of Li-ion, and some even achieve the USABC target (Figure 8.1). However, reversible A^{2+} intercalation has only been

conclusively demonstrated in one of these spinels ($MgMn_2O_4$).[299] The high activation energy barrier for diffusion of multivalent ions in these structures (typically 600 meV) suggests that nanosizing is necessary to achieve a significant, observable reaction. To give some context to the activation energy barriers, typically a barrier of 525 meV is the upper limit for micron-sized particles to achieve reasonable charge/discharge performance (complete charge or discharge achieved in ~2 h). However, when particle size is decreased by an order of magnitude, the activation energy can be 60 meV higher for a similar electrochemical performance to be observed. Therefore, an activation energy barrier of 645 meV may be tolerated in 100 nm particles. For this reason, spinel particles < 100 nm should be targeted for multivalent testing.

$$AB_2O_4 \rightarrow xA^{2+} + A_{1-x}B_2O_4 + 2xe^-$$

Equation 8.1 – The multivalent cathodic charge reaction.

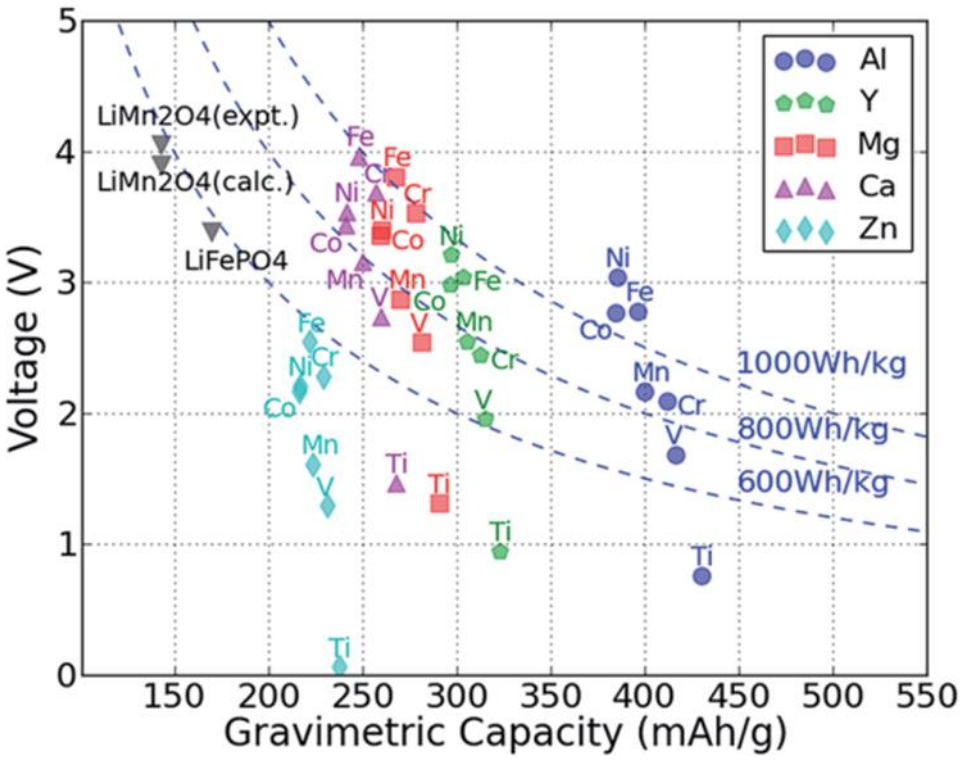

Figure 8.1 – Theoretical energy densities of various spinel compounds in multivalent-ion cells, reprinted from reference 297.

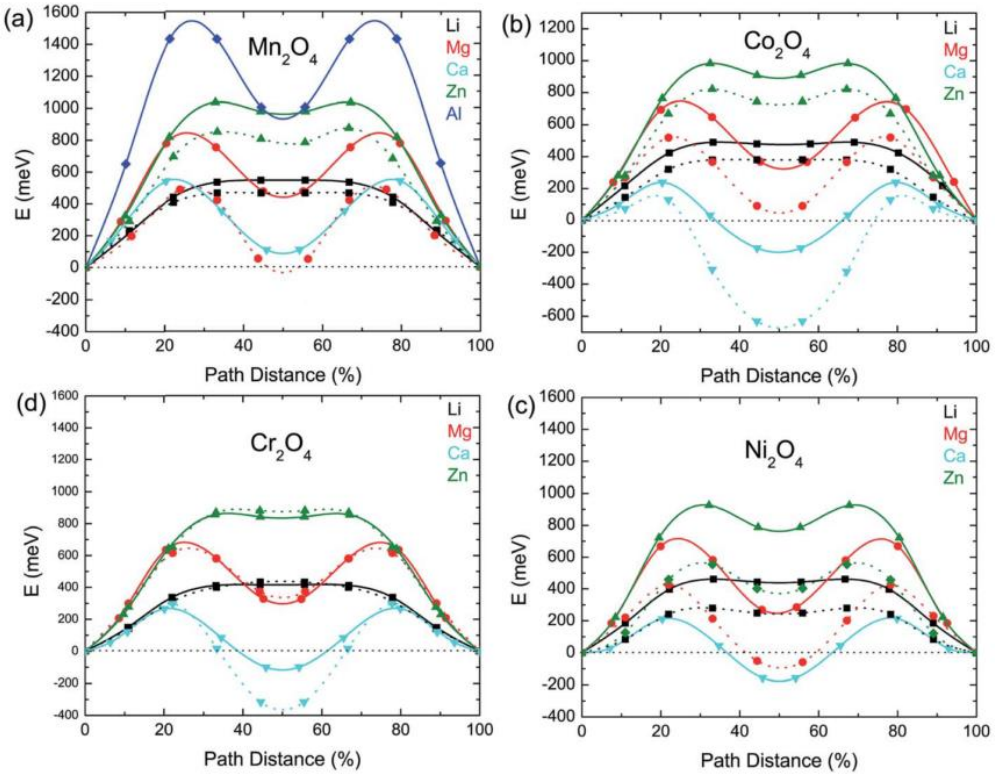

Figure 8.2 – Computed activation energy barriers for solid-state diffusion of Li, Mg, Ca, Zn and Al ions between tetrahedral sites in the high vacancy limit (solid line) and dilute vacancy limit (dotted line) in the spinel hosts: a) Mn_2O_4, b) Co_2O_4, c) Cr_2O_4 and d) Ni_2O_4. Reprinted from reference 297.

Of the spinel compounds listed above, $MgCr_2O_4$ possesses numerous advantages compared to $MgMn_2O_4$. Firstly, Cr^{3+} is a d^3 ion, which means it is especially stable in the octahedral spinel site due to crystal field effects. $MgCr_2O_4$, therefore, has a very low degree of inversion, i.e. little Mg is found on octahedral sites, and little Cr is found on tetrahedral sites.[303] This reduces the potential for diffusion-limiting blockages within the crystal structure. $MgMn_2O_4$, in contrast, nearly always has some degree of inversion. Furthermore, $MgCr_2O_4$ possesses one of the highest energy densities of the candidate compounds, with a high voltage (3.5 V) and capacity (270 mA h g^{-1}), and has lower activation energy than $MgMn_2O_4$ (650 meV vs. 800 meV). Therefore, $MgCr_2O_4$ is a prime candidate for multivalent testing.

8.2.2. Previous syntheses of $MgCr_2O_4$

$MgCr_2O_4$ has been used for a variety of different applications unrelated to Mg-ion; it has a very high melting point of 2350 °C, and does not react with concentrated mineral acids.[304] Therefore, it has employed as a refractory material due to its chemical

stability, but has also shown catalytic activity for the oxidation of light hydrocarbons and organic pollutants.[305,306]

Historically, $MgCr_2O_4$ has been synthesised *via* solid-state processes from metal oxides, and typically required high heat-treatments (1600 °C) and long reaction times, which produced micron-sized particles.[307] To produce high surface area particles, a range of low-temperature techniques have been explored. Chandran *et al*. produced $MgCr_2O_4$ *via* combustion synthesis at 375 °C from Mg and Cr metal nitrates with maleic hydrazide fuel, generating particles with 0.9 µm average particle size (72 m^2 g^{-1} surface area), although with a very wide particle size distribution. De Andrade *et al*. refined $MgCr_2O_4$ synthesis by this technique, successfully achieving $MgCr_2O_4$ particles in the range 5 – 26 nm in size (153 m^2 g^{-1} surface area) using solution combustion synthesis with glycine fuel.

Other solution-based techniques have also been successful in generating nanosized $MgCr_2O_4$. Li *et al*. pioneered a citrate sol-gel process to generate 20 nm particles, chelating $Mg(NO_3)_2$ and $Cr(NO_3)_3$ with citric acid in water, and evaporating the water solvent to leave a dried gel. This gel was calcined at different temperatures to form the nano-$MgCr_2O_4$. They found from a combination of DSC and XRD analysis that the spinel phase began to form at approximately 550 °C, and fully crystallised by 600 °C.

A contrasting method was presented by Morozova *et al*., where a mixed Mg and Cr hydroxide was co-crystallised from nitrate precursors and heated in air. DSC revealed three endotherms with minima at ~100 °C, ~220 °C and ~450 °C. This was attributed to three distinct modes of water loss and/or hydroxyl conversion. The exotherm from crystallisation of $MgCr_2O_4$ was not observed, and the authors suggested the crystallisation process occurred concurrently with hydroxyl conversion. From XRD, they proposed crystallisation to form the spinel phase began at 500 °C and was complete by 600 °C, with particle sizes growing from 10 to 40 nm between 500 – 1000 °C. They postulated the presence of Cr^{4+} in the lattice was responsible for the p-type electronic conductivity observed in the synthesised powder. Cr^{4+} could presumably form with Cr^{3+} or Mg^{2+} vacancies to charge-balance, although no evidence of this was supplied by the authors.

Durrani *et al*. synthesised $MgCr_2O_4$ *via* a two-step hydrothermal and calcination process using $Mg(NO_3)_2$ and $Cr(NO_3)_3$ precursors combined with NaOH, producing 40 nm crystallites at 650 °C calcination temperature (estimated from Scherrer analysis).[308] No characterisation of the initial hydrothermal product was made, aside from the observation of the green colour of the powder. TGA/DSC analysis revealed significant mass loss upon calcination of the hydrothermal product (~37% when heated to 1000 °C), implying significant hydroxyl content in the hydrothermally-produced sample (Figure 8.3). Indeed, the endothermic peak at 260 – 350 °C was attributed (in part) to hydroxyl decomposition, with an exotherm maxima at 442 °C ascribed to $MgCr_2O_4$ crystallisation. They therefore suggested that the binary oxides (MgO and Cr_2O_3) form first, followed by conversion to $MgCr_2O_4$. However, they provided no evidence for this mechanism beyond the TGA/DSC data, which was fairly complex (Figure 8.3). Therefore, it is clear that hydrothermal synthesis alone can produce intermediate products, which can be further heat-treated to generate the $MgCr_2O_4$ spinel structure.

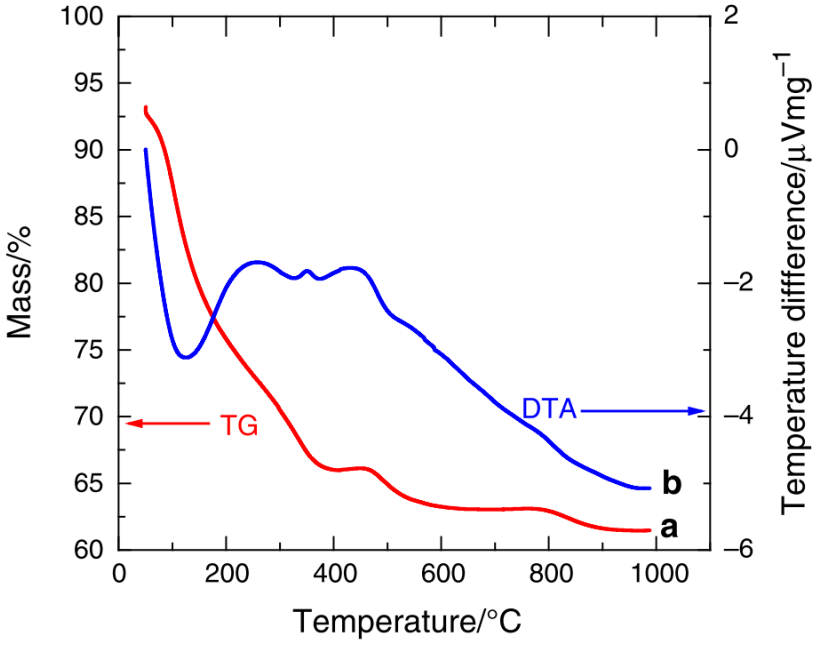

Figure 8.3 – TGA/DSC curves, where the TGA curve is red and the DSC curve is blue, of the calcination of a hydrothermally produced initial product (heating rate 10 °C min^{-1}). Reprinted with permission from Durrani, S. K., Naz, S., Nadeem, M. & Khan, A. A. Thermal, structural, and impedance analysis of nanocrystalline magnesium chromite spinel synthesized via hydrothermal process. *J. Therm. Anal. Calorim.* **116,** 309–320 (2014). Copyright 2014 Springer.[308]

8.3. Experimental

The $MgCr_2O_4$ samples, henceforth referred to as "MCO", were synthesised using the Low-Temperature and High-Temperature Lab-Scale CHFS processes. Low-temperature experiments were conducted with pump P1, P2, and P3 flow rates of 80, 40, 40 and 80, 25, 25 mL min^{-1}, which gave mixing point temperatures of 378 or 335 °C, respectively, in the Low-Temperature Lab-Scale mixer (Figure 8.4, Section 2.1.2.1). The high-temperature reactions, in contrast, were conducted using flow rates of 80, 5 and 5 mL min^{-1}, respectively, which gave a mixing point temperature of 402 °C (Figure 8.5).

The first precursor solution (fed in *via* pump P2) consisted of: $Cr(NO_3)_3 \cdot 9H_2O$ (99%, Acros Organics, Loughborough, UK), $Mg(NO_3)_2 \cdot 6H_2O$ (99%, Sigma Aldrich, Steinheim, Germany) in D.I. water, with concentrations as described in Table 8.1. The second solution, fed in *via* P3, was various concentrations of Acros Organics (86%, Fisher Scientific, Loughborough, UK) in D.I. water.

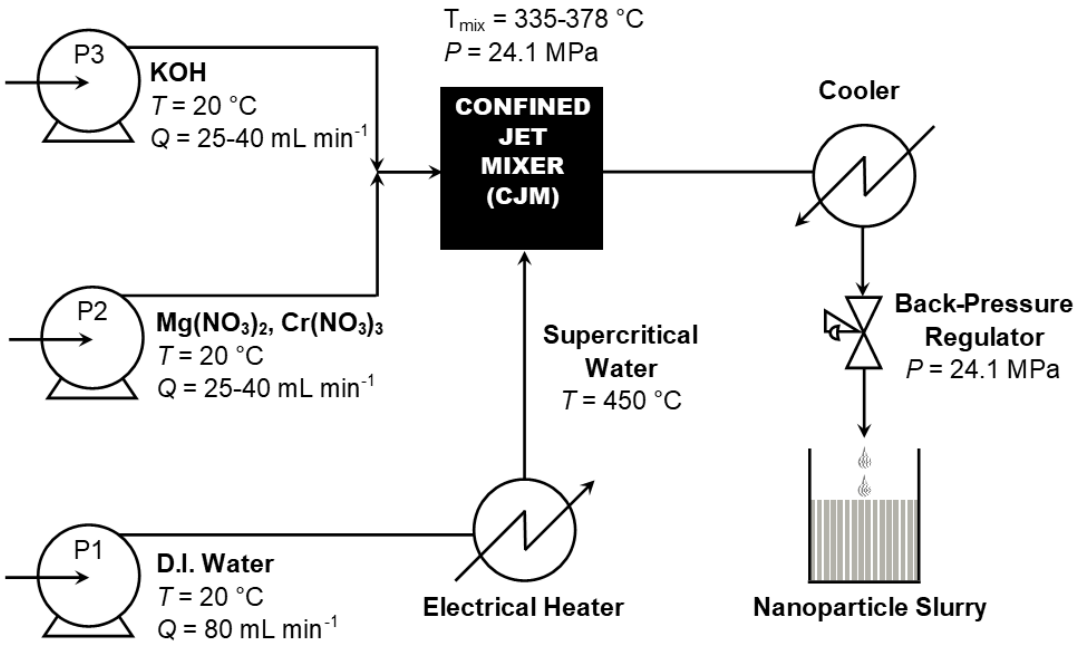

Figure 8.4 – $MgCr_2O_4$ synthesis schematic using the Low-Temperature Lab-Scale CHFS apparatus, displaying the flow-rates employed and the precursors used.

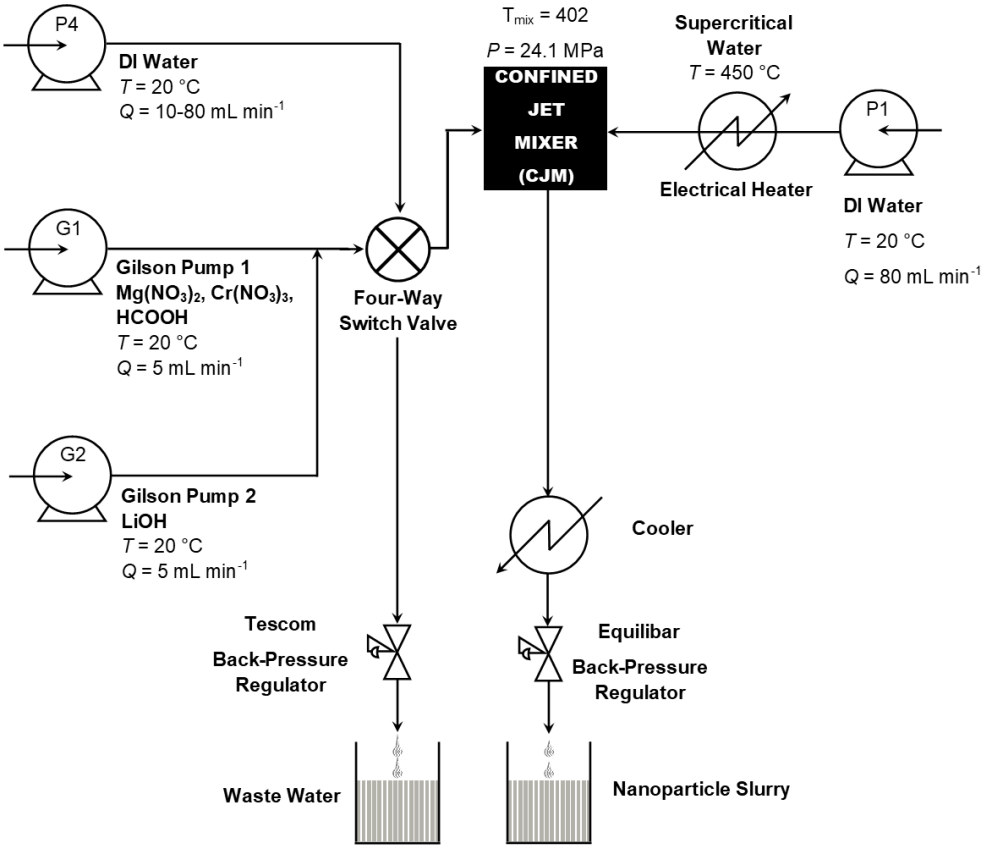

Figure 8.5 – $MgCr_2O_4$ synthesis schematic using the High-Temperature Lab-Scale CHFS apparatus, displaying the flow-rates employed and the precursors used.

The product slurry was collected in a plastic container open to the atmosphere at a production rate of 160, 130 or 90 mL min^{-1}, depending on the flow-rates of the precursor solutions. The slurry was allowed to settle (1 h) and the supernatant siphoned off. Repeated centrifugation and washing with D.I. water was performed (3 × 4500 rpm for 5 minutes) until the conductivity of the supernatant was reduced below 60 µS m^{-1}. The resulting clean, wet paste was freeze-dried as further described in Section 2.1.3.3.

Powder XRD patterns of the samples were collected using set-up **b** in Section 2.1.4.1, over a 2θ range of 2 – 60°, 0.5 ° steps, 10 s per step. Rietveld analysis was performed using MAUD (Material Analysis Using Diffraction) software.[132]

8.4. Results and Discussion

8.4.1. Structural Characterisation

CHFS was employed to attempt to synthesise phase-pure $MgCr_2O_4$ for Mg-ion battery applications, with a range of synthesis temperatures and base concentrations according to Table 8.1. The samples are named "MCO-*x*-*y*", where *x* is the mixing point temperature (in °C) and *y* is the KOH concentration in M. The KOH concentrations were varied between reactions so that the base content was equimolar with the sum of [HCOOH] and [NO_3^-], and additional experiments were performed with an excess of KOH. The Cr_2O_3 sample was synthesised at 335 °C as a comparison, and was named "Cr_2O_3-335-0.3" in an analogous manner.

Table 8.1 – The mixing point temperatures (Tmix), precursor concentrations, yields, observed pH and supernatant colour observed in the MCO synthesis reactions.

Sample name	T_{mix}	[$Mg(NO_3)_2$] / M	[$Cr(NO_3)_3$)] / M	[HCOOH] / M	[KOH] / M	Yield / %	pH	Super-natant
Cr_2O_3-335-0.3	335	0	0.1	0	0.3	140	14	Pale green
MCO-335-0.4	335	0.05	0.1	0	0.4	128	14	Pale green
MCO-335-0.7	335	0.05	0.1	0	0.7	148	14	Pale green
MCO-375-0.4	378	0.05	0.1	0	0.4	103	14	Pale green
MCO-375-0.7	378	0.05	0.1	0	0.7	106	14	Pale green
MCO-402-1.8	402	0.25	0.5	0.3	1.8	N/A	10	Yellow
MCO-402-2.3	402	0.25	0.5	0.3	2.3	N/A	13	Yellow
MCO-402-3.3	402	0.25	0.5	0.3	3.3	N/A	14	Yellow

In general, all synthesised powders were a green-white colour, with yields that were greater than would be expected for pure $MgCr_2O_4$ or Cr_2O_3, implying incomplete formation of the oxide and significant presence of hydroxide. For experiments at the highest temperature (402 °C), formic acid was included in the P2 precursor stream as a precautionary measure to prevent oxidation of Cr(III) to Cr(VI). Formic acid breaks down in supercritical water to give a reducing atmosphere, according to Equation 8.2.[309] Despite this measure, a yellow supernatant was still observed and the samples were immediately disposed of, due to the high carcinogenicity of Cr(VI). It is postulated that the NO_3^- ion acted as the oxidising agent, according to Equation 8.3.

$$HCOOH \rightarrow H_2 + CO_2$$

Equation 8.2 – The decomposition of formic acid in supercritical water to produce H_2 (a reducing agent).

$$Cr^{3+} + 3H_2O + 3NO_3^- \rightarrow Cr^{6+} + 6OH^- + 3NO_2$$

Equation 8.3 – The proposed redox reaction generating Cr(VI) at mixing-point temperatures exceeding 400 °C.

XRD patterns of the $MgCr_2O_4$ products synthesised below 400 °C revealed extremely broad diffraction peaks which matched to the desired phase (PDF Card No. 01-087-1175). These could be unambiguously assigned to the $MgCr_2O_4$ phase, as they did not match the Cr_2O_3 reference (PDF Card No. 38-1479), the Cr_2O_3 sample produced by CHFS (which is likely to be an amorphous-type oxide-hydroxide mixture), MgOH (PDF Card No. 01-086-0441), CrOOH (PDF Card No. 01-074-4780) or $MgCrO_4$ (PDF Card No. 01-074-1225) the only probable alternative phases of the reaction. It is suggested the hydroxide present in these samples caused significant disorder in the crystal structure, which in part resulted in the broad diffraction peaks. The peaks of the samples synthesised at 378 °C were marginally sharper than those at 335 °C, and possibly reflected the increased crystallinity of the samples made at higher temperature.

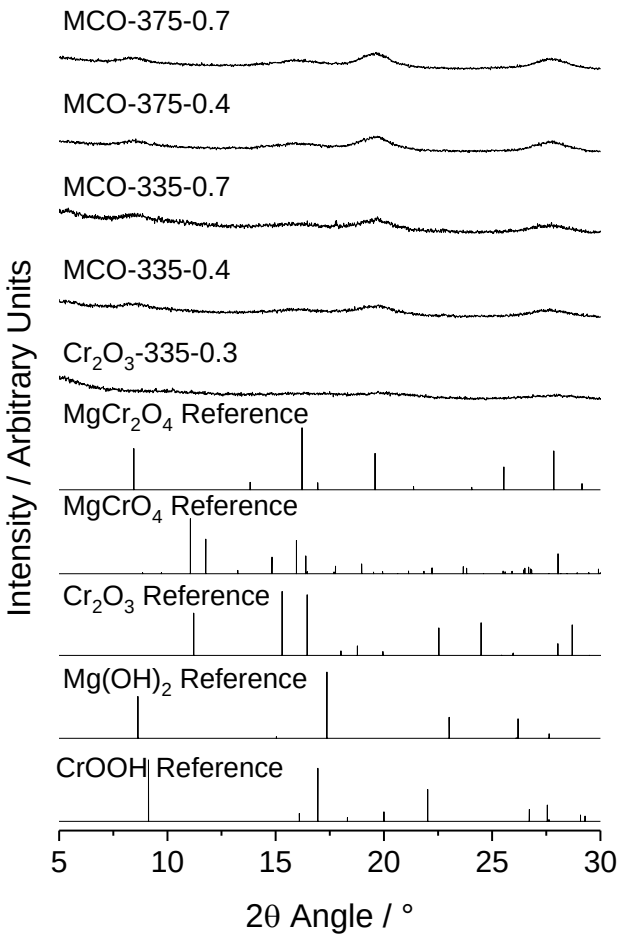

Figure 8.6 – XRD patterns (Mo-Kα radiation) of the initial Cr_2O_3 and $MgCr_2O_4$ synthesis products at various synthesis temperatures and base concentrations, including CrOOH, $Mg(OH)_2$, Cr_2O_3, $MgCrO_4$ and $MgCr_2O_4$ reference patterns.

TGA-DSC analysis of sample MCO-335-0.4 confirmed the temperature-dependent nature of hydroxide to oxide conversion in the MCO samples. Two endotherms were observed during the temperature ramp between 25 °C to 1000 °C; the first (with a minimum at ~80 °C) is attributed to loss of adsorbed water on the nanoparticle surface. The second (with a minimum at ~200 °C) is attributed to hydroxide to oxide conversion, with subsequent water release according to Equation 8.4.

$$MgCr_2O_{4-x}(OH)_{2x} \rightarrow MgCr_2O_4 + xH_2O$$

Equation 8.4 – The conversion of the magnesium chromium oxide-hydroxide mixture to the pure spinel oxide, producing water as a by-product.

The mass loss of 32.5 % over the temperature range resulted in a true yield of 95% for MCO-335-0.4 (as opposed to 140% for the as-prepared sample). It can be seen that the hydroxide conversion endotherm continued to *ca*. 500 °C, which coincided with the end of significant mass loss, and suggested the formation of the oxide was effectively

complete by this temperature. This endotherm was consistent with similar endothermic processes observed in hydrothermally prepared samples, which was attributed to hydroxyl conversion to oxide.[308] In the temperature range 200 – 1000 °C, a large exotherm is observed (maximum at ~600 °C), suggesting crystallisation of the $MgCr_2O_4$ phase occurred smoothly across this region. This could have been a combination of reduced amorphous character and decreasing surface area, as both processes are exothermic.

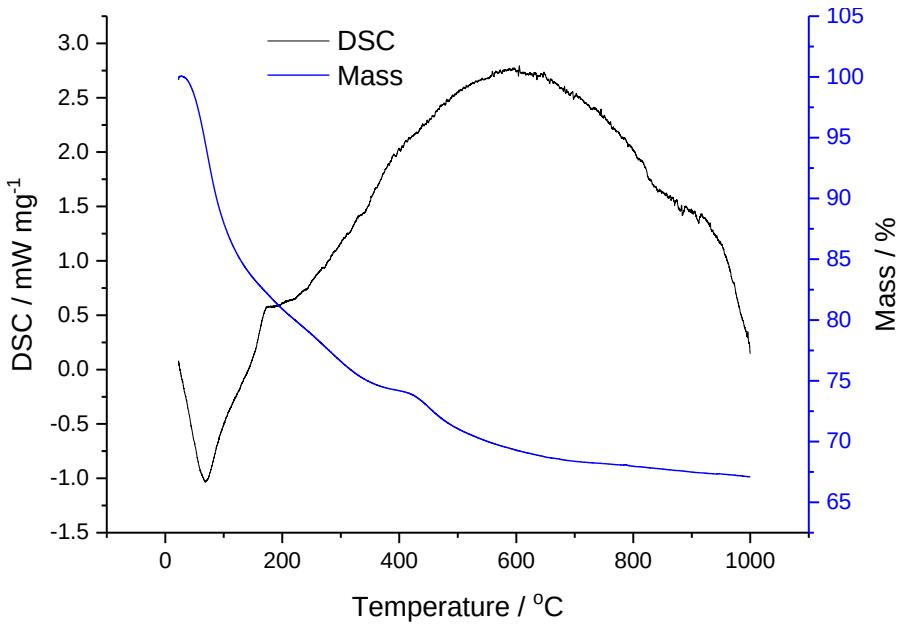

Figure 8.7 – TGA/DSC traces of sample MCO-335-0.4, where the TGA trace is blue and the DSC trace is black, with a heating ramp of 5 °C min^{-1} from room temperature to 1000 °C.

To verify the desired ion ratios were attained in the samples, they were heat-treated at 1000 °C for 24 h to fully crystallise the $MgCr_2O_4$ phase. The heat-treated powders were grey-black, which is the characteristic colour of $MgCr_2O_4$, in contrast to the white-green colour of the as-prepared samples. The diffraction patterns of these heat-treated samples (named HT-1000-MGO-*x*-*y*) all displayed the $MgCr_2O_4$ spinel phase unambiguously (PDF Card No. 01-074-1225, Figure 8.8a). However, a slight element imbalance was implied by the segregation of a trace Cr_2O_3 impurity phase (PDF Card No. 38-1479), which was present in approximately 1 – 2 vol% from Rietveld analysis (Figure 8.8b). This suggested the conversion of the $Mg(NO_3)_2$ precursor within the CHFS reactor was marginally less than $Cr(NO_3)_3$.

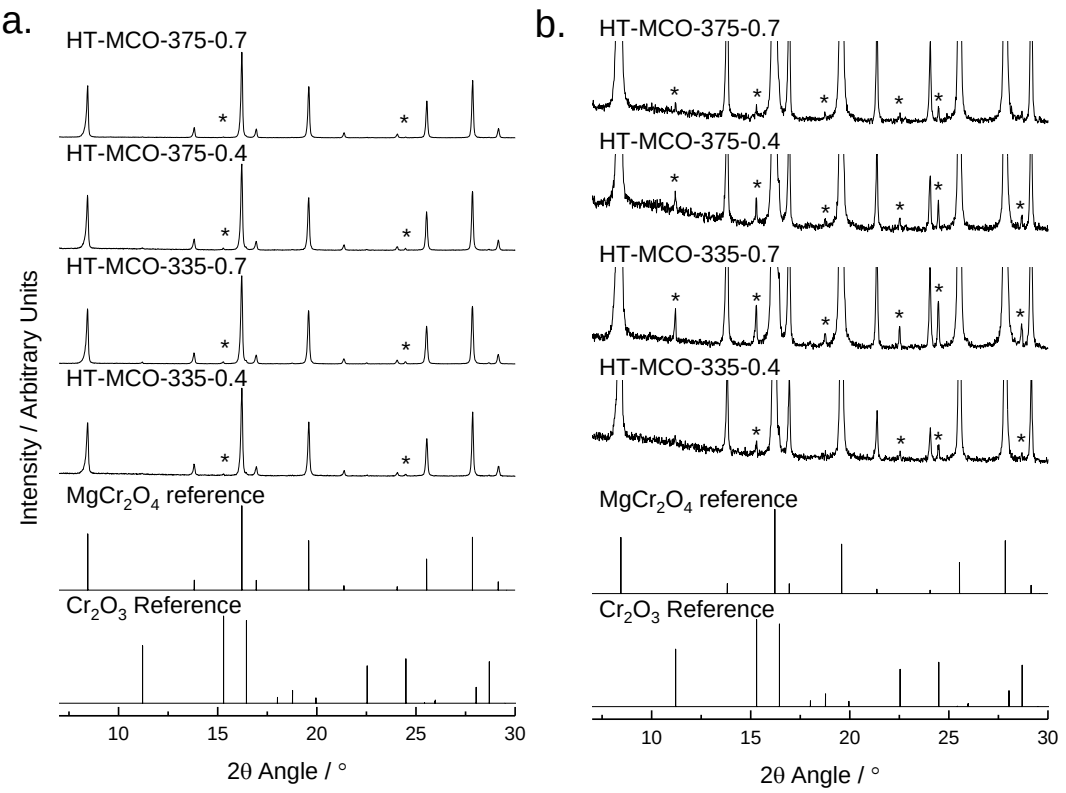

Figure 8.8 – a) XRD patterns (Mo-Kα radiation) of the MCO samples heat-treated at 1000 °C for 24h, with trace Cr_2O_3 impurities present (highlighted with asterisks). b) The same XRD patterns with adjusted *y*-axes to highlight the trace Cr_2O_3 impurities present (highlighted with asterisks). $MgCr_2O_4$ and Cr_2O_3 reference patterns are included for comparison (PDF Card Nos. 01-074-1225 and 38-1479, respectively).

In light of this slight element imbalance, further syntheses were conducted repeating the MCO-335-0.4 synthesis, but with additional experiments with slightly higher $Mg(NO_3)_2$ concentrations (1 and 2 mol% excesses). These samples were named "MCO-*x*-*y*-*z*", where *x* is the mixing point temperature, *y* is the KOH concentration and *z* is the molar excess of $Mg(NO_3)_2$ in mol%. The base concentration was raised from 0.4 to 0.5 M KOH, as the initial product of the repeat experiment MCO-335-0.4-0 had an acidic pH and a yellow supernatant, which implied Cr(VI) formation. The yields were extremely similar to those observed for MCO-335-0.4. XRD patterns of the as-prepared samples revealed similar, broad peaks which matched the $MgCr_2O_4$ reference pattern. XPS of sample MCO-335-0.5-0 confirmed the slight Mg deficiency, with a Mg:Cr ratio of 27:73 rather than 33:67. Heat-treatments at 1000 °C for 24 revealed the slight molar excess of 2 mol% Mg was sufficient to generate the pure $MgCr_2O_4$ phase, with no Cr_2O_3 impurities (Figure 8.9). The mass of the powders were

measured before and after heat-treatment, and gave the adjusted yields displayed in Table 8.2.

Table 8.2 – The mixing point temperatures (T_{mix}), precursor concentrations, yields, observed pH and supernatant colour observed in the MCO stoichiometry-adjusted synthesis reactions.

Sample name	T_{mix}	$[Mg(NO_3)_2]$ / M	$[Cr(NO_3)_3)]$ / M	[KOH] / M	Yield / %	Adjusted Yield / %	pH	Super-natant
MCO-335-0.5-0	335	0.05	0.1	0.5	141	94	14	Pale green
MCO-335-0.5-1	335	0.0505	0.1	0.5	138	93	14	Pale green
MCO-335-0.5-2	335	0.051	0.1	0.5	137	92	14	Pale green

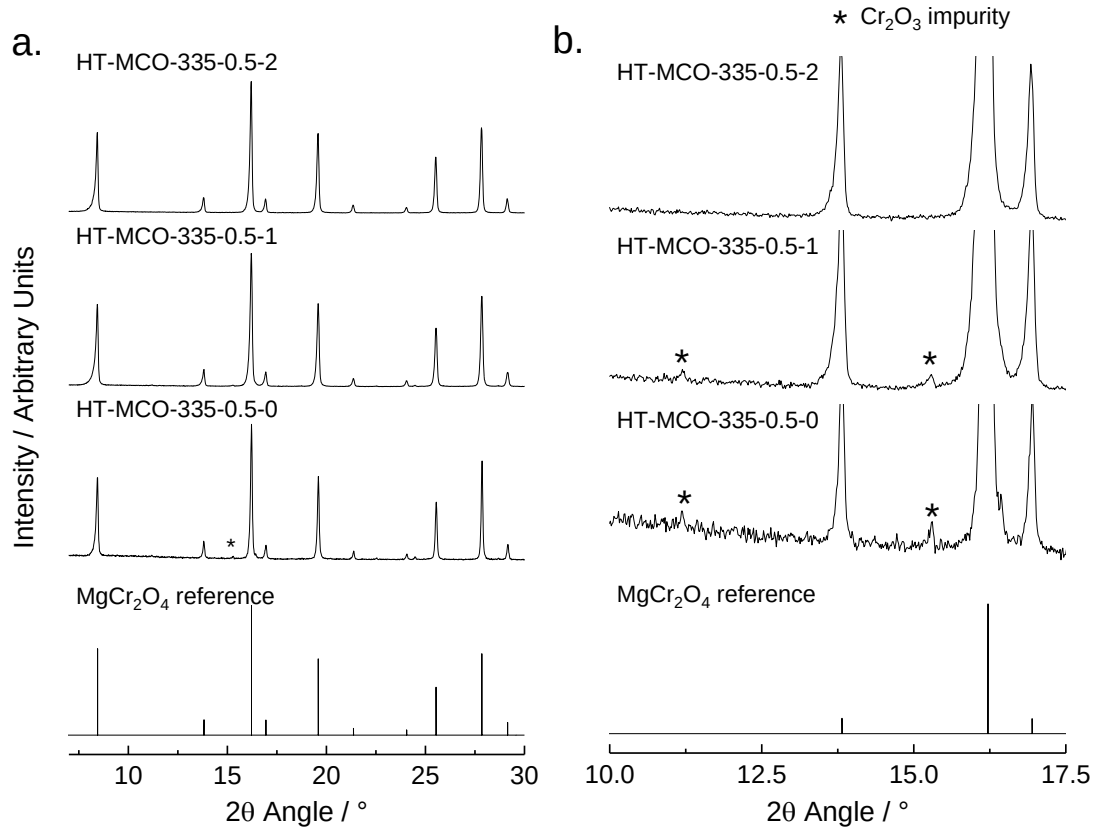

Figure 8.9 – a) XRD patterns (Mo-Kα radiation) of the stoichiometry-adjusted MCO samples heat-treated at 1000 °C for 24h, with the trace Cr_2O_3 impurities marked with asterisks. b) The same XRD patterns with adjusted *y*-axes to highlight the Cr_2O_3 impurity phase. A $MgCr_2O_4$ reference pattern is included for comparison (PDF Card No. 01-074-1225).

It was clear from the TGA-DSC analysis that a minimum temperature of 400 °C is required to convert the hydroxyl species in the as-prepared phases to oxide, forming the $MgCr_2O_4$ spinel. In order to retain high surface area in the samples, flash-heat-treatments of sample MCO-335-0.4 were conducted using the apparatus described in Section 2.1.3.4 for 10 minutes at various temperatures, as indicated in Figure 8.10. This successfully converted the green as-prepared powder to a black powder in all cases, and crude Rietveld refinement of the XRD patterns revealed a combination of increasing crystallinity and decreasing particle size of the flash heat-treated samples with increasing temperature (this is confirmed later in this section with TEM analysis). An impurity peak at 17.8° was observed in some samples, and was attributed to an impurity in the aperture holding the sample (Figure 8.10). No Cr_2O_3 impurities were observed, which possibly indicated the slight off-stoichiometry in this sample is metastable at low temperatures, and only segregated into a separate Cr_2O_3 phase at higher temperatures. Such defects could have been Mg^{2+} vacancies (as the sample was Mg deficient) charge-balanced with Cr^{4+}. It would be encouraging if such an Mg deficiency were stable, as simultaneous Mg^{2+} vacancy generation and Cr^{3+} oxidation to Cr^{4+} is the postulated demagnesiation reaction of the spinel compound. Alternatively, it may have been amorphous and not visible by XRD at lower heat-treatment temperatures.

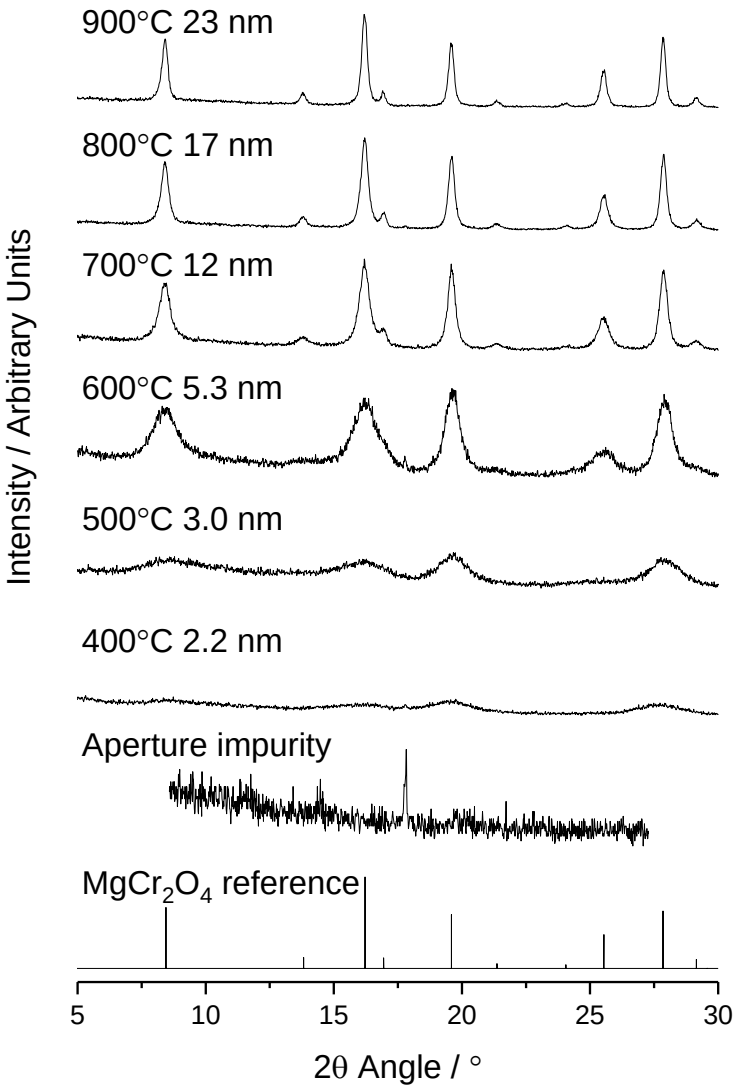

Figure 8.10 – a) XRD patterns (Mo-Kα radiation) of the flash heat-treated samples at temperatures ranging between 400 – 1000 °C, with the diffraction peaks growing more intense and less broad with increasing temperature. A $MgCr_2O_4$ reference pattern is included for comparison (PDF Card No. 01-074-1225). Additionally, a scan of the aperture without any sample contained is displayed, showing the impurity peak at 17.8°.

Larger-batches of the flash-heat-treated samples at 500 °C, 600 °C and 800 °C were repeated, using the sample MCO-335-0.5-0 as a precursor, and were named FHT-*x*-MCO-335-0.5-0, where *x* is the flash-heat-treatment temperature. The trend in the XRD patterns was very similar to the previous flash-heat-treatment experiments, and demonstrated the repeatability of the method.

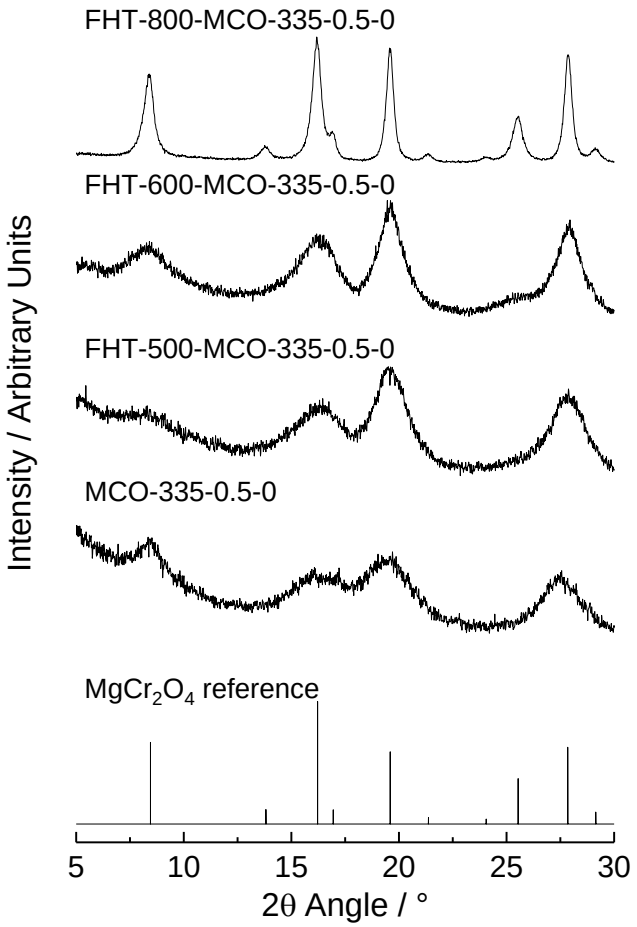

Figure 8.11 – XRD patterns (Mo-Kα radiation) of the repeat flash heat-treatment experiments of MCO-335-0.5-0 at 500, 600 and 800 °C for 10 minutes.

As the X-Ray diffraction peaks of the MCO samples were generally quite broad, Raman spectroscopy was used to probe the local structure of selected as-prepared and heat-treated MCO samples. The as-prepared samples (reaction temperatures of 335 °C and 375 °C, Figure 8.12a-b) displayed a broad signal in the range 200-1000 cm^{-1} (the characteristic range for oxides). Upon flash-heat-treatment, the peaks grew sharper with increasing heat-treatment temperature, although not at the characteristic wavenumbers reported previously for MCO (Figure 8.12c-e).[310,311] In contrast, the sample calcined at 1000 °C displayed extremely sharp signals which could be unambiguously assigned to Raman active modes in $MgCr_2O_4$ (Figure 8.12f, Table 8.3). The broad peaks below 1000 cm^{-1} are highly diagnostic of glassy structures, where local vibrational modes are disrupted by first coordination-shell or second coordination-shell defects.[312] Therefore, the XRD, Raman spectroscopy, and TGA/DSC analyses suggested there is a high degree of local disorder in these

$MgCr_2O_4$ compounds, where the crystallinity of the spinel-like structure was disrupted by the remaining hydroxide present.

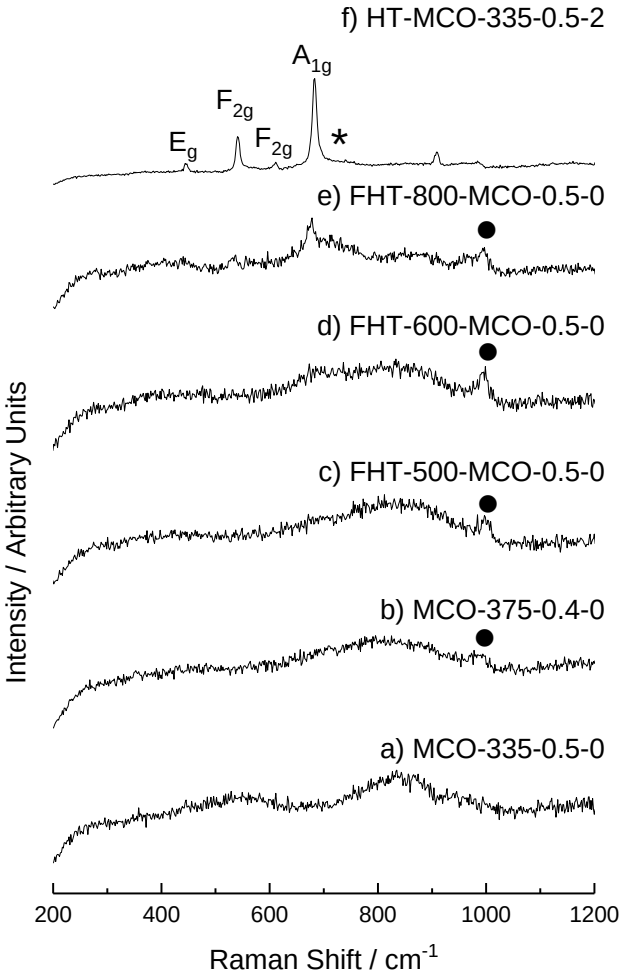

Figure 8.12 – Raman spectroscopy of as-prepared (a and b), flash heat-treated (c – e) and 24 h heat-treated (f) MCO samples, with characteristic Raman-active modes of $MgCr_2O_4$ highlighted. Modes marked with an asterisk have been observed previously in $MgCr_2O_4$, but not assigned. The mode marked with a ● is assigned to the Cr=O bond stretching mode at 975 cm^{-1},[313] although whether this is formally an CrO_3 impurity phase or merely a surface feature of the materials is unclear.

Table 8.3 – The Raman-active modes observed in $MgCr_2O_4$ from literature reports and in sample HT-MCO-335-0.5-2.[310,311]

Raman Active Mode	Literature Wavenumber / cm^{-1}	Observed Wavenumber / cm^{-1}
E_g	447	444
F_{2g}	544	541
F_{2g}	614	609
A_{1g}	687	680

8.4.2. Microscopy and Surface Area analysis

TEM was employed to analyse the particle size and morphology, as the particle sizes were below the resolution of the FE-SEM equipment. EDS analysis confirmed an even dispersion of Mg and Cr within the MCO-335-0.4 material, which was consistent with the assertion that the sample was an amorphous-type $MgCrO_{4-x}(OH)_{2x}$ phase, as opposed to individual $Mg(OH)_2$ and CrO_xOH_y particles. TEM images revealed amorphous particles approximately 2 nm in size (the lack of crystallinity made particle size analysis impossible, as clear particle boundaries could not be observed). The amorphous nature of the agglomerates was confirmed with a Fourier-transform of the TEM image, which mostly displayed an amorphous halo. However, some faint electron diffraction spots were observed, corresponding to a d-spacing of ~ 2 Å. This may correspond to the (3 2 2) $MgCr_2O_4$ lattice spacing, although given the degree of disorder in the structure, the assignation is tentative at best.

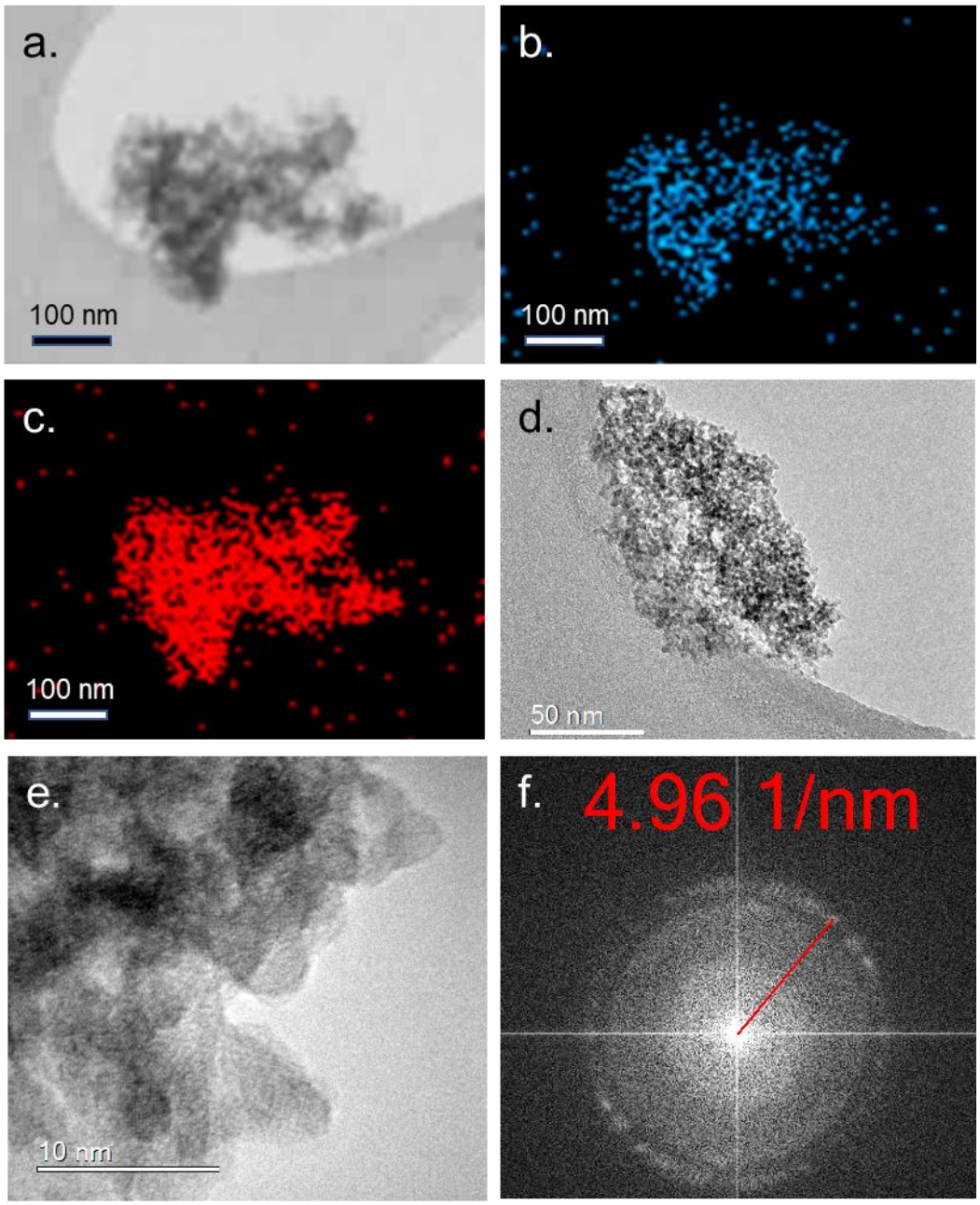

Figure 8.13 – EDS and TEM analysis of MCO-335-0.4: a) The darkfield image of a representative MCO-335-0.4 agglomerate, b) The Mg-Kα signals (blue), c) The Cr-Kα signals (red), d) TEM image of a representative MCO-335-0.4 agglomerate, e) Higher magnification image of the same agglomerate, f) Representative Fourier-Transform of a MCO-335-0.4 TEM image.

The flash heat-treatments successfully generated more crystalline $MgCr_2O_4$ as observed by TEM. Lattice planes could be more clearly observed in the sample with the lowest heat-treatment temperature (Figure 8.14a). With increasing heat-treatment temperature, significant populations of particles > 10 nm were generated according to the particle size distributions (Figure 8.15a-c), with average particle sizes increasing from 3.7 ± 2.4 nm to 16.3 ± 9.6 nm (Figure 8.15d). The heat-treatments also induced

a morphology change, with pseudo-spherical particles observed at lower temperatures, and cuboid morphology favoured at higher temperatures (Figure 8.14a-c). The highest heat-treatment temperature (800 °C) yielded extremely crystalline particles, as evidenced by the clear lattice planes observed in Figure 8.14d. Selected area diffraction was performed on a particle of sample FHT-800-MCO-335-0.5-0, where points in the pattern could be assigned to lattice planes based upon their d-spacing, and revealed the particles were faceted primarily on the (1 1 1) surface, which has been commonly observed in spinel-type compounds.[314] BET analysis was performed on MCO-335-0.5-0 and the flash-heat-treated samples, and confirmed that heat-treatments of 400 and 500 °C were successful in increasing crystallinity without drastically sacrificing surface area (Figure 8.16). Particle sizes were estimated using the spherical approximation (details in Section 2.1.4.7), and correlated well with the particle sizes discerned from TEM.

The particle sizes generated by flash heat-treatment are smaller than any reported $MgCr_2O_4$ spinel sample in literature.[29,304,306,308,315–318] In addition, the specific surface areas of the samples heat-treated at 500 and 600 °C are approximately double the highest achieved for $MgCr_2O_4$ by Andrade *et al.*[317] Therefore, these samples are of interest for multivalent battery electrode assessment, and could be used to probe the effects of particle size and crystallinity on multivalent performance.

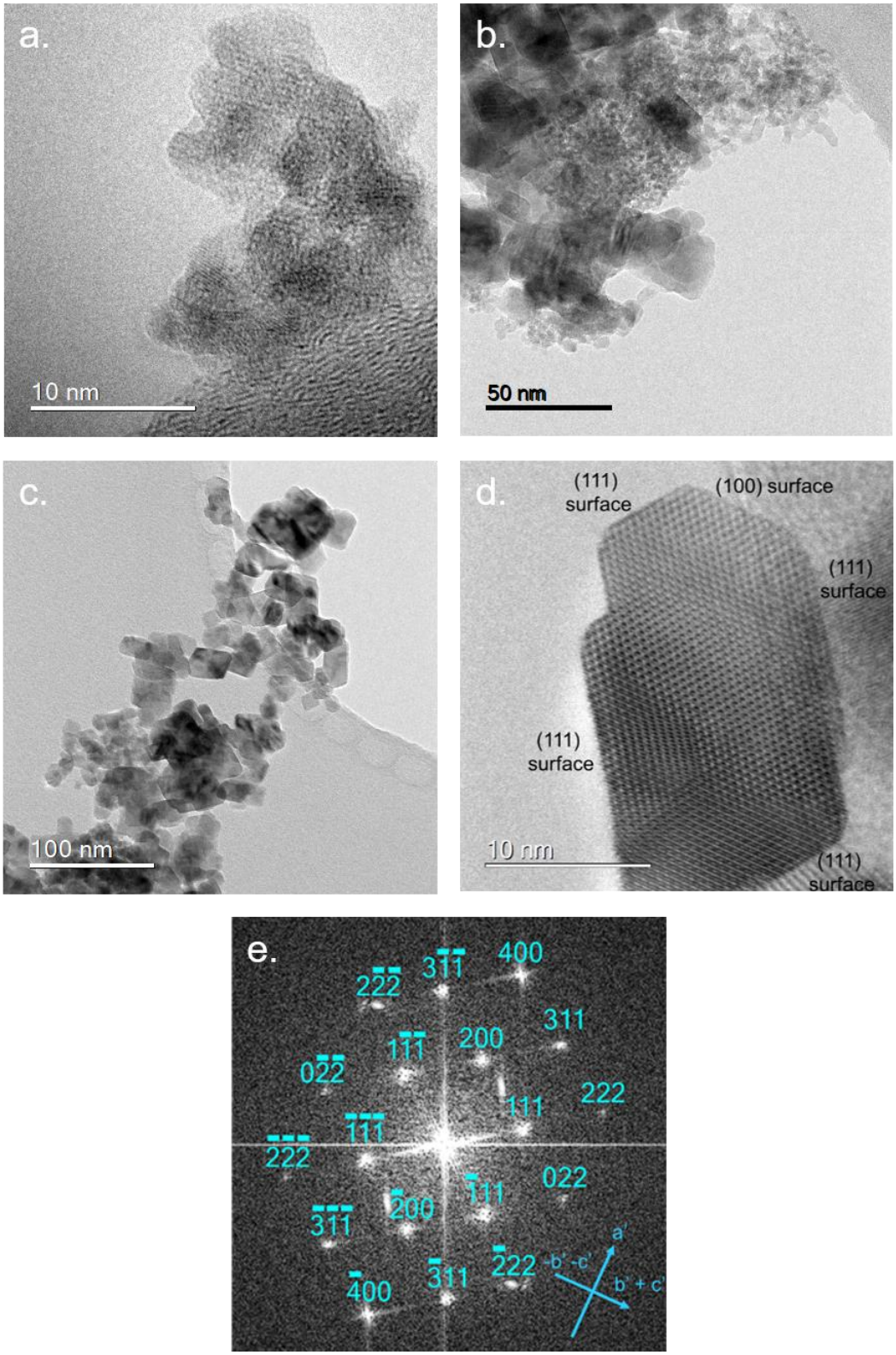

Figure 8.14 – TEM microscopy of samples a) FHT-500-MCO-335-0.5-0, b) FHT-600-MCO-335-0.5-0 and c) FHT-800-MCO-335-0.5-0. d) A magnified TEM image of FHT-800-MCO-335-0.5-0 observed down the [0 1 $\bar{1}$] direction, where selected area diffraction revealed the surface planes. e) Selected area diffraction of FHT-800-MCO-335-0.5-0 observed down the [01$\bar{1}$] axis, with the Miller indices of the diffraction spots indicated.

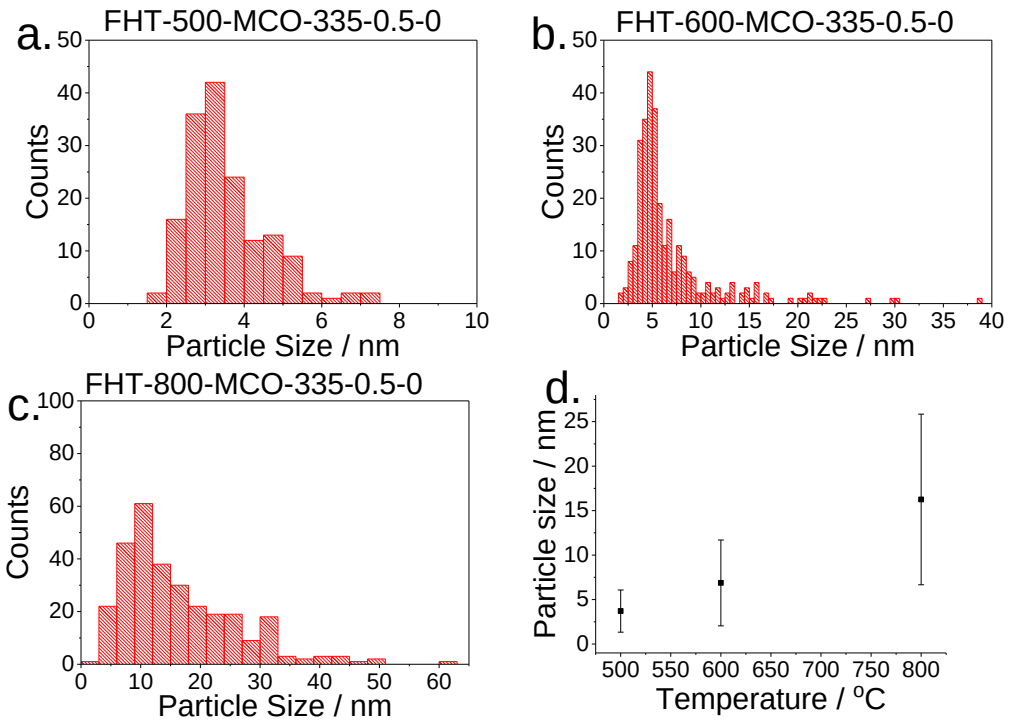

Figure 8.15 – Particle size distributions (from TEM) of samples a) FHT-500-MCO-335-0.5-0, b) FHT-600-MCO-335-0.5-0 and c) FHT-800-MCO-335-0.5-0. d) A plot of average particle size (with standard deviations plotted as error bars) as a function of heat-treatment temperature.

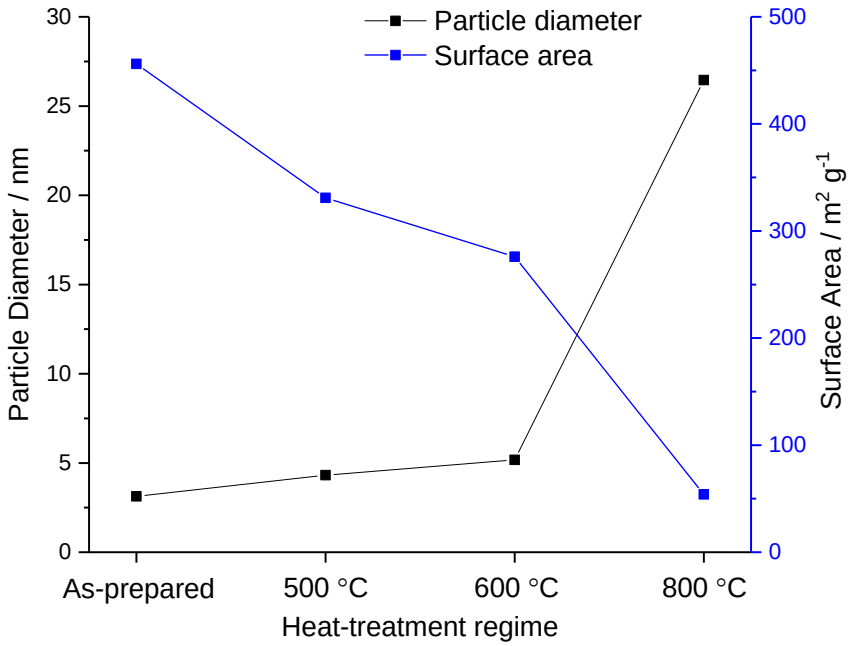

Figure 8.16 – BET surface area analysis of the as-prepared and flash-heat-treated samples, indicating the specific surface areas and estimated particle diameters (using the spherical approximation).

8.5. Conclusions and Further Work

$MgCr_2O_4$ was successfully synthesised *via* a combination of CHFS and flash-heat-treatment for the first time. The heat-treatment temperature had a strong impact on particle size, morphology, and crystallinity, and suggests that the heat-treatment temperature could be tailored to achieve a desired balance between these factors.

It is suggested that the initial phase produced from the CHFS reactor was a glassy spinel phase, which was only partially decomposed $MgCr_2(OH)_8$ hydroxide. Hence a later heat-treatment was required to achieve a more crystalline spinel phase, with the onset of crystallisation occurring at 400 °C or above. Flash heat-treatment was successful in producing more crystalline $MgCr_2O_4$ phases without sacrificing significant surface area.

Further synthesis work that could be attempted to synthesise $MgCr_2O_4$ should focus on generating the crystalline phase without requiring an additional heating step, which may prevent some of the particle growth observed with the flash-heat-treatment study. It is not possible to simply increase the reaction temperature (keeping other reaction conditions the same) to generate crystalline $MgCr_2O_4$ directly from CHFS; higher reaction temperatures resulted in oxidation of Cr^{3+} to Cr^{6+}, and this was not prevented by inclusion of a reducing agent. It is suggested alternative precursors could be used which are less oxidising, such as metal acetates, which possess reducing counterions.

The three flash-heat-treated samples discussed within this chapter will be sent to a specialist multivalent electrochemistry group in the U.S.A. (Cabana Group, UIC) for Mg-ion testing, and will hopefully reveal reversible Mg-ion intercalation chemistry. Mg-ion intercalation is suggested to be very sensitive to particle size, but may also require high-crystallinity particles to enable Mg-ion diffusion. Therefore, the array of $MgCr_2O_4$ particle sizes and crystallinities synthesised in this chapter will be ideal to determine if $MgCr_2O_4$ is an active multivalent material, and which of these two factors has the dominant effect on performance.

9. Conclusions and Further Work

This thesis investigated the synthesis and electrochemical testing of nanometric cathode materials for Li-ion and Mg-ion batteries using a continuous hydrothermal synthesis method. For many of the materials tested, they were the first of their respective phases to be achieved by CHFS. Typically, CHFS-made materials are simple metal oxides, so the production of more complex species with multiple metal ions (or phosphate counter-ions) within this thesis represents a marked improvement on the versatility of this technique.

Furthermore, significant improvements in the electrochemical performance of these materials compared to bulk micron-sized particles was achieved by a combination of nanosizing, doping and surface modification with carbon. Their performance compares favourably with similar materials made in literature, which often rely on high-temperature or poorly-scalable synthesis techniques, and suggests that CHFS has great potential to efficiently generate high-quality nanomaterials for electrochemical devices on a commercial scale.

However, it should be stressed that the intrinsic flaws present in nanoparticulate electrodes were observed within this thesis. Side-reactions with the electrolyte were observed beyond the first charge/discharge cycle for all materials, which led to rapid capacity fade when tested in a full cell. It is suggested, therefore, that further work is required to develop electrolyte additives which stabilise nanoparticulate surfaces. Furthermore, modifying the nanoparticles themselves to reduce side reactions should also be pursued – for example, generating protective surface coatings or embedding them in a larger host material may enable a compromise between the high-rate performance of nanomaterials and the stability of micron-sized materials.

One possible application of nanomaterials which would side-step this issue is within multivalent batteries, particularly Mg-ion. As the Mg-ion battery relies on a Mg-metal anode, it is not inconceivable that small side-reactions could be tolerated, as Mg could be replenished from a slightly oversized Mg anode. Furthermore, the kinetics of Mg insertion/extraction are so poor that nanomaterials may be required to achieve

significant charge storage. Therefore, CHFS-made nanomaterials could potentially enable a successful Mg-ion technology that surpasses Li-ion.

In summary, this thesis has demonstrated the opportunities and deficiencies of nanomaterials made *via* CHFS for electrochemical applications, and has revealed exciting avenues of further work to develop a step-change in energy storage technology

10. References

1. Module 3: Characteristics of Particles - Particle Size Categories. Available at: https://web.archive.org/web/20101203205130/http://www.epa.gov/apti/bces/module3/category/category.htm. (Accessed: 25th August 2017)

2. Saravanan, K., Balaya, P., Reddy, M. V., Chowdari, B. V. R. & Vittal, J. J. Morphology controlled synthesis of $LiFePO_4$/C nanoplates for Li-ion batteries. *Energy Environ. Sci.* **3,** 457 (2010).

3. Park, J. *et al.* Graphene quantum dots: structural integrity and oxygen functional groups for high sulfur/sulfide utilization in lithium sulfur batteries. *NPG Asia Mater.* **8,** e272 (2016).

4. Butler, S. Z. *et al.* Progress, challenges, and opportunities in two-dimensional materials beyond graphene. *ACS Nano* **7,** 2898–2926 (2013).

5. Hu, J., Odom, T. W. & Lieber, C. M. Chemistry and physics in one dimension: Synthesis and properties of nanowires and nanotubes. *Acc. Chem. Res.* **32,** 435–445 (1999).

6. Wu, Y. P., Rahm, E. & Holze, R. Carbon anode materials for lithium ion batteries. *J. Power Sources* **114,** 228–236 (2003).

7. Rajamathi, M. & Seshadri, R. Oxide and chalcogenide nanoparticles from hydrothermal/solvothermal reactions. *Curr. Opin. Solid State Mater. Sci.* **6,** 337–345 (2002).

8. Rai, M., Yadav, A. & Gade, A. Silver nanoparticles as a new generation of antimicrobials. *Biotechnol. Adv.* **27,** 76–83 (2009).

9. Piccinno, F., Gottschalk, F., Seeger, S. & Nowack, B. Industrial production quantities and uses of ten engineered nanomaterials in Europe and the world. *J. Nanoparticle Res.* **14,** (2012).

10. Astruc, D., Lu, F. & Aranzaes, J. R. Nanoparticles as recyclable catalysts: The frontier between homogeneous and heterogeneous catalysis. *Angew. Chemie - Int. Ed.* **44,** 7852–7872 (2005).

11. Kodama, R.H. Magnetic nanoparticles. *J. Magn. Magn. Mater.* **200,** 359–372 (1999).

12. Dry, M. E. The Fischer-Tropsch process: 1950-2000. *Catal. Today* **71,** 227–241 (2002).

13. Lu, L., Li, S. X. & Lu, K. An abnormal strain rate effect on tensile behavior in nanocrystalline copper. *Scr. Mater.* **45,** 1163–1169 (2001).

14. Schuele, W. J. & Deetscreek, V. D. Appearance of a weak ferromagnetism in fine particles of antiferromagnetic materials. *J. Appl. Phys.* **33,** 1136–1137 (1962).

15. Gates, B. D. *et al.* New Approaches to Nanofabrication: Molding, Printing, and Other Techniques. *Chem. Rev.* **105,** 1171–1196 (2005).

16. Reyntjens, S. & Puers, R. A review of focused ion beam applications in microsystem technology. *J. Micromech. Microeng.* **11,** 287–300 (2001).

17. Jugović, D. & Uskoković, D. A review of recent developments in the synthesis procedures of lithium iron phosphate powders. *J. Power Sources* **190,** 538–544 (2009).

18. Devaraju, M. K. & Honma, I. Hydrothermal and Solvothermal Process Towards Development of $LiMPO_4$ (M = Fe, Mn) Nanomaterials for Lithium-Ion Batteries. *Adv. Energy Mater.* **2,** 284–297 (2012).

19. Cho, T.-H. & Chung, H.-T. Synthesis of olivine-type $LiFePO_4$ by emulsion-drying method. *J. Power Sources* **133,** 272–276 (2004).

20. Myung, S.-T., Komaba, S., Hirosaki, N., Yashiro, H. & Kumagai, N. Emulsion drying synthesis of olivine $LiFePO_4$/C composite and its electrochemical properties as lithium intercalation material. *Electrochim. Acta* **49,** 4213–4222 (2004).

21. Bewlay, S., Konstantinov, K., Wang, G. X., Dou, S. X. & Liu, H. K. Conductivity improvements to spray-produced $LiFePO_4$ by addition of a carbon source. *Mater. Lett.* **58,** 1788–1791 (2004).

22. Yang, M.-R., Teng, T.-H. & Wu, S.-H. $LiFePO_4$/carbon cathode materials prepared by ultrasonic spray pyrolysis. *J. Power Sources* **159,** 307–311 (2006).

23. Cushing, B. L., Kolesnichenko, V. L. & O'Connor, C. J. Recent Advances in the Liquid-Phase Syntheses of Inorganic Nanoparticles. *Chem. Rev.* **104,** 3893–

3946 (2004).

24. Hench, L. L. & West, J. K. The Sol-Gel Process. *Chem. Rev.* **90,** 33–72 (1990).

25. Arnold, G. *et al.* Fine-particle lithium iron phosphate $LiFePO_4$ synthesized by a new low-cost aqueous precipitation technique. *J. Power Sources* **119–121,** 247–251 (2003).

26. Zheng, J., Li, X., Wang, Z., Guo, H. & Zhou, S. $LiFePO_4$ with enhanced performance synthesized by a novel synthetic route. *J. Power Sources* **184,** 574–577 (2008).

27. Wang, W. J., Zhao, H. B., Yuan, A. B., Fang, J. H. & Xu, J. Q. Hydrothermal sol-gel method for the synthesis of a multiwalled carbon nanotube-$Na_3V_2(PO_4)_3$ composite as a novel electrode material for lithium-ion batteries. *Wuli Huaxue Xuebao/ Acta Phys. - Chim. Sin.* **30,** 1113–1120 (2014).

28. Yang, J. & Xu, J. J. Nonaqueous Sol-Gel Synthesis of High-Performance $LiFePO_4$. *Electrochem. Solid-State Lett.* **7,** A515 (2004).

29. Li, S. P., Jia, X. L. & Qi, Y. F. Synthesis of Nano-Crystalline Magnesium Chromate Spinel by Citrate Sol-Gel Method. *Adv. Mater. Res.* **284–286,** 730–733 (2011).

30. Di Lecce, D., Hu, T. & Hassoun, J. Electrochemical features of $LiMnPO_4$ olivine prepared by sol-gel pathway. *J. Alloys Compd.* **693,** 730–737 (2017).

31. Oskam, G. Metal oxide nanoparticles : synthesis, characterization and application. *J. Sol-Gel Sci. Technol.* **37,** 161–164 (2006).

32. Jolivet, J.-P. *Metal Oxide Chemistry and Synthesis: From Solution to Solid State*. (Wiley, 2000).

33. LaMer, V. K. & Dinegar, R. H. Theory, Production and Mechanism of Formation of Monodispersed Hydrosols. *J. Am. Chem. Soc.* **72,** 4847–4854 (1950).

34. Nielsen, A. E. *Kinetics of Precipitation*. (Pergamon Press, 1964).

35. Krüger, H. Techniques for the Kinetic Study of Fast Reactions in Solution. *Chem. Soc. Rev.* **11,** 227–255 (1982).

36. Zhang, J., Huang, F. & Lin, Z. Progress of nanocrystalline growth kinetics based on oriented attachment. *Nanoscale* **2,** 18–34 (2010).

37. Lifshitz, I. M. & Slyozov, V. V. The Kinetics of Precipitation from Supersaturated Solid Solutions. *J. Phys. Chem. Solids* **19,** 35–50 (1961).

38. Wagner, C. Theorie der Alterung von Niederschlägen durch Umlösen (Ostwald-Reifung). *Zeitschrift für Elektrochemie, Berichte der Bunsengesellschaft für Phys. Chemie* **65,** 581–591 (1961).

39. Yu, S. H. Hydrothermal/solvothermal processing of advanced ceramic materials. *J. Ceram. Soc. Japan* **109,** S65–S75 (2001).

40. Cansell, F. *et al.* Supercritical fluid processing: a new route for materials synthesis. *J. Mater. Chem.* **9,** 67–75 (1999).

41. Chen, J. & Whittingham, M. Hydrothermal synthesis of lithium iron phosphate. *Electrochem. commun.* **8,** 855–858 (2006).

42. Yang, S., Zhou, X., Zhang, J. & Liu, Z. Morphology-controlled solvothermal synthesis of $LiFePO_4$ as a cathode material for lithium-ion batteries. *J. Mater. Chem.* **20,** 8086–8091 (2010).

43. Tajimi, S., Ikeda, Y., Uematsu, K., Toda, K. & Sato, M. Enhanced electrochemical performance of $LiFePO_4$ prepared by hydrothermal reaction. *Solid State Ionics* **175,** 287–290 (2004).

44. Meligrana, G., Gerbaldi, C., Tuel, A., Bodoardo, S. & Penazzi, N. Hydrothermal synthesis of high surface $LiFePO_4$ powders as cathode for Li-ion cells. *J. Power Sources* **160,** 516–522 (2006).

45. Ni, J. *et al.* Hydrothermal preparation of $LiFePO_4$ nanocrystals mediated by organic acid. *J. Power Sources* **195,** 2877–2882 (2010).

46. Ellis, B., Kan, W. H., Makahnouk, W. R. M. & Nazar, L. F. Synthesis of nanocrystals and morphology control of hydrothermally prepared $LiFePO_4$. *J. Mater. Chem.* **17,** 3248–3254 (2007).

47. Darr, J. A., Zhang, J., Makwana, N. M. & Weng, X. Continuous Hydrothermal Synthesis of Inorganic Nanoparticles; Applications and Future Directions. *Chem. Rev.* **in press,** 1–141 (2017).

48. Darr, J. A. & Poliakoff, M. New Directions in Inorganic and Metal-Organic Coordination Chemistry in Supercritical Fluids. *Chem. Rev.* **99,** 495–541 (1999).

49. Weingärtner, H. & Franck, E. U. Supercritical water as a solvent. *Angew. Chemie - Int. Ed.* **44,** 2672–2692 (2005).

50. Fernández, D. P., Mulev, Y., Goodwin, A. R. H. & Levelt-Sengers, J. M. H. A Database for the Static Dielectric Constant of Water and Steam. *J. Phys. Chem. Ref. Data* **24,** 33–69 (1995).

51. Dielectric Constant. Available at: http://macro.lsu.edu/HowTo/solvents/DielectricConstant.htm. (Accessed: 25th August 2017)

52. Botti, A., Bruni, F. & Ricci, M. A. Neutron diffraction study of high density supercritical water. *J. Chem. Phys.* **109,** 3180 (1998).

53. Matubayasi, N., Wakai, C. & Nakahara, M. Structural study of supercritical water. I. Nuclear magnetic resonance. *J. Chem. Phys.* **107,** 9133 (1997).

54. Kohl, W., Lindner, H. A. & Franck, E. U. Raman Spectra of Water to 400 ^{o}C and 3000 bar. *Ber. Bunsenges. Phys. Chem.* **95,** 1586–1593 (1991).

55. Franck, E. U. & Roth, K. Infrared absorption of HDO in water at high pressures and temperatures. *Discuss. Faraday Soc*. **43,** 108–114 (1967).

56. Chialvo, A. A. & Cummings, P. T. Molecular-based modeling of water and aqueous solutions at supercritical conditions. *Adv. Chem. Phys.* **109,** 115–205 (1999).

57. Hoffmann, M. M., Darab, J. G., Palmer, B. J. & Fulton, J. L. A Transition in the Ni^{2+} Complex Structure from Six to Four-Coordinate upon Formation of Ion Pair Species in Supercritical Water: An X-ray Absorption Fine Structure, Near Infrared, and Molecular Dynamics Study. *J. Phys. Chem. A* **103,** 8471–8482 (1999).

58. Seward, T. M., Henderson, C. M. B., Charnock, J. M. & Dobson, B. R. An X-ray absorption (EXAFS) spectroscopic study of aquated Ag^{+} in hydrothermal solutions to 350°C. *Geochim. Cosmochim. Acta* **60,** 2273–2282 (1996).

59. Adschiri, T., Kanazawa, K. & Arai, K. Rapid and continuous hydrothermal crystallization of metal oxide particles in supercritical water. *J. Am. Ceram. Soc.* 75**,** 1019–1022 (1992).

60. Kanamura, K. *et al.* Preparation and electrochemical characterization of $LiCoO_2$ particles prepared by supercritical water synthesis. *Electrochem. Solid-State Lett.* **3,** 256–258 (2000).

61. Matson, D. W., Linehan, J. C. & Bean, R. M. Ultrafine Iron-Oxide Powders Generated Using a Flow-through Hydrothermal Process. *Mater. Lett.* **14,** 222–226 (1992).

62. Buehler, M. F., Darab, J. G., Matson, D. W. & Linehan, J. C. Bench-scale synthesis of nanoscale material. in *Technology 2003 Conference* (1993).

63. Adschiri, T., Hakuta, Y. & Arai, K. Hydrothermal Synthesis of Metal Oxide Fine Particles at Supercritical Conditions. *Ind. Eng. Chem. Res.* **39,** 4901–4907 (2000).

64. Cabanas, A. & Poliakoff, M. The continuous hydrothermal synthesis of nano-particulate ferrites in near critical and supercritical water. *J. Mater. Chem.* **11,** 1408–1416 (2001).

65. Rangappa, D., Naka, T., Ohara, S. & Adschiri, T. Preparation of Ba-Hexaferrite Nanocrystals by an Organic Ligand-Assisted Supercritical Water Process. *Cryst. Growth Des.* **10,** 11–15 (2010).

66. Lester, E. *et al.* Impact of reactor geometry on continuous hydrothermal synthesis mixing. *Mater. Res. Innov.* **14,** 19–26 (2010).

67. Hellstern, H. L. et al. Development of a Dual-Stage Continuous Flow Reactor for Hydrothermal Synthesis of Hybrid Nanoparticles. *Ind. Eng. Chem. Res.* **54,** 8500−8508 (2015).

68. Aoki, N. *et al.* Kinetics study to identify reaction-controlled conditions for supercritical hydrothermal nanoparticle synthesis with flow-type reactors. *J. Supercrit. Fluids* **110,** 161–166 (2016).

69. Hong, S.-A. *et al.* Continuous synthesis of lithium iron phosphate ($LiFePO_4$) nanoparticles in supercritical water: Effect of mixing tee. *J. Supercrit. Fluids*

73, 70–79 (2013).

70. Kawasaki, S., Sue, K., Ookawara, R., Wakashima, Y. & Suzuki, A. Development of Novel Micro Swirl Mixer for Producing Fine Metal Oxide Nanoparticles by Continuous Supercritical Hydrothermal Method. *J. Oleo Sci.* **59,** 557–562 (2010).

71. Sue, K. *et al.* Continuous Hydrothermal Synthesis of Fe_2O_3 Nanoparticles Using a Central Collision-Type Micromixer for Rapid and Homogeneous Nucleation at 673 K and 30 MPa. *Ind. Eng. Chem. Res.* **49,** 8841–8846 (2010).

72. Denis, C. J. Nucleation and growth of industrial nanomaterials in a continuous hydrothermal reactor. (University College London, 2016).

73. Blood, P. J., Denyer, J. P., Azzopardi, B. J., Poliakoff, M. & Lester, E. A versatile flow visualisation technique for quantifying mixing in a binary system: Application to continuous supercritical water hydrothermal synthesis (SWHS). *Chem. Eng. Sci.* **59,** 2853–2861 (2004).

74. Lester, E. *et al.* Reaction engineering: The supercritical water hydrothermal synthesis of nano-particles. *J. Supercrit. Fluids* **37,** 209–214 (2006).

75. Tighe, C. J. *et al.* Investigation of counter-current mixing in a continuous hydrothermal flow reactor. *J. Supercrit. Fluids* **62,** 165–172 (2012).

76. Gruar, R., Tighe, C. & Darr, J. Scaling-up a confined jet reactor for the continuous hydrothermal manufacture of nanomaterials. *Ind. Eng. Chem. Res.* **52,** 5270–5281 (2013).

77. World Population Prospects. Population Division of the Department of Economic and Social Affairs of the United Nations Secretariat. 1–57 (2008).

78. BBC News. Leighton Buzzard electricity facility tests 'largest battery'. (2014). Available at: http://www.bbc.co.uk/news/uk-england-beds-bucks-herts-30476591. (Accessed: 25th August 2017)

79. Chalk, S. G. & Miller, J. F. Key challenges and recent progress in batteries, fuel cells, and hydrogen storage for clean energy systems. *J. Power Sources* **159,** 73–80 (2006).

80. Greenword, N. N. & Earnshaw, A. *Chemistry of the Elements*. (Butterworth-

Heinemann, 1997).

81. Vanýsek, P. in *Handbook of Chemistry and Physics* (Chemical Rubber Company, 2011).

82. Bard, A. J. & Faulkner, L. R. *Electrochemical Methods. Fundamentals and Applications.* (John Wiley and Sons Inc, 2001).

83. Lide, D. R. *CRC Handbook of Chemistry and Physics*. (CRC Press, 2006).

84. Gao, X.-P. & Yang, H.-X. Multi-electron reaction materials for high energy density batteries. *Energy Environ. Sci.* **3,** 165–240 (2010).

85. Goodenough, J. B. & Kim, Y. Challenges for Rechargeable Li Batteries. *Chem. Mater.* **22,** 587–603 (2010).

86. Shannon, R. D. Revised effective ionic radii and systematic studies of interatomic distances in halides and chalcogenides. *Acta Crystallogr. Sect. A* **32,** 751–767 (1976).

87. Verma, P., Maire, P. & Novák, P. A review of the features and analyses of the solid electrolyte interphase in Li-ion batteries. *Electrochim. Acta* **55,** 6332–6341 (2010).

88. Peled, E. The Electrochemical Behavior of Alkali and Alkaline Earth Metals in Nonaqueous Battery Systems—The Solid Electrolyte Interphase Model. *J. Electrochem. Soc.* **126,** 2047 – 2051 (1979).

89. Mizushima, K., Jones, P. C., Wiseman, P. J. & Goodenough, J. B. Li_xCoO_2 ($0<x<1$): A New Cathode Material For Batteries of High Energy Density. *Mater. Res. Bull.* **15,** 783–789 (1980).

90. Momma, K. & Izumi, F. VESTA 3 for three-dimensional visualization of crystal, volumetric and morphology data. *J. Appl. Crystallogr.* **44,** 1272–1276 (2011).

91. Padhi, A. K., Nanjundaswamy, K. S. & Goodenough, J. B. Phospho-olivines as Positive Electrode Materials for Rechargeable Lithium Batteries. *J. Electrochem. Soc.* **144,** 1188–1194 (1997).

92. Thackeray, M., David, W., Bruce, P. G. & Goodenough, J. B. Lithium insertion into manganese spinels. *Mater. Res. Bull.* **18,** 461–472 (1983).

93. Peramunage, D. & Abraham, K. M. Preparation of Micron-Sized $Li_4Ti_5O_{12}$ and Its Electrochemistry in Polyacrylonitrile Electrolyte-Based Lithium Cells. *J. Electrochem. Soc.* **145,** 2609–2615 (1998).

94. Hu, Y. S., Kienle, L., Guo, Y. G. & Maier, J. High lithium electroactivity of nanometer-sized rutile TiO_2. *Adv. Mater.* **18,** 1421–1426 (2006).

95. Huang, S. Y., Kavan, L., Exnar, I. & Gratzel, M. Rocking Chair Lithium Battery Based on Nanocrystalline TiO_2 (Anatase). *J. Electrochem. Soc.* **142,** L142–L144 (1995).

96. Zhang, Y. *et al.* High-energy cathode materials for Li-ion batteries: A review of recent developments. *Sci. China Technol. Sci.* **58,** 1809–1828 (2015).

97. McNulty, D., Buckley, D. N. & O'Dwyer, C. Synthesis and electrochemical properties of vanadium oxide materials and structures as Li-ion battery positive electrodes. *J. Power Sources* **267,** 831–873 (2014).

98. Reddy, M. V., Subba Rao, G. V. & Chowdari, B. V. R. Metal oxides and oxysalts as anode materials for Li ion batteries. *Chem. Rev.* **113,** 5364–5457 (2013).

99. Poizot, P., Laruelle, S., Grugeon, S., Dupont, L. & Tarascon, J.-M. Nano-sized transition-metal oxides as negative-electrode materials for lithium-ion batteries. *Nature* **407,** 496–499 (2000).

100. Obrovac, M. N. & Krause, L. J. Reversible Cycling of Crystalline Silicon Powder. *J. Electrochem. Soc.* **154,** A103–A108 (2007).

101. Tarascon, J.-M. *et al.* New concepts for the search of better electrode materials for rechargeable lithium batteries. *Comptes Rendus Chim.* **8,** 9–15 (2005).

102. Paz-Garcia, J. M. *et al.* 4D analysis of the microstructural evolution of Si-based electrodes during lithiation: Time-lapse X-ray imaging and digital volume correlation. *J. Power Sources* **320,** 196–203 (2016).

103. Zhao, H., Zhu, Z., Yin, C., Guo, H. & Ng, D. H. L. Electrochemical characterization of micro-sized Sb/SnSb composite anode. *Mater. Chem. Phys.* **110,** 201–205 (2008).

104. Ma, X.-H. *et al.* Facile synthesis of flower-like and yarn-like α-Fe_2O_3 spherical

clusters as anode materials for lithium-ion batteries. *Electrochim. Acta* **93,** 131–136 (2013).

105. Zhou, G. *et al.* Graphene-wrapped Fe_3O_4 anode material with improved reversible capacity and cyclic stability for lithium ion batteries. *Chem. Mater.* **22,** 5306–5313 (2010).

106. Wang, H. et al. Mn_3O_4 – Graphene Hybrid as a High-Capacity Anode Material for Lithium Ion. *J. Am. Chem. Soc.* **132**, 13978–13980 (2010).

107. Wu, H. & Cui, Y. Designing nanostructured Si anodes for high energy lithium ion batteries. *Nano Today* **7,** 414–429 (2012).

108. Derrien, G., Hassoun, J., Panero, S. & Scrosati, B. Nanostructured Sn-C composite as an advanced anode material in high-performance lithium-ion batteries. *Adv. Mater.* **19,** 2336–2340 (2007).

109. Badway, F., Cosandey, F., Pereira, N. & Amatucci, G. G. Carbon Metal Fluoride Nanocomposites. *J. Electrochem. Soc.* **150,** A1209-A1318 (2003).

110. Rauh, R. D., Abraham, K. M., Pearson, G. F., Surprenant, J. K. & Brummer, S. B. A Lithium/Dissolved Sulfur Battery with an Organic Electrolyte. *J. Electrochem. Soc.* **126,** 523–527 (1979).

111. Ogasawara, T., Débart, A., Holzapfel, M., Novák, P. & Bruce, P. G. Rechargeable Li_2O_2 electrode for lithium batteries. *J. Am. Chem. Soc.* **128,** 1390–1393 (2006).

112. Zeng, Z. et al. Visualization of electrode-electrolyte interfaces in LiPF 6/EC/DEC electrolyte for lithium ion batteries via in situ TEM. Nano Lett. 14, 1745–1750 (2014).

113. Aurbach, D., Markovsky, B., Shechter, A., Ein-Eli, Y. & Cohen, H. A Comparative Study of Synthetic Graphite and Li Electrodes in Electrolyte Solutions Based on Ethylene Carbonate-Dimethyl Carbonate Mixtures. J. Electrochem. Soc. 143, 3809–3820 (1996).

114. Fong, R., von Sacken, U. & Dahn, J. R. Studies of Lithium Intercalation into Carbons Using Nonaqueous Electrochemical Cells. J. Electrochem. Soc. 137, 2009–2013 (1990).

115. El Ouatani, L., Dedryvère, R., Siret, C., Biensan, P. & Gonbeau, D. Effect of Vinylene Carbonate Additive in Li-Ion Batteries: Comparison of LiCoO2/C, LiFePO4/C, and LiCoO2/Li4Ti5O12 Systems. J. Electrochem. Soc. 156, A468–A477 (2009).

116. Ota, H., Sakata, Y., Inoue, A. & Yamaguchi, S. Analysis of Vinylene Carbonate Derived SEI Layers on Graphite Anode. J. Electrochem. Soc. 151, A1659–A1669 (2004).

117. Shin, J.-S. et al. Effect of Li2CO3 additive on gas generation in lithium-ion batteries. J. Power Sources 109, 47–52 (2002).

118. Ein-Eli, Y. *et al.* The dependence of the performance of Li-C intercalation anodes for Li-ion secondary batteries on the electrolyte solution composition. *Electrochim. Acta* **39,** 2559–2569 (1994).

119. Peled, E., Golodnitsky, D. & Ardel, G. Advanced Model for Solid Electrolyte Interphase Electrodes in Liquid and Polymer Electrolytes. *J. Electrochem. Soc.* **144,** L208–L210 (1997).

120. Andersson, A. M., Henningson, A., Siegbahn, H., Jansson, U. & Edström, K. Electrochemically lithiated graphite characterised by photoelectron spectroscopy. *J. Power Sources* **119–121,** 522–527 (2003).

121. Edström, K., Herstedt, M. & Abraham, D. P. A new look at the solid electrolyte interphase on graphite anodes in Li-ion batteries. *J. Power Sources* **153,** 380–384 (2006).

122. Zaban, A. & Aurbach, D. Impedance spectroscopy of lithium and nickel electrodes in propylene carbonate solutions of different lithium salts A comparative study. *J. Power Sources* **54,** 289–295 (1995).

123. Aurbach, D. Review of selected electrode-solution interactions which determine the performance of Li and Li ion batteries. *J. Power Sources* **89,** 206–218 (2000).

124. Edström, K., Gustafsson, T. & Thomas, J. O. The cathode-electrolyte interface in the Li-ion battery. *Electrochim. Acta* **50,** 397–403 (2004).

125. Wagemaker, M. & Mulder, F. M. Properties and promises of nanosized

insertion materials for li-ion batteries. *Acc. Chem. Res.* **46,** 1206–1215 (2013).

126. Guo, Y.-G., Hu, J.-S. & Wan, L.-J. Nanostructured Materials for Electrochemical Energy Conversion and Storage Devices. *Adv. Mater.* **20,** 2878–2887 (2008).

127. Chaudhry, A. *et al.* Instant nano-hydroxyapatite: a continuous and rapid hydrothermal synthesis. *Chem. Commun.* **21,** 2286–2288 (2006).

128. Weng, X. *et al.* High-throughput continuous hydrothermal synthesis of an entire nanoceramic phase diagram. *J. Comb. Chem.* **11,** 829–834 (2009).

129. Gruar, R. I. Synthesis and Characterisation of Nanomaterials Produced Using Laboratory and Pilot Scale Continuous Hydrothermal Flow Reactors. (2012).

130. Makwana, N. M. Photoactive and UV Attenuating Nanomaterial and Heterojunction Devices. (2016).

131. Wagner, W. & Pruß, A. The IAPWS formulation 1995 for the thermodynamic properties of ordinary water substance for general and scientific use. *J. Phys. Chem. Ref. Data* **31,** 387–535 (2002).

132. Lutterotti, L., Matthies, S. & Wenk, H.-R. MAUD (Material Analysis Using Diffraction): a user friendly Java program for Rietveld Texture Analysis and more. in Twelfth International Conference on Textures of Materials (ICOTOM-12) 1599 (1999).

133. UCL chem 3007 practical lab to make a printed cathode for a Li ion battery. Available at: https://www.youtube.com/watch?v=kVatkIDngzI&t=1s. (Accessed: 29th August 2017)

134. part 2 coin cell assembly and glovebox. Available at: https://www.youtube.com/watch?v=sPT59a9qsCc&t=12s. (Accessed: 29th August 2017)

135. Tanaka, N. & Tamamushi, R. Kinetic parameters of electrode reactions. *Electrochim. Acta* **9,** 963–989 (1964).

136. Andersson, A., Kalska, B., Häggström, L. & Thomas, J. Lithium extraction/insertion in $LiFePO_4$: an X-ray diffraction and Mössbauer spectroscopy study. *Solid State Ionics* **130,** 41–52 (2000).

137. Yu, Y. S. *et al.* Dependence on Crystal Size of the Nanoscale Chemical Phase Distribution and Fracture in Li_xFePO_4. *Nano Lett.* **15,** 4282–4288 (2015).

138. Pietsch, P. et al. Quantifying microstructural dynamics and electrochemical activity of graphite and silicon-graphite lithium ion battery anodes. Nat. Commun. 7, 12909 (2016).

139. Jiang, J. & Dahn, J. R. ARC studies of the thermal stability of three different cathode materials: LiCoO2; Li[Ni0.1Co0.8Mn0.1]O2; and LiFePO4, in LiPF6 and LiBoB EC/DEC electrolytes. Electrochem. commun. 6, 39–43 (2004).

140. Andersson, A., Thomas, J., Kalska, B. & Häggström, L. Thermal Stability of LiFePO4 Based Cathodes. Electrochem. Solid-State Lett. 3, 66–68 (2000).

141. Dreyer, W. et al. The thermodynamic origin of hysteresis in insertion batteries. Nat. Mater. 9, 448–453 (2010).

142. Laffont, L. et al. Study of the LiFePO4/FePO4 two-phase system by high-resolution electron energy loss spectroscopy. Chem. Mater. 18, 5520–5529 (2006).

143. Chen, G., Song, X. & Richardson, T. J. Electron Microscopy Study of the LiFePO4 to FePO4 Phase Transition. Electrochem. Solid-State Lett. 9, A295–A298 (2006).

144. Yuan, L.-X. et al. Development and challenges of LiFePO4 cathode material for lithium-ion batteries. Energy Environ. Sci. 4, 269–284 (2011).

145. Delmas, C., Maccario, M., Croguennec, L., Le Cras, F. & Weill, F. Lithium deintercalation in $LiFePO_4$ nanoparticles via a domino-cascade model. *Nat. Mater.* **7,** 665–671 (2008).

146. Gouveia, D. *et al.* Spectroscopic studies of Li_xFePO_4 and $Li_xM_{0.03}Fe_{0.97}PO_4$ (M=Cr,Cu,Al,Ti). *Phys. Rev. B* **72,** 024105-1–024105-6 (2005).

147. Ramana, C. V., Mauger, A., Gendron, F., Julien, C. M. & Zaghib, K. Study of the Li-insertion/extraction process in $LiFePO_4/FePO_4$. *J. Power Sources* **187,** 555–564 (2009).

148. Sharma, N. *et al.* Direct evidence of concurrent solid-solution and two-phase reactions and the nonequilibrium structural evolution of $LiFePO_4$. *J. Am. Chem.*

Soc. **134,** 7867–7873 (2012).

149. Dodd, J. L., Yazami, R. & Fultz, B. Phase Diagram of Li_xFePO_4. *Electrochem. Solid-State Lett.* **9,** A151–A155 (2006).

150. Delacourt, C., Poizot, P., Tarascon, J.-M. & Masquelier, C. The existence of a temperature-driven solid solution in Li_xFePO_4 for $0 \leq x \leq 1$. *Nat. Mater.* **4,** 254–260 (2005).

151. Gibot, P. *et al.* Room-temperature single-phase Li insertion/extraction in nanoscale Li_xFePO_4. *Nat. Mater.* **7,** 741–747 (2008).

152. Liu, H. *et al.* Capturing metastable structures during high-rate cycling of $LiFePO_4$ nanoparticle electrodes. *Science* **344,** 1480–1487 (2014).

153. Morgan, D., Van der Ven, A. & Ceder, G. Li Conductivity in Li_xMPO_4 (M = Mn, Fe, Co, Ni) Olivine Materials. *Electrochem. Solid-State Lett.* **7,** A30–A32 (2004).

154. Islam, M., Driscoll, D., Fisher, C. & Slater, P. Atomic-scale investigation of defects, dopants, and lithium transport in the $LiFePO_4$ olivine-type battery material. *Chem. Mater.* **17,** 5085–5092 (2005).

155. Ouyang, C., Shi, S., Wang, Z., Huang, X. & Chen, L. First-principles study of Li ion diffusion in $LiFePO_4$. *Phys. Rev. B* **69,** 104303-1–104303-5 (2004).

156. Yu, D. Y. W. *et al.* Study of $LiFePO_4$ by Cyclic Voltammetry. *J. Electrochem. Soc.* **154,** A253–A257 (2007).

157. Nishimura, S. *et al.* Experimental visualization of lithium diffusion in Li_xFePO_4. *Nat. Mater.* **7,** 707–711 (2008).

158. Takahashi, M., Tobishima, S., Takei, K. & Sakurai, Y. Characterization of $LiFePO_4$ as the cathode material for rechargeable lithium batteries. *J. Power Sources* **97–98,** 508–511 (2001).

159. Zhi, X. *et al.* The cycling performance of $LiFePO_4$/C cathode materials. *J. Power Sources* **189,** 779–782 (2009).

160. Utsunomiya, T., Hatozaki, O., Yoshimoto, N., Egashira, M. & Morita, M. Influence of particle size on the self-discharge behavior of graphite electrodes in lithium-ion batteries. *J. Power Sources* **196,** 8675–8682 (2011).

161. Croce, F. *et al.* A Novel Concept for the Synthesis of an Improved $LiFePO_4$ Lithium Battery Cathode. *Electrochem. Solid-State Lett.* **5,** A47–A50 (2002).

162. Ravet, N. *et al.* Electroactivity of natural and synthetic triphylite. *J. Power Sources* **97–98,** 503–507 (2001).

163. Julien, C. M. *et al*. Nanoscopic scale studies of $LiFePO_4$ as cathode material in lithium-ion batteries for HEV application. *Ionics* **13,** 395–411 (2007).

164. Rho, Y.-H., Nazar, L. F., Perry, L. & Ryan, D. Surface Chemistry of $LiFePO_4$ Studied by Mössbauer and X-Ray Photoelectron Spectroscopy and Its Effect on Electrochemical Properties. *J. Electrochem. Soc.* **154,** A283–A289 (2007).

165. Dedryvere, R. *et al.* X-Ray Photoelectron Spectroscopy Investigations of Carbon-Coated Li_xFePO_4 Materials. *Chem. Mater.* **20,** 7164–7170 (2008).

166. Wang, Y., Wang, Y., Hosono, E., Wang, K. & Zhou, H. The design of a $LiFePO_4$/carbon nanocomposite with a core-shell structure and its synthesis by an in situ polymerization restriction method. *Angew. Chem. Int. Ed. Engl.* **47,** 7461–7465 (2008).

167. Jiang, Z. & Jiang, Z. Effects of carbon content on the electrochemical performance of $LiFePO_4$/C core/shell nanocomposites fabricated using $FePO_4$/polyaniline as an iron source. *J. Alloys Compd.* **537,** 308–317 (2012).

168. Doeff, M., Hu, Y., McLarnon, F. & Kostecki, R. Effect of surface carbon structure on the electrochemical performance of $LiFePO_4$. *Electrochem. Solid-State Lett.* **6,** A207–A209 (2003).

169. Gaberscek, M., Dominko, R. & Jamnik, J. Is small particle size more important than carbon coating? An example study on LiFePO4 cathodes. Electrochem. commun. 9, 2778–2783 (2007).

170. Zhang, W.-J. Comparison of the Rate Capacities of LiFePO4 Cathode Materials. J. Electrochem. Soc. 157, A1040–A1046 (2010).

171. Yamada, A. et al. Olivine-type cathodes: Achievements and problems. J. Power Sources 119–121, 232–238 (2003).

172. Chung, S.-Y., Bloking, J. T. & Chiang, Y.-M. Electronically conductive phospho-olivines as lithium storage electrodes. Nat. Mater. 1, 123–128 (2002).

173. Meethong, N., Kao, Y.-H., Speakman, S. & Chiang, Y.-M. Aliovalent Substitutions in Olivine Lithium Iron Phosphate and Impact on Structure and Properties. Adv. Funct. Mater. 19, 1060–1070 (2009).

174. Ravet, N. et al. Correspondence. Nature 2, 702–703 (2003).

175. Wagemaker, M., Ellis, B., Lutzenkirchen-Hecht, D., Mulder, F. & Nazar, L. Proof of supervalent doping in olivine LiFePO4. Chem. Mater. 20, 6313–6315 (2008).

176. Yang, M.-R. & Ke, W.-H. The Doping Effect on the Electrochemical Properties of LiFe0.95M0.05PO4 (M=Mg2+, Ni2+, Al3+, or V3+) as Cathode Materials for Lithium-Ion Cells. J. Electrochem. Soc. 155, A729–A732 (2008).

177. Omenya, F. *et al.* Can Vanadium Be Substituted into $LiFePO_4$? *Chem. Mater.* **23,** 4733–4740 (2011).

178. Ma, J., Li, B., Du, H., Xu, C. & Kang, F. The Effect of Vanadium on Physicochemical and Electrochemical Performances of $LiFePO_4$ Cathode for Lithium Battery. *J. Electrochem. Soc.* **158,** A26–A32 (2011).

179. Pan, M., Lin, X. & Zhou, Z. Electrochemical performance of $LiFePO_4$/C doped with F synthesized by carbothermal reduction method using NH_4F as dopant. *J. Solid State Electrochem.* **16,** 1615–1621 (2012).

180. Chen, M.-S., Wu, S. & Pang, W. K. Effects of vanadium substitution on the cycling performance of olivine cathode materials. *J. Power Sources* **241,** 690–695 (2013).

181. Lin, H. *et al.* A GGA+U study of lithium diffusion in vanadium doped $LiFePO_4$. *Solid State Commun.* **152,** 999–1003 (2012).

182. Wen, Y., Zeng, L., Tong, Z., Nong, L. & Wei, W. Structure and properties of $LiFe_{0.9}V_{0.1}PO_4$. *J. Alloys Compd.* **416,** 206–208 (2006).

183. Hong, J., Wang, C. S., Chen, X., Upreti, S. & Whittingham, M. S. Vanadium Modified $LiFePO_4$ Cathode for Li-Ion Batteries. *Electrochem. Solid-State Lett.* **12,** A33–A38 (2009).

184. Sun, C. *et al.* Improved high-rate charge/discharge performances of $LiFePO_4$/C via V-doping. *J. Power Sources* **193,** 841–845 (2009).

185. Zhang, L. *et al.* Effect of Vanadium Incorporation on Electrochemical Performance of $LiFePO_4$ for Lithium-Ion Batteries. *J. Phys. Chem. C* **115,** 13520–13527 (2011).

186. Jin, Y., Yang, C. P., Rui, X. H., Cheng, T. & Chen, C. H. V_2O_3 modified $LiFePO_4$/C composite with improved electrochemical performance. *J. Power Sources* **196,** 5623–5630 (2011).

187. Ma, J., Li, B. & Kang, F. Improved electrochemical performances of nanocrystalline $LiFePO_4$/C composite cathode via V-doping and VO_2(B) coating. *J. Phys. Chem. Solids* **73,** 1463–1468 (2012).

188. Omenya, F., Chernova, N. A., Wang, Q., Zhang, R. & Whittingham, M. S. The structural and electrochemical impact of Li and Fe site substitution in $LiFePO_4$. *Chem. Mater.* **25,** 2691–2699 (2013).

189. Harrison, K. *et al.* Temperature dependence of aliovalent-vanadium doping in $LiFePO_4$ cathodes. *Chem. Mater.* **25,** 768–781 (2013).

190. Zhuang, D. -G. *et al.* One-step Solid-state Synthesis and Electrochemical Performance of Nb-doped $LiFePO_4$/C. *Acta Phys. Sin.* **22,** 840–844 (2006).

191. Liu, H., Li, C., Cao, Q., Wu, Y. P. & Holze, R. Effects of heteroatoms on doped $LiFePO_4$/C composites. *J. Solid State Electrochem.* **12,** 1017–1020 (2007).

192. Hoang, K. & Johannes, M. D. First-principles studies of the effects of impurities on the ionic and electronic conduction in $LiFePO_4$. *J. Power Sources* **206,** 274–281 (2012).

193. Xu, C., Lee, J. & Teja, A. S. Continuous hydrothermal synthesis of lithium iron phosphate particles in subcritical and supercritical water. *J. Supercrit. Fluids* **44,** 92–97 (2008).

194. Hong, S.-A. *et al.* Continuous synthesis of lithium iron phosphate nanoparticles in supercritical water: Effect of process parameters. *Chem. Eng. J.* **229,** 313–323 (2013).

195. Aimable, A., Aymes, D., Bernard, F. & Le Cras, F. Characteristics of $LiFePO_4$ obtained through a one step continuous hydrothermal synthesis process working in supercritical water. *Solid State Ionics* **180,** 861–866 (2009).

196. Hong, S.-A. *et al.* Carbon coating on lithium iron phosphate ($LiFePO_4$): Comparison between continuous supercritical hydrothermal method and solid-state method. *Chem. Eng. J.* **198–199,** 318–326 (2012).

197. Song, K. H. *et al.* US20120021288 A1. (2012).

198. Wu, O. Continuous Hydrothermal Flow Synthesis of Lithium ion Battery Materials. (University College London, 2014).

199. Johnson, I. D. *et al.* Pilot-scale continuous synthesis of a vanadium-doped $LiFePO_4$/C nanocomposite high-rate cathodes for lithium-ion batteries. *J. Power Sources* **302,** 410–418 (2016).

200. Franger, S., Le Cras, F., Bourbon, C. & Rouault, H. Comparison between different $LiFePO_4$ synthesis routes and their influence on its physico-chemical properties. *J. Power Sources* **119–121,** 252–257 (2003).

201. Kellici, S. *et al.* High-throughput continuous hydrothermal flow synthesis of Zn-Ce oxides: unprecedented solubility of Zn in the nanoparticle fluorite lattice. *Philos. Trans. A.* **368,** 4331–49 (2010).

202. Ravel, B. & Newville, M. ATHENA, ARTEMIS, HEPHAESTUS: Data analysis for X-ray absorption spectroscopy using IFEFFIT. *J. Synchrotron Radiat.* **12,** 537–541 (2005).

203. Binstead, N. EXCURV98: CCLRC Daresbury Laboratory Computer Program. (1998).

204. Gómez-Hortigüela, L., Corà, F. & Catlow, C. R. A. Complementary mechanistic properties of Fe- and Mn-doped aluminophosphates in the catalytic aerobic oxidation of hydrocarbons. *Phys. Chem. Chem. Phys.* **15,** 6870–6874 (2013).

205. Maurelli, S., Berlier, G., Chiesa, M., Musso, F. & Cora, F. Structure of the Catalytic Active Sites in Vanadium Doped Alumino Phosphate Microporous Materials. New Evidence from Spin Density Studies. *J. Phys. Chem. C* **118,** 19879-19888 (2014).

206. Lii, K. H., Wang, Y. P., Chen, Y. B. & Wang, S. L. The 207. Uebou, Y., Okada, S., Egashira, M. & Yamaki, J. I. Cathode properties of

pyrophosphates for rechargeable lithium batteries. *Solid State Ionics* **148,** 323–328 (2002).

207. Uebou, Y., Okada, S., Egashira, M. & Yamaki, J. I. Cathode properties of pyrophosphates for rechargeable lithium batteries. *Solid State Ionics* **148,** 323–328 (2002).

208. Johnson, I. D. *et al.* High power Nb-doped $LiFePO_4$ Li-ion battery cathodes; pilot-scale synthesis and electrochemical properties. *J. Power Sources* **326,** 476–481 (2016).

209. Ma, Z., Shao, G., Wang, G., Zhang, Y. & Du, J. Effects of Nb-doped on the structure and electrochemical performance of $LiFePO_4$/C composites. *J. Solid State Chem.* **210,** 232–237 (2014).

210. Takehara, Z. Future prospects of the lithium metal anode. *J. Power Sources* **68,** 82–86 (1997).

211. Chevrier, V. L. *et al.* Evaluating Si-Based Materials for Li-Ion Batteries in Commercially Relevant Negative Electrodes. *J. Electrochem. Soc.* **161,** 783–791 (2014).

212. Liu, X. H. *et al.* Ultrafast electrochemical lithiation of individual Si nanowire anodes. *Nano Lett.* **11,** 2251–2258 (2011).

213. Su, X. *et al.* Silicon-Based Nanomaterials for Lithium-Ion Batteries: A Review. *Adv. Energy Mater.* **4,** 1300882 (2014).

214. Cui, L.-F., Ruffo, R., Chan, C. K., Peng, H. & Cui, Y. Crystalline-amorphous core-shell silicon nanowires for high capacity and high current battery electrodes. *Nano Lett.* **9,** 491–495 (2009).

215. Erk, C., Brezesinski, T., Sommer, H., Schneider, R. & Janek, J. Toward silicon anodes for next-generation lithium ion batteries: A comparative performance study of various polymer binders and silicon nanopowders. *ACS Appl. Mater. Interfaces* **5,** 7299–7307 (2013).

216. Broussely, M. *et al.* Main aging mechanisms in Li ion batteries. *J. Power Sources* **146,** 90–96 (2005).

217. Xu, K. Nonaqueous Liquid Electrolytes for Lithium-Based Rechargeable

Batteries. *Chem. Rev.* **104,** 4303-4417 (2004).

218. Yamane, H., Inoue, T., Fujita, M. & Sano, M. A causal study of the capacity fading of $Li_{1.01}Mn_{1.99}O_4$ cathode at 80°C , and the suppressing substances of its fading. *J. Power Sources* **99,** 60–65 (2001).

219. Zhang, S. S. A review on electrolyte additives for lithium-ion batteries. *J. Power Sources* **162,** 1379–1394 (2006).

220. Loveridge, M. J. *et al.* Towards High Capacity Li-ion Batteries Based on Silicon-Graphene Composite Anodes and Sub-micron V-doped $LiFePO_4$ Cathodes. *Sci. Rep.* **6,** 37787 (2016).

221. Lübke, M. *et al.* VO_2 nano-sheet negative electrodes for lithium-ion batteries. *Electrochem. commun.* **64,** 56–60 (2016).

222. Lübke, M. *et al.* High power TiO_2 and high capacity Sn-doped TiO_2 nanomaterial anodes for lithium-ion batteries. *J. Power Sources* **294,** 94–102 (2015).

223. Mohr, P. J., Taylor, B. N. & Newell, D. B. CODATA recommended values of the fundamental physical constants: 2010. *Rev. Mod. Phys.* **84,** 1527–1605 (2012).

224. Tishchenko, V. *et al.* Detailed report of the MuLan measurement of the positive muon lifetime and determination of the Fermi constant. *Phys. Rev. D* **87,** 052003 (2013).

225. Adam, J. *et al.* New Constraint on the Existence of the $\mu^+ \rightarrow e^+ \gamma$ Decay. *Phys. Rev. Lett.* **110,** 201801 (2013).

226. Sugiyama, J. *et al.* Li diffusion in Li_xCoO_2 probed by Muon-Spin spectroscopy. *Phys. Rev. Lett.* **103,** 147601 (2009).

227. Amores, M., Ashton, T. E., Baker, P. J., Cussen, E. J. & Corr, S. A. Fast microwave-assisted synthesis of Li-stuffed garnets and insights into Li diffusion from muon spin spectroscopy. *J. Mater. Chem. A* **4,** 1729–1736 (2016).

228. Hayano, R. S. *et al.* Zero-and low-field spin relaxation studied by positive muons. *Phys. Rev. B* **20,** 850–859 (1979).

229. Sugiyama, J. *et al.* Magnetic and diffusive nature of $LiFePO_4$ investigated by

muon spin rotation and relaxation. *Phys. Rev. B* **84,** 054430 (2011).

230. Sugiyama, J. *et al.* Diffusive behavior in $LiMPO_4$ with M=Fe, Co, Ni probed by muon-spin relaxation. *Phys. Rev. B* **85,** 054111 (2012).

231. Baker, P. J. *et al.* Probing magnetic order in $LiMPO_4$ (M= Ni, Co, Fe) and lithium diffusion in Li_xFePO_4. *Phys. Rev. B* **84,** 174403 (2011).

232. Ashton, T. E. *et al.* Muon studies of Li^+ diffusion in $LiFePO_4$ nanoparticles of different polymorphs. *J. Mater. Chem. A* **2,** 6238–6245 (2014).

233. Prosini, P., Lisi, M., Zane, D. & Pasquali, M. Determination of the chemical diffusion coefficient of lithium in $LiFePO_4$. *Solid State Ionics* **148,** 45–51 (2002).

234. Churikov, A. V *et al.* Determination of lithium diffusion coefficient in $LiFePO_4$ electrode by galvanostatic and potentiostatic intermittent titration techniques. *Electrochim. Acta* **55,** 2939–2950 (2010).

235. Hong, S.-A. *et al.* Small capacity decay of lithium iron phosphate ($LiFePO_4$) synthesized continuously in supercritical water: Comparison with solid-state method. *J. Supercrit. Fluids* **55,** 1027–1037 (2011).

236. Ellis, B., Perry, L. K., Ryan, D. H. & Nazar, L. F. Small Polaron Hopping in Li_xFePO_4 Solid Solutions : Coupled Lithium-Ion and Electron Mobility. *J. Am. Chem. Soc.* **126,** 11416–11422 (2006).

237. Giblin, S. R. *et al.* Optimising a muon spectrometer for measurements at the ISIS pulsed muon source. *Nucl. Instrum. Methods Phys. Res. A* **751,** 70–78 (2014).

238. Pratt, F. L. WIMDA: A muon data analysis program for the Windows PC. *Phys. B Condens. Matter* **289–290,** 710–714 (2000).

239. Okada, S. *et al.* Cathode properties of phospho-olivine $LiMPO_4$ for lithium secondary batteries. *J. Power Sources* **97–98,** 430–432 (2001).

240. Yamada, A. & Chung, S.-C. Crystal Chemistry of the Olivine-Type $Li(Mn_yFe_{1-y}])PO_4$ and $(Mn_yFe_{1-y}])PO_4$ as Possible 4 V Cathode Materials for Lithium Batteries. *J. Electrochem. Soc.* **148,** A960–A967 (2001).

241. Aravindan, V., Gnanaraj, J., Lee, Y.-S. & Madhavi, S. $LiMnPO_4$ – A next

generation cathode material for lithium-ion batteries. *J. Mater. Chem. A* **1,** 3518–3539 (2013).

242. Asari, Y., Suwa, Y. & Hamada, T. Formation and diffusion of vacancy-polaron complex in olivine-type $LiMnPO_4$ and $LiFePO_4$. *Phys. Rev. B* **84,** 1–7 (2011).

243. Kim, S.-W., Kim, J., Gwon, H. & Kang, K. Phase Stability Study of $Li_{1-x}MnPO_4$ ($0 \leq x \leq 1$) Cathode for Li Rechargeable Battery. *J. Electrochem. Soc.* **156,** A635–A638 (2009).

244. Ji, H. *et al.* General synthesis and morphology control of $LiMnPO_4$ nanocrystals via microwave-hydrothermal route. *Electrochim. Acta* **56,** 3093–3100 (2011).

245. Rangappa, D., Sone, K., Zhou, Y., Kudo, T. & Honma, I. Size and shape controlled $LiMnPO_4$ nanocrystals by a supercritical ethanol process and their electrochemical properties. *J. Mater. Chem.* **21,** 15813 (2011).

246. Wang, D. *et al.* Improving the Electrochemical Activity of $LiMnPO_4$ Via Mn-Site Substitution. *J. Electrochem. Soc.* **157,** A225–A229 (2010).

247. Hu, X. *et al.* Sandwich nanostructured LiMnPO4/C as enhanced cathode materials for lithium-ion batteries. *J. Mater. Sci.* **4,** 3597–3612 (2016).

248. Wen, F. *et al.* Mesoporous $LiMnPO_4$/C nanoparticles as high performance cathode material for lithium ion batteries. *Electrochim. Acta* **214,** 85–93 (2016).

249. Kwon, N. H. & Fromm, K. M. Enhanced electrochemical performance of < 30 nm thin $LiMnPO_4$ nanorods with a reduced amount of carbon as a cathode for lithium ion batteries. *Electrochim. Acta* **69,** 38–44 (2012).

250. Shiratsuchi, T., Okada, S., Doi, T. & Yamaki, J. I. Cathodic performance of $LiMn_{1-x}M_xPO_4$ (M = Ti, Mg and Zr) annealed in an inert atmosphere. *Electrochim. Acta* **54,** 3145–3151 (2009).

251. Lee, J. W. *et al.* Electrochemical lithiation and delithiation of $LiMnPO_4$: Effect of cation substitution. *Electrochim. Acta* **55,** 4162–4169 (2010).

252. Vadivel Murugan, A., Muraliganth, T. & Manthiram, A. One-Pot Microwave-Hydrothermal Synthesis and Characterization of Carbon-Coated $LiMPO_4$ (M=Mn, Fe, and Co) Cathodes. *J. Electrochem. Soc.* **156,** A79–A83 (2009).

253. Chen, G., Wilcox, J. D. & Richardson, T. J. Improving the Performance of

Lithium Manganese Phosphate Through Divalent Cation Substitution. *Electrochem. Solid-State Lett.* **11,** A190–A194 (2008).

254. Chen, G., Shukla, A. K., Song, X. & Richardson, T. J. Improved kinetics and stabilities in Mg-substituted $LiMnPO_4$. *J. Mater. Chem.* **21,** 10126 (2011).

255. Hong, J., Wang, F., Wang, X. & Graetz, J. $LiFe_xMn_{1-x}PO_4$: A cathode for lithium-ion batteries. *J. Power Sources* **196,** 3659–3663 (2011).

256. Zhang, B., Wang, X., Liu, Z., Li, H. & Huang, X. Enhanced Electrochemical Performances of Carbon Coated Mesoporous $LiFe_{0.2}Mn_{0.8}PO_4$. *J. Electrochem. Soc.* **157,** A285–A288 (2010).

257. Muraliganth, T. & Manthiram, A. Understanding the Shifts in the Redox Potentials of Olivine $LiM_{1-y}M_yPO_4$ (M= Fe, Mn, Co, and Mg) Solid Solution Cathodes. *J. Phys. Chem. C* **114,** 15530–15540 (2010).

258. Martha, S. K. *et al.* $LiMn_{0.8}Fe_{0.2}PO_4$: An Advanced Cathode Material for Rechargeable Lithium Batteries. *Angew. Chemie Int. Ed.* **48,** 8559–8563 (2009).

259. Wang, H. *et al.* $LiMn_{1-x}Fe_xPO_4$ Nanorods Grown on Graphene Sheets for Ultrahigh-Rate-Performance Lithium Ion Batteries. *Angew. Chemie Int. Ed.* **50,** 7364–7368 (2011).

260. Oh, S.-M. *et al.* Double-Structured $LiMn_{0.85}Fe_{0.15}PO_4$ Coordinated with $LiFePO_4$ for Rechargeable Lithium Batteries. *Angew. Chemie Int. Ed.* **51,** 1853–1856 (2012).

261. Gan, Y. *et al.* Enhancing the performance of $LiMnPO_4$/C composites through Cr doping. *J. Alloys Compd.* **620,** 350–357 (2015).

262. Dai, E., Fang, H., Yang, B., Ma, W. & Dai, Y. Synthesis of vanadium doped $LiMnPO_4$ by an improved solid-state method. *Ceram. Int.* **41,** 8171–8176 (2015).

263. Yang, G. *et al.* The doping effect on the crystal structure and electrochemical properties of $LiMn_xM_{1-x}PO_4$ (M = Mg, V, Fe, Co, Gd). *J. Power Sources* **196,** 4747–4755 (2011).

264. Su, L. *et al.* Effect of vanadium doping on electrochemical performance of $LiMnPO_4$ for lithium-ion batteries. *J. Solid State Electrochem.* **18,** 755–762

(2014).

265. Gutierrez, A. *et al.* High-Capacity, Aliovalently Doped Olivine $LiMn_{1-3x/2}V_x\square_{x/2}PO_4$ Cathodes without Carbon Coating. *Chem. Mater.* **26,** (2014).

266. Clemens, O., Bauer, M., Haberkorn, R., Springborg, M. & Beck, H. P. Synthesis and Characterization of Vanadium-Doped LiMnPO4-Compounds: $LiMn(PO_4)_x(VO_4)_{1-x}$ ($0.8 \leq x \leq 1.0$). *Chem. Mater.* **24,** 4717−4724 (2012).

267. Wang, F., Yang, J., NuLi, Y. & Wang, J. Composites of $LiMnPO_4$ with $Li_3V_2(PO_4)_3$ for cathode in lithium-ion battery. *Electrochim. Acta* **103,** 96–102 (2013).

268. Zhang, J. *et al.* Multicore-shell carbon-coated lithium manganese phosphate and lithium vanadium phosphate composite material with high capacity and cycling performance for lithium-ion battery. *Electrochim. Acta* **169,** 462–469 (2015).

269. Hu, C. *et al.* Improving the electrochemical activity of LiMnPO4 via Mn-site co-substitution with Fe and Mg. *Electrochem. commun.* **12,** 1784–1787 (2010).

270. Yi, H. *et al.* Optimized electrochemical performance of LiMn0.9Fe0.1−xMgxPO4/C for lithium ion batteries. *Electrochim. Acta* **56,** 4052–4057 (2011).

271. Johnson, I. D., Loveridge, M., Bhagat, R. & Darr, J. A. Mapping Structure-Composition-Property Relationships in V and Fe Doped $LiMnPO_4$ Cathodes for Lithium-Ion Batteries. *ACS Comb. Sci.* **18,** 665−672 (2016).

272. Ozawa, K. Lithium-ion rechargeable batteries with $LiCoO_2$ and carbon electrodes: the $LiCoO_2$/C system. *Solid State Ionics* **69,** 212–221 (1994).

273. Whittingham, M. S. Lithium batteries and cathode materials. *Chem. Rev.* **104,** 4271–4301 (2004).

274. Rougier, A., Gravereau, P. & Delmas, C. Optimization of the Composition of the $Li_{1-x}Ni_{1+x}O_2$ Electrode Materials: Structural, Magnetic, and Electrochemical Studies. *J. Electrochem. Soc*. **143**, 1168–1175 (1993).

275. Dyer, L. D., Borie, B. S. & Smith, P. G. Alkali Metal-Nickel Oxides of the Type $MNiO_2$. *J. Am. Chem. Soc.* **76**, 1499–1503 (1954)

276. Goodenough, J. B., Wickham, D. G. & Croft, W. J. Some Magnetic and Crystallographic Properties of the System $Li^{+}_{x}Ni^{++}_{1-2x}Ni^{+++}_{x}O$. *J. Phys. Chem. Solids* **5**, 107–116 (1958).

277. Dahn, J. R., Fuller, E. W., Obrovac, M. & von Sacken, U. Thermal stability of Li_xCoO_2, Li_xNiO_2 and λ-MnO_2 and consequences for the safety of Li-ion cells. *Solid State Ionics* **69,** 265–270 (1994).

278. Spahr, M. E., Novák, P., Schnyder, B., Haas, O. & Nesper, R. Characterization of Layered Lithium Nickel Manganese Oxides Synthesized by a Novel Oxidative Coprecipitation Method and Their Electrochemical Performance as Lithium Insertion Electrode Materials. *J. Electrochem. Soc.* **145,** 1113–1121 (1998).

279. Venkatraman, S. & Manthiram, A. Structural and Chemical Characterization of Layered $Li_{1-x}Ni_{1-y}Mn_yO_{2-\delta}$ ($y = 0.25$ and 0.5, and $0 \leq (1 - x) \leq 1$) Oxides. *Chem. Mater.* **15,** 5003–5009 (2003).

280. Kim, J. M. & Chung, H. T. The first cycle characteristics of $LiNi_{1/3}Co_{1/3}Mn_{1/3}O_2$ charged up to 4.7 V. *Electrochim. Acta* **49,** 937–944 (2004).

281. Ngala, J. K. *et al.* The synthesis , characterization and electrochemical behavior of the layered $LiNi_{0.4}Mn_{0.4}Co_{0.2}O_2$ compound. *J. Mater. Chem.* **14,** (2004).

282. Shaju, K. M., Subba Rao, G. V. & Chowdari, B. V. R. Performance of layered $Li(Ni_{1/3}Co_{1/3}Mn_{1/3})O_2$ as cathode for Li-ion batteries. *Electrochim. Acta* **48,** 145–151 (2002).

283. 2016 Chevrolet Volt Battery System. Available at: https://media.gm.com/content/dam/Media/microsites/product/Volt_2016/doc/VOLT_BATTERY.pdf. (Accessed: 1st August 2017)

284. Adschiri, T., Hakuta, Y., Kanamura, K. & Arai, K. Continuous production of $LiCoO_2$ fine crystals for lithium batteries by hydrothermal synthesis under supercritical condition. *High Press. Res.* **20,** 373–384 (2001).

285. Lee, J.-W. *et al.* Synthesis of $LiNi_{1/3}Co_{1/3}Mn_{1/3}O_2$ cathode materials by using a supercritical water method in a batch reactor. *Electrochim. Acta* **55,** 3015–3021 (2010).

286. Shin, Y. H. *et al.* Continuous hydrothermal synthesis of HT-$LiCoO_2$ in supercritical water. *J. Supercrit. Fluids* **50,** 250–256 (2009).

287. Canepa, P. *et al.* Odyssey of Multivalent Cathode Materials: Open Questions and Future Challenges. *Chem. Rev.* **In press,** (2017).

288. Aurbach, D. *et al.* Prototype systems for rechargeable magnesium batteries. *Nature* **407,** 724–727 (2000).

289. Levi, E., Gofer, Y. & Aurbach, D. On the way to rechargeable Mg batteries: The challenge of new cathode materials. *Chem. Mater.* **22,** 860–868 (2010).

290. Aurbach, D., Weissman, I., Gofer, Y. & Levi, E. Nonaqueous magnesium electrochemistry and its application in secondary batteries. *Chem. Rec.* **3,** 61–73 (2003).

291. Wang, Z., Su, Q. & Deng, H. Single-layered V_2O_5 a promising cathode material for rechargeable Li and Mg ion batteries: an ab initio study. *Phys. Chem. Chem. Phys.* **15,** 8705–8709 (2013).

292. Spahr, M. E., Novák, P., Haas, O. & Nesper, R. Electrochemical insertion of lithium, sodium, and magnesium in molybdenum(VI) oxide. *J. Power Sources* **54,** 346–351 (1995).

293. Eroglu, D., Ha, S. & Gallagher, K. G. Fraction of the theoretical specific energy achieved on pack level for hypothetical battery chemistries. *J. Power Sources* **267,** 14–19 (2014).

294. Campanella, L. & Pistoia, G. MoO_3: A New Electrode Material for Nonaqueous Secondary Battery Applications. *J. Electrochem. Soc.* **118,** 1905–1908 (1971).

295. Gershinsky, G., Yoo, H. D., Gofer, Y. & Aurbach, D. Electrochemical and Spectroscopic Analysis of Mg^{2+} Intercalation into Thin Film Electrodes of Layered Oxides: V_2O_5 and MoO_3. *Langmuir* **29,** 10964−10972 (2013).

296. Sa, N. *et al.* Is alpha-V_2O_5 a cathode material for Mg insertion batteries? *J. Power Sources* **323,** 44–50 (2016).

297. Liu, M. *et al.* Spinel compounds as multivalent battery cathodes: a systematic evaluation based on ab initio calculations. *Energy Environ. Sci* **8,** 964–974 (2015).

298. Emly, A. & Van Der Ven, A. Mg intercalation in layered and spinel host crystal structures for Mg batteries. *Inorg. Chem.* **54,** 4394–4402 (2015).

299. Kim, C. *et al.* Direct observation of reversible magnesium ion intercalation into a spinel oxide host. *Adv. Mater.* **27,** 3377–3384 (2015).

300. Tepavcevic, S. *et al.* Nanostructured Layered Cathode for Rechargeable Mg-Ion Batteries. *ACS Nano* **9,** 8194–8205 (2015).

301. Novák, P. & Desilvestro, J. Electrochemical Insertion of Magnesium in Metal Oxides and Sulfides from Aprotic Electrolytes. *J. Electrochem. Soc.* **140,** 140–144 (1993).

302. Thackeray, M. M., Johnson, P. J., Bruce, P. G., de Picciolotto, L. A. & Goodenough, J. B. Electrochemical extraction of lithium from $LiMn_2O_4$. *Mater. Res. Bull.* **19,** 179–187 (1984).

303. O'Neill, H. St. C. & Dollase, W. A. Crystal structures and cation distributions in simple spinels from powder XRD structural refinements: $MgCr_2O_4$, $ZnCr_2O_4$, Fe_3O_4 and the temperature dependence of the cation distribution in $ZnAl_2O_4$. *Phys. Chem. Miner.* **20,** 541–555 (1994).

304. Morozova, L. V & Popov, V. P. Synthesis and investigation of magnesium chromium spinel. *Glas. Phys. Chem.* **36,** 86–91 (2010).

305. Finocchio, E., Busca, G., Lorenzelli, V. & Escribano, V. S. FTIR studies on the selective oxidation and combustion of light hydrocarbons at metal oxide surfaces. *J. Chem. Soc. Faraday Trans.* **93,** 175–180 (1997).

306. Tripathi, V. K. & Nagarajan, R. Rapid Synthesis of Mesoporous, Nano-Sized $MgCr_2O_4$ and Its Catalytic Properties. *J. Am. Ceram. Soc.* **99,** 814–818 (2016).

307. Nagata, K., Nishiwaki, R., Nakamura, Y. & Maruyama, T. Kinetic mechanisms of the formations of $MgCr_2O_4$ and $FeCr_2O_4$ spinels from their metal oxides. *Solid State Ionics* **49,** 161–166 (1991).

308. Durrani, S. K., Naz, S., Nadeem, M. & Khan, A. A. Thermal, structural, and impedance analysis of nanocrystalline magnesium chromite spinel synthesized via hydrothermal process. *J. Therm. Anal. Calorim.* **116,** 309–320 (2014).

309. Seong, G. & Adschiri, T. The reductive supercritical hydrothermal process, a

novel synthesis method for cobalt nanoparticles: synthesis and investigation on the reaction mechanism. *Dalton Trans.* **43,** 10778–10786 (2014).

310. Wang, Z., Neill, H. S. C. O., Lazor, P. & Saxena, S. K. High pressure Raman spectroscopic study of spinel $MgCr_2O_4$. *J. Phys. Chem. Solids* **63**, 2057–2061 (2002).

311. Lenaz, D. & Lughi, V. Raman study of $MgCr_2O_4$-$Fe^{2+}Cr_2O_4$ and $MgCr_2O_4$-$MgFe_2^{3+}O_4$ synthetic series: The effects of Fe^{2+} and Fe^{3+} on Raman shifts. *Phys. Chem. Miner.* **40,** 491–498 (2013).

312. Gouadec, G. & Colomban, P. Raman Spectroscopy of nanomaterials: How spectra relate to disorder, particle size and mechanical properties. *Prog. Cryst. Growth Charact. Mater.* **53,** 1–56 (2007).

313. Weckhuysen, B. M. & Wachs, I. E. Raman spectroscopy of supported chromium oxide catalysts. Determination of chromium-oxygen bond distances and bond orders. *J. Chem. Soc, Faraday Trans.* **92,** 1969–1973 (1996).

314. Petitto, S. C., Marsh, E. M., Carson, G. A. & Langell, M. A. Cobalt oxide surface chemistry: The interaction of CoO(1 0 0), Co_3O_4(1 1 0) and Co_3O_4(1 1 1) with oxygen and water. *J. Mol. Catal. A Chem.* **281,** 49–58 (2008).

315. Stefanescu, M. *et al.* Novel low temperature synthesis method for nanocrystalline zinc and magnesium chromites. *Thermochim. Acta* **526,** 130–136 (2011).

316. Spratt, H. J., Palmer, S. J. & Frost, R. L. Thermal decomposition of synthesised layered double hydroxides based upon Mg/(Fe,Cr) and carbonate. *Thermochim. Acta* **479,** 1–6 (2008).

317. de Andrade, M. J., Lima, M. D., Bonadiman, R. & Bergmann, C. P. Nanocrystalline pirochromite spinel through solution combustion synthesis. *Mater. Res. Bull.* **41,** 2070–2079 (2006).

318. Chandran, R. G. & Patil, K. C. A rapid method to prepare crystalline fine particle chromite powders. *Mater. Lett.* **12,** 437–441 (1992).

11. Appendix I: Rietveld Refinement Plots

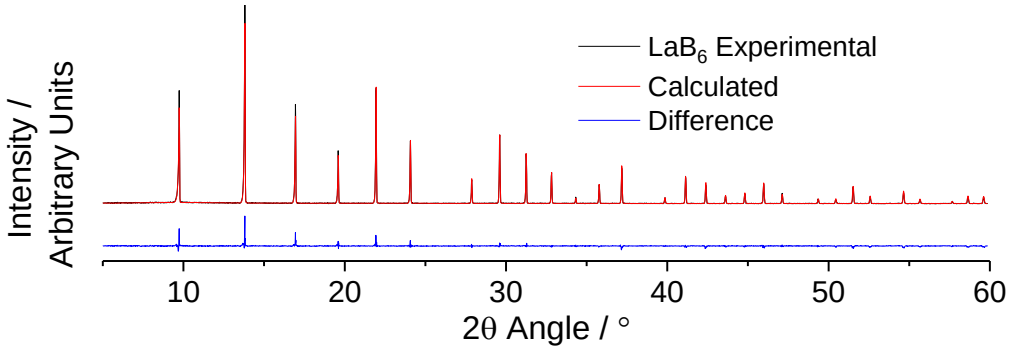

Figure 11.1 – Experimental (black) and calculated (red) diffraction patterns for a LaB_6 standard (set-up **c**, Section 2.1.4.1, Mo-Kα radiation), with the difference (blue) plotted underneath. R_{wp} = 17.7, χ^2 = 1.02.

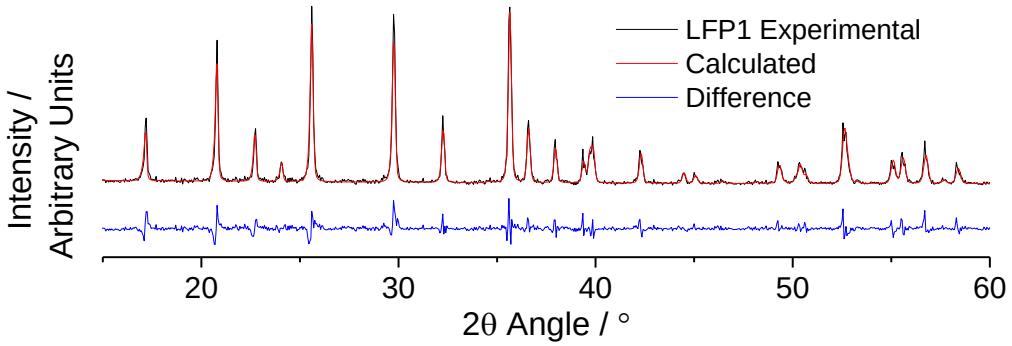

Figure 11.2 – Experimental (black) and calculated (red) diffraction patterns for sample LFP1 from Rietveld refinement (set-up **a**, Section 2.1.4.1, Cu-Kα radiation), with the difference (blue) plotted underneath. R_{wp} =22.6, χ^2 = 1.25.

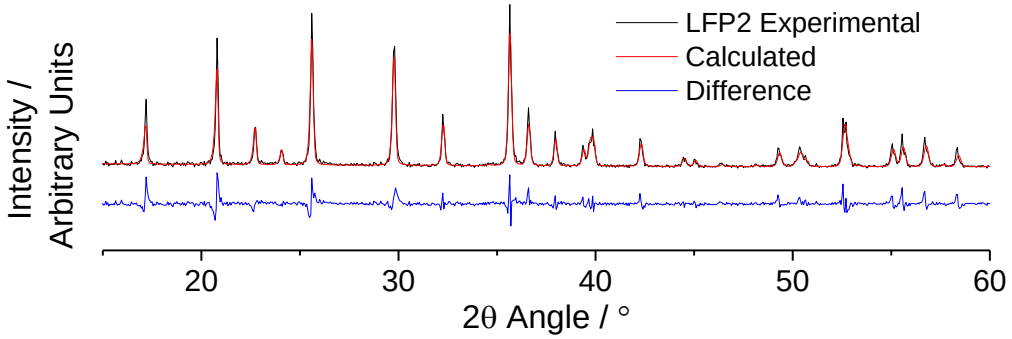

Figure 11.3 – Experimental (black) and calculated (red) diffraction patterns for sample LFP2 from Rietveld refinement (set-up **a**, Section 2.1.4.1, Cu-Kα radiation), with the difference (blue) plotted underneath. R_{wp} = 24.5, χ^2 = 1.39.

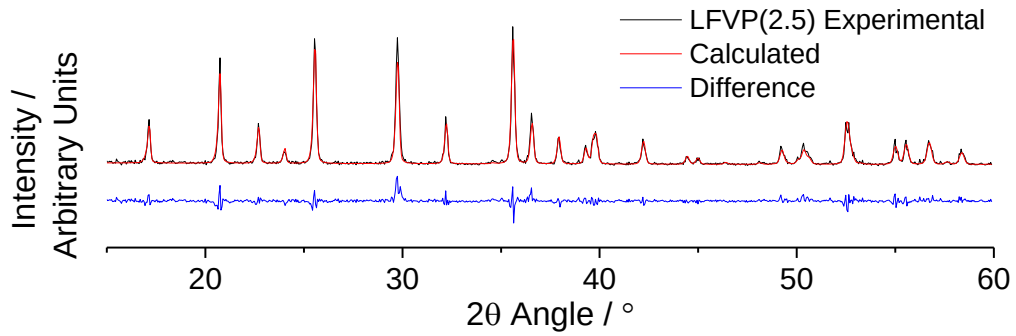

Figure 11.4 – Experimental (black) and calculated (red) diffraction patterns for sample LFVP(2.5) from Rietveld refinement (set-up **a**, Section 2.1.4.1, Cu-Kα radiation), with the difference (blue) plotted underneath. R_{wp} = 30.2, χ^2 = 1.60.

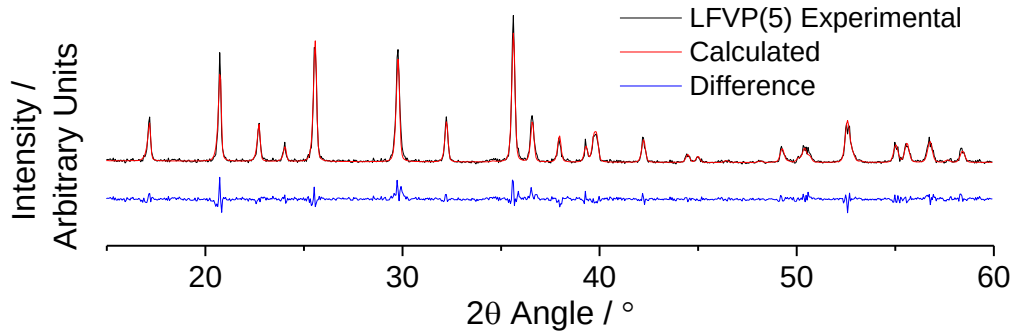

Figure 11.5 – Experimental (black) and calculated (red) diffraction patterns for sample LFVP(5) from Rietveld refinement (set-up **a**, Section 2.1.4.1, Cu-Kα radiation), with the difference (blue) plotted underneath. R_{wp} = 27.1, χ^2 = 1.44.

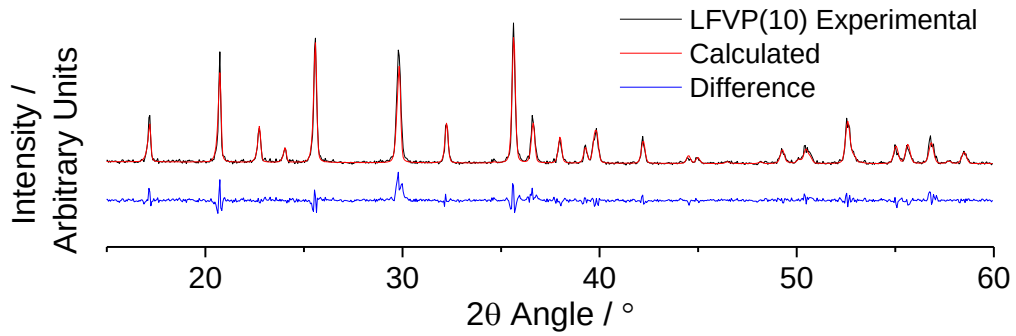

Figure 11.6 – Experimental (black) and calculated (red) diffraction patterns for sample LFVP(10) from Rietveld refinement (set-up **a**, Section 2.1.4.1, Cu-Kα radiation), with the difference (blue) plotted underneath. R_{wp} = 26.1, χ^2 = 1.40.

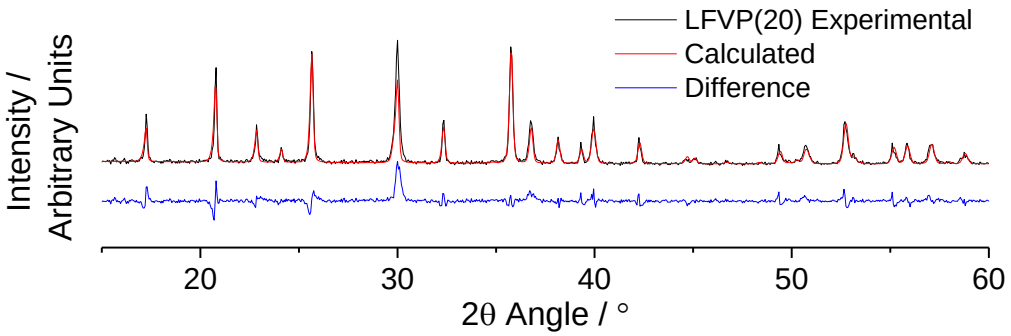

Figure 11.7 – Experimental (black) and calculated (red) diffraction patterns for sample LFVP(20) from Rietveld refinement (set-up **a**, Section 2.1.4.1, Cu-Kα radiation), with the difference (blue) plotted underneath. R_{wp} = 26.7, χ^2 = 1.47.

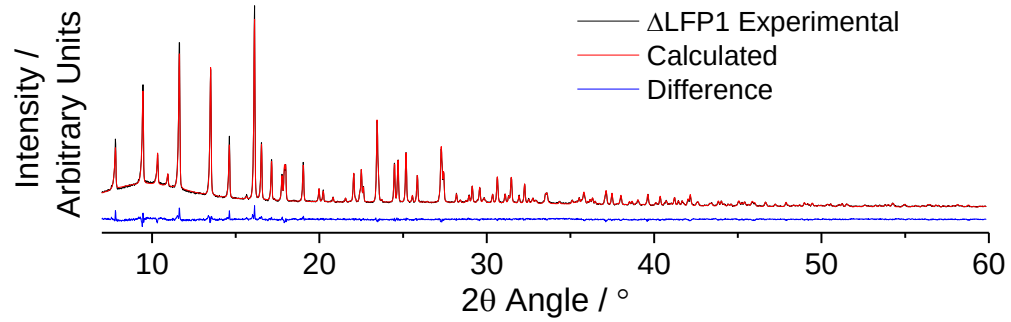

Figure 11.8 – Experimental (black) and calculated (red) diffraction patterns for sample ΔLFP1 from Rietveld refinement (set-up **c**, Section 2.1.4.1, Mo-Kα radiation), with the difference (blue) plotted underneath. R_{wp} = 4.48, χ^2 = 1.34.

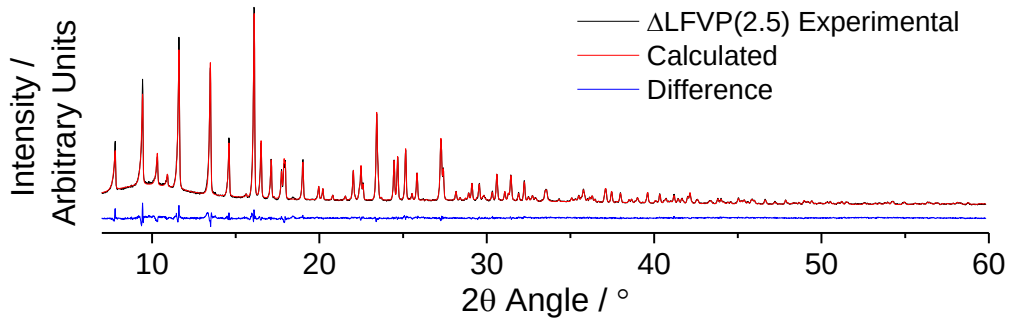

Figure 11.9 – Experimental (black) and calculated (red) diffraction patterns for sample ΔLFVP(2.5) from Rietveld refinement (set-up **c**, Section 2.1.4.1, Mo-Kα radiation), with the difference (blue) plotted underneath. R_{wp} = 4.87, χ^2 = 1.40.

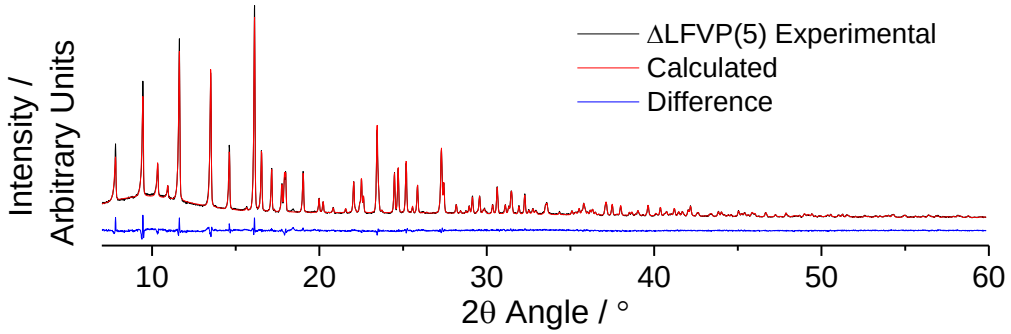

Figure 11.10 – Experimental (black) and calculated (red) diffraction patterns for sample ΔLFVP(5) from Rietveld refinement (set-up **c**, Section 2.1.4.1, Mo-Kα radiation), with the difference (blue) plotted underneath. R_{wp} = 4.75, χ^2 = 1.33.

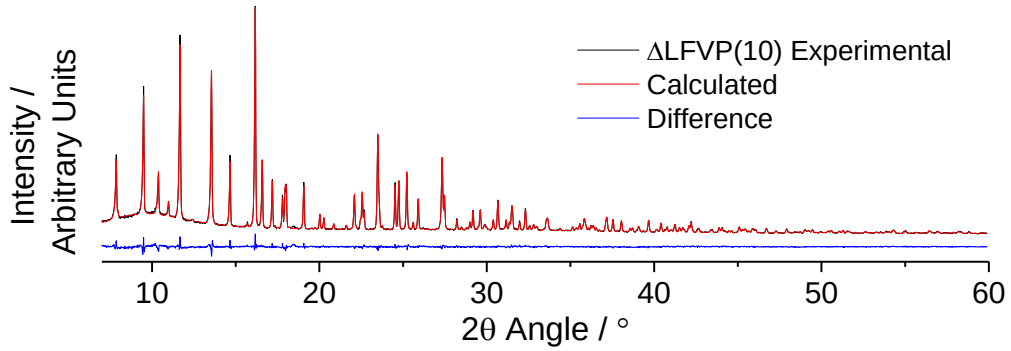

Figure 11.11 – Experimental (black) and calculated (red) diffraction patterns for sample ΔLFVP(10) from Rietveld refinement (set-up **c**, Section 2.1.4.1, Mo-Kα radiation), with the difference (blue) plotted underneath. R_{wp} = 4.24, χ^2 = 1.18.

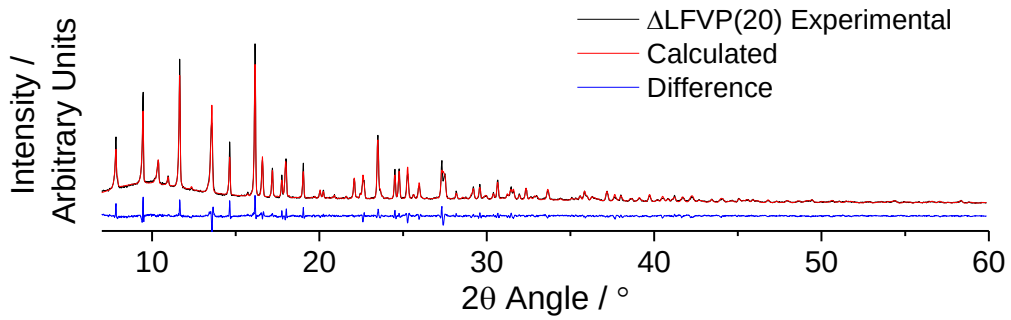

Figure 11.12 – Experimental (black) and calculated (red) diffraction patterns for sample ΔLFVP(20) from Rietveld refinement (set-up **c**, Section 2.1.4.1, Mo-Kα radiation), with the difference (blue) plotted underneath. R_{wp} = 7.45, χ^2 = 1.98.

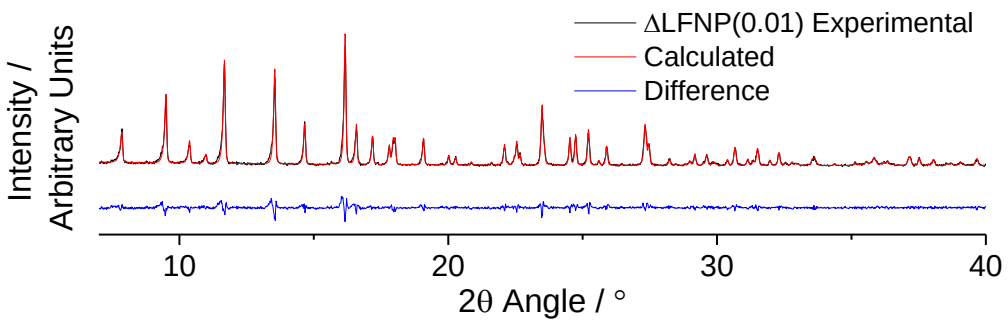

Figure 11.13 – Experimental (black) and calculated (red) diffraction patterns for sample ΔLFNP(0.01) from Rietveld refinement (set-up **b**, Section 2.1.4.1, Mo-Kα radiation), with the difference (blue) plotted underneath. R_{wp} = 17.2, χ^2 = 1.14.

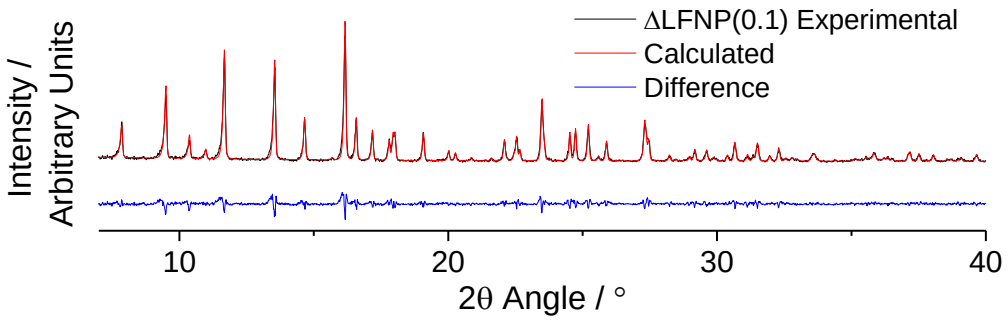

Figure 11.14 – Experimental (black) and calculated (red) diffraction patterns for sample ΔLFNP(0.1) from Rietveld refinement (set-up **b**, Section 2.1.4.1, Mo-Kα radiation), with the difference (blue) plotted underneath. R_{wp} = 17.6, χ^2 = 1.23.

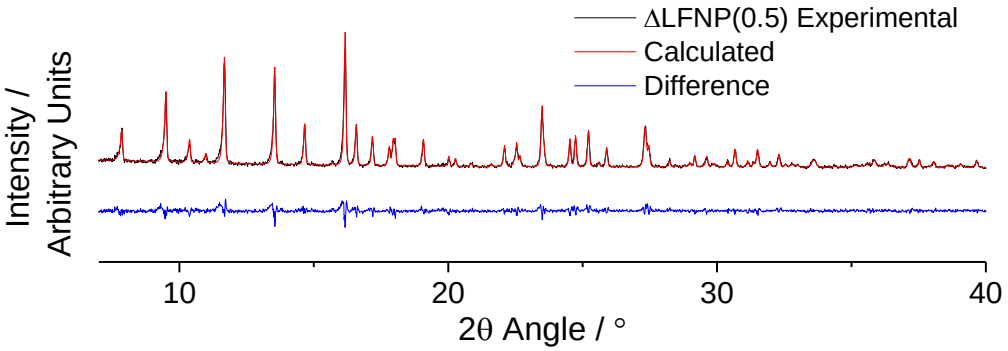

Figure 11.15 – Experimental (black) and calculated (red) diffraction patterns for sample ΔLFNP(0.5) from Rietveld refinement (set-up **b**, Section 2.1.4.1, Mo-Kα radiation), with the difference (blue) plotted underneath. R_{wp} = 17.1, χ^2 = 1.03.

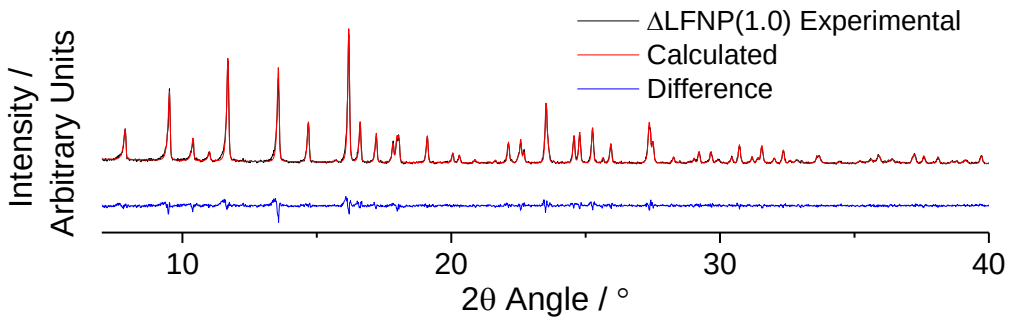

Figure 11.16 – Experimental (black) and calculated (red) diffraction patterns for sample ΔLFNP(1.0) from Rietveld refinement (set-up **b**, Section 2.1.4.1, Mo-Kα radiation), with the difference (blue) plotted underneath. R_{wp} = 15.5, χ^2 = 1.04.

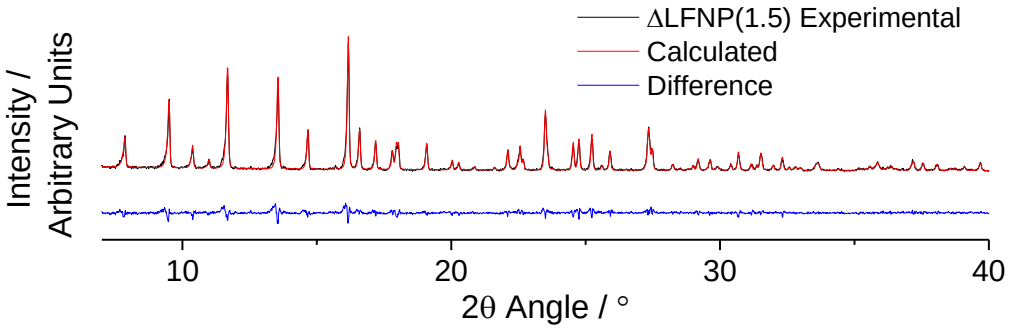

Figure 11.17 – Experimental (black) and calculated (red) diffraction patterns for sample ΔLFNP(1.5) from Rietveld refinement (set-up **b**, Section 2.1.4.1, Mo-Kα radiation), with the difference (blue) plotted underneath. R_{wp} = 16.3, χ^2 = 1.10.

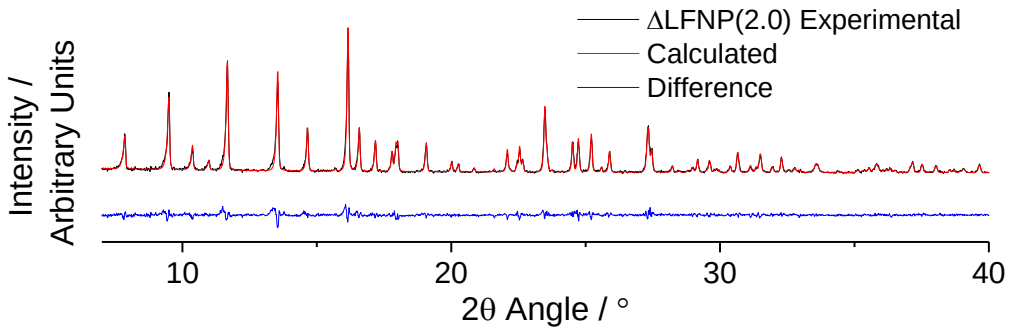

Figure 11.18 – Experimental (black) and calculated (red) diffraction patterns for sample ΔLFNP(2.0) from Rietveld refinement (set-up **b**, Section 2.1.4.1, Mo-Kα radiation), with the difference (blue) plotted underneath. R_{wp} = 15.6, χ^2 = 1.09.

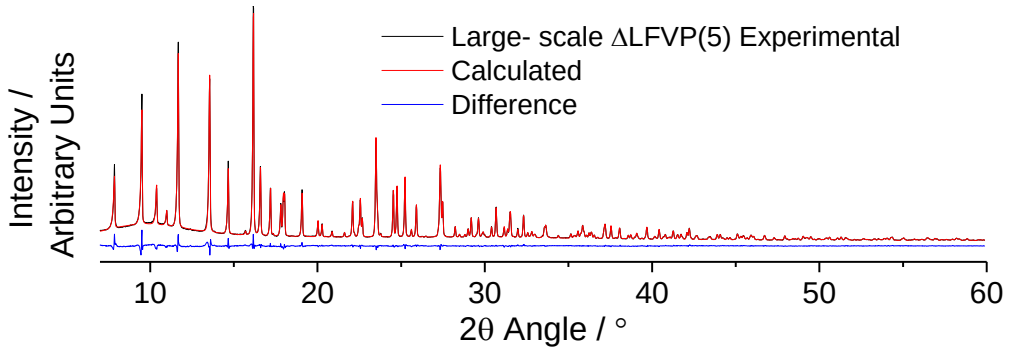

Figure 11.19 – Experimental (black) and calculated (red) diffraction patterns for large-scale sample ΔLFVP(5) from Rietveld refinement (set-up **c**, Section 2.1.4.1, Mo-Kα radiation), with the difference (blue) plotted underneath. R_{wp} = 3.75, χ^2 = 2.17.

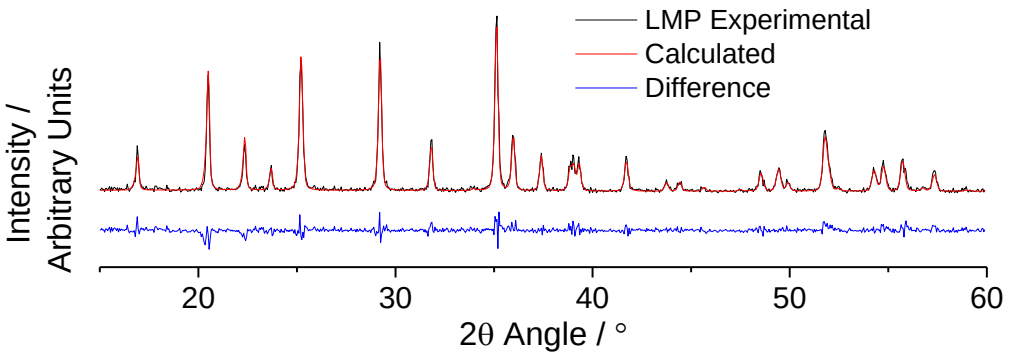

Figure 11.20 – Experimental (black) and calculated (red) diffraction patterns for sample LMP from Rietveld refinement (set-up **a**, Section 2.1.4.1, Cu-Kα radiation), with the difference (blue) plotted underneath. R_{wp} = 22.0, χ^2 = 1.07.

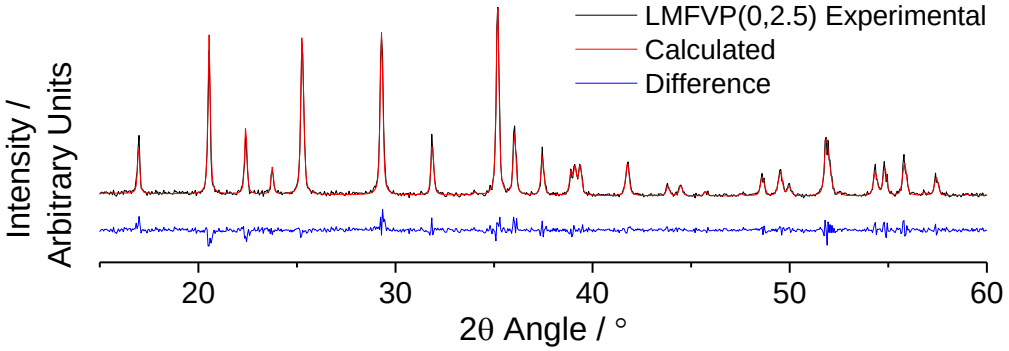

Figure 11.21 – Experimental (black) and calculated (red) diffraction patterns for sample LMFVP(0,2.5) from Rietveld refinement (set-up **a**, Section 2.1.4.1, Cu-Kα radiation), with the difference (blue) plotted underneath. R_{wp} = 20.3, χ^2 = 1.07.

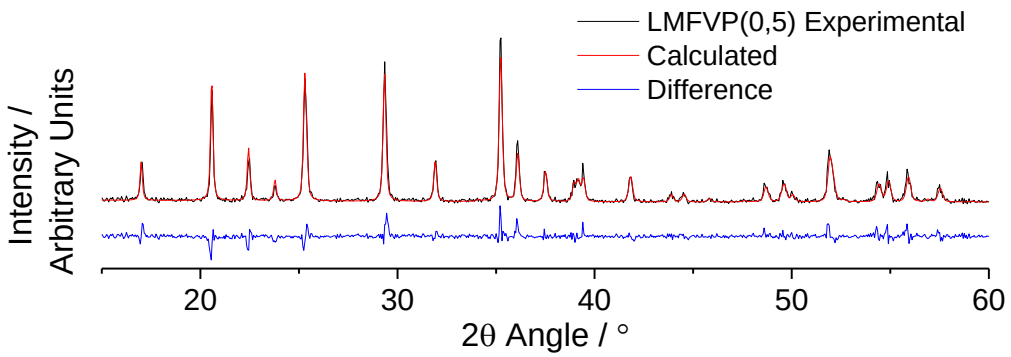

Figure 11.22 – Experimental (black) and calculated (red) diffraction patterns for sample LMFVP(0,5) from Rietveld refinement (set-up **a**, Section 2.1.4.1, Cu-Kα radiation), with the difference (blue) plotted underneath. R_{wp} = 21.1, χ^2 = 1.06.

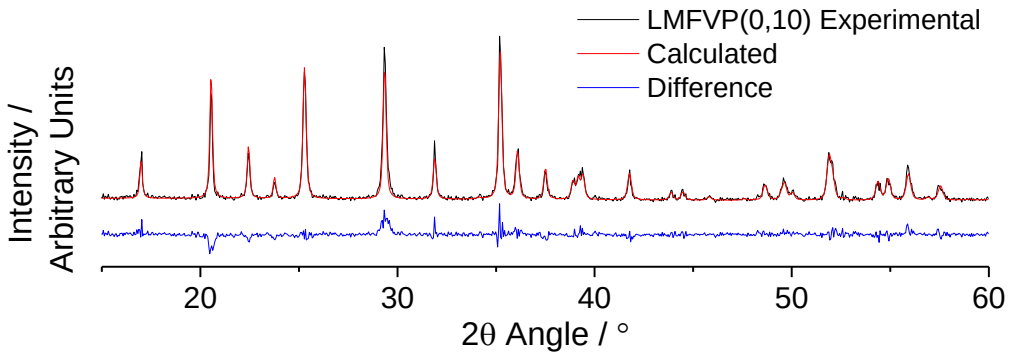

Figure 11.23 – Experimental (black) and calculated (red) diffraction patterns for sample LMFVP(0,10) from Rietveld refinement (set-up **a**, Section 2.1.4.1, Cu-Kα radiation), with the difference (blue) plotted underneath. R_{wp} = 22.1, χ^2 = 1.15.

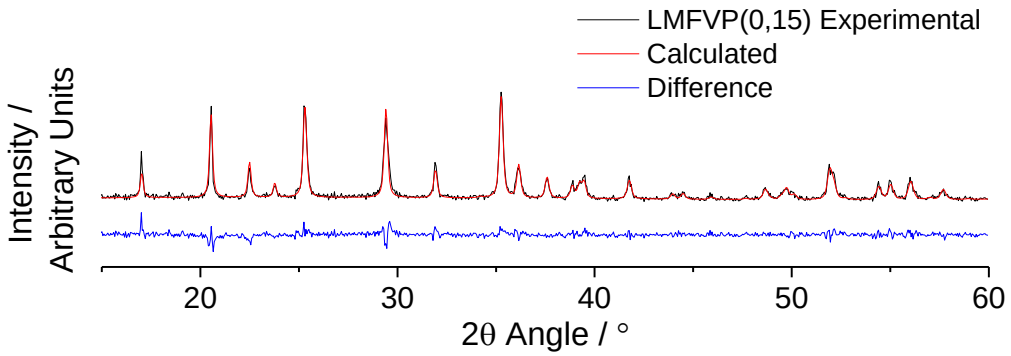

Figure 11.24 – Experimental (black) and calculated (red) diffraction patterns for sample LMFVP(0,15) from Rietveld refinement (set-up **a**, Section 2.1.4.1, Cu-Kα radiation), with the difference (blue) plotted underneath. R_{wp} = 21.7, χ^2 = 1.11.

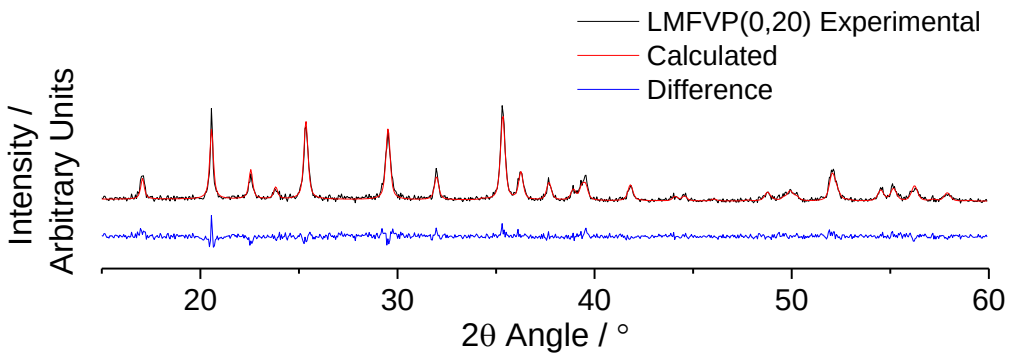

Figure 11.25 – Experimental (black) and calculated (red) diffraction patterns for sample LMFVP(0,20) from Rietveld refinement (set-up **a**, Section 2.1.4.1, Cu-Kα radiation), with the difference (blue) plotted underneath. R_{wp} = 20.2, χ^2 = 1.02.

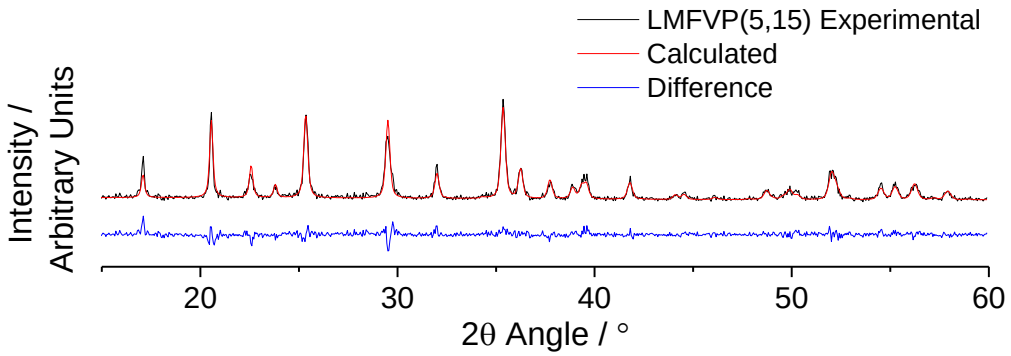

Figure 11.26 – Experimental (black) and calculated (red) diffraction patterns for sample LMFVP(5,15) from Rietveld refinement (set-up **a**, Section 2.1.4.1, Cu-Kα radiation), with the difference (blue) plotted underneath. R_{wp} = 22.0, χ^2 = 1.10.

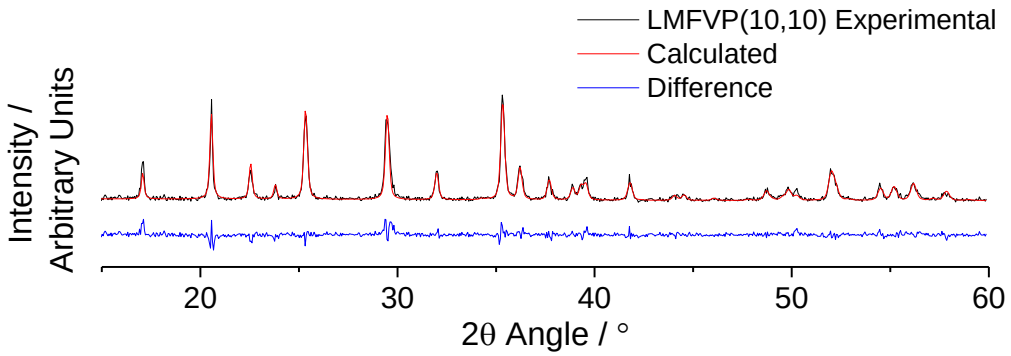

Figure 11.27 – Experimental (black) and calculated (red) diffraction patterns for sample LMFVP(10,10) from Rietveld refinement (set-up **a**, Section 2.1.4.1, Cu-Kα radiation), with the difference (blue) plotted underneath. R_{wp} = 23.1, χ^2 = 1.10.

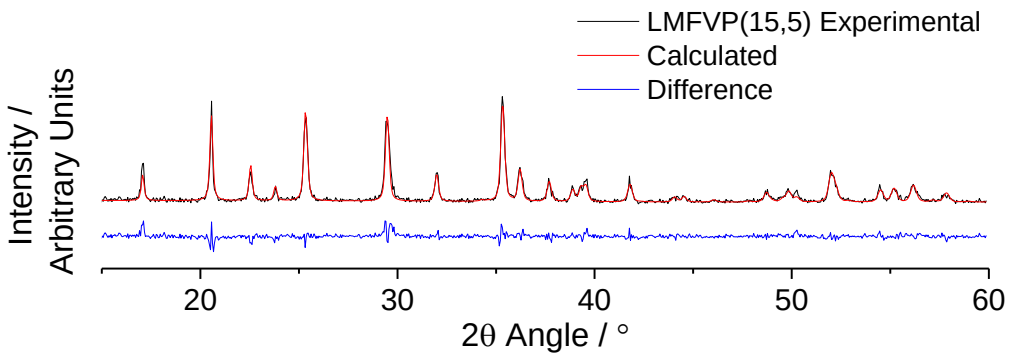

Figure 11.28 – Experimental (black) and calculated (red) diffraction patterns for sample LMFVP(15,5) from Rietveld refinement (set-up **a**, Section 2.1.4.1, Cu-Kα radiation), with the difference (blue) plotted underneath. R_{wp} = 20.4, χ^2 = 1.06.

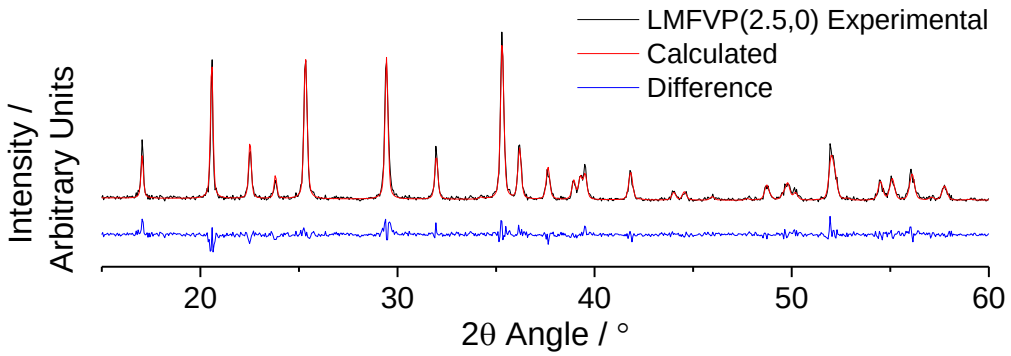

Figure 11.29 – Experimental (black) and calculated (red) diffraction patterns for sample LMFVP(2.5,0) from Rietveld refinement (set-up **a**, Section 2.1.4.1, Cu-Kα radiation), with the difference (blue) plotted underneath. R_{wp} = 23.0, χ^2 = 1.11.

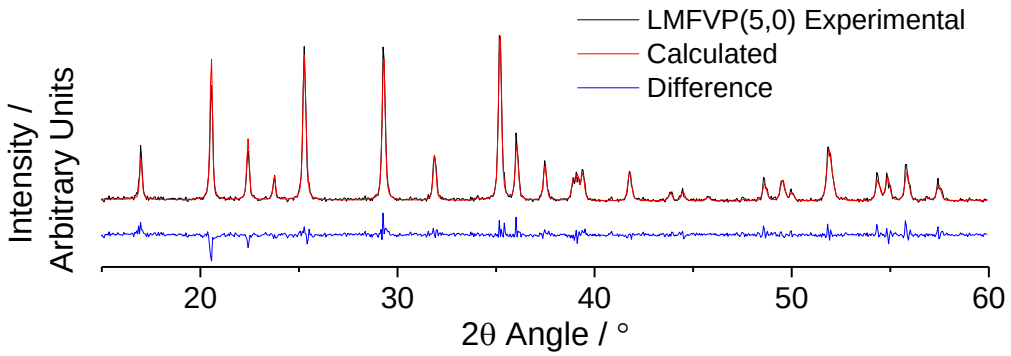

Figure 11.30 – Experimental (black) and calculated (red) diffraction patterns for sample LMFVP(5,0) from Rietveld refinement (set-up **a**, Section 2.1.4.1, Cu-Kα radiation), with the difference (blue) plotted underneath. R_{wp} = 20.9, χ^2 = 1.05.

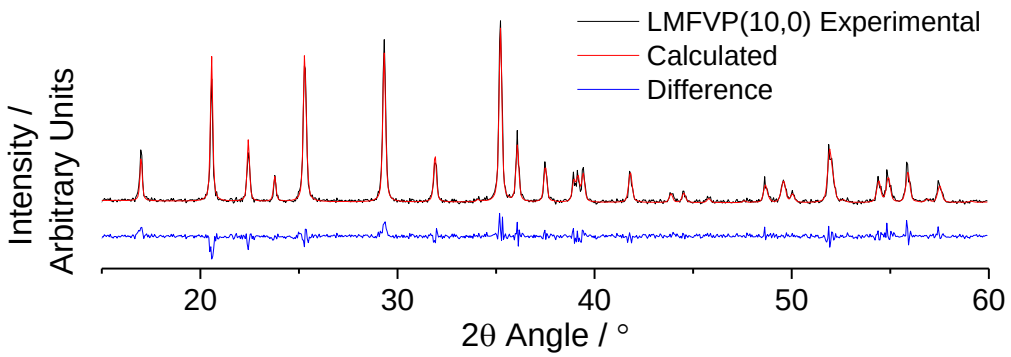

Figure 11.31 – Experimental (black) and calculated (red) diffraction patterns for sample LMFVP(10,0) from Rietveld refinement (set-up **a**, Section 2.1.4.1, Cu-Kα radiation), with the difference (blue) plotted underneath. R_{wp} = 23.5, χ^2 = 1.18.

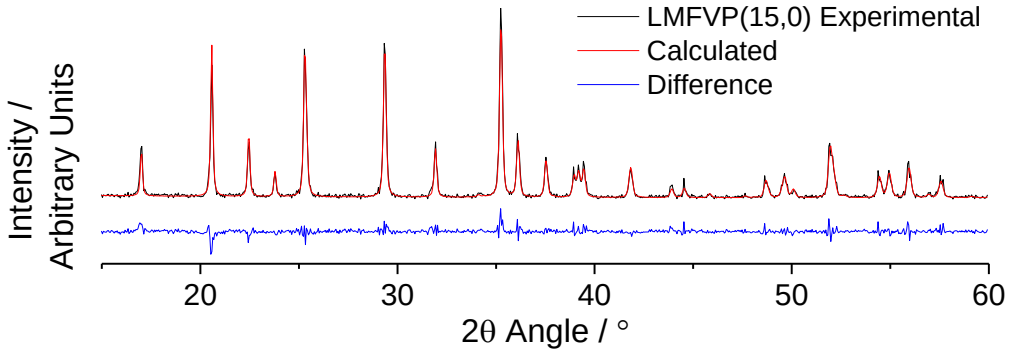

Figure 11.32 – Experimental (black) and calculated (red) diffraction patterns for sample LMFVP(15,0) from Rietveld refinement (set-up **a**, Section 2.1.4.1, Cu-Kα radiation), with the difference (blue) plotted underneath. R_{wp} = 21.4, χ^2 = 1.07.

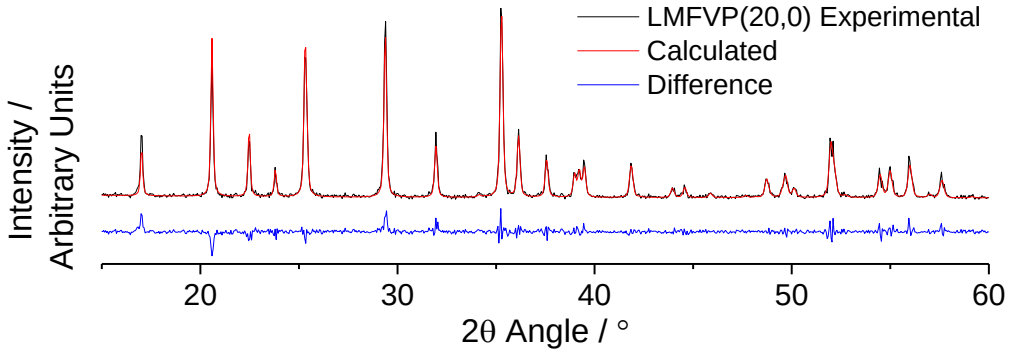

Figure 11.33 – Experimental (black) and calculated (red) diffraction patterns for sample LMFVP(20,0) from Rietveld refinement (set-up **a**, Section 2.1.4.1, Cu-Kα radiation), with the difference (blue) plotted underneath. R_{wp} = 21.2, χ^2 = 1.10.

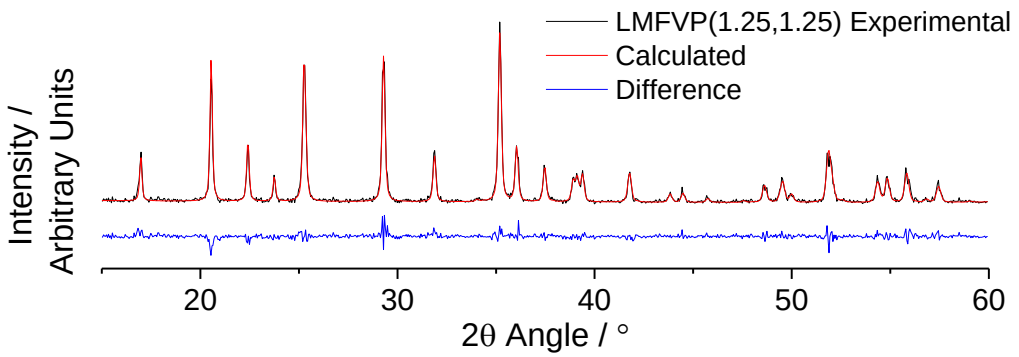

Figure 11.34 – Experimental (black) and calculated (red) diffraction patterns for sample LMFVP(1.25,1.25) from Rietveld refinement (set-up **a**, Section 2.1.4.1, Cu-Kα radiation), with the difference (blue) plotted underneath. R_{wp} = 20.9, χ^2 = 1.06.

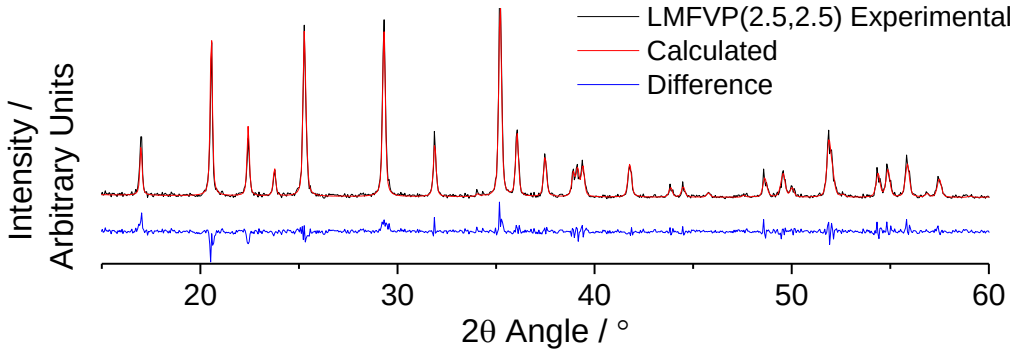

Figure 11.35 – Experimental (black) and calculated (red) diffraction patterns for sample LMFVP(2.5,2.5) from Rietveld refinement (set-up **a**, Section 2.1.4.1, Cu-Kα radiation), with the difference (blue) plotted underneath. R_{wp} = 20.0, χ^2 = 1.06.

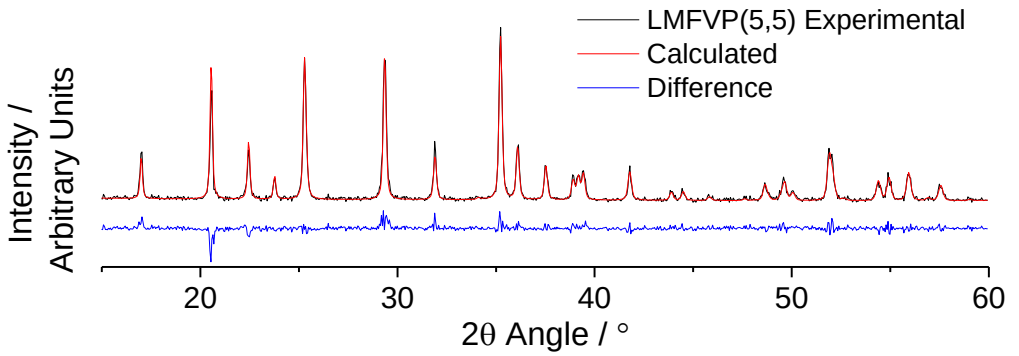

Figure 11.36 – Experimental (black) and calculated (red) diffraction patterns for sample LMFVP(5,5) from Rietveld refinement (set-up **a**, Section 2.1.4.1, Cu-Kα radiation), with the difference (blue) plotted underneath. R_{wp} = 21.3, χ^2 = 1.09.

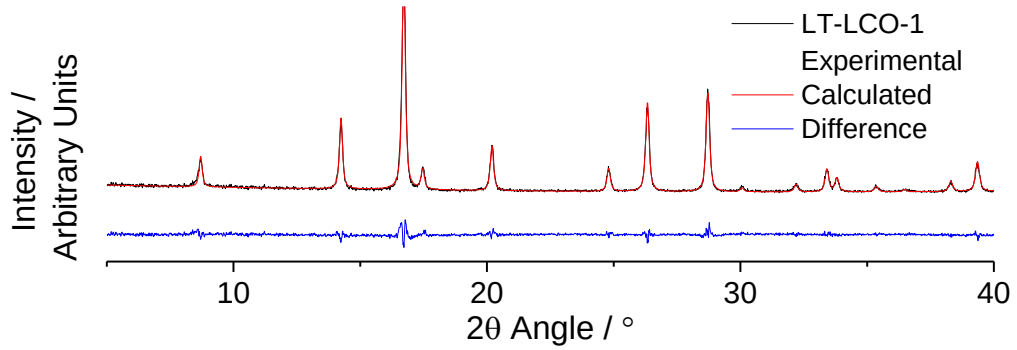

Figure 11.37 – Experimental (black) and calculated (red) diffraction patterns for sample LT-LCO-1 from Rietveld refinement (set-up **b**, Section 2.1.4.1, Mo-Kα radiation) to estimate the Co_3O_4:$LiCoO_2$ volume ratio, with the difference (blue) plotted underneath. R_{wp} = 13.1, χ^2 = 1.07.

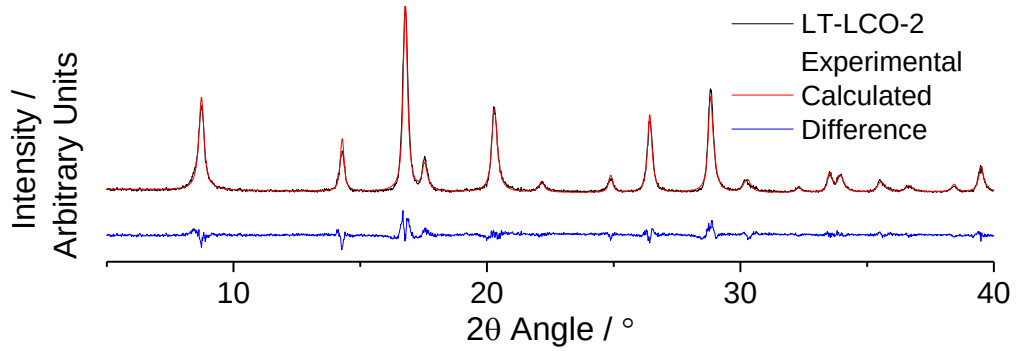

Figure 11.38 – Experimental (black) and calculated (red) diffraction patterns for sample LT-LCO-2 from Rietveld refinement (set-up **b**, Section 2.1.4.1, Mo-Kα radiation) to estimate the Co_3O_4:$LiCoO_2$ volume ratio, with the difference (blue) plotted underneath. R_{wp} = 16.4, χ^2 = 1.59.

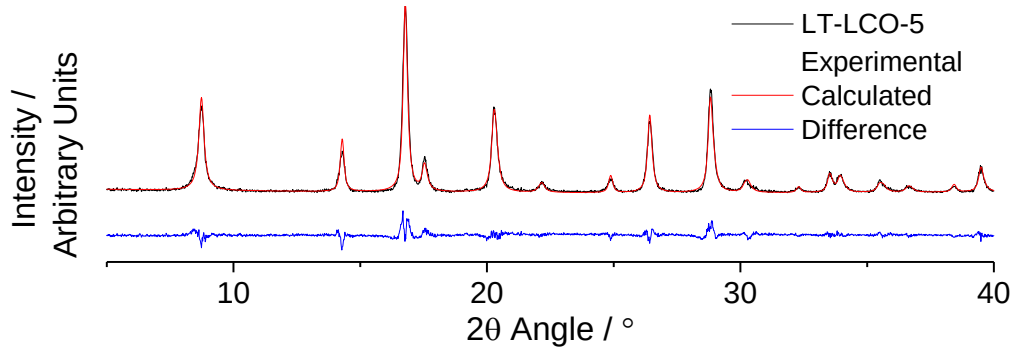

Figure 11.39 – Experimental (black) and calculated (red) diffraction patterns for sample LT-LCO-5 from Rietveld refinement (set-up **b**, Section 2.1.4.1, Mo-Kα radiation) to estimate the Co_3O_4:$LiCoO_2$ volume ratio, with the difference (blue) plotted underneath. R_{wp} = 16.9, χ^2 = 1.47.

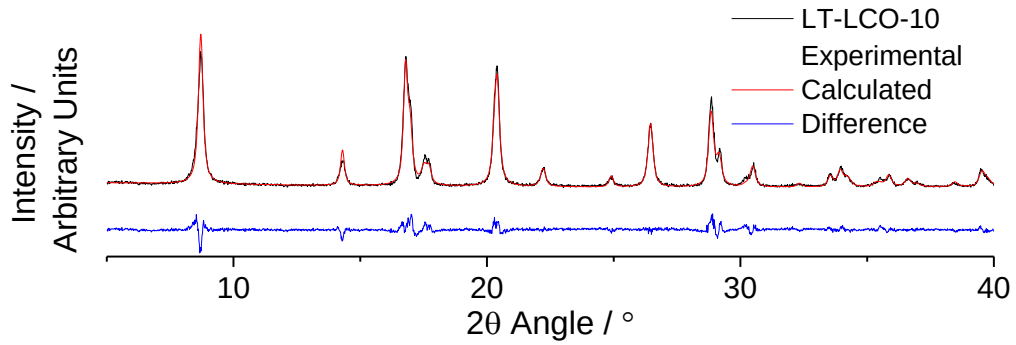

Figure 11.40 – Experimental (black) and calculated (red) diffraction patterns for sample LT-LCO-10 from Rietveld refinement (set-up **b**, Section 2.1.4.1, Mo-Kα radiation) to estimate the Co_3O_4:$LiCoO_2$ volume ratio, with the difference (blue) plotted underneath. R_{wp} = 16.2, χ^2 = 1.46.

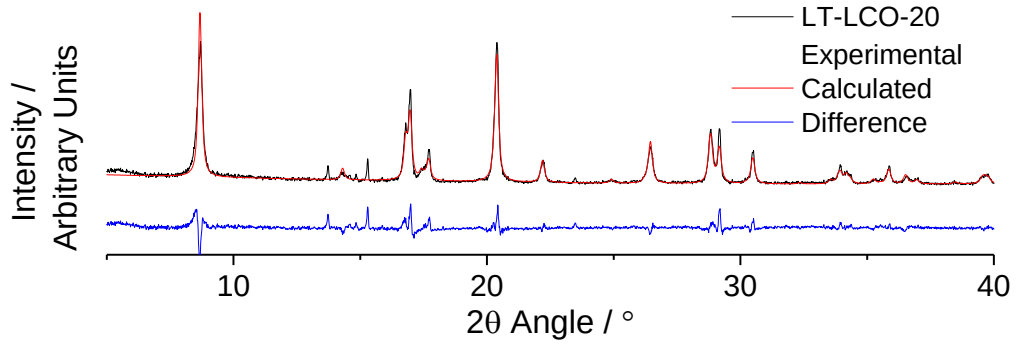

Figure 11.41 – Experimental (black) and calculated (red) diffraction patterns for sample LT-LCO-20 from Rietveld refinement (set-up **b**, Section 2.1.4.1, Mo-Kα radiation) to estimate the Co_3O_4:$LiCoO_2$ volume ratio, with the difference (blue) plotted underneath. R_{wp} = 17.4, χ^2 = 1.65.

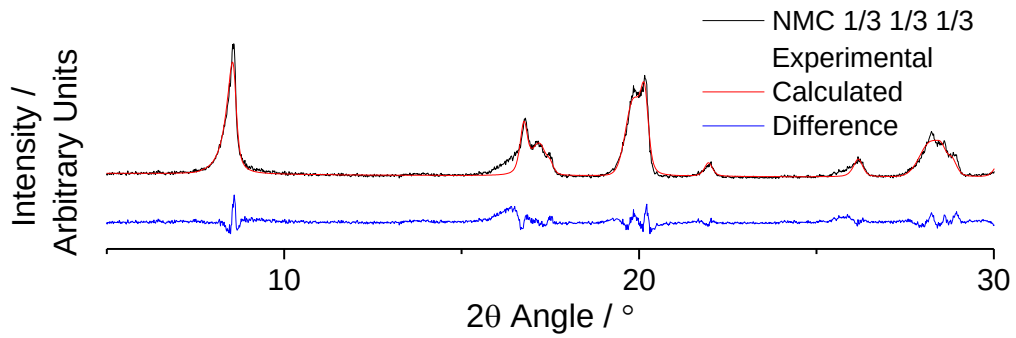

Figure 11.42 – Experimental (black) and calculated (red) diffraction patterns for sample NMC 1/3 1/3 1/3 from Rietveld refinement (set-up **b**, Section 2.1.4.1, Mo-Kα radiation) to estimate the NMC:NiO volume ratio, with the difference (blue) plotted underneath. R_{wp} = 17.9, χ^2 = 1.83.

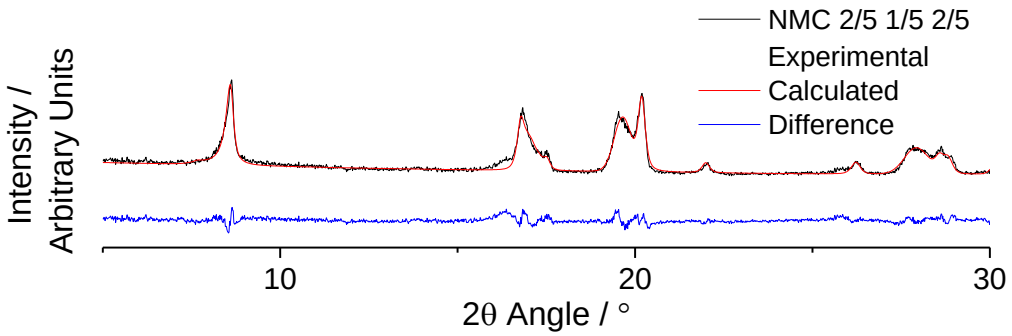

Figure 11.43 – Experimental (black) and calculated (red) diffraction patterns for sample NMC 2/5 1/5 2/5 from Rietveld refinement (set-up **b**, Section 2.1.4.1, Mo-Kα radiation) to estimate the NMC:NiO volume ratio, with the difference (blue) plotted underneath. R_{wp} = 13.5, χ^2 = 1.54.

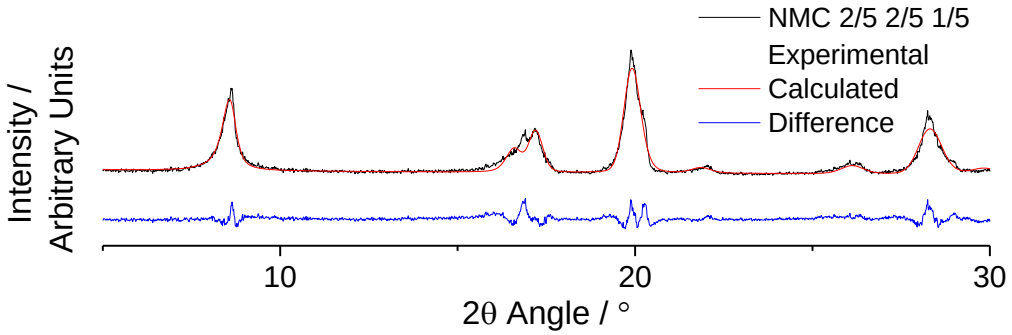

Figure 11.44 – Experimental (black) and calculated (red) diffraction patterns for sample NMC 2/5 2/5 1/5 from Rietveld refinement (set-up **b**, Section 2.1.4.1, Mo-Kα radiation) to estimate the NMC:NiO volume ratio, with the difference (blue) plotted underneath. R_{wp} = 16.9, χ^2 = 1.74.

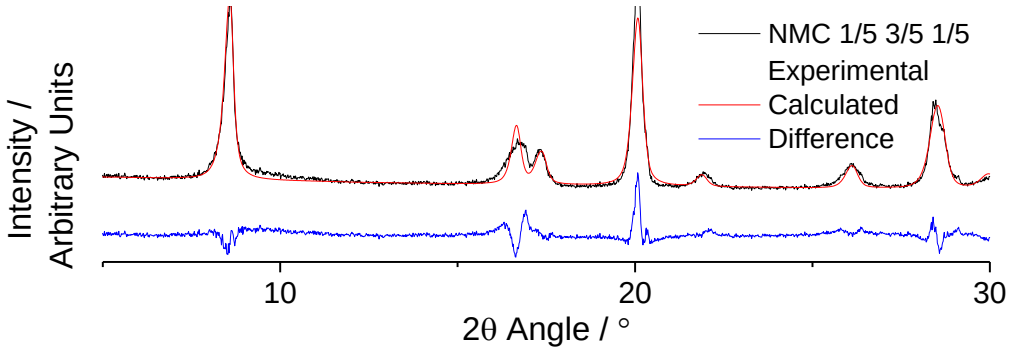

Figure 11.45 – Experimental (black) and calculated (red) diffraction patterns for sample NMC 1/5 3/5 1/5 from Rietveld refinement (set-up **b**, Section 2.1.4.1, Mo-Kα radiation) to estimate the NMC:NiO volume ratio, with the difference (blue) plotted underneath. R_{wp} = 16.9, χ^2 = 2.14.

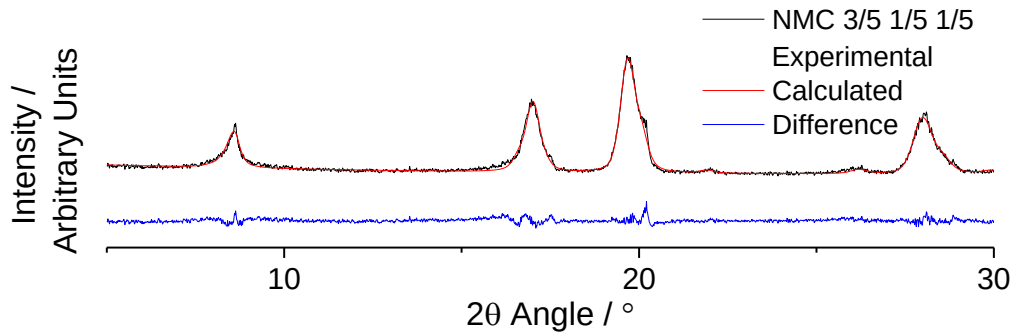

Figure 11.46 – Experimental (black) and calculated (red) diffraction patterns for sample NMC 3/5 1/5 1/5 from Rietveld refinement (set-up **b**, Section 2.1.4.1, Mo-Kα radiation) to estimate the NMC:NiO volume ratio, with the difference (blue) plotted underneath. R_{wp} = 12.6, χ^2 = 1.45.

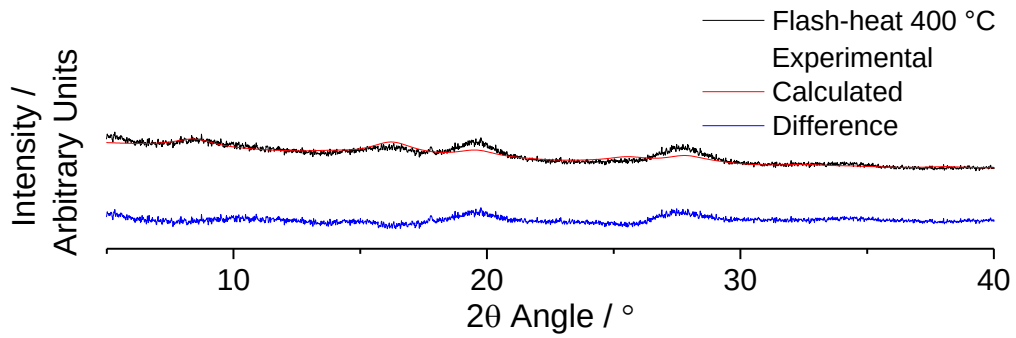

Figure 11.47 – Experimental (black) and calculated (red) diffraction patterns for sample MCO-335-0.4 (flash heat-treated at 400 °C for 10 min) from Rietveld refinement (set-up **b**, Section 2.1.4.1, Mo-Kα radiation) to estimate particle size, with the difference (blue) plotted underneath. R_{wp} = 13.2, χ^2 = 1.60.

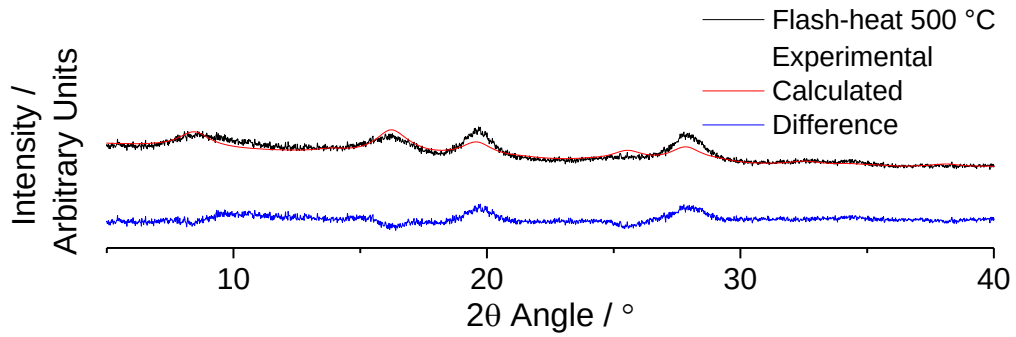

Figure 11.48 – Experimental (black) and calculated (red) diffraction patterns for sample MCO-335-0.4 (flash heat-treated at 500 °C for 10 min) from Rietveld refinement (set-up **b**, Section 2.1.4.1, Mo-Kα radiation) to estimate particle size, with the difference (blue) plotted underneath. R_{wp} = 14.0, χ^2 = 1.78.

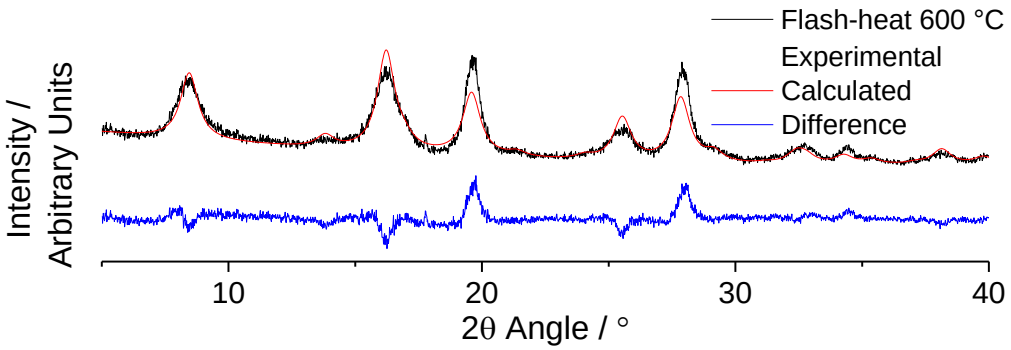

Figure 11.49 – Experimental (black) and calculated (red) diffraction patterns for sample MCO-335-0.4 (flash heat-treated at 600 °C for 10 min) from Rietveld refinement (set-up **b**, Section 2.1.4.1, Mo-Kα radiation) to estimate particle size, with the difference (blue) plotted underneath. R_{wp} = 13.6, χ^2 = 1.72.

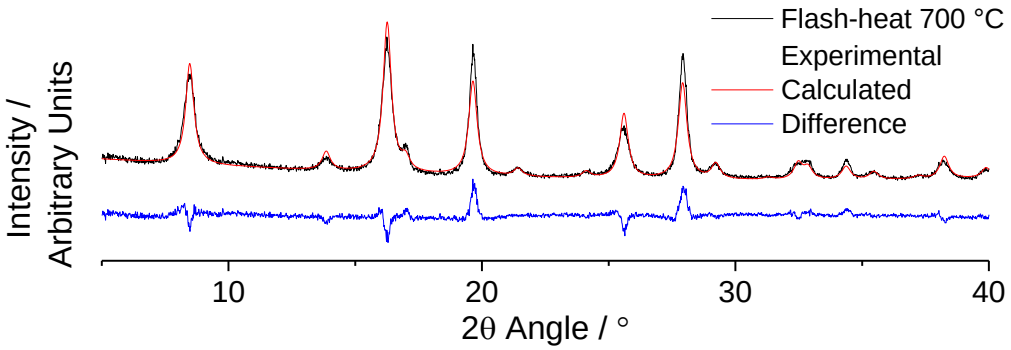

Figure 11.50 – Experimental (black) and calculated (red) diffraction patterns for sample MCO-335-0.4 (flash heat-treated at 700 °C for 10 min) from Rietveld refinement (set-up **b**, Section 2.1.4.1, Mo-Kα radiation) to estimate particle size, with the difference (blue) plotted underneath. R_{wp} = 13.0, χ^2 = 1.54.

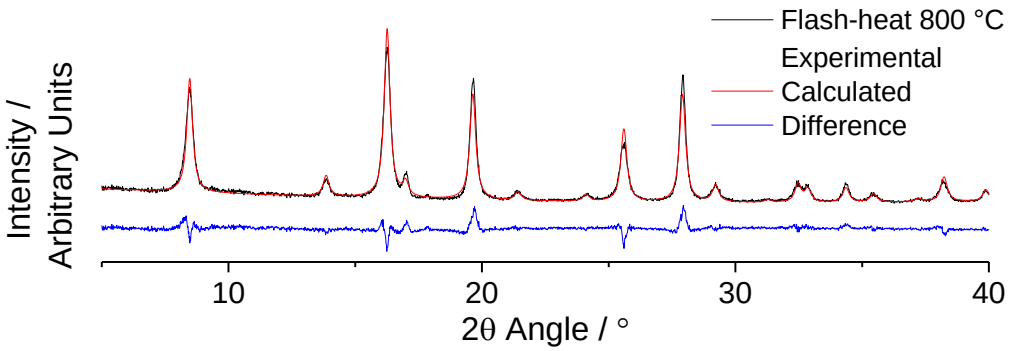

Figure 11.51 – Experimental (black) and calculated (red) diffraction patterns for sample MCO-335-0.4 (flash heat-treated at 800 °C for 10 min) from Rietveld refinement (set-up **b**, Section 2.1.4.1, Mo-Kα radiation) to estimate particle size, with the difference (blue) plotted underneath. R_{wp} = 12.3, χ^2 = 1.44.

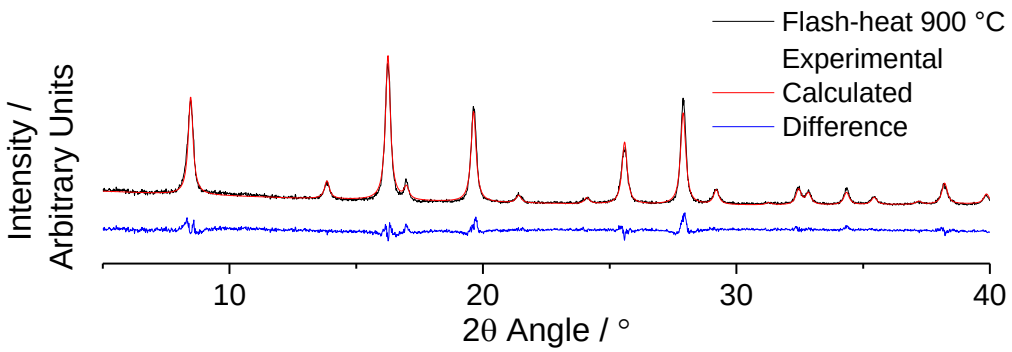

Figure 11.52 – Experimental (black) and calculated (red) diffraction patterns for sample MCO-335-0.4 (flash heat-treated at 900 °C for 10 min) from Rietveld refinement (set-up **b**, Section 2.1.4.1, Mo-Kα radiation) to estimate particle size, with the difference (blue) plotted underneath. R_{wp} = 12.8, χ^2 = 1.34.